

Universiteit
Leiden
The Netherlands

Structure and substructure in the stellar halo of the Milky Way

Pila Diez, B.

Citation
Pila Diez, B. (2015, June 16). *Structure and substructure in the stellar halo of the Milky Way*. Retrieved from https://hdl.handle.net/1887/33295

Version:	Not Applicable (or Unknown)
License:	Leiden University Non-exclusive license
Downloaded from:	https://hdl.handle.net/1887/33295

Note: To cite this publication please use the final published version (if applicable).

Cover Page



Universiteit Leiden



The handle http://hdl.handle.net/1887/33295 holds various files of this Leiden University dissertation.

Author: Pila Díez, Berenice
Title: Structure and substructure in the stellar halo of the Milky Way
Issue Date: 2015-06-16

Structure and substructure in the stellar halo of the Milky Way

Proefschrift

ter verkrijging van
de graad van Doctor aan de Universiteit Leiden,
op gezag van Rector Magnificus prof.mr. C.J.J.M. Stolker,
volgens besluit van het College voor Promoties
te verdedigen op dinsdag 16 juni 2015
klokke 11.15 uur

door

Berenice Pila Díez

geboren te Logroño, Spanje
in 1986

Promotiecommissie

Promotor:	Prof. dr. K. H. Kuijken	
Referent:	Prof. dr. E. Tolstoy	University of Groningen
Overige leden:	Prof. dr. H. J. A. Röttgering	University of Leiden
	Prof. dr. S. F. Portegies Zwart	University of Leiden
	Dr. A. G. A. Brown	University of Leiden
	Dr. H. Hoekstra	University of Leiden

ISBN 978-90-9029080-5

An electronic version of this thesis is available at http://openaccess.leidenuniv.nl
Its content can be copied and distributed provided that permission is granted for all journal-published material. Credit should be given to the author for original content or to the authors of any referenced material.

The work described in this thesis is part of the Netherlands' Research School for Astronomy (NOVA).

The cover shows an image of M54, a globular cluster of the Sagittarius dwarf galaxy (Credit:ESO/VLT, ID:eso1428a). The foreground displays an edited picture of Leiden's Observatory (Oude Sterrewacht). Both the foreground and the graphic design are copyright of the thesis author. The font is Charter Bold, by Bitstream Inc. (designer: Matthew Carter).

To my parents, for opening my eyes to Science and the night sky;
to Jesús, for everything past, present and future.

Believe those who are seeking the truth;
doubt those who have found it.
(André Gide, 1952)

Contents

1 Introduction **7**
1.1 A Universe of galaxies 7
1.2 Stellar tracers for Galactic structure 12
1.3 The Milky Way 18
1.4 This thesis 22

2 A skewer survey of the Galactic halo from deep CFHT and INT images **23**
2.1 Introduction 24
2.2 Observations and data processing 24
2.3 Stellar radial density profiles 31
2.4 Discussion 40
2.5 Conclusions 47

3 A KiDS view on the structure of the Galactic halo **49**
3.1 Introduction 50
3.2 Survey and stellar catalogues 50
3.3 Stellar radial density profiles 53
3.4 Discussion 66
3.5 Conclusions 72

4 Finding halo streams with a pencil-beam survey – new wraps in the Sagittarius stream **75**
4.1 Introduction 76
4.2 Observations and data processing 77
4.3 The Sagittarius stream 85
4.4 The Palomar 5 stream and the Orphan stream 96
4.5 Conclusions 100

5 A search for stellar tidal debris of defunct dwarf galaxies around globular clusters in the inner Galactic halo **103**
5.1 Introduction 104

5.2 Observations and data reduction 106
5.3 Methodology 112
5.4 Results 124
5.5 Discussion 129
5.6 Conclusions 144

6 Search for halo substructure in KiDS **147**
6.1 Introduction 148
6.2 Observations and data processing 149
6.3 Search for overdensities 149
6.4 Discussion 167
6.5 Conclusions 169

Bibliography **171**

Samenvatting **179**

Summary **183**

Curriculum Vitae **187**

Acknowledgements **189**

Abbreviations

BHB Blue Horizontal Branch

CMD Colour Magnitud Diagram

EBS Eastern Band Structure

MSTO Main Sequence TurnOff

Pal 5 Palomar 5

RC Red Clump

RGB Red Giant Branch

Sgr Sagittarius

Technical and instrumental acknowledgements

This thesis is based on observations made with ESO Telescopes at the La Silla Paranal Observatory as part of the KiDS public survey.

It is also based on observations made with the Isaac Newton Telescope through program IDs I10AN006, I10AP005, I10BN003, I10BP005, I11AN009, I11AP013 and MegaPrime/MegaCam, a joint project of CFHT and CEA/IRFU, at the Canada-France-Hawaii Telescope (CFHT). The Isaac Newton Telescope is operated on the island of La Palma by the Isaac Newton Group in the Spanish Observatorio del Roque de los Muchachos of the Instituto de Astrofísica de Canarias. The CFHT is operated by the National Research Council (NRC) of Canada, the Institut National des Science de l'Univers of the Centre National de la Recherche Scientifique (CNRS) of France, and the University of Hawaii.

Most of the data processing and analysis in this work has been carried out using Python and, in particular, the open source modules Scipy, Numpy, AstroAsciiData and Matplotlib. Topcat and Stilts have been used for occasional table manipulation.

Chapter 1

Introduction

1.1 A Universe of galaxies

Galaxies are the fundamental blocks of the Universe's large scale structure. Galaxies are gravitationally bound entities that reside at the centre of dark matter (sub)haloes, and contain sufficient baryonic matter to trigger star formation, localized chemical and nuclear reactions that produce electromagnetic radiation. Galaxies consist of gas, dust, icy molecules, stars, planets and dark matter in varying proportions. Gas, dust and ice molecules together with planets' interiors, surfaces and atmospheres are involved in chemical reactions, and the basic elements of the Periodic Table —ranging from hydrogen to iron—are involved in the nuclear reactions that take place in the stellar interiors. Because of the different energies at which these processes take place, they show their signatures in electromagnetic radiation over a wide range of wavelengths.

Galaxies come in a wide range of sizes, masses, and shapes, which are a reflection of their evolutionary stage and past history, and they can be classified in the Hubble diagram (see Figure 1.1). Irregular galaxies host stars that follow complex orbits without a well defined rotation centre, and may be abundant in gas and dust (with the exception of dwarf irregulars). Spiral galaxies are also gas-rich star-forming systems but, unlike irregular galaxies, they are rotation supported, resulting in a well-defined set of structural components: an inner bulge, a disk with spiral arms, an ellipsoidal halo and, sometimes, a central bar. It is believed that the presence or absence of a bar is dependent on the mass available in the galaxy –especially the central mass of the galaxy– and on the gas+stars to dark matter mass ratio, as well as on its interaction history. These two types of galaxies contain clouds of cold gas dense enough to undergo gravitational collapses and keep producing stars. By contrast, elliptical galaxies are no star-forming and ellipsoidal, with their stars having metastable orbits around a well defined centre. Elliptical galaxies, however, have also by and large exhausted or heated their cold molecular gas, and cannot form any new generation of stars. For this reason their

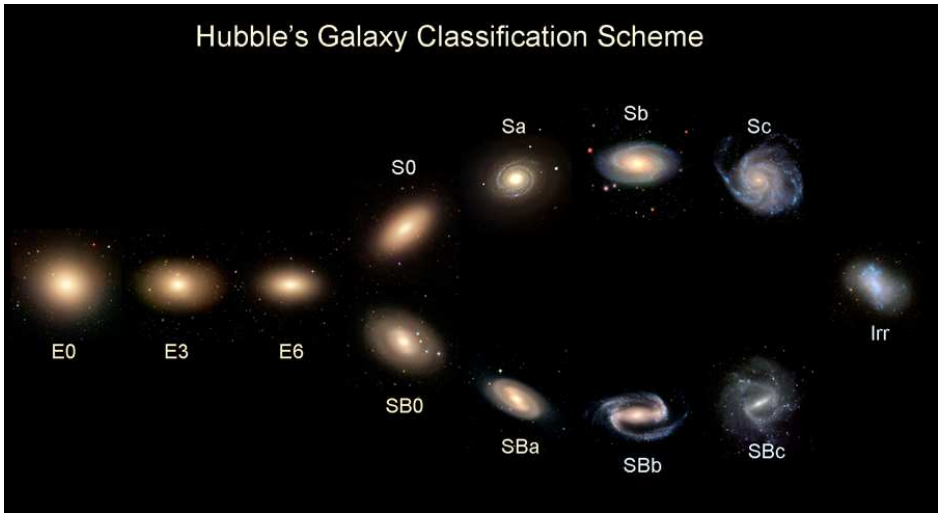


Figure 1.1: Hubble's classification diagram, as built by the Galaxy Zoo project. E indicate elliptical galaxies, S and SB indicate spiral and spiral-barred galaxies respectively, and Irr indicates the irregular type.

spectra are dominated by old low-mass stars. These two characteristics (stellar orbits and cold gas content) thus lead to morphological differences between types of galaxies and a fundamental difference in their stellar population make-up, which is reflected in their spectral energy distributions (SED).

Galaxies cover a large range of total luminosities, from $10^3 L_\odot$ to $10^{12} L_\odot$, giving rise to a relative classification of galaxies into (ultra-)faint, intermediate, bright or ultra-luminous galaxies. They can also have a variety of masses, from $10^5 M_\odot$ to $< 10^{13} M_\odot$ in total mass, leading to a classification into dwarf, medium and giant galaxies. Irregular and spiral galaxies are typically associated with the intermediate and smaller mass ranges, whereas elliptical galaxies are associated with all mass ranges. The current theory for galaxy formation links this observed distribution to their assembly history and evolution through the process of gravitational accretion (Cole et al. 1994), as we will see in the following section.

1.1.1 Galaxy formation and evolution

It is well known that a closed, isolated, isotropic and perfectly uniform system can be considered in equilibrium, and therefore will not undergo any evolution in the absence of external forces. To the best of our knowledge, the Universe is a closed, isolated and isotropic system, but it is not and was not a perfectly uniform system at the Epoch of Recombination and photon decoupling, as the Cosmic Microwave Background shows. This lack of uniformity is the reason why we observe a dynamic and evolving Universe, instead of a simple homogeneously

expanding Universe. However any theory of galaxy formation needs to explain how these inhomogeneities originated and how they evolved into an increasingly clustered and inhomogeneous state.

The theory of the Big Bang states that the Universe was born from a singularity in a very high density state that underwent a brief exponential expansion early on (the Inflation). It has continued to expand and cool since. The current paradigm for the early Universe is that primordial quantum fluctuations were amplified by the Inflation and left tiny density variations spread throughout the Universe, which grew through gravitational instability. These density variations were the seeds for current galaxies. As a small overdensity starts to gravitationally attract matter, the more matter it accretes, becoming an increasingly strong gravitational well. Eventually these density seeds accreted enough gas to form clouds that could (gravitationally) collapse and produce the first stars and galaxies. These protogalaxies in turn merged with each other into increasingly massive galaxies. This merging growth mechanism—known as the hierarchical formation scenario—comprises, together with the Big Bang theory, gravity and the early Universe observations, the current paradigm for galaxy formation (White & Rees 1978).

Gravitational interactions between galaxies can involve processes of four types. They can lead to mass growth or mass loss, as well as morphological and dynamical changes. These possible processes are high-speed encounters, galaxy mergers, tidal stripping and dynamical friction. Simply put, high-speed encounters are those in which the difference in velocity between the two galaxies is enough in comparison to their gravitational pull to prevent them from slowing down and becoming orbitally bound objects (i.e., their interaction is limited to one event), and they are characterized by high-speed processes that perturb the galaxies. Often this type of interactions require numerical simulations in order to be understood, but, in the simpler case in which the internal velocity dispersion of the perturbed galaxies is much smaller than the encounter velocity, the interaction can be approximated as a tidal shock, which causes cooling and expansion of the system, and potential mass loss.

Galaxy mergers are the direct result of a close encounter in which two systems have a sufficiently low orbital energy to make them slow down and mix with each other, eventually losing all morphological signs of one or both of the progenitors and becoming one integrated system. "Any bound orbit will eventually lead to a merger because the tidal interaction between two galaxies always transfers orbital energy into internal energy", but "if the angular momentum is high and if the orbital energy is not low enough, the merger will not happen in a Hubble time[1]" (Mo et al. 2010). Additionally, mergers can also happen between initially unbound galaxies, provided that the tidal interactions of the encounter drain sufficient orbital energy from the system. Merging events can be roughly separated into two types based on their progenitors mass ratio: major or minor. Major mergers are those involving two galaxies of similar masses (with a mass ratio lower than a factor of 4), whereas minor mergers are those involving two galaxies of quite

different masses. Major mergers cause the violent relaxation of the resulting remnant, and often lead to the quick consumption or expulsion of the cold gas. This eventually turns the resulting system into a galaxy populated by old stars with a red dominated spectrum. Minor mergers involve phase mixing and Landau damping, and often result in a system that resembles (morphologically speaking) the most massive progenitor.

Tidal stripping entails the removal of material from the outer regions of a collisionless system as a result of tidal forces. This process is typical in orbitally bound systems (metastable) or in systems that are on the way to becoming orbitally bound or fully accreted (unstable). The key element of this process is that the tidal forces, in combination with the rotation centrifugal forces of the system, exceed the binding forces for some of the material in the satellite body—the material situated further than a critical distance from the centre of the satellite, a distance called the tidal radius. As a result of tidal stripping, tidal streams and tails form out of the stripped material, leading and trailing the satellite approximately along its orbit. Tidal tails can also be observed not only in satellite galaxies or globular clusters (Mateo et al. (1996),Odenkirchen et al. (2001)) but also in the merging of (disk) galaxies (Toomre & Toomre 1972).

Finally, dynamical friction is the process by which a galaxy moving in a much less dense environment experiences a drag as it transfers energy and momentum to the particles in the environment. This causes orbits to decay with time, bringing the galaxy experiencing the friction towards the centre of the host's potential well. Since the drag force is proportional to the square of the mass of the galaxy, there is a mass segregation in the orbital decay, bringing more massive galaxies deeper into the gravitational well, and leaving them more susceptible to mergers or tidal stripping.

There is abundant observational evidence for all these processes in the local Universe: stripped gas and stellar streams around galaxies (Figure 1.2), galaxy collisions (Figure 1.3) or even ram pressure stripping in galaxies falling through a galaxy cluster (Figure 1.4). However there is also ample evidence of these processes having occurred earlier in the Universe's history. Medium and high-redshift research shows statistical evidence for the merger, mass growth and type-evolution of galaxies (from star-forming to quiescent), as summarized in Figure 1.5 (Muzzin et al. 2013). This figure illustrates how the number density of quiescent galaxies has been increasing over time for all mass ranges, and that the high-mass cut-off has grown with time (indicating mergers). Simultaneously, the number density of high mass star-forming galaxies has been virtually constant, while low-mass star-forming galaxies outnumber the quiescent ones (indicating mergers and an eventual quenching of star-forming galaxies). This, in combination with the typical spectral energy distribution (SED) of quiescent and star-forming galaxies, supports the hierarchical formation scenario and the morphological and mass

[1]The Hubble time is an estimate for the age of the Universe, based on the approximation that the Universe has always been expanding at the same rate it does today.



Figure 1.2: Faint stellar tidal streams around the edge-on galaxy NGC 5907. Image credit: R. J. Gabany in collaboration with Martínez-Delgado et al. (2010a).

evolution of galaxies.

Numerical cosmological simulations have provided a context for these observations, and have shown that the underlying mechanisms for hierarchical formation (the primordial small density variations, in combination with cold dark matter and gravity) can actually reproduce the observed history and match (most of) the current observations. Once the simulations complete the (currently ongoing) transition from dark matter-only to ones that include hydrodynamics (gas) and stellar processes like feedback, stellar winds, or central AGNs, and overcome current resolution limitations, these comparisons can grow further in sophistication. Together with improvements in the observed census of the properties of galaxies, such research will further refine our understanding of the processes that drive galaxy formation.

1.1.2 A unique test case: the Milky Way

The Milky Way—a medium-sized, modestly star-forming spiral galaxy—poses a unique case study of galactic structure, evolution and minor merging in the Local Universe. As observers located within the Milky Way, we have a 360 deg view of the Galaxy, in contrast with the one-directional view (either face-on or edge-on) we have of any other galaxy. Additionally, as opposed to what happens with most other galaxies except those in our closest vicinity, in the Milky Way we have access to spatially resolved stellar populations and spatially resolved kinematics. This means that the disk, bulge, spiral arms and halo can be studied not just as bulk components with major features, but as resolved stellar systems. Finally

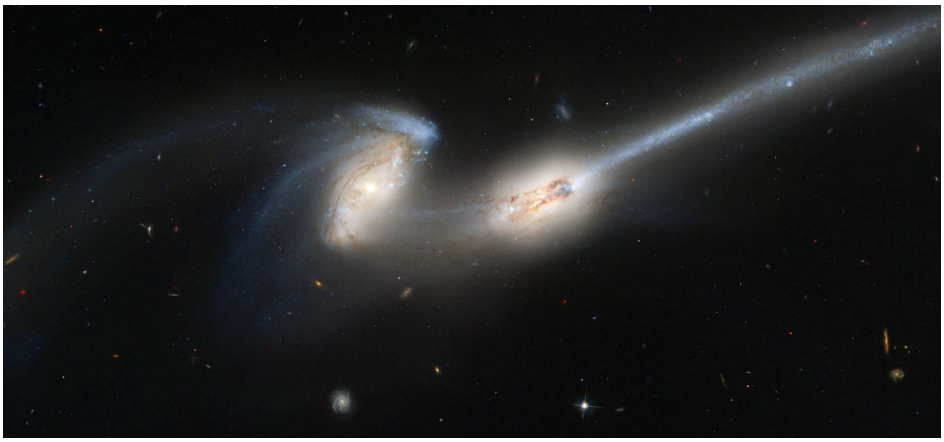


Figure 1.3: The Mice galaxies (NGC 4676) in the process of merging. Tidal tails can be observed. Image credit: NASA, H. Ford (JHU), G. Illingworth (UCSC/LO), M.Clampin (STScI), G. Hartig (STScI), the ACS Science Team, and ESA – APOD 2004-06-12.

our proximity allows us to probe intrinsically fainter stars and therefore study obscured or distant regions. Similarly it gives us the possibility to build a very accurate census of satellite galaxies, potentially complete at the ultra-faint end save the zone of avoidance determined by the Galactic disk.

The study of the Milky Way through detailed analysis of its resolved stellar populations is known as "Galactic Archaeology".

1.2 Stellar tracers for Galactic structure

As stars orbit their host galaxy, they suffer the perturbative influence of molecular clouds, star clusters, dark matter, spiral arms or nearby massive objects, even if overall the gravitational potential is close to a steady state. Spiral galaxies consist of a central stellar bulge, a stellar thin disk and (potentially) a thick disk, and a stellar halo. The stars in the disk are affected by transient spiral density waves that accelerate and decelerate them in their orbits, but on the whole stellar disks can be considered to be in a quasi-steady state. This may not be true for the stars in the halo, however: at large radii dynamical times are long, and hence perturbations and accretions due to minor mergers and subhaloes persist over many Gyr. Studying the distribution, kinematics, chemical composition and age of stars in the intermediate and outer halo can therefore provide significant understanding on the structure, evolution and accretion history of the Galaxy. This task can be carried out using photometric data, spectroscopic data or simulations. Particularly, when using only photometric techniques, combining measurements of different types of stars at distinct evolutionary stages, with diverse ages and

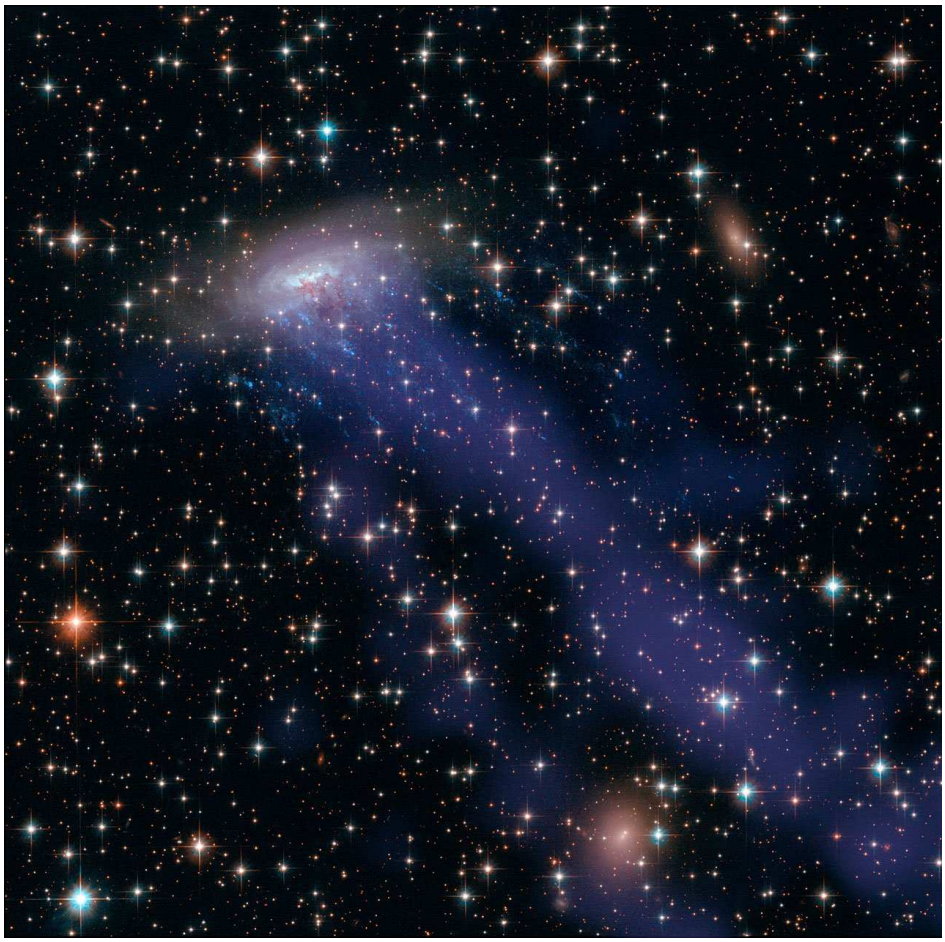


Figure 1.4: A gas stream in X-rays (Chandra X-Ray Observatory), ram pressure stripped from galaxy ESO 137-001 as it falls through the galaxy cluster Abell 3627 (Hubble Space Telescope). Credit: NASA, ESA, CXC.

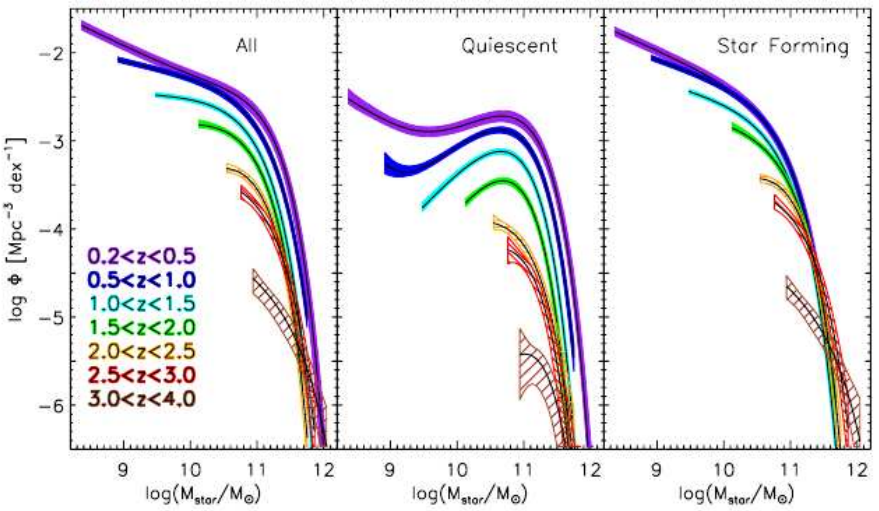


Figure 1.5: Galaxy number density distribution along different stellar masses for different redshifts. The different panels represent the general distribution (left), the quiescent population (centre) and the star forming population (right). Credit: Muzzin et al. (2013).

metallicities and located in different regions can help build a full picture of the present-day Galaxy as well as its formation and accretion history.

1.2.1 The H-R diagram

One of the fundamental photometric tools for resolved galactic Astrophysics or resolved stellar populations is the Hertzsprung–Russell diagram (H-R diagram).

The strength of the H-R diagram (left panel on Figure 1.6) lies in its descriptive and classifying power, applicable both to fundamental and observable properties of stars. The H-R diagram locates stars in a 2-dimensional parameter space of surface temperature and intrinsic brightness, in which stars nicely separate into several evolutionary stage loci. From an observational point of view, the H-R diagram is constructed from the spectral type or photometric colour of the stars and their absolute magnitude, which requires to have an estimate for each star's distance.

Stars in the H-R diagram can be grouped along isochrones (right panel on Figure 1.6). These, as their name indicates, are the loci for stars of equal age (and equal composition) but different mass in the H-R diagram. Isochrones characterize stars that have been born from the same parent cloud and are particularly useful to trace groups of stars that have similar age and are located at similar distances.

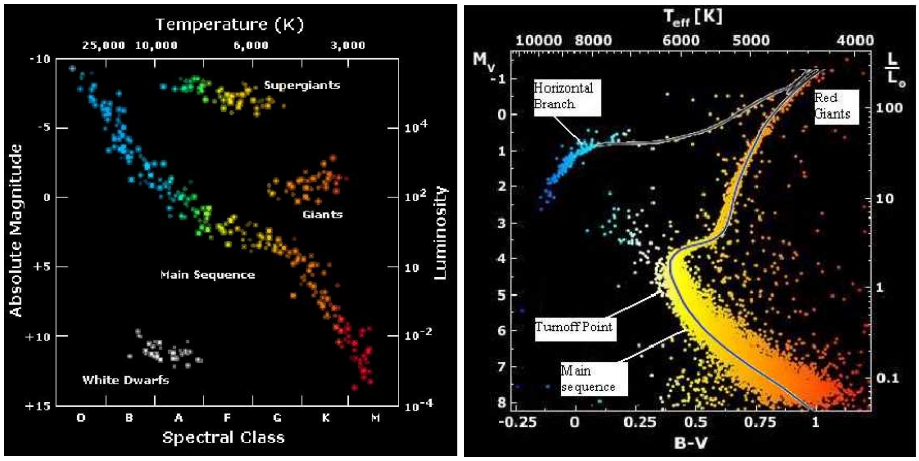


Figure 1.6: Left: the Hertzsprung–Russell diagram of stars. The y-axes represent absolute magnitude (left) and luminosity (right) ad the x-axes represent effective temperature (top) and spectral class (bottom). Right: The colour magnitude diagram for globular cluster M55; a theoretical isochrone for M55 is shown (black line). The y-axes represent absolute magnitude (left) and luminosity (right), whereas the x-axes represent effective temperature (top) and colour (bottom). Credits: Cristopher Schneider (left), and B.J. Mochejska and J. Kaluzny (right).

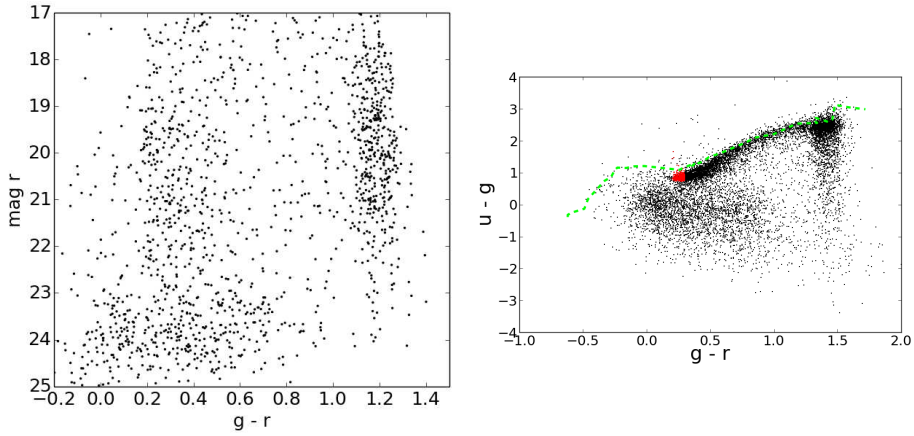


Figure 1.7: Left: Colour magnitude diagram (CMD) in the direction of galaxy cluster Abell 990; stars at different evolutionary stages are not distinctly grouped mainly because of the distance effect on apparent magnitudes. Right: Colour colour diagram for a set of CFHT-INT fields (chapter 3). The green dashed line indicates the theoretical location of the main sequence stars; the black dots indicate the observed colours for point-like sources.

1.2.2 Observational characteristics of stellar populations

In practice, the observational equivalent of an H-R diagram is constructed from the apparent magnitude and a photometric colour (the ratio of the flux of a star measured through two filters), and is called a colour magnitude diagram (CMD). In such a diagram, the different evolutionary stages can mix severely along the y-axis when there is a distribution of distances along the line of sight. Similarly, varying metallicities and ages bring small variations in temperature for stars with the same mass and evolutionary stage, moderately broadening in colour the stellar loci and evolutionary tracks. These effects make it impossible to directly recognize types of stars (see Figure 1.7, left panel) unless an overdense stellar population with a well defined distance is present in the observed field. Conversely, because photometric colours are distance-independent, it is possible to some extent to recover the information contained within the H-R diagram by constructing an observation colour-colour diagram (Figure 1.7, right panel). This type of diagram can be successful in recovering a main sequence locus, for instance; but, on the other hand and depending on the set of filters, might be unsuccessful in fully separating the main sequence from the supergiants at the red end (Covey et al. 2007).

Stellar populations encode part of the formation history of any galaxy, since they contain sibling stars formed at the same time from the same parent cloud. If stars from a given stellar population are still confined to a small region (in

young open clusters that have not had time to dissolve yet or in the halo, where dynamic time scales are longer), a clear overdensity can be identified in the form of an isochrone in a CMD, and a statistical approach can be used to accurately characterize its age and metallicity by fitting theoretical isochrones. Hence determining the birth-epoch of the stars and their contribution to the Galaxy's structure.

The particular relevance of theoretical isochrones for Galactic Archaeology lies not only in their power to characterize the age and the metallicity of a given stellar population, but also on the possibility of estimating its distance to us provided that the other two parameters (metallicity and age) are known. The metallicity of a star can be accurately measured through spectroscopy, and its age can be derived with reasonable accuracy assuming a distance or a mass is known. However, with just photometric data these parameters can only be estimated provided that very accurate colours are known. In such a case the star can also be classified according to its spectral type and evolutionary stage.

Thorough models of stellar interiors and stellar atmospheres have been developed in the last decades to derive expected absolute magnitudes for specific evolutionary stages and build robust sets of theoretical isochrones (Girardi et al. (2010); Marigo et al. (2008); Dotter et al. (2008a), for instance). However, on top of observational uncertainties and despite the very precise theoretical isochrones, some intrinsic challenges remain since an age-metallicity degeneracy in absolute magnitude and colour is present for some evolutionary stages. The reason for this is, on the one hand, that an increasing metal content always cools the temperature of stellar atmospheres and decreases their luminosity because of the associated photon absorption. This moves the stars redwards and faintwards in the H-R diagram. On the other hand, the age of stars also affects their effective temperature, with different evolutionary stages being more sensitive to age than others (some examples are provided in section 1.2.3).

1.2.3 Stellar evolution stages suitable for Galactic studies

Especially relevant to Galactic Archaeology are those stars that, because of a small scatter in their intrinsic brightness, a bright evolutionary stage or a high number density, can be used as distance tracers, age tracers or spatial density tracers (respectively). A brief description and characterization of those types now follows.

Main sequence stars are by far the most abundant type of stars, because all stars must undergo this phase at the beginning of their lives and the less massive stars can spend many Gigayears in this stage. However, precisely these most abundant low-mass main sequence stars are intrinsically faint, and main sequence stars cover a continuous range of absolute magnitudes. Both facts make them poor distance and spatial density tracers. However, there is one exception, that of the so called main sequence turnoff point (MSTO), which—for a given population of stars with the same age—represents the mass or spectral type for which stars are currently abandoning the core hydrogen-burning phase. Provided that an estimate

for the distance to the stellar population exists (from Cepheid or RR Lyrae stars, from horizontal branch stars or from the tip of the red giant branch stars), a fit to the MSTO can be used to determine the age and metallicity of the population. On the other hand, if the age and metallicity of a stellar population are known from spectroscopic works, a theoretical isochrone can be used, in combination with the distance modulus, to estimate the distance.

The red giant branch (RGB) stars are low-to-intermediate mass stars ($0.3 - 8M_{\odot}$) that have finished fusing hydrogen into helium in their cores but are still fusing it in a shell surrounding the helium core. They are intrinsically bright and relatively numerous, which makes them good spatial density tracers. Furthermore the tip of the branch (TRGB) has an intrinsic absolute magnitude ($M_I = -4.0 \pm 0.05$, Madore & Freedman (1993), Frayn & Gilmore (2003)), which also makes them accurate distance tracers when a single population can be identified in the CMD.

The red clump (RC) is an overdensity in the H-R diagram consisting of cold (either metal-rich or young) horizontal branch stars, and therefore already fusing helium into carbon in their cores. The RC has an intrinsic absolute magnitude thought to be independent of age and metallicity ($M_r = 0.6$, Bellazzini et al. (2006c)), a very narrow colour range (a very specific temperature, Correnti et al. (2010)), it is easily identified in the CMD and it indicates an intermediate age population.

The blue horizontal branch (BHB) stars are also helium-burning stars, located blueward of the RRLyrae stars. They are the least massive and oldest among the horizontal branch stars, and very metal poor. They are intrinsically bright and blue and therefore one of the most practical distance tracers in the halo, provided that the BHB tail is avoided. They have a specific colour-colour range (Deason et al. 2011) and also a specific absolute magnitude ($M_g = 0.5 \pm 0.1$), which makes them accurate distance tracers. Nonetheless, RR Lyrae stars, which are pulsating HB stars in the instability strip, are optimal distance indicators owing to the relation between their pulsating period and their absolute magnitude.

Substantial and continued efforts by the astronomical community have yielded accurate photometric selection criteria for these types of stars and reduced contamination by stellar types with similar colours. This conveniently allows for practical multi-band analytic star selection and direct distance photometric parallax calculations of BHB, RC, TRGB and MSTO stars.

1.3 The Milky Way

As briefly stated above, the Milky Way is a disk spiral galaxy, moderately star-forming and medium sized. It is one of two dominant galaxies in the so called Local Group halo, together with the Andromeda Galaxy. Both galaxies are heading towards each other and will collide in approximately 4 Gyr, eventually producing a merger remnant.

The dynamic constraints from satellite galaxies and globular clusters indicate

that the dark matter content of the Galaxy (that of the dark matter halo) is $1 - 3 \cdot 10^{12} M_{\odot}$(Battaglia et al. 2006), whereas the baryonic mass is estimated to be less than $\sim 10^{11} M_{\odot}$. About 75% of the baryonic mass is located in the disk, and most of the remaining baryonic mass resides in the bulge. On the other hand, the dark matter mass contained within 50 kpc (the distance to the Large Magellanic Cloud) is only about one quarter of the estimated total (Sakamoto et al. 2003).

1.3.1 The structure of the Milky Way

The central 3 kpc of the Milky Way are dominated by a bulge, with a peanut shape and matching kinematics, indicating the presence of a bar. The bulge is mainly composed of an old population of stars, with a small range of ages but a large dispersion in metallicity and a metallicity gradient along the minor axis of the bulge (Zoccali et al. 2008). This suggests that the Milky Way's bulge is a mixture between a classical bulge (originated early in the history of the Galaxy) and a pseudo-bulge originated from a buckled disc, but the time of this buckling and therefore the age of the bulge as a structure is yet unclear.

The disk hosts most of the cold gas and dust of the Galaxy, and therefore most of the star formation. It is often described as a combination of two subcomponents: a thin disk with a vertical scale height ~ 300 pc and extending not further out than $R_{GC} \leq 15$ kpc, and a thick disk with scale height ~ 900 pc and only old stars. Additionally, the disk is warped in its outer regions. The actual origin of the thick disk is still unclear. Possible explanations are thin disk heating, early low-inclination satellite accretions and an early turbulent gas disk that gives rise to star formation and eventually settles into a thin disk. Moreover, the presence of the accretion substructure denominated the Monoceros ring confuses the proper delimitation of the thick disk. One of the main challenges for the future consists of finding a proper and robust definition for these two components, be it kinematical, chemical, structural or, preferably, dynamical.

The stellar halo is a spheroidal component that spans all radii from the central parts of the bulge out to probably 100 kpc. It contains globular clusters and stellar debris, as well as some of the satellite galaxies. The stellar debris can take the form of shells and clouds (when the material has long ago departed from the progenitor and it is populating the apogalacticon in wide, heating-up orbits) or the form of streams (elongated strips of stars in relatively round orbits or still close to the progenitor or the perigalacticon). Additionally, there are also ancient debris, but these are only recognizable in the phase space since by now they have already spatially mixed up (phase wrapped) with the rest of the halo. The ESA satellite Gaia, currently in operation, is expected to help unravel the halo phase space with unprecedented accuracy and reach the old heated debris contained within the disk and the inner halo. Current calculations indicate that only 60% of the halo's total luminosity density can be explained by a smooth ancient spheroidal component (Bell et al. 2008); the other 40% most likely has been accreted.

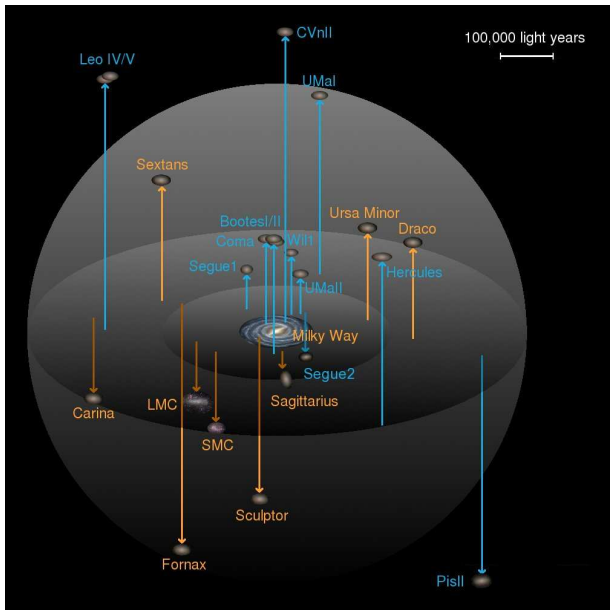


Figure 1.8: Satellite galaxies circa the Milky Way (incomplete list). Credit: J.T.A. de Jong, after J. Bullock.

1.3.2 The satellites of the Milky Way

The halo is dim and not very densely populated by stars, but interesting accretion phenomena take place in it. As soon as accurate extragalactic distance indicators became available, two prominent Southern sky objects, the Small and the Large Magellanic Clouds, were quickly identified as satellite galaxies orbiting the Milky Way. Later on, with the advent of radio observations, their tidal interaction with the Milky Way was discovered in the form of a gas bridge. However, only in 1996 the first evidence was gathered for a current disruption and cannibalizing event in the Milky Way: the Sagittarius dwarf galaxy (discovered in 1994) is being torn apart and assimilated by the Milky Way, in a stripping process that wraps two tails at least 180 deg around the Milky Way. Since then, with the advent of deep large-area surveys, many more satellite galaxies have been discovered within ~ 400 kpc of the Galactic centre, as well as several narrow and wide streams. The census of satellite galaxies (over 30, with 8 to 9 new additions just in 2015 and only 8 additions between the '30s and the '90s) and the census of stellar debris (inaugurated in 1996 and populated since 2006) have genuinely exploded in the last decade. It seems that, for now, the next discovery or improvement in the characterization is always one photometric tracer, one surface magnitude or one magnitude deeper away than allowed by the current telescopes.

In the years between the classification of the Magellanic Clouds as satellite

galaxies and the discovery of such a rich population of satellite dwarf galaxies, many Globular clusters—clustered groups of old stars and metallicities different from that of the field halo stars—have been discovered and added to the list of halo objects. They are systems with only one or two stellar populations and no detected dark matter content. Some of them are considered to be native to the Milky Way, while others are currently catalogued as natives of dwarf galaxy haloes accreted into the Milky Way's halo. The connection between globular clusters and the lowest-mass dwarf galaxies, their role in the galaxy formation scenario, and their differences with the field stars of the halo are yet to be fully understood and placed within a single picture of the formation and evolution of the halo.

1.3.3 Stars in the halo

Halo stars are typically found at very large heliocentric distances, making them hard to detect. However, their distances and their presence in lines of sight away from the disk makes them much easier to identify, both spatially and on CMDs. With CCD astronomy and the state-of-the-art $4-8$ meter telescopes, we have reached enough sensitivity to finally survey the halo in a systematic and statistically significant way, both photometrically and spectroscopically.

The halo is mainly populated by old, metal-poor stars. The main reason for this is that it is not an actively star-forming region in any galaxy. Cold molecular clouds are absent from our halo, since this type of gas easily sinks towards the disk, and only there acquires high enough densities to undergo a star-forming Jean's instability collapse. Therefore the halo is formed by old stars from early generations, whose parental clouds were barely enriched with outflowing metals from previous generations.

Since halo stars are old stars, all of its most massive stars (O, B and A spectral types) have by now finished their lives, and only the least massive of them can be observed as white dwarves. Typical halo main sequence turnoff point stars are of spectral type F, with early F and late A stars having already evolved into red giants and horizontal branch giants. As stated earlier, the brightness of red giants and horizontal branch stars makes them good distant halo tracers. And both the main sequence turnoff point and the white dwarf sequence are particularly interesting to photometrically determine the age of a given equidistant halo population. However the white dwarf sequence is even more costly to observe than the main sequence due to its intrinsic faintness. Therefore, the use of red giants and horizontal branch giants has been wide-spread and main sequence turnoff point stars have been exploited to some extent, but the use of the white dwarf sequence has been limited to specific targets (like globular clusters) or extremely deep Hubble Space Telescope archival data (Hansen et al. 2002, 2013).

The stars in the halo have specific chemical abundances that separate them from the disk stars and from the old bulge population. Similarly, specific chemical abundances can be used to separate average halo field stars from accreted stars born in satellite galaxies or globular clusters with a different metal enrichment history. The current and recent spectroscopic surveys are only the first wave

leading towards a full taxonomy of the stellar halo and a complete picture of its formation history.

Overall the hierarchical formation scenario offers a framework to interpret the minor merger history of the Milky Way, and it means that we can dynamically, spatially and chemically distinguish two broad groups of stars in the halo: those belonging to the smooth field component and those accreted, which can be dynamically cold or already spatially-mixed.

1.4 This thesis

In this thesis we target the stellar halo of the Milky Way with the aim of understanding its structure, stellar populations and current accretion history. In chapters 2 and 3 we address the structural properties of the smooth component of the stellar halo. In particular we select near main sequence turnoff point stars and use them to build stellar density profiles along several lines of sight. We fit stellar halo models to these density profiles, derive the structural parameters for the best fits and determine the most plausible model. In chapter 4 we develop an algorithm to recover halo overdensities in the form of main sequence signatures from Colour Magnitude Diagrams where a foreground and background statistical subtraction to enhance the signal is not possible because of the absence of nearby control fields. We apply this method to several fields and successfully measure distances to the Orphan stream, the Palomar 5 stream and the Sagittarius stream, while finding potentially new weak overdensities. In chapter 5 we apply this method to the search for streams and underlying adjacent stellar populations around globular clusters. And, finally, in chapter 6 we explore the KiDS data release 1 and 2 footprints in search for halo substructure and overdensities. We trace the Sagittarius stream in the southern sky using main sequence turnoff point stars, and we also identify the Virgo Overdensity, the Eastern Band Structure, the Sagittarius stream and a Palomar 5 tail in the northern hemisphere. We search for potentially new overdensities such as cold streams, satellite galaxies or globular clusters but find none in the area so far probed. We conclude by reporting the future expectations for up-coming KiDS data releases.

Chapter 2

A skewer survey of the Galactic halo from deep CFHT and INT images

Authors

B. Pila-Díez, J.T.A. de Jong, K. Kuijken, R.F.J. van der Burg and H. Hoekstra

Abstract

We study the density profile and shape of the Galactic halo using deep multi-colour images from the MENeaCS and CCCP projects, over 33 fields selected to avoid overlap with the Galactic plane. Using multicolour selection and PSF homogenization techniques we obtain catalogues of F stars (near-main sequence turnoff stars) out to Galactocentric distances up to 60kpc. Grouping nearby lines of sight, we construct the stellar density profiles through the halo in eight different directions by means of photometric parallaxes. Smooth halo models are then fitted to these profiles. We find clear evidence for a steepening of the density profile power law index around $R = 20$ kpc, from -2.50 ± 0.04 to -4.85 ± 0.04, and for a flattening of the halo towards the poles with best-fit axis ratio 0.79 ± 0.02. Furthermore, we cannot rule out a mild triaxiality ($w = 0.88 \pm 0.07$). We recover the signatures of well-known substructure and streams that intersect our lines of sight. These results are consistent with those derived from wider but shallower surveys, and augur well for upcoming, wide-field surveys of comparable depth to our pencil beam surveys.

Accepted for publication in Astronomy & Astrophysics

Preprint in arXiv:1502.02460 [astro-ph.GA]

2.1 Introduction

The stellar halo of the Milky Way only contains a tiny fraction of its stars, yet it provides important clues about the formation of the Galaxy and galaxy formation in general. Within the paradigm of hierarchical structure formation, galaxies evolve over time, growing by means of mergers and accretion of smaller systems. While in the central parts of galaxies the signatures of such events are rapidly dissipated, the long dynamical timescales allow accretion-induced substructures to linger for Gigayears in their outermost regions. Thus, the stellar structure of the outer halos of galaxies such as the Milky Way can help constrain not only the formation history of individual galaxies, but also cosmological models of structure formation.

Owing to the intrinsic faintness of stellar halos, the Milky Way is our best bet for a detailed study of such structures. However, even studying the Galactic stellar halo is fraught with difficulties; very sensitive data are required to probe stars at these large distances (out to 100 kpc), and spread over sufficiently large areas to constrain the overall structure as well as localized substructures. In recent decades the advent of CCD-based all-sky surveys such as the Sloan Digital Sky Survey (SDSS York et al. 2000; Ahn et al. 2014) in the optical and the 2 Micron All Sky Survey (2MASS Skrutskie et al. 2006) in the infrared have unlocked unprecedented views of the outer regions of the Galaxy. This has led to the discovery of many previously unknown substructures (e.g. Newberg et al. 2002; Belokurov et al. 2006b; Grillmair 2006b; Belokurov et al. 2007b; Jurić et al. 2008; Bell et al. 2008) and to improved knowledge of the overall structure in these outskirts (e.g. Chen et al. 2001; Jurić et al. 2008; de Jong et al. 2010; Sesar et al. 2010a, 2011; Faccioli et al. 2014). Nevertheless, most of these recent analyses are still limited to either the inner parts of the stellar halo ($R_{GC} \leq 30$ kpc) or to particular, sparse stellar tracers (e.g. K-giants or RR Lyrae).

In this paper we use deep photometry obtained with the Canada-France-Hawaii Telescope (CFHT) MegaCam and the Wide Field Camera (WFC) at the Isaac Newton Telescope (INT), scattered over a large range of Galactic latitudes and longitudes to probe main sequence turn-off (MSTO) stars out to distances of 60 kpc. Combining our data into eight independent lines of sight through the Galactic halo, we are able to constrain the overall structure of the outer halo, and to probe the substructure in these outermost regions. In section 2 we describe the data set used for this analysis and the construction of our deep star catalogues. Section 3 presents the derived stellar density profiles and smooth Galactic model fits. We discuss our results in section 4 and present our conclusions in section 5.

2.2 Observations and data processing

2.2.1 Survey and observations

We use g and r images from the MENeaCS and the CCCP surveys (Sand et al. 2012; Hoekstra et al. 2012; Bildfell et al. 2012) together with several archival

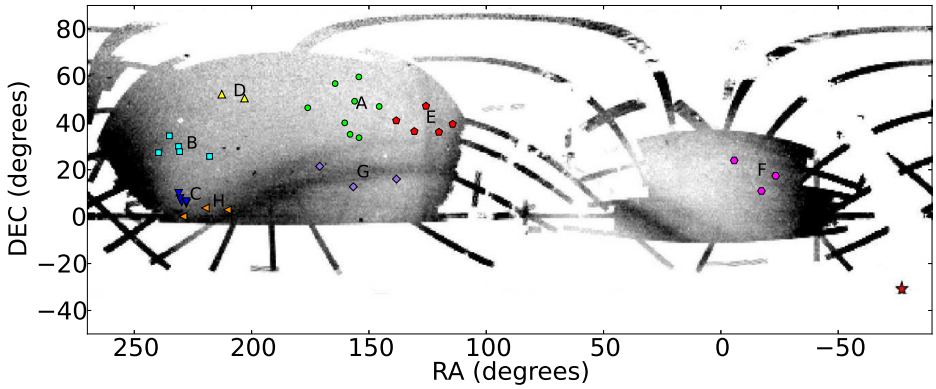


Figure 2.1: Equatorial map showing the position of all the fields used in this work. The different colours and symbols indicate how the fields have been grouped to calculate the different density profiles. The background image is the SDSS-DR8 map from Koposov et al. (2012), which shows the footprint of the Sagittarius stream and the location of the Sagittarius dwarf galaxy. When grouping the fields, we have also taken into account the presence of this stream, the Triangulum-Andromeda overdensity, and the anticentre substructures (ACS, EBS, and Monoceros), in trying to combine their effect in certain profiles and avoid it in others.

cluster fields from the CFHT-MegaCam instrument. We combine these data with U and i images from a follow-up campaign with the INT-WFC instrument (van der Burg et al., in prep.). Whereas these surveys targeted a preselected sample of galaxy clusters, the pointings constitute a "blind" survey of the Milky Way stellar halo since their distribution is completely independent of any prior knowledge of the halo's structure and substructure.

Our pointings are distributed over the region of the sky visible to both the CFHT and the INT (see Figure 2.1). To optimize the star-galaxy separation (see section 2.2.2) we restrict our analysis to exposures with image quality of subarcsecond seeing, typically $<\approx 0.9$ arcsec in the r band. This limitation, combined with the varying fields of view and observing conditions between the data sets, leads to pointing footprint sizes that range between 0.24 and 1.14 deg^2.

2.2.2 Image correction of the PSF distortion [and implications for the star-galaxy separation]

Previous research by our group has shown that the performance of standard star-galaxy separation methods based on the size and ellipticity of the sources can be improved by homogenizing the point-spread function (PSF) across an image prior to its photometric analysis (Pila-Díez et al. 2014). In addition, such a correction also provides the benefit of allowing us to perform fixed aperture photometry and colour measurements.

In order to homogenize the PSF of our images, we use a code (Pila-Díez et al. 2014) that, as a first step, takes the shape of the bright stars in a given image and uses it to map the varying PSF and, as a second step, convolves this map with a spatially variable kernel designed to transform everywhere the original PSF into a gaussian PSF.

2.2.3 Catalogues

From the PSF-homogenized exposures we create photometric catalogues using Source Extractor (Bertin & Arnouts 1996). For the g and the r data, we stack the different exposures in each band to create a single calibrated image, and we extract the band catalogues from them. We perform a star-galaxy separation based on the brightness, size and ellipticity of the sources and we match the surviving sources in the two catalogues to produce a gr-catalogue of stars for each field of view (see Pila-Díez et al. (2014)). The limiting magnitudes of these gr star catalogues reach $m_{AB} \sim 25.0$ at the 5.0σ level in the r band.

For the U and the i fields of view, we produce several photometric catalogues, one for each individual exposure. We correct the magnitudes in the i catalogues for the dependency of the illumination on pixel position. For each pointing and band, the exposure catalogues are calibrated to a common zero point and combined to produce a single-band catalogue. In these single-band catalogues, the resulting magnitude for each source is calculated as the median of the contributions of all the individual exposures. At this point the U and the i magnitudes are converted from the INT to the CFHT photometric system using the following equations, which we derive by calibrating our mixed INT-CFHT colours to the colour stellar loci of the CFHT Legacy Survey (Erben et al. (2009), Hildebrandt et al. (2009)):

$$i_{MegaCam} = i_{INT} - 0.12 * (r_{Mega} - i_{INT}) \quad (2.1)$$

$$u_{MegaCam} = u_{INT} - 0.15 * (u_{INT} - g_{Mega})\,. \quad (2.2)$$

Finally we position-match the sources from the U-, the i- and the gr-catalogues to create a final catalogue of stellar sources for each field of view. These final $ugri$-catalogues are shallower than the gr-catalogues because of the lesser depth of the i and the U observations (see Table 2.1). Figure 2.2 shows the colour-magnitude diagrams (CMDs) for the final $ugri$ and gr catalogues (top and centre, respectively), and the difference between them (bottom). The bottom panel highlights that, in the colour regime of the halo ($0.2 < g - r < 0.3$), the combination of the four bands removes mainly very faint, unresolved galaxies.

We correct for interstellar extinction using the maps from Schlegel et al. (1998) and transform the magnitudes in the $ugri$-stellar catalogues from the CFHT to the SDSS photometric system. For this we use the equations on the Canadian

Table 2.1: Groups of pointings as shown in Figures 2.1, 2.5, 2.6 and 2.8. The table shows the central coordinates for each group, the number of individual fields of view contributing to it, its total area and the stellar completeness limit in the r band.

Group	RA (deg)	Dec (deg)	l (deg)	b (deg)	$n_{\rm fields}$	Σ (deg^2)	$\rm mag_{lim,r,*}$
A	160.654338	43.98310	171.335811	59.15040	8	5.60	22.8
B	231.593130	29.13513	45.577138	55.93598	5	3.98	22.7
C	229.347757	6.91624	9.425402	49.92775	4	3.44	24.1
D	210.062933	51.67173	99.735627	62.24580	2	0.64	23.4
E	121.918411	41.20348	179.233500	31.26694	5	2.73	22.7
F	342.735895	17.09581	86.019738	-36.99391	3	2.17	23.2
G	157.028363	17.15674	222.142793	55.48268	3	2.02	23.1
H	220.659749	2.00187	354.337092	53.38989	3	2.04	24.2

Astronomy Data Center MegaCam website[1]

$$u_{MegaCam} = u_{SDSS} - 0.241 \cdot (u_{SDSS} - g_{SDSS}) \quad (2.3)$$

$$g_{MegaCam} = g_{SDSS} - 0.153 \cdot (g_{SDSS} - r_{SDSS}) \quad (2.4)$$

$$r_{MegaCam} = r_{SDSS} - 0.024 \cdot (g_{SDSS} - r_{SDSS}) \quad (2.5)$$

$$i_{MegaCam} = i_{SDSS} - 0.003 \cdot (r_{SDSS} - i_{SDSS}) \quad (2.6)$$

and invert them to turn our measurements into SDSS magnitudes. Subsequently we calibrate each field directly to SDSS using stellar photometry from DR8. The resulting photometry matches the colour-colour stellar loci of Covey et al. (2007) as shown in Figure 2.3. Unless explicitly stated otherwise, all magnitudes in this paper are expressed in the SDSS system.

In order to reduce the noise when analysing the radial stellar density distribution of the halo, we combine the catalogues from nearby pointings, grouping them according to their position in the sky. This step is important because of the nature of our survey, which is composed of relatively small, scattered fields of view. We use a friends-of-friends (FoF) algorithm to group the different pointings. We request two friends not to be apart by more than 20 degrees, and in a few cases we clean or split a resulting group (red pentagons or blue and orange triangles in Figure 2.1) or combine others (purple diamonds) to account for the positions of the galactic disk or major halo substructures. Because the different pointings in our surveys have different completeness limits, these grouped or combined catalogues –which we name A,B,C,... H– are finally filtered to meet the completeness magnitude threshold of their most restrictive contributor[2].

[1] www2.cadc-ccda.hia-iha.nrc-cnrc.gc.ca/megapipe/docs/filters.html

[2] To determine the completeness limit of each field of view, we fit its magnitude distribution to a gaussian –representing the population of faint galaxies– and another variable function –representing the stellar distribution along the whole magnitude range–. We choose as the completeness limit either the transition point between the two distributions (the valley) or, if instead there is a plateau, the turning point of the whole distribution (the knee).

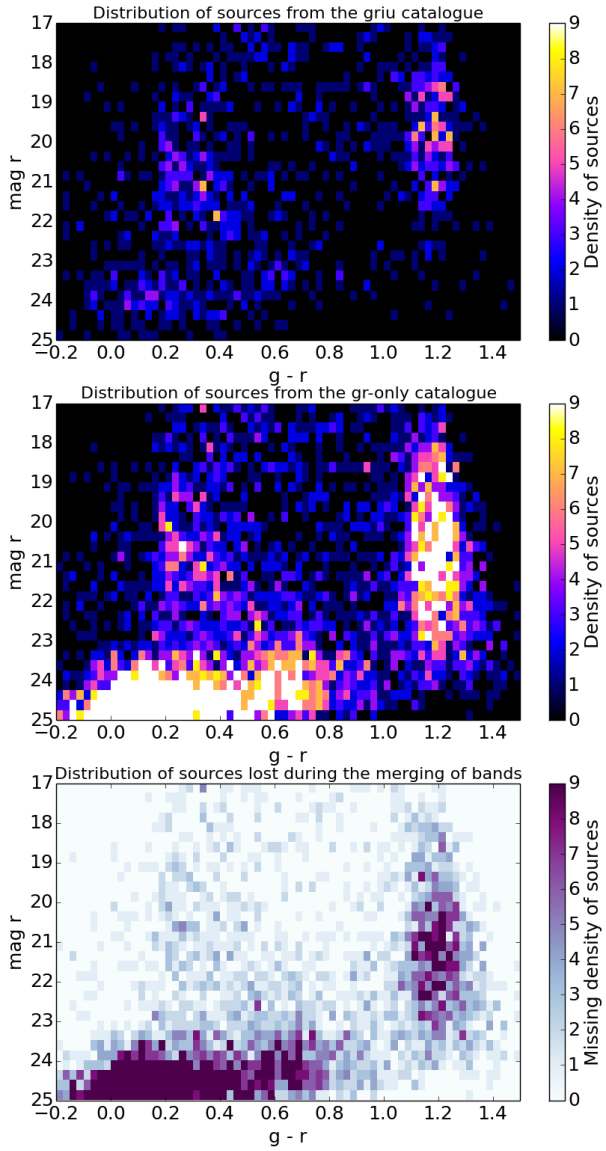


Figure 2.2: Hess diagrams showing the number of sources per colour-magnitude bin in the *ugri* catalogue (top), in the *gr* catalogue (centre) and the difference between both (bottom) for field A1033. Most of the sources lost when combining the catalogues correspond to faint magnitudes, because the i and the U observations are shallower. The effect is the removal of most of the faint galaxies (located in the $-0.2 < g - r < 0.7$ and $r > 23$ region in the central panel), most of the faintest disk M dwarves ($1.1 < g - r < 1.3$) and a number of faint objects (in the i or the U bands) scattered throughout the $(g - r, r)$ diagram.

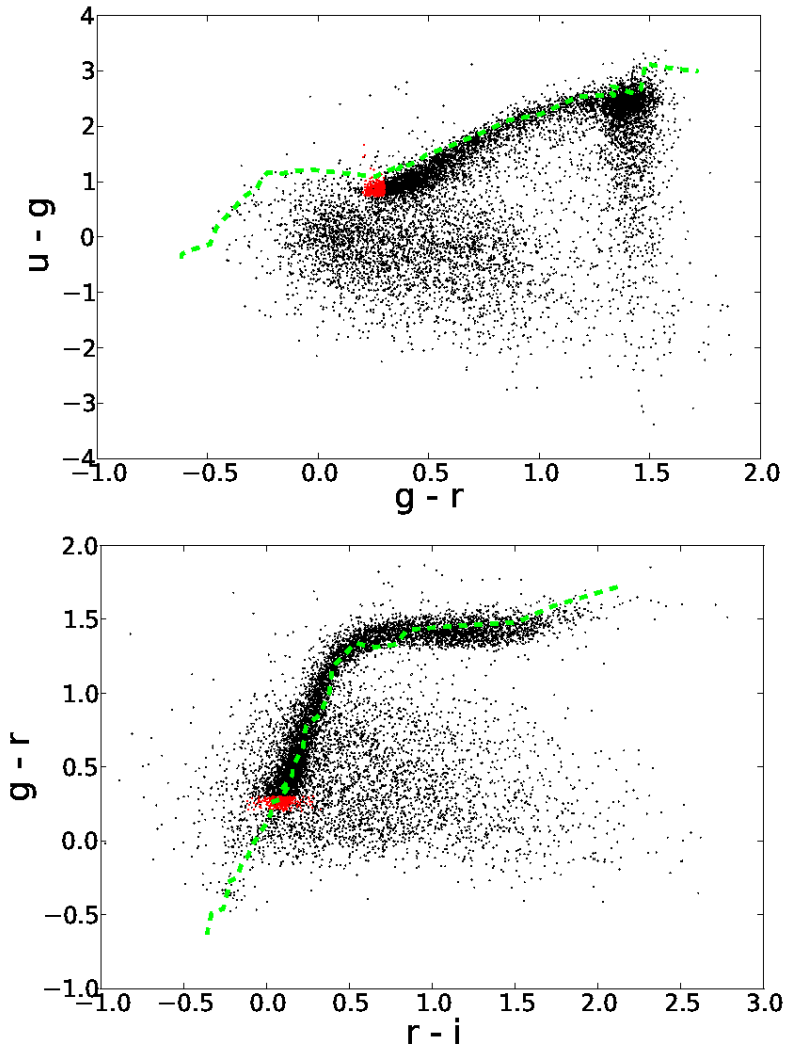


Figure 2.3: Colour-colour diagrams (CCDs) corresponding to the fields in group A (pointings marked as light green circles in Figure 2.1). The sources in the *ugri* catalogues (black) and the subset of near-MSTO stars (red) have been calibrated to SDSS using DR8 stellar photometry. The main sequence stellar loci (green dashed lines) are the ones given in Tables 3 and 4 of Covey et al. (2007). Quasars and white dwarf-M dwarf pairs are abundant in the $u-g<1$, $-0.3<g-r<0.7$ space.

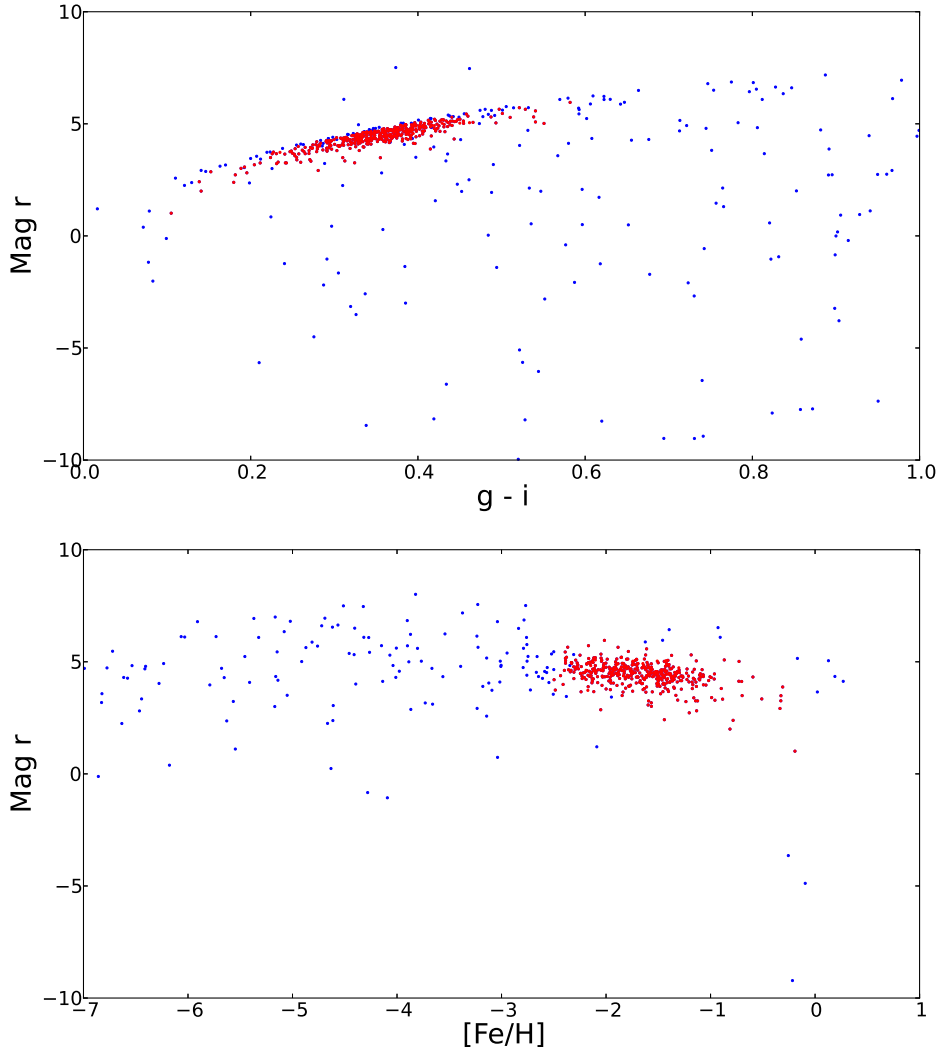


Figure 2.4: Estimated absolute magnitude in the r band (M_r) and estimated metallicity ($[Fe/H]$) for group A for the sources typically considered as halo stars (blue) and those that we have selected as near-MSTO stars (red). The sources selected as halo members meet $0.2 < g - r < 0.3$ and $g, r, i > 17$. The subset of near-MSTO stars, additionally meets $M_r > -2$, $-2.5 \leq [Fe/H] \leq 0$ and $0.1 < g - i < 0.6$.

2.3 Stellar radial density profiles

2.3.1 Star selection and construction of the radial stellar density profiles

The coordinates and the completeness limits of the groups are given in Table 2.1. We use halo main sequence turnoff stars in our fields as tracer of the stellar halo: at the completeness limits of the data such stars can be identified as far out as 60 kpc from the Galactic centre. We fit several Galactic stellar distribution models to these density profiles and derive a number of structural parameters for the stellar halo. Previous works have already used main sequence turnoff point (MSTO) stars, near-MSTO stars, BHB and blue stragglers of type A and RRLyrae as stellar tracers for the Galactic stellar halo. We compare and discuss our findings to theirs in section 2.4.2.

In order to select the near main sequence turnoff stars we make use of two empirical photometric variables. The ratio $[Fe/H]$ is calculated following the photometric metallicity relation by Bond et al. (2010), and the absolute magnitude M_r is calculated following the photometric parallax relation from Ivezić et al. (2008):

$$[Fe/H] = -13.13 + 14.09x + 28.04y - 5.51xy - 5.90x^2 - 58.68y^2 + 9.14x^2y - 20.61xy^2 + 58.20y^3, \quad (2.7)$$

where $x = u - g$ and $y = g - r$. This relation is valid in the $g - i < 0.6$ and $-2.5 \leq [Fe/H] \leq 0$ range, which is compatible with the regime of our near-MSTO star selection.

$$M_r = -0.56 + 14.32z - 12.97z^2 + 6.127z^3 - 1.267z^4 + 0.0967z^5 - 1.11[Fe/H] - 0.18[Fe/H]^2, \quad (2.8)$$

where $z = g - i$. The tested validity regime of this equation encompasses the $0.2 < g - i < 1.0$ range, meaning that the absolute brightnesses of our near-MSTO stars have been properly estimated. We extrapolate the relation for the $0.1 < g - i < 0.2$ range, which is justified owing to the smooth and slow change of M_r with z.

We select the halo near-MSTO stars by requiring

$$0.2 < g - r < 0.3\,; \quad (2.9)$$

$$g, r, i > 17\,; \quad (2.10)$$

$$0.1 < g - i < 0.6\,; \quad (2.11)$$

$$5.0 > M_r > -2\,; \quad (2.12)$$

$$-2.5 \leq [Fe/H] \leq 0\,. \quad (2.13)$$

The first two restrictions (2.9 and 2.10) retrieve stars typically associated with the halo, in particular distant main sequence F stars (see Table 3 from Covey et al. (2007)). This selection however, can be significantly contaminated by quasars and white dwarf-M dwarf pairs, which are abundant in (but not restricted to) the $-0.2 < g - r < 0.3$ range (see Figure 2.3). To reduce the presence of these interlopers and select the bulk of the F stars population, we apply restrictions 2.11 (based on Table 4 in Covey et al. (2007)) and 2.12. Constraint 2.13 ensures that the final sources are at most as metal rich as the Sun (to account for possible contributions from metal-rich satellites) and not more metal-poor than 0.003 times the Sun.

The decrease in interlopers attained by applying restrictions 2.11, 2.12, and 2.13 compared to only applying restrictions 2.9 and 2.10 is illustrated in Figure 2.3, where the red dots indicate the final selection of halo near-MSTO stars and the black dots represent the whole catalogue of star-like sources. It is clear that the final selection of near-MSTO stars does not span the whole range of sources encompassed between $g - r = 0.2$ and $g - r = 0.3$. The effect of the $[Fe/H]$ and M_r selection is further illustrated in Figure 2.4.

Using the estimated absolute brightness, we calculate the distance modulus and the heliocentric distance for all the near-MSTO stars. We define distance modulus bins of size $\Delta\mu = 0.2$ mag and $\Delta\mu = 0.4$ mag, and count the number of near-MSTO stars per bin for each group of fields (A,B,C,...). The choice of distance bins is motivated by a compromise between maximising the radial distance resolution and minimising the Poisson noise in the stellar number counts. We test this compromise by exploring two distance modulus bin sizes, which correspond to distance bin sizes of the order of 10^2 pc and 10 kpc, respectively.

We then calculate the number density per bin and its uncertainty as follows:

$$\rho_{l,b,D} = \frac{N_{l,b,\Delta\mu}}{0.2 \cdot ln(10) \cdot D_{hC}^3 \cdot \Delta\Omega \cdot \Delta\mu}, \tag{2.14}$$

$$E_\rho = \sqrt{(\frac{\rho}{\sqrt{N}})^2 + (\frac{\rho}{\sqrt{n_{fields}}})^2}, \tag{2.15}$$

where $\Delta\Omega$ is the area covered by each group, D_{hC} is the heliocentric distance, l and b are the galactic coordinates and $N_{l,b,\Delta\mu}$ is the number of stars per bin in a given direction of the sky. Particularly,

$$\Delta\Omega = \frac{4\pi}{41253}\Sigma(\mathrm{deg}^2) \tag{2.16}$$

and the area of each group (Σ) depends on the individual area of each field contributing to it (Table 2.1).

The results for these number density calculations can be seen in Figure 2.5, where we plot the logarithmic number density against the galactocentric distance[3], R_{GC}, for each group (or line of sight). For this and the subsequent analysis, we only consider bins with $R_{GC} > 5$kpc, $|z| > 10$ kpc (to avoid the inner regions of

the Galaxy) and a distance modulus of $\mu \leq mag_{lim} - 4.5$ (to guarantee a complete sample of the faintest near-MSTO stars[4]).

Figure 2.5 shows that the density profiles decrease quite smoothly for $40 - 60$ kiloparsecs and for most of the lines of sight.

2.3.2 Fitting procedure

We fit several models of the Galactic stellar number density distribution to the data, ranging from a basic axisymmetric power law to more complex models with triaxiality and a break in the power law. The models take the following mathematical forms, with x, y, and z being the cartesian galactocentric coordinates with the Sun at (8,0,0) kpc (Malkin 2012):

- Axisymmetric model

$$\rho(x,y,z) \quad = \quad \rho_0 \cdot \left(x^2 + y^2 + \frac{z^2}{q^2} \right)^{n/2}, \tag{2.17}$$

  where $q = c/a$ is the polar axis ratio or the oblateness of the halo;

- Triaxial model

$$\rho(x,y,z) \quad = \quad \rho_0 \cdot \left(x^2 + \frac{y^2}{w^2} + \frac{z^2}{q^2} \right)^{n/2}, \tag{2.18}$$

  where $w = b/a$ is the ratio between the axes in the Galactic plane;

- Broken power law, with varying power index at R_{break}

$$\rho(x,y,z) = \begin{cases} \rho_0 \cdot (R_{ellip})^{\,n_{in}}, & R_{ellip} < R_{break} \\ \rho_0 \cdot (R_{ellip})^{\,n_{out}} \cdot R_{break}^{n_{in}-n_{out}}, & R_{ellip} \geq R_{break} \end{cases} \tag{2.19}$$

$$R_{ellip} = \left(x^2 + y^2 + \frac{z^2}{q^2} \right)^{1/2};$$

---

[3] $R_{GC} = \sqrt{R^2 + z^2}$

where R and z are the radial and vertical coordinates on the cylindrical galactocentric reference system.

[4] This constraint guarantees that there are no distance completeness issues due to our specific type of stellar tracers and due to the different depths of our fields. The only subset affected by incompleteness is that of $mag_{lim} - 5.0 < \mu < mag_{lim} - 4.5$ for the stars in the $4.5 < M_r < 5.0$ range; and its average loss is of 20% over the total number of near-MSTO stars ($-2.0 < M_r < 5.0$) in the same distance range. Several tests on different upper distance thresholds for the density profiles show that the distance modulus constraint of $\mu \leq mag_{lim} - 4.5$ is enough to guarantee that all the lines of sight contribute robust density measurements at the furthest distances and that the incompleteness in $mag_{lim} - 5.0 < \mu < mag_{lim} - 4.5$ for the $4.5 < M_r < 5.0$ near-MSTO stars has no statistically significant effect on the best fit parameters.

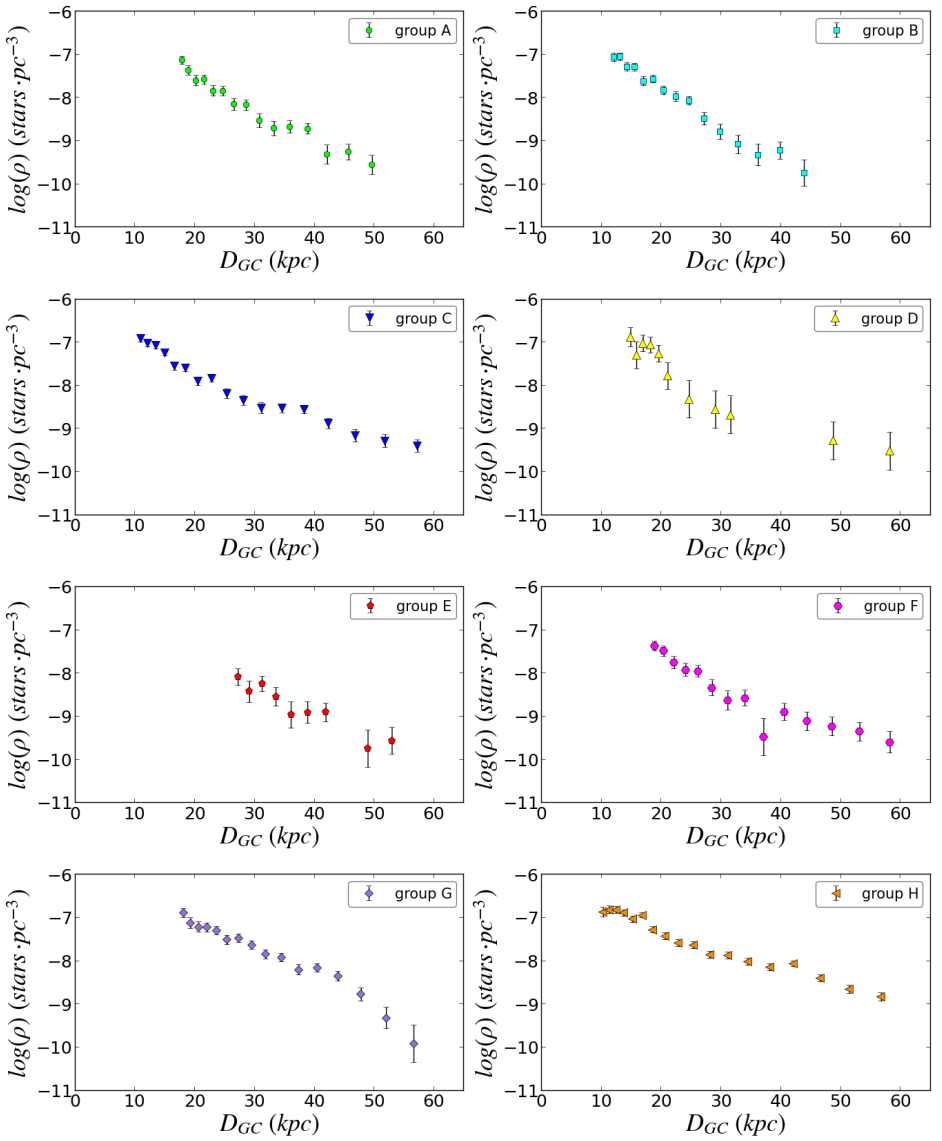


Figure 2.5: Logarithmic stellar density profiles versus distance for the near Main Sequence turnoff point stars (near-MSTO) from the fields in groups A (green circles), B (cyan squares), C (blue downward triangles), D (yellow upward triangles), E (red pentagons), F (pink hexagons), G (purple diamonds) and H (orange leftward triangles). Their symbols match those in Figure 2.1.

- Broken power law, with varying power index and oblateness at R_{break}

$$\rho(x,y,z) = \begin{cases} \rho_{0,in} \cdot \left(x^2 + y^2 + \frac{z^2}{q_{in}^2}\right)^{n_{in}/2}, & R_{GC} \leq R_{break} \\ \rho_{0,out} \cdot \left(x^2 + y^2 + \frac{z^2}{q_{out}^2}\right)^{n_{out}/2}, & R_{GC} > R_{break}, \end{cases} \tag{2.20}$$

  where the inner power law is fit to data that meets $R_{GC} \leq R_{break}$ and the outer power law is applied to data that meets $R_{GC} > R_{break}$.

We fit all these models to the data using the "curve-fit" method from Python's Scipy.optimize, which uses the Levenberg-Marquardt algorithm for non-linear least squares fitting. The objective function takes the form of a χ^2, and we also calculate a reduced χ^2 for analysis purposes,

$$\chi^2 = \sum_{i=1}^{N_{data}} \left(\frac{\rho_{data,i} - \rho_{model,i}}{E_{\rho,i}}\right)^2, \tag{2.21}$$

$$\chi^2_{red} = \frac{\chi^2}{N_{data} - N_{params}}, \tag{2.22}$$

where N_{data} and N_{params} are the number of data points and the number of free parameters, respectively.

The influence of the photometric uncertainties on the density profiles and the best fit parameters is evaluated through a set of Monte Carlo simulations that randomly modify the g,r,i,u magnitudes of each star within the limits of the photometric uncertainties. Through this method we find that the variation of the Monte Carlo best fit parameters aligns with the uncertainties of our best fit parameters (derived from the second derivative of the fits by the "curve-fit" method). The centre of these variations is within 1σ of our direct findings.

We fit all models to four data sets: with and without [known] substructures and binned in 0.2 and 0.4 magnitude cells. In this way we can check the robustness of our results to different binning options and we are able to compare what would be the effect of substructure on our understanding of the smooth halo if we were to ignore it or unable to recognize it as such. Specifically, we cut the distance bins at $R_{GC} < 25$ kpc in group E to avoid contributions by the structures in the direction of the galactic anticentre (the Monoceros ring, the Anticentre Structure and the Eastern Band Structure), the distance bins within $15 < D_{hC} < 40$ kpc in group G to avoid contributions by the Sagittarius stream, and the distance bins within $20\,\text{kpc} < D_{hC} < 60$ kpc in group H to avoid contributions again by the Sagittarius stream.

2.3.3 Results

The best fit parameters for each model resulting from fitting these four data sets are summarized in Tables 2.2 to 2.5. Table 2.2 contains the results of fitting the

$\Delta\mu = 0.2$ mag binned data excluding regions with substructure, whereas Table 2.3 contains the results of fitting to all the 0.2 mag bins. Similarly Table 2.4 covers the fits to $\Delta\mu = 0.4$ mag data without substructure bins, and Table 2.5, to all 0.4 mag bins. The reduced χ^2 and the initial parameters have also been recorded in these tables.

We compare the fitting results for the four different data sets recorded in Tables 2.2 to 2.5 and find that the fits for which the substructure has been masked significantly outperform those that have been allowed to fit all the available data. The difference on χ^2_{red} for all these models and bin sizes is in every case at least a factor of 2.3 or larger. We find that allowing the models to fit data that contains substructure does not affect largely most of the structural parameters (polar axis ratios are compatible within the uncertainties and power law indices have close values) except that it decreases the disk axis ratio w by at least 10%, suggesting a strong departure from the axisymmetric model that is not implicit in the filtered data sets. Henceforth we will restrict the remaining discussion to the results derived from the cleanest data sets.

Comparing the parameters resulting from the best fits to the masked 0.2 mag and 0.4 mag data, we find that the fits to 0.2 mag binned data perform better for all the models (χ^2_{red} ratio of two). Nonetheless, all the measurements for the different structural parameters in the two data sets are compatible with each other within the uncertainties. The best fits for the four models and their residuals for our eight lines of sight are shown in Figures 2.6a and 2.6b for the masked 0.2 mag binned data. It is clear that the differences between the fitted models along these sight lines are small.

Our data are inconclusive regarding triaxiality, but are compatible with either a mildly triaxial halo or with no triaxiality. For the 0.2 mag data set, the triaxial model fits slightly better than the axisymmetric model and returns $w = 0.87 \pm 0.09$. For the 0.4 mag data set, however, the axisymmetric model fits slightly better and the triaxial model returns a disk axis ratio compatible with 1. In both data sets the other best-fitting parameters are practically identical for the two models. This indicates that the cost of the extra parameter is not supported by the 0.4 mag data. Thus, it is hard to derive a precise value for the disk axis ratio and to conclude if it is truly triaxial, but a weighted average of w and the general analysis show confidently that $w > 0.8$.

We increase the complexity of the axisymmetric model by adding two degrees of freedom and considering a change in the power law index n at a specific break distance R_{break} (a broken power law). For this purpose, we use a grid of values to explore all the parameters except the density scale factor ρ_0, which we left free to fit (see below for the grid characterization). This model decreases the χ^2_{red} in both the 0.2 and the 0.4 mag binned cases, indicating that our data is better fit by a broken power law than by a simple axisymmetric model or a triaxial model. It turns the single power law index from $n = -4.26 \pm 0.06$ into a less steep inner index $n_{in} = -2.50 \pm 0.04$ and a steeper outer index $n_{out} = -4.85 \pm 0.04$ (measurements here are for weighted averages between the 0.2 and 0.4 mag data).

Table 2.2: Best fit parameters for the four different Galactic stellar distribution models resulting from removing the data that is affected by known halo substructures (the Sagittarius stream and the anticentre substructures). For the fitting, the data has been binned in 0.2 mag distance modulus cells.

Model	χ^2_{red}	$\rho_0\,(\mathrm{pc}^{-3})\cdot 10^{-3}$	R_{break} (kpc)	n	n_{in}	n_{out}	q	q_{in}	q_{out}	w
axisymmetric	1.90	14 ± 6	–	-4.31 ± 0.09	–	–	0.79 ± 0.06	–	–	–
triaxial	1.86	14 ± 6	–	-4.28 ± 0.09	–	–	0.77 ± 0.06	–	–	0.87 ± 0.09
broken p.l.$_n$	1.52	0.071 ± 0.003	19.0 ± 0.5	–	-2.40 ± 0.05	-4.80 ± 0.05	0.77 ± 0.03	–	–	–
broken p.l.$_{n,\,q}$	1.99, 1.51	1 ± 3	19_{fixed}	–	-3.3 ± 0.6	-4.9 ± 0.2	–	0.7 ± 0.2	0.88 ± 0.07	–
initial parameters	–	0.001	40.0	-3.00	-3.00	-3.50	0.70	0.70	0.8	1.00

Table 2.3: Same as in Table 2.2 but this time fitting all the available data (including those regions containing stellar counts from known substructures and detected overdensities).

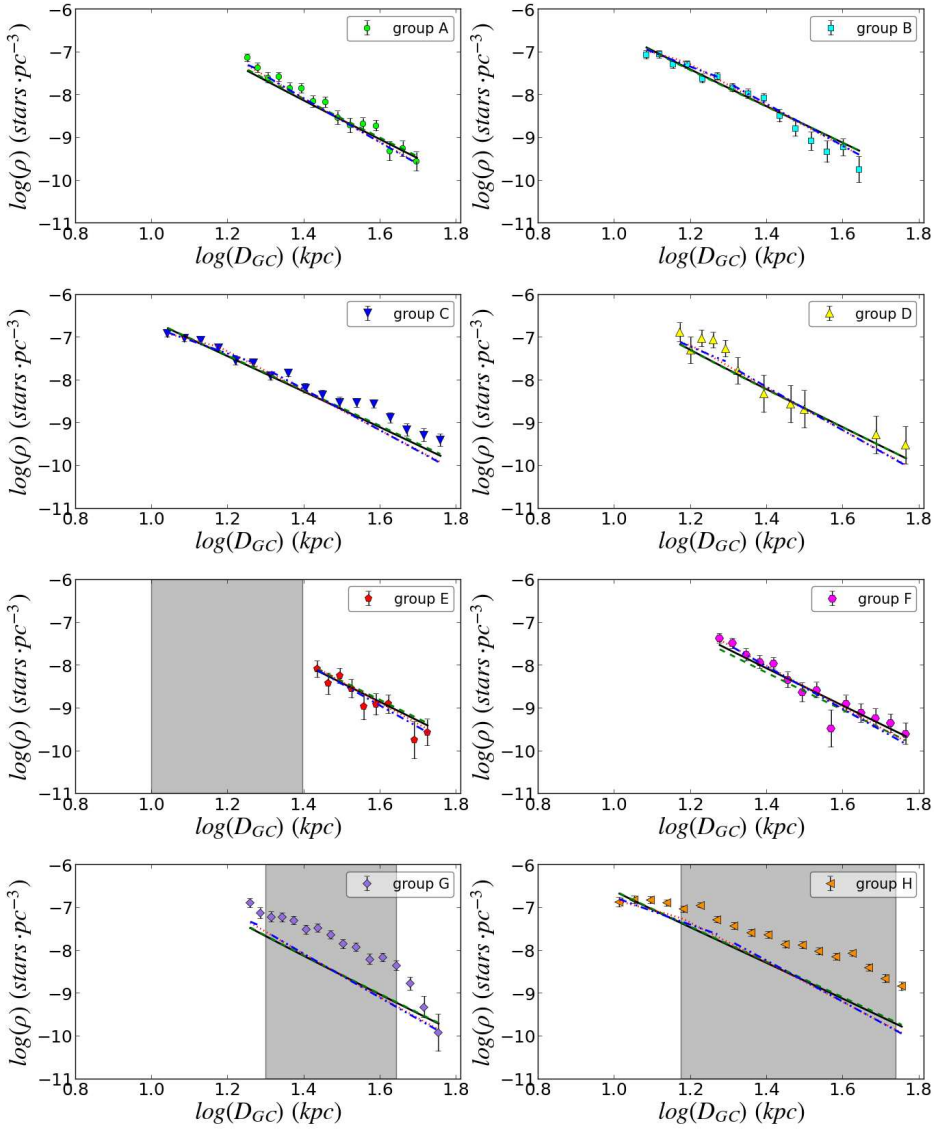
Model	χ^2_{red}	$\rho_0\,(\mathrm{pc}^{-3})\cdot 10^{-3}$	R_{break} (kpc)	n	n_{in}	n_{out}	q	q_{in}	q_{out}	w
axisymmetric	4.71	8 ± 3	–	-4.15 ± 0.08	–	–	0.83 ± 0.06	–	–	–
triaxial	4.59	7 ± 2	–	-4.07 ± 0.08	–	–	0.82 ± 0.06	–	–	0.77 ± 0.07
broken p.l.$_n$	4.24	0.17 ± 0.01	21.0 ± 0.5	–	-2.80 ± 0.05	-4.80 ± 0.05	0.84 ± 0.03	–	–	–
broken p.l.$_{n,\,q}$	3.36,4.79	1 ± 2	21_{fixed}	–	-3.3 ± 0.4	-5.0 ± 0.2	–	0.7 ± 0.2	0.89 ± 0.08	–
initial parameters	–	0.001	40.0	-3.00	-3.00	-3.50	0.70	0.70	0.8	1.00

Table 2.4: Same as in Table 2.2 but this time fitting the data binned in 0.4 mag distance modulus cells.

Model	χ^2_{red}	$\rho_0\,(\mathrm{pc}^{-3})\cdot 10^{-3}$	R_{break} (kpc)	n	n_{in}	n_{out}	q	q_{in}	q_{out}	w
axisymmetric	3.89	12 ± 4	–	-4.26 ± 0.08	–	–	0.77 ± 0.05	–	–	–
triaxial	3.97	12 ± 5	–	-4.25 ± 0.08	–	–	0.77 ± 0.06	–	–	0.9 ± 0.1
broken p.l.$_n$	2.61	0.11 ± 0.01	20.0 ± 0.5	–	-2.60 ± 0.05	-4.90 ± 0.05	0.81 ± 0.03	–	–	–
broken p.l.$_{n,\,q}$	4.95,2.34	1 ± 1	20_{fixed}	–	-3.2 ± 0.4	-5.0 ± 0.3	–	0.7 ± 0.2	0.82 ± 0.08	–
initial parameters	–	0.001	40.0	-3.00	-3.00	-3.50	0.70	0.70	0.8	1.00

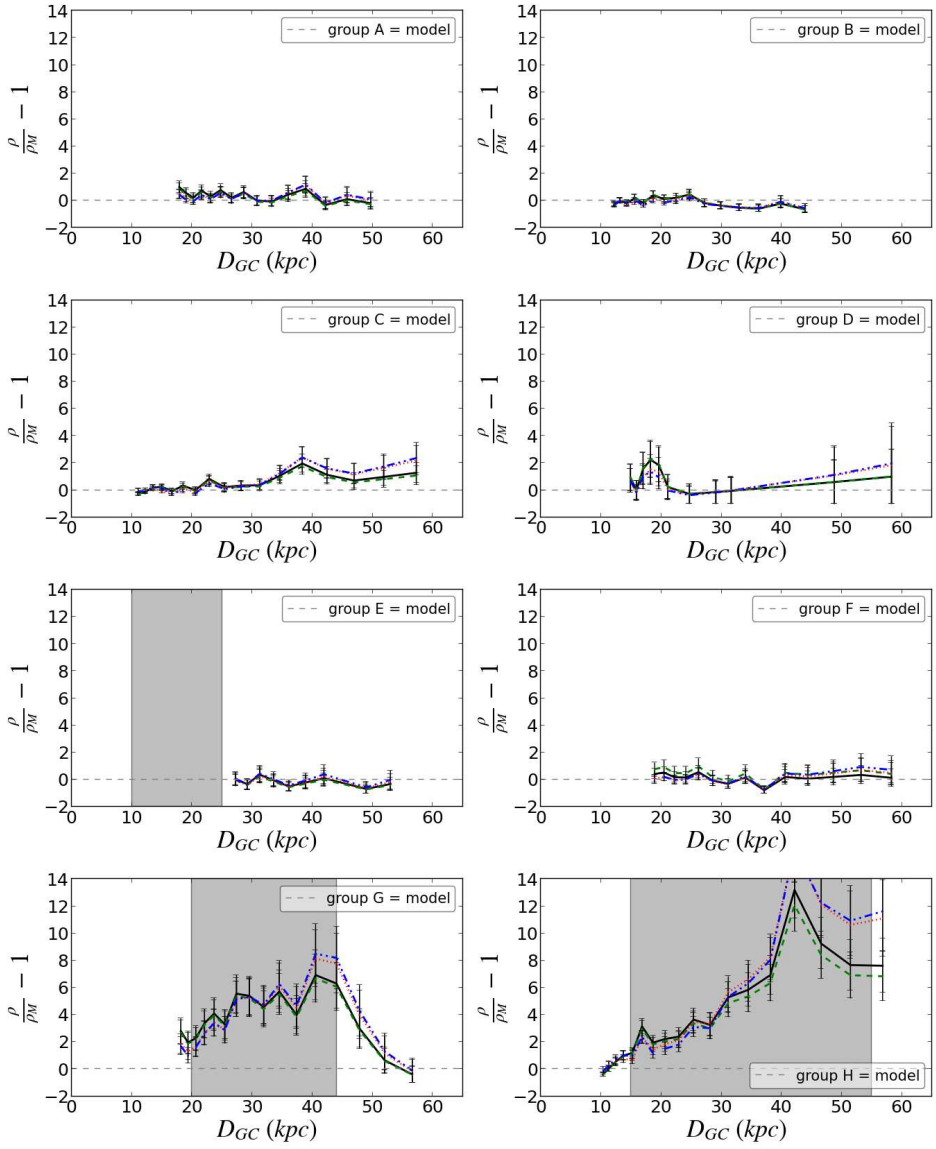
Table 2.5: Same as in Table 2.4 but this time fitting all the available data (including those regions containing stellar counts from known substructures and detected overdensities).

Model	χ^2_{red}	$\rho_0\,(\mathrm{pc}^{-3})\cdot 10^{-3}$	R_{break} (kpc)	n	n_{in}	n_{out}	q	q_{in}	q_{out}	w
axisymmetric	9.13	7 ± 2	–	-4.10 ± 0.07	–	–	0.81 ± 0.05	–	–	–
triaxial	9.19	7 ± 2	–	-4.07 ± 0.07	–	–	0.81 ± 0.06	–	–	0.86 ± 0.09
broken p.l.$_n$	7.74	0.058 ± 0.005	20.0 ± 0.05	–	-2.40 ± 0.05	-4.8 ± 0.05	0.84 ± 0.03	–	–	–
broken p.l.$_{n,\,q}$	6.05,9.2	0.6 ± 0.9	20_{fixed}	–	-3.1 ± 0.4	-4.9 ± 0.2	–	0.7 ± 0.2	0.86 ± 0.07	–
initial parameters	–	0.001	40.0	-3.00	-3.00	-3.50	0.70	0.70	0.8	1.00



(a) Fitted density profiles for the 0.2 mag binned data.

Figure 2.6: Density profiles in decimal logarithmic scale and the best fit models from Table 2.2 (fitted to masked 0.2 binned data). The different lines represent the axisymmetric (black solid line), the triaxial (green dashed line), the broken power law with varying power index (red dotted line) and the broken power law with varying power index and oblateness (blue dashed-dotted- dotted line) models. The grey areas denote data that have been masked from the fitting to account for the presence of substructure.



(b) Data-to-model residuals for the 0.2 mag binned data.

Figure 2.6: Residuals between the data and the best fit models from panel 2.6a. The different lines and the shaded areas follow the same colour and symbol code.

It also increases the central value of the polar axis ratio q within the uncertainties, from a weighted $q = 0.77 \pm 0.04$ to a weighted $q = 0.79 \pm 0.02$. Globally, the disk axis ratio seems to be the most stable parameter throughout the different model fits to our data, returning a moderately oblate halo.

Finally we fix the break distance at the best fit value found by the broken power law model (R_{break} = 19 kpc and 20 kpc for the 0.2 and 0.4 mag binned data, respectively) and add another parameter to it, allowing not only n, but also q to change at the break distance. We find that the best fits to this model return such large error bars for the inner halo that, in practice, it yields unconstrained measurements: $\Delta\rho_0 \leq \rho_0$, Δn_{in} is 12-18% of n_{in} and Δq_{in} is 30% of q_{in}.

We explore each model to investigate possible parameter degeneracies, tolerance ranges and potential local minima in our best fits. For this we fix all the parameters in the four models except the density scale factor ρ_0, and we run the fits across a grid of parameter values. In particular, the grids are built following $q^2, w^2 \in [0.1, 2.0; \delta = 0.05]$, $n \in [-5.0 - 1.0; \delta = 0.1]$, $n_{in} \in [-4.0, -1.0; \delta = 0.1]$, $n_{out} \in [-7.0, -3.0; \delta = 0.2]$ and $R_{br} \in [15, 50; \delta = 1]$, where δ is the incremental step for each parameter. We find that there is a degeneracy between R_{br} and n_{in} for the simple broken power law model for both binnings (see Figure 2.7).

Finally our measurements for the density scale factor ρ_0 (ρ at $R_{GC} = 1$ kpc) are the result of large extrapolations and merely serve as normalizations for our fits. For that reason we do not discuss these values in detail.

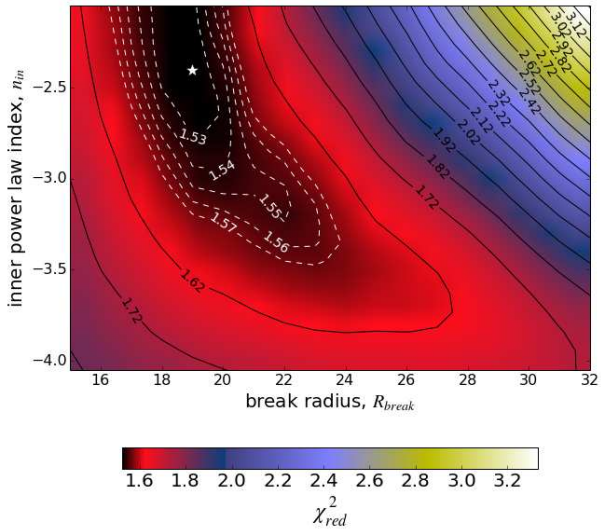
2.4 Discussion

2.4.1 Robustness of the best fit structural parameters

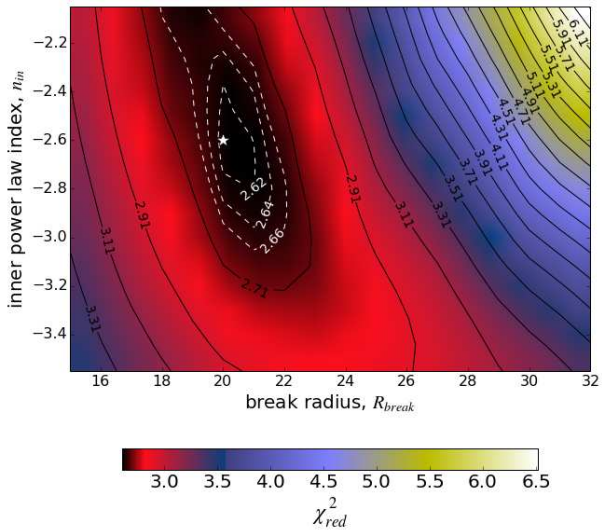
In order to determine how the data available to us influences the results from our best fits, we remove the different lines of sight one at a time and repeat the fits. In this way we can determine which are the most critical lines of sight and what is their effect on our results.

We find that most of them have no significant influence on the best fit parameters of the different halo models. However, starting with the polar axis ratio we find that removing group A increases slightly its value ($q \approx 0.85$) and removing groups C or E decreases it slightly ($q \approx 0.70$) in both the axisymmetric and triaxial model in the two data sets. Regarding the power law index, again groups A or C have an influence, but group B as well. Removing groups A or B increases n to $\approx -4.1 \pm 0.1$, whereas removing C decreases it to $n \approx -4.6$. When considering a triaxial halo, we find that groups A, B or C increase the disk axis ratio w by ~ 0.10, and that removing groups E or F decreases it to $w \approx 0.7$. Additionally, in conditions of triaxiality, the lack of group E reduces q further to $q \approx 0.60$.

Thus removing group E turns out to be critical for both q and w, representing a rather differently looking halo (significantly oblate and quite elliptical in the plane). Group F also has a similar effect on w but not on q. The reason why group E has such a strong influence in the determination of a possible triaxiality is that it is by far the closest group to the Galactic anticentre. Other groups



(a) χ^2_{red} map for the filtered 0.2 mag binned data set.



(b) χ^2_{red} map for the filtered 0.4 mag binned data set.

Figure 2.7: χ^2_{red} isocontours maps for n_{in} and R_{br} from the simple broken power law model. The minimum is indicated with a white star. The black solid isocontours range from $min(\chi^2_{red}) + 0.1$ to the maximum value, whereas the white dashed isocontours range from $min(\chi^2_{red}) + 0.01$ to $min(\chi^2_{red}) + 0.05$. The maps illustrate a degeneracy between both parameters in the best fits.

also influence the measurements of the different parameters, but have a smaller influence on the general picture we would derive. Overall we see that the lines of sight we use can have a drastic effect on the w results and a significant but moderate effect on q and n. This means that a global view of the halo is essential owing to its complex structure.

2.4.2 Comparison to previous studies

Previous investigations using near-MSTO stars have explored both the inner and the outer halo out to moderate distances ($30 - 40$ kpc), and similar regimes have been probed with blue horizontal branch stars and blue struggler stars, MSTO stars or multiple stellar halo tracers. Studies involving RRLyrae stars have reached further out to 50kpc. Remarkably, the depth of our data allows us to probe further than any previous study (out to 60 kpc) in several directions, independently of the stellar tracer.

In this section we compare our findings regarding the structural parameters of the stellar halo to those of the following results in the literature:

- Jurić et al. (2008) use near-MSTO stars from the SDSS-DR3 and DR4 as stellar tracers, and cover the $5\,\mathrm{kpc} < R_{GC} < 15$ kpc range. They comprise 5450 deg^2 in the northern Galactic hemisphere and 1088 deg^2 in the south.

- Sesar et al. (2011) use as well near-MSTO stars from the CFHT Legacy Survey, and explore the $5\,\mathrm{kpc} < R_{GC} < 35$ kpc range. Two of their four fields explore the South Galactic Cap.

- Deason et al. (2011) use type A blue horizontal branch (BHB) stars and blue stragglers (BS), reaching out to $R_{GC} = 40$kpc.

- de Jong et al. (2010) use CMD fitting of SEGUE stellar photometry to probe the total stellar mass density from $R_{GC} = 7$ kpc to $R_{GC} = 30$ kpc along a "picket fence" of 2.5 degree wide strips at fixed Galactic longitude spanning a large range of Galactic latitudes.

- Chen et al. (2001) use more general MSTO stars from two high latitude regions of SDSS to the North and the South of the Galactic plane ($49\,\mathrm{deg} < |b| < 64\,\mathrm{deg}$). They explore the inner halo regime ($R_{GC} \lesssim 30$ kpc).

- Bell et al. (2008) use also more general MSTO stars from SDSS-DR5 spanning $5 < R_{GC} < 40$ kpc.

- Faccioli et al. (2014) use RRLyrae in the $9\,\mathrm{kpc} < R_{GC} < 49$ kpc range. Their multiepoch data comes from the Xuyi Schmidt Telescope Photometric Survey (XSTPS) in combination with SDSS colours, and covers 376.75 deg^2 at $RA \approx 150$ deg and $Dec \approx 27$ deg.

- Sesar et al. (2010a) use RRLyrae stars from SDSS-II in the stripe 82 region. Although their data originally spans $5\,\mathrm{kpc} < R_{GC} < 110$ kpc, the reanalysis

performed by Faccioli et al. (2014) to derive structural parameters truncates the sample at 49 kpc.

- Watkins et al. (2009) use as well RRLyrae from SDSS in stripe 82, and the comparative derivation of structural parameters by Faccioli et al. (2014) also truncates it at 49 kpc. Stripe 82 is located in the South Galactic Cap.

The result of this comparison is summarized in Table 2.6. We note that the oblateness values for Faccioli et al. (2014), Sesar et al. (2010a) and Watkins et al. (2009) are not the result of absolute best fits to a set of free parameters, but the best fits to free R_{br}, n_{in} and n_{out} with fixed prior values for a quite oblate ($q = 0.59^{+0.02}_{-0.03}$) and a moderately oblate halo ($q = 0.70 \pm 0.01$).

All surveys that reach beyond $R_{GC} = 30$ kpc coincide in the need for a break in the power-law index of the halo density. Regarding possible triaxiality, only a few of the studies report constraints on w. Those that do, have either reported 'finding unreasonable values' (Sesar et al. 2011) or have obtained limits on triaxiality similar to ours ($w > 0.8$, Bell et al. (2008)).

On the break radius, there is a general consensus towards $R_{break} \approx 27$ kpc. The only exception is that of Bell et al. (2008), who find a value very close to our measurement (~ 20 kpc). These discrepancies, however, can be explained by the effect of the R_{break}-n_{in} degeneracy discussed in section 2.3.3.

The inner and outer halo power law indices mostly fall in the $[-2.3, -3.0]$ and $[-3.6, -5.1]$ ranges. Our inner power law index $n_{in} = -2.50 \pm 0.04$ is consistent with these results, particularly with the lower end. In the case of the outer halo power index ($n_{out} = -4.85 \pm 0.04$), the comparison is less trivial. First, only Sesar et al. (2011) and Deason et al. (2011) have provided measurements for n_{out} based on fits with a free q parameter ($n_{out} = -3.8 \pm 0.1$ and $-4.6^{+0.2}_{-0.1}$, respectively). Second, only one work with n_{out} measurements (Sesar et al. 2011) uses a stellar tracer similar to ours (the others use A-BHB and BS stars, or RRLyrae stars). Most important, a good constraint on n_{out} requires deep data, and none of these earlier surveys reach as deep as our data set. Our steep outer index, although well in the range of previous measurements, might well indicate a progressive steepening of the halo density, though it would be good to test this with additional sight lines of comparable depth. In any case, it seems safe to conclude that $n_{out} < -4.0$.

The best fit values for the polar axis ratio or oblateness q range from 0.5 to 0.9, with most of the measurements concentrated within $(0.55, 0.70)$. The values of q do not seem to depend on whether a break was detected or not, nor on the limiting distance of the survey or on the stellar tracer. The discrepancies can thus be attributed either to methodological differences or to differences in the spatial coverage of the data samples. However, it is difficult to determine the actual cause. Our results ($q = 0.79 \pm 0.02$) do not fit well within the most constricted range but rather match the upper part of the broader range.

Finally it is noteworthy that the choice of stellar tracer across the different works does not seem to cause any significant bias on the best fit parameters.

Table 2.6: Comparison between the best fit structural parameters found in this work (weighted averages for the parameters of the 0.2 and 0.4 mag data sets) and those reported by other groups in previous works. The different works have been labelled as follows: J08 (Jurić et al. 2008), S11 (Sesar et al. 2011), D11 (Deason et al. 2011), dJ10 (de Jong et al. 2010), Ch01 (Chen et al. 2001), B08 (Bell et al. 2008), F14 (Faccioli et al. 2014), and S10 (Sesar et al. 2010a) and W09 (Watkins et al. 2009) as reanalysed in F14. The fitted models in F14, S10 and W09 have fixed oblateness and test two different values motivated by the previous findings in S11 and D11.

Work	stellar tracer	dist. range (kpc)	χ^2_{red}	R_{br} (kpc)	n	n_{in}	n_{out}	q	w
this work-axisym.	near-MSTO	$[10, 60]$	1.9	–	-4.28 ± 0.06	–	–	0.78 ± 0.04	–
this work-triax.	near-MSTO	$[10, 60]$	1.9	–	-4.26 ± 0.06	–	–	0.77 ± 0.04	0.88 ± 0.07
this work-broken	near-MSTO	$[10, 60]$	1.5	19.5 ± 0.4	–	-2.50 ± 0.04	-4.85 ± 0.04	0.79 ± 0.02	–
J08	near-MSTO	$[5, 15]$	$[2, 3]$	–	–	-2.8 ± 0.3	–	0.65 ± 0.15	–
S11	near-MSTO	$[5, 35]$	3.9	27.8 ± 0.8	–	-2.62 ± 0.04	-3.8 ± 0.1	0.70 ± 0.02	excluded
D11	A-BHB, -BS	$[-, 40]$	–	27.1 ± 1	–	-2.3 ± 0.1	$-4.6^{+0.2}_{-0.1}$	$0.59^{+0.02}_{-0.03}$	–
dJ10	multiple	$[7, 30]$	$[3.9, 4.2]$	–	-2.75 ± 0.07	–	–	0.88 ± 0.03	–
Ch01	MSTO	$[-, 30]$	–	–	-2.5 ± 0.3	–	–	0.55 ± 0.06	–
B08	MSTO	$[5, 40]$	2.2	~ 20	-3 ± 1	–	–	$[0.5, 0.8]$	≥ 0.8
F14	RRLyrae	$[9, 49]$	0.8	28.5 ± 5.6	–	-2.8 ± 0.4	-4.4 ± 0.7	$q_{fix} = 0.70 \pm 0.01$	–
"	RRLyrae	$[9, 49]$	1.04	26.5 ± 8.9	–	-2.7 ± 0.6	-3.6 ± 0.4	$q_{fix} = 0.59^{+0.02}_{-0.03}$	–
S10	RRLyrae	$[9, 49]$	1.1	34.6 ± 2.8	–	-2.8 ± 0.2	-5.8 ± 0.9	$q_{fix} = 0.70 \pm 0.01$	–
"	RRLyrae	$[9, 49]$	1.52	26.2 ± 7.4	–	-3.0 ± 0.3	-3.8 ± 0.3	$q_{fix} = 0.59^{+0.02}_{-0.03}$	–
W09	RRLyrae	$[9, 49]$	1.1	27.6 ± 3.3	–	-2.5 ± 0.3	-4.3 ± 0.4	$q_{fix} = 0.70 \pm 0.01$	–
"	RRLyrae	$[9, 49]$	0.69	26.9 ± 3.1	–	-2.1 ± 0.3	-4.0 ± 0.3	$q_{fix} = 0.59^{+0.02}_{-0.03}$	–

2.4.3 Detection of overdensities and identification

We analyse the data-to-models residuals for the different lines of sight in Figure 2.6b in search for overdensities. We find that, in general, all the lines of sight present regions with data-to-models deviations of a maximum factor of two. Additionally, certain lines of sight –C,D, G, and H– present more significant deviations spanning from a few kiloparsecs to tens of kiloparsecs in distance. We discuss these overdensities in greater detail below, and we also discuss expected overdensities that show no signature in our data.

The most prominent overdensities in the data-to-model residuals correspond to the northern wrap of the Sagittarius (Sgr) stream. This stream overlaps in projection with groups G and H (see Figure 2.8). For group G, the residuals indicate overdensities in the distance range where we expect to find both the Sgr and the Orphan stream ($20 < D_{hC} \lesssim 40$ kpc or $25 < D_{GC} \lesssim 44$ kpc, Pila-Díez et al. (2014)). The overdensities indeed peak between $R_{GC} = 25$ kpc and 45 kpc, reaching $\rho/\rho_M = 7 \pm 2$, and drop sharply afterwards. Group H probes the Sgr stream closer to the Galactic centre but also for larger distances than group G. Based both on extensive data (summarized in Pila-Díez et al. (2014)) and in models (Law & Majewski (2010b) and Peñarrubia et al. (2010)), we expect this stream to span the $20 < D_{hC} < 60$ kpc or $16 < R_{GC} < 55$ kpc range at these coordinates. This expectation is met all along: they steadily increase from $R_{GC} \approx 15$ kpc, depart from $\rho/\rho_M = 3 \pm 1$ at $R_{GC} = 30$ kpc, reach $\rho/\rho_M = 6 \pm 2$ at $R_{GC} = 40$ kpc and peak at $R_{GC} = 45$ kpc with $max(\rho/\rho_M) = (12, 15) \pm 2$. However, they do not decrease near $R_{GC} = 55$ kpc but seem to stay stable with a significant $\rho/\rho_M > 7 \pm 2$). This suggests a thicker branch than predicted by the models, but in agreement with previous RRLyrae measurements (Ibata et al. (2001c), Totten & Irwin (1998) and Dohm-Palmer et al. (2001) as summarized in Figure 17 of Majewski et al. (2003)).

Two more modest overdensities that do not appear in the literature seem to be present in groups C and D. In group C, a weak but consistent overdensity spans a distance range of $R_{GC} \approx 35$ kpc to $R_{GC} \approx 60$ kpc. In group D, a sharp bump extends over a few kiloparsecs around $R_{GC} \leq 20$ kpc.

We have looked for other known overdensities that position-match our lines of sight (see Figure 2.8), but found no indication of them in the residuals. The first one corresponds to the tidal tails of the NGC5466 globular cluster (Belokurov et al. 2006a), which overlap with one field in group A and another one in group B (A1361 centred at $(RA, Dec) = (176.09, 46.39)$ and A1927 at $(RA, Dec) = (217.92, 25.67)$). This is a very weak cold substructure located at $R_{GC} \approx= 16$ kpc and extending for 45 deg with an average width of 1.4 deg (Grillmair & Johnson 2006). As such, it is not surprising to find no signature in the density profiles.

The second one is the ensemble of three known overdensities in the direction of group E: the Anti Center Stream ($R_{GC} = 18 \pm 2$ kpc, Rocha-Pinto et al. (2003) and Li et al. (2012)), the Monoceros ring ($R_{GC} \approx 18$ kpc, Li et al. (2012)) and the Eastern Band Structure ($R_{GC} = 20 \pm 2$ kpc, Li et al. (2012)). These substructures

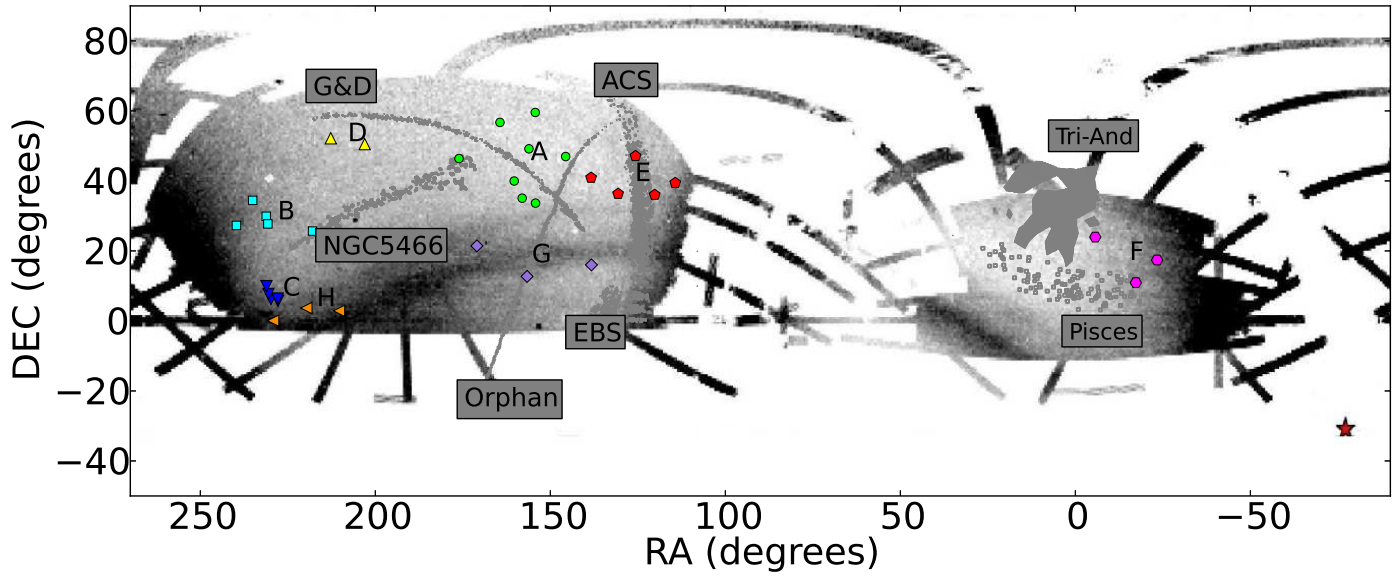


Figure 2.8: Equatorial map showing the position of all the fields used in this work and the closest cold stellar overdensities to them. These overdensities are used for comparison and discussion of the stellar density profile data-to-model residuals throughout section 2.4.3. The labels in the figure correspond to the Anticentre Structure (ACS), the Eastern Band Structure (EBS), the NGC5466 stream, the Grillmair & Dionatos stream (G&D), the Orphan stream, the Triangulum-Andromeda overdensity (Tri-And) and the Pisces overdensity. The background image is the SDSS-DR8 map from Koposov et al. (2012), which shows the footprint of the Sagittarius stream. The Monoceros ring also appears partially in this background image, as a dark region overlapping the western part of the Galactic disk in the anticentre region, eastwards of the ACS.

are masked from our fits and residuals when we impose $|z| > 10$ kpc to avoid the influence of the thick disk, and therefore, they cannot be detected.

The Triangulum-Andromeda overdensity ((Martin et al. 2007)) falls close to one of the fields in group F. Despite this proximity, the residuals show no evidence for an overdensity at the expected distance of $R_{GC} \approx 30$ kpc, indicating that the overdensity does not extend further in this direction.

2.5 Conclusions

In this paper we have used wide-field images from the CFHT and the INT telescopes in eight broad lines of sight spread across the sky to produce deep photometric catalogues of halo near main sequence turnoff (near-MSTO) stars. Our images have been corrected for PSF inhomogeneities, resulting in catalogues with fixed-aperture colour measurements and improved star-galaxy separation. Thanks to the depth and quality of our data, we reach stellar completeness limits ranging from 22.7 mag to 24.2 mag in the r band, which translate into a 60 kpc distance limit for near-MSTO stars.

We calculate galactocentric distances for the stars based on the photometric parallax method by Ivezić et al. (2008) and the metallicity estimator by Bond et al. (2010). We bin them by distance modulus, and calculate the stellar number density distribution along the eight different lines of sight.

In selecting the halo near-MSTO stars, we have used additional constraints than the standard $0.2 < g - r < 0.3$ and $g, r, i > 17$ cuts in order to obtain a cleaner sample. Particularly, by applying additional cuts based on g-i colour, absolute magnitude and metallicity, we get a sample of mainly F stars significantly decontaminated from quasars and white dwarf-M dwarf pairs.

We fit several galactic halo models of the stellar distribution to our eight lines of sight, and explore the structural parameters resulting from the best fits, as well as the influence of substructure in those parameters. We find that the halo is best represented by a broken power law with index $n_{in} = -2.50 \pm 0.04$ in the inner halo ($R < R_{break} = 19.5 \pm 0.04$) and $n_{out} = -4.85 \pm 0.04$ in the outer halo. Our data cannot constrain whether a change in the polar axis ratio also accompanies the break in the halo. The best fit values for the polar axes ratio indicate a moderately oblate halo: $q = 0.79 \pm 0.02$. The simpler (non-broken) triaxial power law models favour a practically axisymmetric halo, with $w \geq 0.88 \pm 0.07$ and the rest of parameters equal to those of the axisymmetric one.

We find that fitting models to data that contains substantial substructure can bias significantly the perception of triaxiality, decreasing the disk axis ratio w by 10%. We also find that different distance modulus bin sizes and the inclusion or exclusion of particular lines of sight can moderately influence our measurements of some structural parameters. This calls for carefully crafted analysis and tailored tests in any future studies. When compared to previous works, the choice of stellar tracer seems to have no significant influence on the values of the structural parameters, at least for these distance ranges.

Comparing our density profiles to the smooth model fits, we recover the presence of the Sagittarius stream in groups G and H. The Sagittarius stream in the direction of group H seems to extend further out from the Galactic centre than the models have so far predicted, and confirms previous RRLyrae detections associated with the stream at such distances (Ibata et al. (2001c), Totten & Irwin (1998) and Dohm-Palmer et al. (2001)). We also find evidence of more modest substructures extending over a long range of distances in group C ($35 \leq R_{GC} \leq 60$ kpc) and quite concentrated in distance in group D ($R_{GC} \approx 20$ kpc).

Our pencil beam survey has demonstrated that even a relatively small numbers of narrow fields of view, provided they are sampled sufficiently deep and with an abundant tracer, can place competitive limits on the global density profile and shape of the Galactic halo. The advent of similarly deep, wide-area surveys - like KiDS, VIKING and LSST- therefore promises to enhance substantially our understanding of the halo.

Chapter 3

A KiDS view on the structure of the Galactic halo

Authors

B. Pila-Díez, J.T.A. de Jong and K. Kuijken

Abstract

We study the density profile and shape of the Galactic halo using deep multi-colour images from the Kilo Degree Survey (KiDS) on the VLT Survey Telescope, in combination with previous MENeaCS and CCCP surveys to strengthen the constraining power through multiple lines of sight. The significant photometric depth and the Southern lines of sight of KiDS allow us to probe new regions of the halo. We build catalogues of near Main Sequence Turnoff point stars by homogenizing the PSF of the images, separating stars from galaxies through fixed-aperture photometry and using a multicolour selection for halo F stars. We calculate galactocentric distances for these stars and build density profiles along several lines of sight out to 60 kpc. We then add lines of sight from our earlier analysis of the MENeaCS and the CCCP surveys, and fit global halo models to the density profiles. We find that the stellar halo is best described by a power law model with a break in the power index, located within $[22, 30)$ kpc. The inner power law index is dependent on the value of the break distance ($n_{in} = [-3.30, -3.90) \pm 0.05$), whereas the outer power law index is quite stable ($n_{in} = -4.6 \pm 0.1$). We find a polar axis ratio of $q = 0.77 \pm 0.05$, in agreement with previous works, and an indication of a very mild triaxiality $w = 0.94 \pm 0.05$. We also recover data-to-model deviations matching previously known overdensities such as the Sagittarius stream and the Virgo Overdensity, and possible extensions of these or other substructures to greater distances than expected.

3.1 Introduction

Hierarchical galaxy formation is a natural consequence of the current cosmological model. Many of the oldest stars are expected to have formed in small galaxies, long before they were swallowed up into larger objects, and some are expected to have formed in-situ or evaporated from early low-mass globular clusters. Consequently, the oldest stars provide a fossil record of the beginnings of galaxy formation. Even though these stars only comprise a tiny fraction of the mass of present-day galaxies, their study is therefore worthwhile. The Galaxy is a unique environment in which to trace old stars, because stellar populations can be isolated star-by-star, even in regions where the surface brightness is well below observational limits in external galaxies.

Extensive studies of the star distribution in the Galactic outskirts have been undertaken (mostly in the Northern hemisphere) and have revealed a wealth of substructure in the form of streams and satellites—clear evidence of past accretion and merger processes (York et al. (2000); Ahn et al. (2014) and Skrutskie et al. (2006)). Also, the overall structural parameters of the stellar halo have been measured, yielding a picture of an ellipsoidal distribution with a radial density profile in the form of a broken power law. As data have improved, it has become possible to probe the halo with fainter, more abundant stars, close to the main sequence turnoff: a significant advance over older studies based on horizontal branch or red giant stars.

In this paper we use deep photometry from the Kilo Degree Survey (KiDS) obtained with the VLT Survey Telescope (VST) and its wide-field camera OmegaCAM to probe main sequence turn-off (MSTO) stars out to distances of 60 kpc. The KiDS main distinguishing attributes are both its footprint on the Southern sky and its outstanding depth, wich make it competitive in terms of the distant and faint or the otherwise uncharted halo. We split the current KiDS data into ten broad lines of sight through the Galactic halo to constrain its general stellar structure and probe potential substructure. We combine them with previous data from the Canada-France-Hawaii Telescope (CFHT) MegaCam and the Wide Field Camera (WFC) at the Isaac Newton Telescope (INT) – providing eight additional lines of sight– in order to increase its constraining power (Pila-Díez et al. 2015). In section 2 we describe the observations and the data processing relevant to our stellar catalogues and to our analysis. In section 3 we cover the star selection, the building of the density profiles and the smooth halo models that we consider. Finally, in section 4 we discuss and give context to our findings, and in section 5 we summarize our conclusions.

3.2 Survey and stellar catalogues

3.2.1 The Kilo Degree Survey

One of the Public Surveys conducted with the VLT Survey Telescope (VST), the Kilo-Degree Survey (KiDS, de Jong et al. 2013) is currently in the process

of imaging 1500 square degrees of extragalactic sky in four optical broad-band filters (u, g, r and i). The survey area is split between two fields, one in the northern and one in the southern Galactic cap. Aimed primarily at constraining the dark matter distribution in the universe through weak gravitational lensing, KiDS delivers deep and high quality images with typical image quality (PSF FWHM) ranging from $0.7''$ in r to $1.1''$ in u. KiDS limiting magnitudes are approximately 2 magnitudes fainter than those of SDSS: 24.3 in u, 25.1 in g, 24.9 in r and 23.7 in i.

The individual pointings are 1×1 deg^2. They are built up from four (u) or five (gri) dithers to fill inter-CCD gaps, with each position visited once for each filter, yielding the final survey depth in one go. During the first years of operation, the Galaxy And Mass Assembly (GAMA, Driver et al. 2011) fields have been prioritized to maximize the synergy with these deep spectroscopic data.

The KiDS data used in this work are from the first and second public data releases. Figure 3.1 shows the location of the included fields on the sky and the planned final coverage. A detailed description of the data reduction is provided in the release notes or on the KiDS website[1], but here follows a brief summary. Following cross-talk correction, satellite track removal and flat-fielding, an illumination correction is applied in order to flatten the photometry over the field-of-view. The photometric calibration is based on nightly zeropoints, after which the overlaps between CCDs from the different dither positions are used to tie all CCDs and dither together, resulting in photometry consistent to the 1–2% level over the full field-of-view. Small absolute zeropoint offsets between pointings persist since the patchy distribution of the included survey tiles yet prevents a full cross-calibration. After solving for the astrometric solution of all dithers together, stacked images are produced together with weight maps, masks for bright stars and other image defects, and source catalogs. The stacked images provided in the public data releases form the input for our further analysis.

We carry out a point-spread function (PSF) homegenization across each image. This homogenization provides improved fixed aperture photometry, corrected shape measurements and, indirectly, refined colours and enhanced star-galaxy separation. The code for the PSF homogenization –described in (Pila-Díez et al. 2014)– measures the shapes of the bright stars across a given image, maps the varying PSF and finally convolves the map with a spatially variable kernel in order to return gaussian PSFs.

From these images, photometric "Gaussian Aperture and PSF (GAaP)" catalogues are produced using Gaussian aperture weight functions $\omega^2\cdot\exp[-r^2/2(\omega^2-p^2)]/(\omega^2-p^2)$ at the positions of SExtractor-detected sources. As long as the aperture radius ω is larger than the Gaussian PSF dispersion p, this aperture function yields the correct total flux for isolated point sources (irrespective of ω). For extended sources, however, these aperture fluxes increase with ω.

[1] http://kids.strw.leidenuniv.nl/DR2

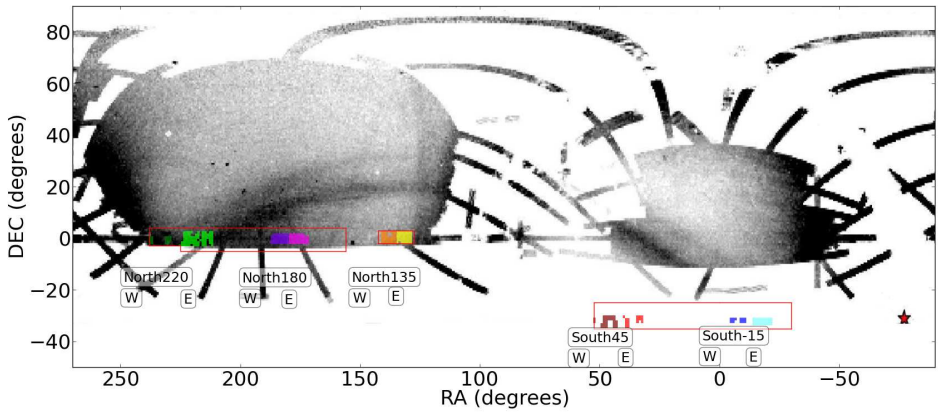


Figure 3.1: Equatorial map showing the position of all the KiDS fields used in this work (Data Releases 1 and 2). The different colours indicate the lines of sight in which the fields have been grouped to calculate the different density profiles. The background image is the SDSS-DR8 density map from Koposov et al. (2012), which shows the footprint of the Sagittarius stream and the location fo the Sagittarius dwarf galaxy. The red line denotes the expected KiDS footprint upon completion of the survey.

3.2.2 Catalogues

Stars and galaxies are separated by measuring their flux at $\omega = 0.5$" and 0.7" apertures in the r band, and keeping only those sources with $F_{0.5}/F_{0.7} \in [0.975, 1.025]$, that are detected at $> 5\sigma$ significance. A stellar completeness limit of $r = 23.2$ mag is imposed to avoid contamination by the small, round, fainter galaxies. And duplicate objects on overlapping tiles are removed.

The apparent magnitudes are dereddened using the interstellar extinction maps from Schlegel et al. (1998), and the GAaP photometry is corrected for a tile-based seeing dependency detected on the KiDS-to-SDSS offsets (see Figure 3.2). This dependency, a sign of residual flux at large radii after the PSF Gaussianization, is corrected through direct measurements (if the tile overlaps with SDSS data) or through a filter-specific interpolation. Once corrected for these offsets, GAaP provides a much smoother and flatter photometry on a star-by-star account than other photometry measuring tools, since it corrects for the PSF variation across each field of view. Last we transform the KiDS magnitudes to the SDSS system by appying the colour terms:

$$
\begin{aligned}
u_{SDSS} &= u_{KiDS} + 0.053 \cdot (u_{KiDS} - g_{KiDS}) - 0.0028 \cdot (g_{KiDS} - r_{KiDS}) \\
g_{SDSS} &= g_{KiDS} + 0.053 \cdot (g_{KiDS} - r_{KiDS}) \\
r_{SDSS} &= r_{KiDS} + 0.336 \cdot (g_{KiDS} - r_{KiDS}) \\
i_{SDSS} &= i_{KiDS} - 0.012 \cdot (r_{KiDS} - i_{KiDS}) - 0.0004 \cdot (g_{KiDS} - r_{KiDS})
\end{aligned}
$$

Table 3.1: Groups of pointings of KiDS as shown in Figures 3.1, 3.4, 3.5a and 3.6a. The table shows the central coordinates for each group, the number of individual fields of view contributing to it, its total area and the stellar completeness limit in the r band.

Group KiDS-	RA (deg)	Dec (deg)	l (deg)	b (deg)	$n_{\rm fields}$	Σ (deg^2)	$\rm mag_{lim,r,*}$
North220W	233.395758	0.12301	4.996485	42.63794	5	5.55	23.2
North220E	218.282384	-0.30425	348.794941	53.26131	24	24.45	23.2
North180W	183.806111	-0.02812	283.687780	61.48308	18	18.23	23.2
North180E	176.151782	-0.38023	269.928812	58.14329	19	18.29	23.2
North135W	138.175020	0.10505	230.730761	31.01870	17	18.49	23.2
North135E	131.554071	0.76375	226.214265	25.68091	20	19.78	23.2
South45W	46.602118	-32.24177	231.091424	-60.36720	8	9.68	23.2
South45E	35.744934	-31.99697	232.203287	-69.55028	6	5.52	23.2
South-15W	351.902387	-31.61901	14.081849	-71.22605	4	4.93	23.2
South-15E	342.302882	-31.81892	15.507201	-63.07876	12	13.29	23.2

The final photometry follows the expected colour-colour stellar loci from Covey et al. (2007) (see Figure 3.3).

Finally the KiDS fields are split in ten broad lines of sight based on their sky distribution (see Figure 3.1). The number of fields per line of sight, the central coordinates of these lines of sight and their affective area are recorded in Table 3.1. The effective areas have been calculated based on a finely spatially binned grid where we count the number of stars per bin as a way to determine the combined effect of masks and weights and tiles edges over the final catalogue of stars.

3.3 Stellar radial density profiles

3.3.1 Star selection and density profiles

We select near main sequence turnoff point (MSTO) stars as tracers for the overall stellar structure of the halo. To select them, we estimate their iron-to-hydrogen ratio and their absolute magnitude in the r band through two empirical photometric relations (Bond et al. (2010) and Ivezić et al. (2008), respectively):

$$[Fe/H] = -13.13 + 14.09x + 28.04y - 5.51xy - 5.90x^2 - 58.68y^2 + 9.14x^2y - 20.61xy^2 + 58.20y^3\,, \quad (3.1)$$

$$M_r = -0.56 + 14.32z - 12.97z^2 + 6.127z^3 - 1.267z^4 + 0.0967z^5 - 1.11[Fe/H] - 0.18[Fe/H]^2\,, \quad (3.2)$$

where $x = u - g$, $y = g - r$ and $z = g - i$. Relation 3.1 is valid in the $g - i < 0.6$ and $-2.5 \leq [Fe/H] \leq 0$ range, whereas relation 3.2 is valid in the $0.2 < g - i < 1.0$ range. Both regimes are compatible (and –for a small range– smoothly extrapolatable) to the colour regime of the nearMSTO stars.

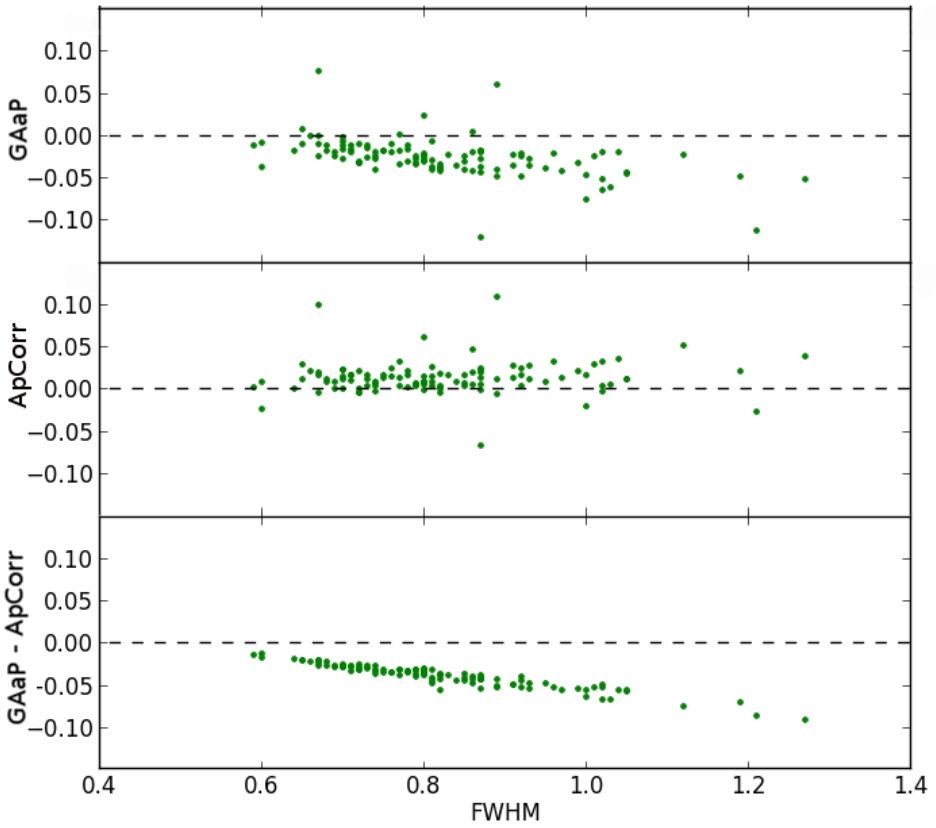


Figure 3.2: Relation between the KiDS-to-SDSS photometric offsets and the full-width at half-maximum (FWHM) in the g band for all the KiDS tiles that overlap with SDSS data. **Top:** KiDS-to-SDSS offsets based on GAaP photometry. The average offsets depart from zero with incresing FWHM. **Centre:** KiDS-to-SDSS offsets based on aperture-corrected photometry. The average offsets stay close to zero for all values of FWHM. **Bottom:** difference between the top and central panels (between GAaP and aperture-corrected photometries), to remove the tile-based scatter and illustrate the seeing dependency in GAaP. A similar relation is observed for the u, r and i filters.

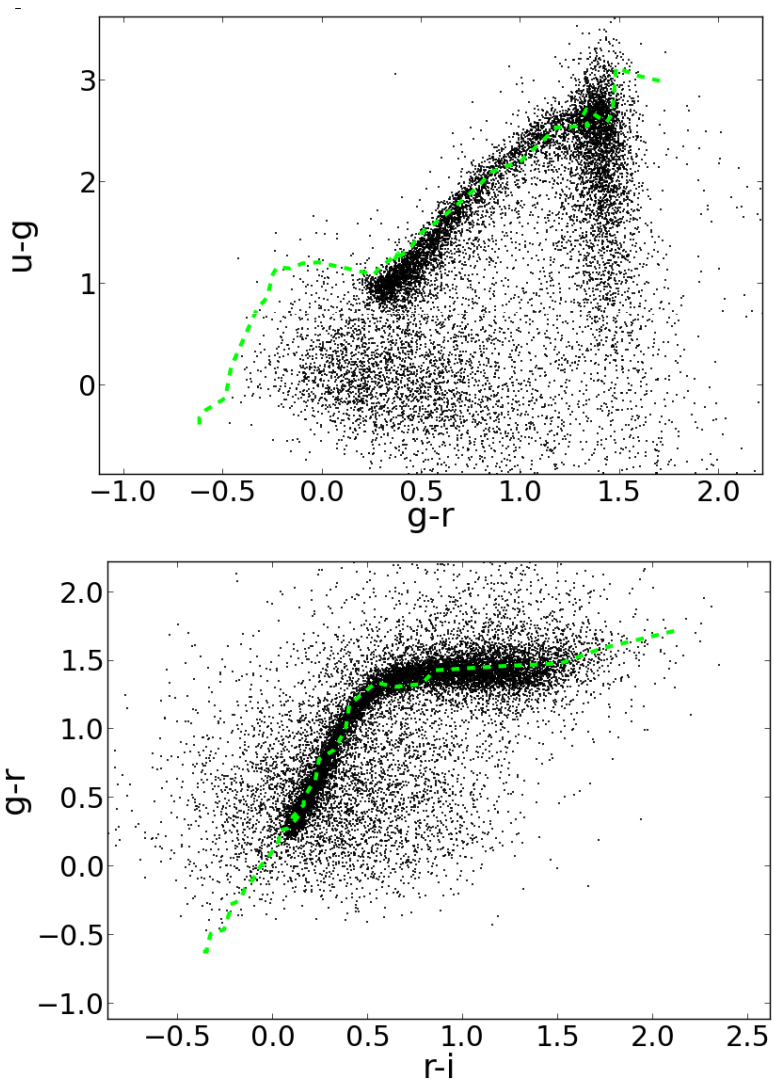


Figure 3.3: Colour-colour diagrams (CCDs) corresponding to one of the tiles in KiDS-North135E. The sources in the stellar catalogue (black) have been calibrated to SDSS's stellar photometry. The main sequence stellar loci (green dashed lines) are from Covey et al. (2007) (Tables 3 and 4).

We use the following cuts on the stellar colours, estimated [Fe/H] and estimated M_r to isolate the halo nearMSTO stars:

$$0.2 < g - r < 0.3\,; \tag{3.3}$$
$$g, r, i > 17\,; \tag{3.4}$$
$$0.1 < g - i < 0.6\,; \tag{3.5}$$
$$5.0 > M_r > -2\,; \tag{3.6}$$
$$-2.5 \leq [Fe/H] \leq 0\,. \tag{3.7}$$

These cuts provide a subset of halo, metal poor, distant, main sequence F stars and help decrease the contamination by quasars and white-dwarf/M-dwarf pairs (see Covey et al. (2007) for a general reference, or Pila-Díez et al. (2015) for an application to nearMSTO halo stars).

We derive the distance modulus and the heliocentric distance for each nearMSTO star from the estimated absolute brightness. At the stellar completeness limit of KiDS, this allows us to reach as far out as 60 kpc. We bin the nearMSTO stellar distribution in units of size $\Delta\mu = 0.2$ mag. We count the stars in each bin and calculate the stellar number density and its uncertainty (through partial derivatives) for the different lines of sight:

$$\rho_{l,b,D} = \frac{N_{l,b,\Delta\mu}}{0.2 \cdot ln(10) \cdot D_{hC}^3 \cdot \Delta\Omega \cdot \Delta\mu}\,; \tag{3.8}$$
$$E_\rho = \sqrt{(\frac{\rho}{\sqrt{N}})^2 + (\frac{\rho}{\sqrt{n_{fields}}})^2}\,. \tag{3.9}$$

where $N_{l,b,\Delta\mu}$ is the number of stars per bin in a given direction of the sky, D_{hC} is the heliocentric distance, $\Delta\Omega$ is the spherical area of each line of sight, and l and b denote the galactic coordinates for that line of sight. In practical terms:

$$\Delta\Omega = \frac{4\pi}{41253}\Sigma(\mathrm{deg}^2)\,, \tag{3.10}$$

where (Σ) is the effective area of each line of sight (Table 3.1).

The resulting density profiles are illustrated in Figure 3.4 for galactocentric distances. The figures and the following analysis and discussion are restricted to bins that meet $R_{GC} > 5$kpc, $|z| > 10$ kpc and a distance modulus of $\mu \leq mag_{lim} - 4.5 = 18.7$ mag (to avoid the Galactic thick disk and for completeness[2] of the faintest near-MSTO stars, respectively).

3.3.2 Fitting procedure

We fit a number of structural models of the Galactic stellar halo to the density profiles, first by only fitting the KiDS lines of sight, and later by fitting both the

[2]The incompleteness in the $mag_{lim} - 5.0 \leq \mu \leq mag_{lim} - 4.5$ distance range originating in equation 3.6 is on average 20% of the total number of near-MSTO stars present within the same distance range.

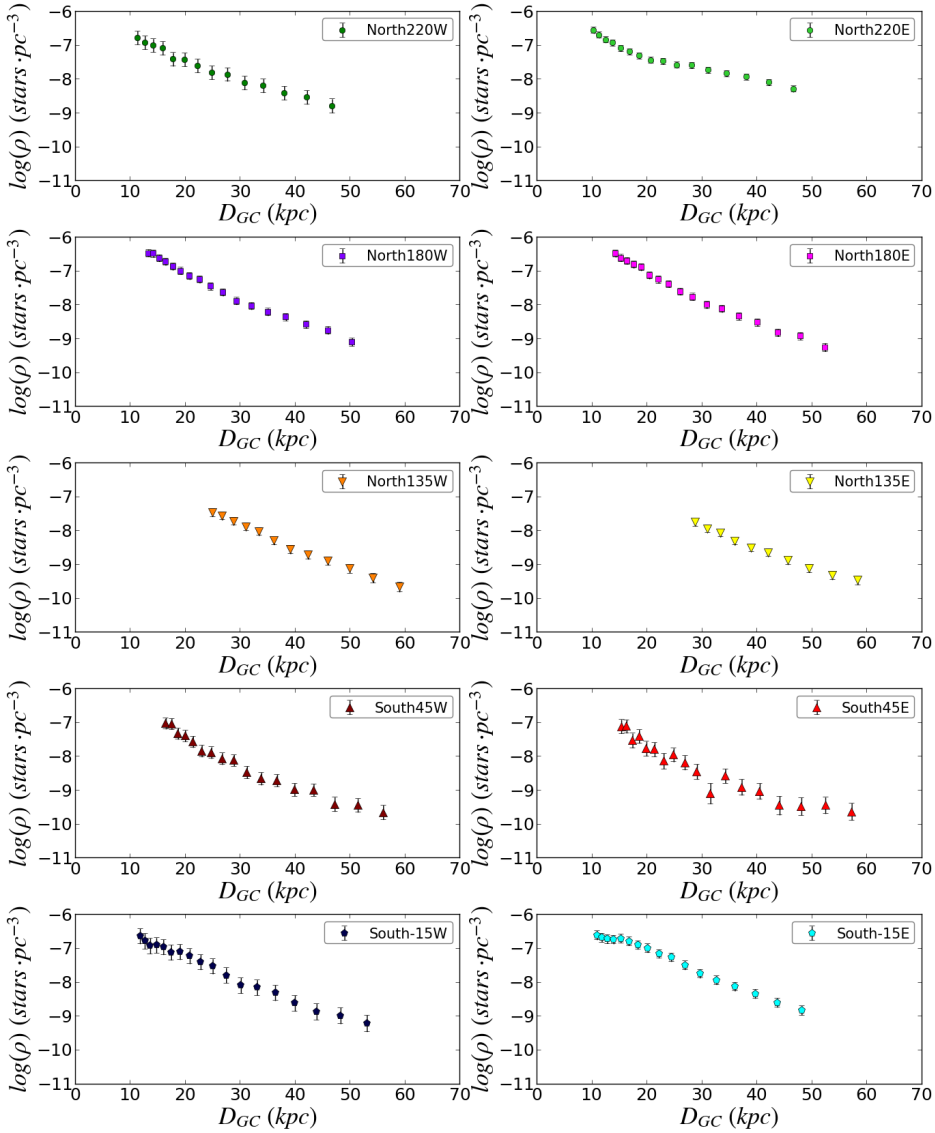


Figure 3.4: Stellar density profiles versus galactocentric distance for the near Main Sequence turnoff point stars (nearMSTO) from the KiDS lines of sight KiDS-North220W (dark green), KiDS-North220E (light green), KiDS-North180W (purple), KiDS-North180E (pink), KiDS-North135W (orange), KiDS-North135E (yellow), KiDS-South45W (brown), KiDS-South45E (red), KiDS-South-15W (blue) and KiDS-South-15E (cyan). Their colours match those in Figure 3.1.

KiDS and the CFHT-INT lines of sight presented in Pila-Díez et al. (2015) since the combination provides a more complete view of the stellar halo and returns better constraints.

The models are expressed in the galactocentric cartesian coordinate system (x, y and z). For the heliocentric to the galactocentric transformation, we assume that the Sun is located at (8,0,0) kpc (Malkin 2012). We fit the following models:

- Axisymmetric model:

$$\rho(x,y,z) \quad = \quad \rho_0 \cdot \left(x^2 + y^2 + \frac{z^2}{q^2} \right)^{n/2}, \tag{3.11}$$

  where $q = c/a$ is the polar axis ratio (or oblateness) of the halo.

- Triaxial model:

$$\rho(x,y,z) \quad = \quad \rho_0 \cdot \left(x^2 + \frac{y^2}{w^2} + \frac{z^2}{q^2} \right)^{n/2}, \tag{3.12}$$

  where $w = b/a$ is the axis ratio in the Galactic plane.

- Broken power law (change in the power index at R_{break}):

$$\rho(x,y,z) = \begin{cases} \rho_0 \cdot (R_{ellip})^{\,n_{in}}, & R_{ellip} < R_{break} \\ \rho_0 \cdot (R_{ellip})^{\,n_{out}} \cdot R_{break}^{\,n_{in}-n_{out}}, & R_{ellip} \geq R_{break} \end{cases} \tag{3.13}$$

$$R_{ellip} = \left(x^2 + y^2 + \frac{z^2}{q^2} \right)^{1/2}$$

- Double broken power law (change in the power index and the oblateness at R_{break}):

$$\rho(x,y,z) = \begin{cases} \rho_{0,in} \cdot \left(x^2 + y^2 + \frac{z^2}{q_{in}^2} \right)^{n_{in}/2}, & R_{GC} \leq R_{break} \\ \rho_{0,out} \cdot \left(x^2 + y^2 + \frac{z^2}{q_{out}^2} \right)^{n_{out}/2}, & R_{GC} > R_{break}\,. \end{cases} \tag{3.14}$$

We fit all these models to the data using Python's "curve-fit" method from its Scipy.optimize library (built on the Levenberg-Marquardt algorithm) in order to obtain the best fit values for the structural parameters. For the double broken power law model, we use a fixed value of R_{break}, which is the one suggested by the best fit of the simple broken power law model. Additionally, for the triaxial and the simple broken power law models, we also explore the fits to the data through a grid of fixed parameters where only the density scale factor (ρ_0) is allowed to vary freely. This allows us to evaluate the structural parameters in those cases where

the model is overparameterized in relation to the available data, and to check for local minima. The grids are built so that the different parameters evolve in the following ranges with specific incremental steps (δ): $q^2, w^2 \in [0.1, 2.0; \delta = 0.05]$, $n \in [-5.0 - 1.0; \delta = 0.1]$, $n_{in} \in [-4.0, -1.0; \delta = 0.1]$, $n_{out} \in [-7.0, -3.0; \delta = 0.2]$.

We determine the best-fit parameters by minimizing

$$\chi^2 = \sum_{i=1}^{N_{data}} \left(\frac{\rho_{data,i} - \rho_{model,i}}{E_{\rho,i}} \right)^2 . \tag{3.15}$$

We use its corresponding reduced expression for analysis and comparison between the models:

$$\chi^2_{red} = \frac{\chi^2}{N_{data} - N_{params}} , \tag{3.16}$$

whith N_{data} and N_{params} being the number of data bins and the number of free parameters in the model, respectively.

We mask out certain distance bins in the different lines of sight so that they are not considered for the models fitting. These masked regions correspond to the (3D) location of known halo stellar overdensities. In particular we excise the Sagittarius stream in the KiDS-North220 and KiDS-South-15 fields (at $D_{helioC} \in [30, 60]$ kpc and $D_{helioC} \in [15, 35]$ kpc, respectively), the Virgo Overdensity in the KiDS-North180 fields (at $D_{helioC} \in [6, 25]$ kcp) and the antincentre substructures –the Monoceros ring, the Eastern Band Structure (EBS) and the Anti Centre Structure (ACS)– in the KiDS-North135 fields (at $D_{helioC} \in [9, 15]$ kpc). As noted in Pila-Díez et al. (2015), not removing the substructure can have an impact on the structural parameters, with variations of $0.2 - 0.4$ for the inner power law index and 15% on the disk axis ratio, but not necessarily limited to these values or these parameters.

Finally we test the influence of the photometric uncertainties on the best fit values through a set of Monte Carlo simulations. We randomly modify the u, g, r, i magnitudes of each star within the boundaries provided by their photometric uncertainties, and produce a large number of mock catalogues. By fitting the axisymmetric model to each of them, we can create a statistic on the resulting structural parameters. We find that their variation is well accounted for by the statistical uncertainties returned by the fits, meaning that the simulated parameters fall within 1σ of our observed parameters.

3.3.3 Results

The best fit parameters for the independent fit of the ten KiDS lines of sight, for the independent fit of the eight CFHT-INT lines of sight (Pila-Díez et al. 2015) and for the combined fit of the KiDS plus the CFHT-INT lines of sights are presented in Tables 3.2, 3.3 and 3.4. The best fit parameters resulting from the grid fits are signaled by an asterisk after the name of the model and after the χ^2_{red} value. In the case of the triaxial model for the combined surveys, two

values of χ^2_{red} (resulting from the free-parameters fitting and the gridded fitting) are quoted, with both having converging best fit values for the paremeters.

The density profiles and the best fit models for the combined lines of sight are illustrated in Figure 3.5, where the masked out regions containing known substructure have been indicated with grey areas. The data-to-model residuals for the best fits of the combined lines of sight are shown in Figure 3.6.

If we compare the χ^2_{red} in Tables 3.2, 3.3 and 3.4, two facts become apparent. The first one is that the χ^2_{red} of the CFHT-INT-only fits are systematically smaller than those of the KiDS-only and KiDS plus CFHT-INT fits. This suggests that the KiDS density profiles deviate more strongly from a smooth halo, be it because of accreted overdensities or because of actual departures of the smooth halo from the models. Considering that the KiDS-North135W/E and the KiDS-South45W/E profiles follow the models perfectly (see Figure 3.6a), we rule out an intrinsic bias in the KiDS photometric calibration as the possible cause of the χ^2_{red} differences.

The second fact is that, in the three first fitting scenarios (axisymmetric, triaxial and simple broken power law model), the χ^2_{red} tends to decrease with model complexity. In particular, the χ^2_{red} suggests that the simple broken power law performs better than the triaxial and axisymmetric models, even if we account for the difference in the number of parameters between a free fit and a grid fit. The triaxial model performs slightly better than the axisymmetric model in the KiDS-only fits, but returns an extreme best fit value for the disk axis ratio ($w = 1.4 \pm 0.1$) and shows a large degeneracy along w. This suggests that the geometry of the KiDS footprint is not enough to constrain a possible triaxiality. When analysed for the CFHT-INT-only or the combined fits, the triaxiality loses any degeneracy and comes in agreement with inner Galaxy measurements ($w = 0.87 \pm 0.09$ and $w = 0.94 \pm 0.05$, respectively); however, it does this at the expense of a χ^2_{red} equal (once we take into account the smaller number of free parameters in the grid fits) to that of the axisymmetric model and converging ρ_0, n and q parameters. This is suggestive of a very mild triaxiality.

In general, all the fits –except that of the degenerate triaxial model fit to KiDS-only data– agree on a global power law index within $n \in [-4.2, -4.4]$, an outer power law index within $n_{out} \in [-4.6, -5.0]$ (including uncertainties) and a polar axis ratio within $q \in [0.74 \pm 0.05, 0.81 \pm 0.05]$. However, the different sets of fitted data return different break distances, R_{break}, that also affect the values of the inner power law index, n_{in} (from 19.0 ± 0.5 kpc to 30.5 ± 0.5 kpc and -2.45 ± 0.05 to -3.70 ± 0.05, respectively). We will discuss this further in section 3.4.2.

Finally, it is worth noting that both in the KiDS-only fits and the KiDS plus CFHT-INT fits, the complex broken power law model (the one with two possible values for n and for q) returns best fit values for the inner and outer oblatenesses that are in agreement with each other and with the oblateness of the other models (within uncertainties). This suggests that, based on our data, there is no need for a break in the polar axis ratio.

Table 3.2: Best fit parameters for the four different Galactic stellar distribution models fitted to the ten KiDS lines of sight. The data that is affected by known halo substructures (the Sagittarius stream, the Virgo Overdensity and the anticentre substructures) have been masked out for the fitting. Models and χ^2_{red} signaled with an asterisk indicate that their best fit values are the result of fitting through a parameter grid, and therefore have intrinsically smaller χ^2_{red} than those resulting from an all-free-parameters fit.

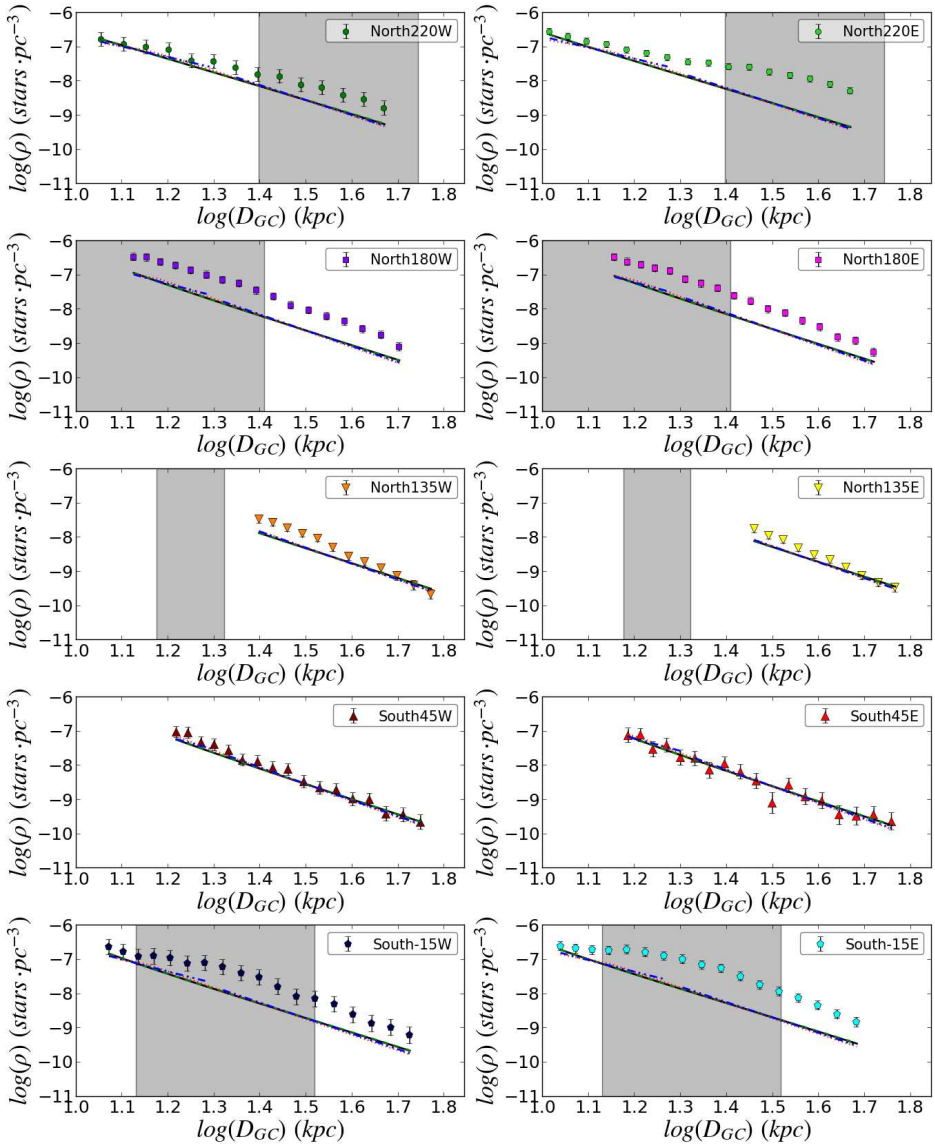
Model	χ^2_{red}	$\rho_0\,(\mathrm{pc}^{-3})\cdot 10^{-3}$	R_{break} (kpc)	n	n_{in}	n_{out}	q	q_{in}	q_{out}	w
axisymmetric	2.30	23 ± 8	–	-4.31 ± 0.08	–	–	0.79 ± 0.04	–	–	–
triaxial*	2.15*	13 ± 1	–	-4.30 ± 0.05	–	–	0.89 ± 0.05	–	–	1.4 ± 0.1
broken p.l.$_n$*	2.09*	3.9 ± 0.2	30.5 ± 0.5	–	-3.70 ± 0.05	-5.00 ± 0.05	0.81 ± 0.05	–	–	–
broken p.l.$_{n,\,q}$	1.39,2.86	5.3 ± 6	30.5_{fixed}	–	-3.8 ± 0.3	-4.9 ± 0.3	–	0.8 ± 0.1	0.79 ± 0.06	–
initial parameters	–	0.001	40.0	-3.00	-3.00	-3.50	0.70	0.70	0.8	1.00

Table 3.3: Same as in Table 3.2 but this time fitting the models to the CFHT-INT data (as presented in Table 2 of Pila-Díez et al. (2015)).

Model	χ^2_{red}	$\rho_0\,(\mathrm{pc}^{-3})\cdot 10^{-3}$	R_{break} (kpc)	n	n_{in}	n_{out}	q	q_{in}	q_{out}	w
axisymmetric	1.90	14 ± 6	–	-4.31 ± 0.09	–	–	0.79 ± 0.06	–	–	–
triaxial*	1.86*	14 ± 6	–	-4.28 ± 0.09	–	–	0.77 ± 0.06	–	–	0.87 ± 0.09
broken p.l.$_n$*	1.52*	0.071 ± 0.003	19.0 ± 0.5	–	-2.40 ± 0.05	-4.80 ± 0.05	0.77 ± 0.03	–	–	–
broken p.l.$_{n,\,q}$	1.99,1.51	1 ± 3	19_{fixed}	–	-3.3 ± 0.6	-4.9 ± 0.2	–	0.7 ± 0.2	0.88 ± 0.07	–
initial parameters	–	0.001	40.0	-3.00	-3.00	-3.50	0.70	0.70	0.8	1.00

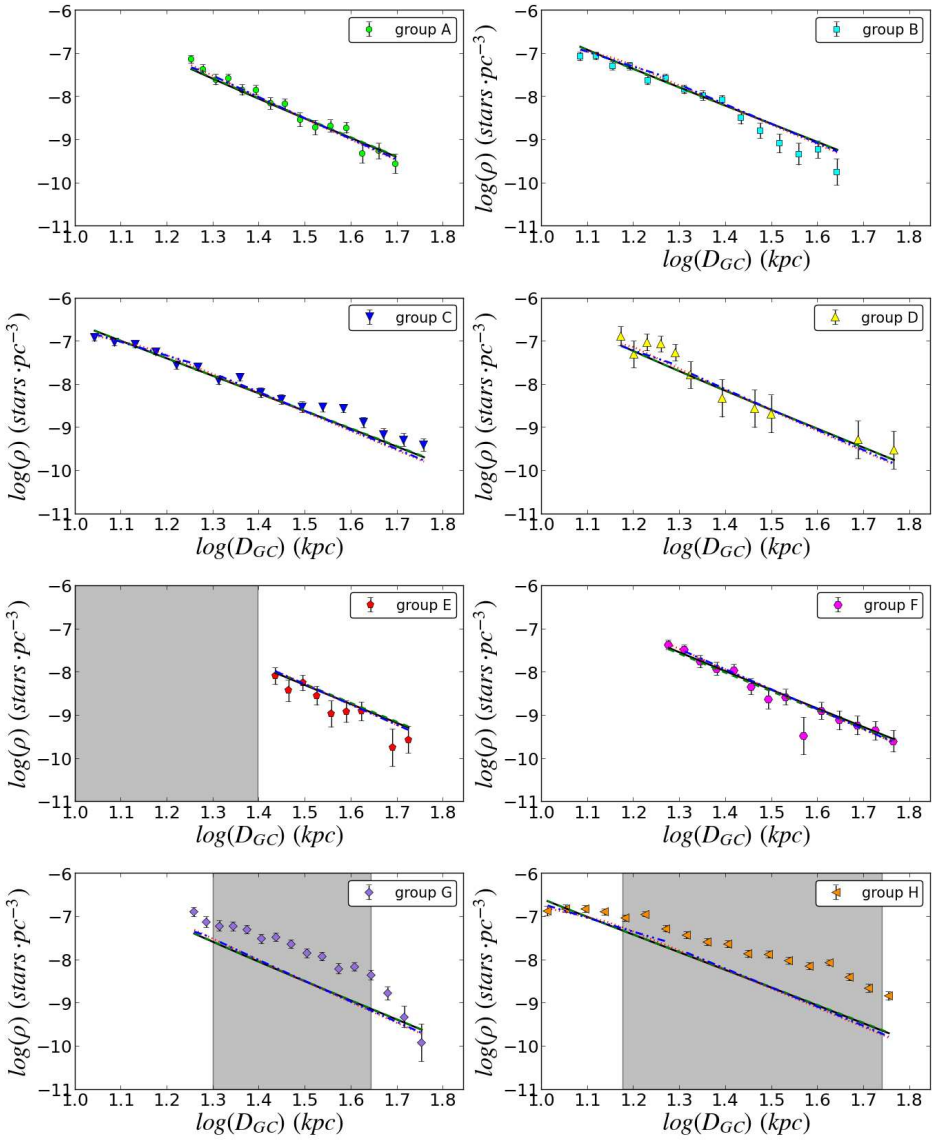
Table 3.4: Same as in Table 3.2 and Table 3.3 but this time fitting the models to both the KiDS and the CFHT-INT data.

Model	χ^2_{red}	$\rho_0\,(\mathrm{pc}^{-3})\cdot 10^{-3}$	R_{break} (kpc)	n	n_{in}	n_{out}	q	q_{in}	q_{out}	w
axisymmetric	2.53	16 ± 5	–	-4.27 ± 0.07	–	–	0.75 ± 0.03	–	–	–
triaxial	2.53//2.50*	17 ± 5	–	-4.26 ± 0.07	–	–	0.74 ± 0.04	–	–	0.94 ± 0.05
broken p.l.$_n$*	2.36*	0.10 ± 0.01	19.0 ± 0.5	–	-2.45 ± 0.05	-4.6 ± 0.05	0.74 ± 0.05	–	–	–
broken p.l.$_{n,\,q}$	1.80,2.64	1 ± 2	19.0_{fixed}	–	-3.3 ± 0.5	-4.6 ± 0.1	–	0.8 ± 0.1	0.76 ± 0.04	–
initial parameters	–	0.001	40.0	-3.00	-3.00	-3.50	0.70	0.70	0.8	1.00



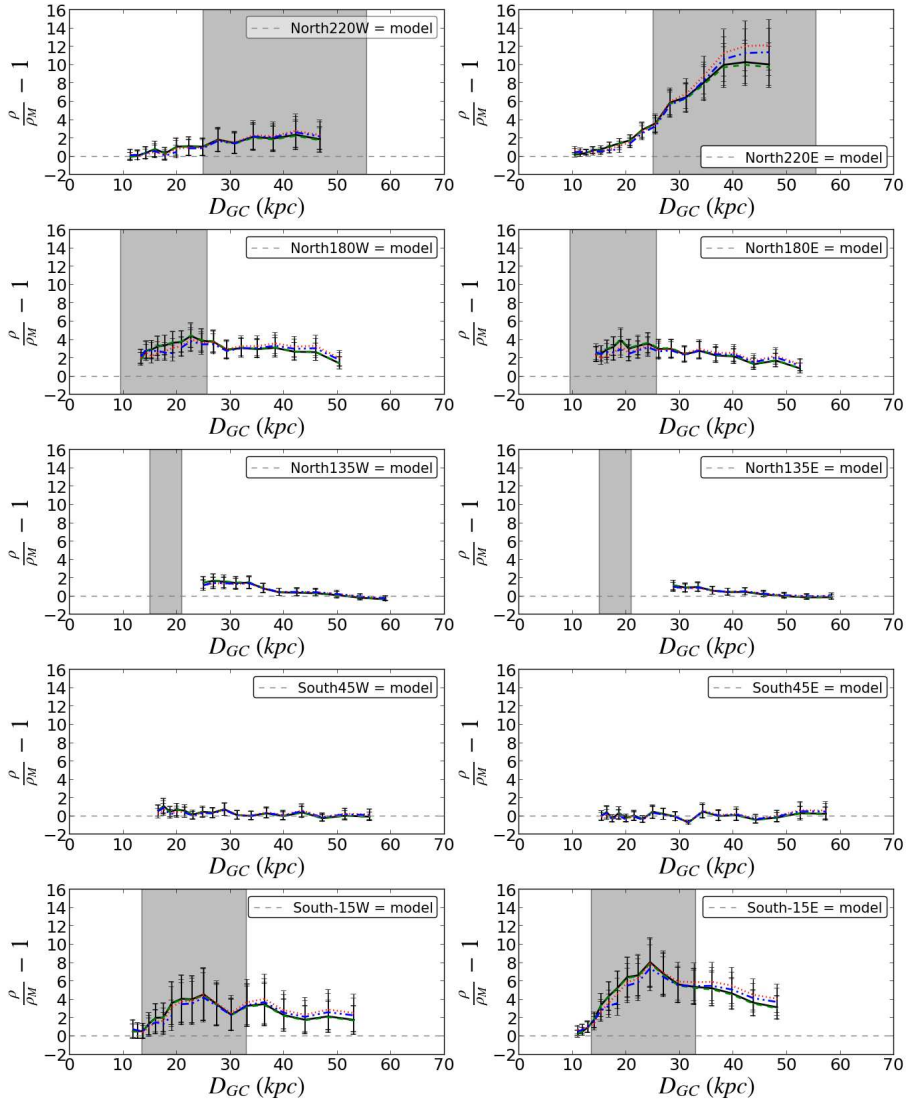
(a) Fitted density profiles for the KiDS lines of sight.

Figure 3.5: Density profiles in decimal logarithmic scale and the models' best fits from Table 3.4 for the KiDS lines of sight. The different lines represent the axisymmetric (black solid line), the triaxial (green dashed line), the broken power law with varying power index (red dotted line) and the broken power law with varying power index and oblateness (blue dashed-dotted- dotted line) models. The grey areas denote data that have been masked from the fitting due to the presence of substructure.



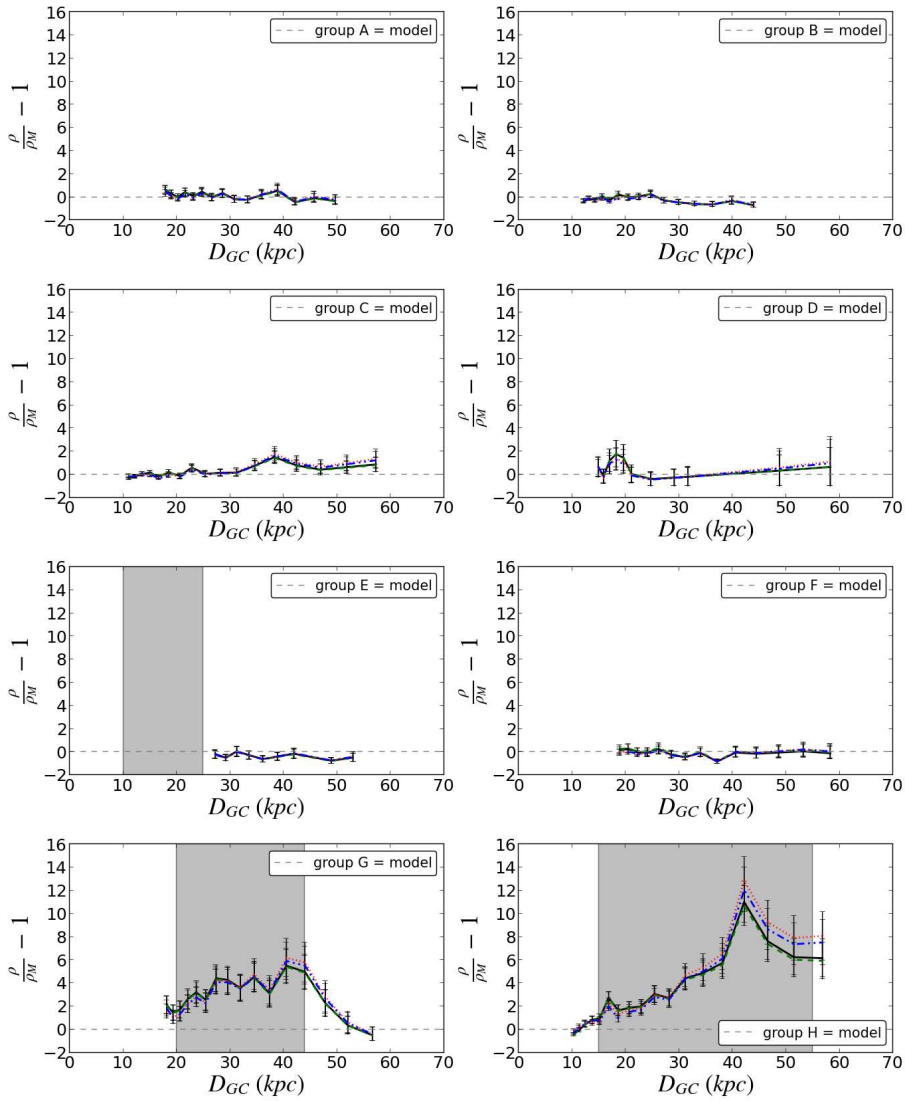
(b) Fitted density profiles for the CFHT-INT lines of sight.

Figure 3.5: Density profiles in decimal logarithmic scale and the models' best fits from Table 3.4 for the CFHT-INT lines of sight. The different lines and the shaded areas follow the same code as in Figure 3.5a.



(a) Data-to-model residuals for the KiDS lines of sight.

Figure 3.6: Residuals between the data and the models' best fits from Table 3.4 for the KiDS lines of sight. The different lines and the shaded areas follow the same code as in Figure 3.5a.



(b) Data-to-model residuals for the CFHT-INT lines of sight.

Figure 3.6: Residuals between the data and the models' best fits from Table 3.4 for the CFHT-INT lines of sight. The different lines and the shaded areas follow the same code as in Figure 3.5a.

3.4 Discussion

3.4.1 Robustness of the best fit structural parameters

We test the influence of the different lines of sight on the best fit parameters in search for potential sources of bias. For this, we remove the KiDS lines of sight one at a time and perform the free-parameters fits for the axisymmetric, triaxial and simple broken power law models on the KiDS plus CFHT-INT density profiles (a similar test for CFHT-INT-only lines of sight can be found in Pila-Díez et al. (2015)).

By doing this for the axisymmetric model, we find that any line of sight removal keeps the n new values within the uncertainties of the overall results. However removing KiDS-North180W/E from the set decreases q slightly beyond the uncertainty of the overall oblateness, while removing KiDS-North135W/E increases it in a similary manner. Those same lines of sight move the n values in the same directions, but within the uncertainty limits.

Checking for the triaxial model, we find that in this case any line of sight removal keeps the n, q and w new values within the uncertainties of the overall results, with no significant deviations. KiDS-North180W/E and KiDS-North135W/E seem to have the largest influences in the same directions they had for the axisymmetric case. Additionally, removing one of KiDS-North135W/E decreases w the most.

Finally we test the influence of the different lines of sight for the freely fit simple broken power law model. When fitting all the available lines of sight, the returned parameters were unconstrained and the break distance was much larger than the distances probed by our data. This motivated the use of a parameters-grid for fitting. When we remove the KiDS lines of sight one at a time, we find a similar behaviour in all the cases except that of KiDS-North180W. Interestingly, removing this line of sight returns constrained values for the parameters, meaning that this is the line of sight introducing most of the uncertainty into the fit(s). In practice, however, we cannot exploit this improvement in the fits to our advantage, because removing KiDS-North180W places the break distance beyond the scope of our data, at $R_{break} = 65 \pm 7$ kpc, with a $\chi^2_{red} = 2.28$, effectively representing an axisymmetric model.

Overall, we can conclude that removing any single line of sight does not significantly change the fit results.

3.4.2 KiDS vs CFHT-INT

When fitting the axisymmetric model to either one of the two surveys or to their combination, although the χ^2_{red} for the KiDS fit worsens (it is 20% larger than for the CFHT-INT fit), the three fits return consistent results for the halo structural parameters.

When fitting for triaxiality, it is clear that the w value found for the KiDS fit is large and implausible, as compared to previous measurements of the disk axis

ratio and our current knowledge of the Milky Way. The reason for this improbable value is that there is only one line of sight in our KiDS data set at reasonably low Galactic latitude, and therefore the constraining power for w is poor. Once combined with the CFHT-INT data set, the constraining power increases and returns values within the anticipated range. As it should be expected for a value of w close to 1, all the triaxial model fits return values for the other parameters in agreement with those of the axisymmetric model fits.

For the broken power law model, the fits to the different data sets return comparable results for the outer halo (n_{out}) and the oblateness. This can be explained by the fact that both surveys amply sample the outer halo, with most data points at distances larger than 25 kpc. The only real inconsistency between the fits to the two data sets happens for the break radius and, subsequently, for the inner power law index (n_{in}), which we investigate further.

The colour maps and isocontours in Figure 3.7 map the best fits χ^2_{red} values for different values of the structural parameters for the KiDS (left), the CFHT-INT (centre) and the combined data sets (right). It becomes clear from these diagrams that the break distance is poorly constrained, and that n_{in} is strongly dependent on the survey. In the case of the KiDS-only fits, the best fit values of n_{in} are a function of the best fit values of R_{break}. In the case of CFHT-INT-only and the combined surveys, the fits favour a small value for R_{break}, but at the same time the sparsity of data points at $R_{GC} < 20$ kpc renders the value of n_{in} degenerate.

An explanation for this degeneracy of n_{in} and for such a small absolute best fit value of R_{break} in the CFHT-INT and the combined data sets lies within the density profiles. A close inspection of the density profiles shows that these break distance values match the distance where most of the CFHT-INT lines of sight are beginning. Particularly, only three out of the eight lines of sight are contributing density bins below the 19 kpc threshold (lines B, C and H), and only two of those three are fitted uninterruptedly further out, probing the alleged transition (H is masked out at $D_{helioC} = 20$ kpc or $R_{GC} = 15$ kpc). This suggests that the fitting algorithm is indeed trying to adjust to the lack of data rather than trying to fit a true transition within the data. The disappearance of the n_{in} degeneracy beyond $R_{break} > 22$ kpc suggests that the true value of the break distance lies somewhere between this transition point and the value suggested by the KiDS-only lines of sight. This is, somewhere between 22 kpc and 31 kpc, rather than at 19 kpc. An exploration of the grid parameters and their χ^2_{red} when the break distance is fixed at the average value from the literature (27 kpc, see Table 3.5), shows that the best fit in such a case holds a practically identical value of χ^2_{red} to that of the absolute minimum (with a difference of only 1.7%).

In conclusion, the relatively small amount of data at $R_{GC} < 30$ kpc causes us to be unable to constrain R_{break} very well, and probably introduces a bias towards small R_{break} values and degenerate n_{in} values through the CFHT-INT data set. Ideally, with more data available at short galactocentric distances in a wider survey (or combination of surveys), one would fit models of both the thick disk and the halo, as a way to remove our $|z| > 10$ kpc constraint on the density

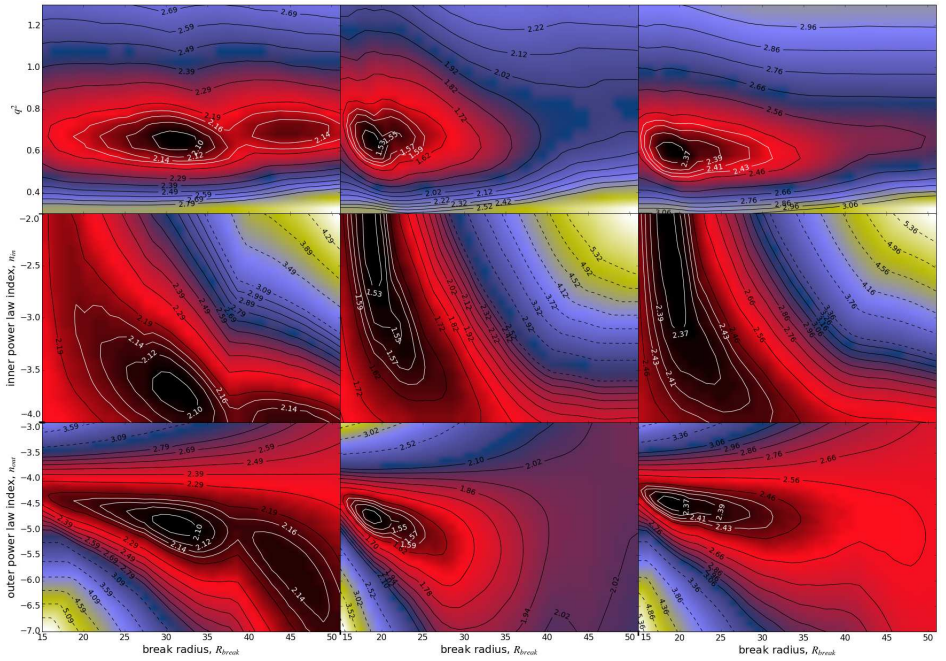


Figure 3.7: χ^2_{red} isocontours maps showing the relation between a given structural parameter and the break distance based on the grid fits for the simple broken power law model. **Left panels:** fits to the KiDS data set. **Central column panels:** fits to the CFHT-INT data set. **Right panels:** fits to the combined data sets. **Top panels:** polar axis ratio versus break distance. **Central row panels:** inner power law index versus break distance. **Bottom panels:** outer power law index versus break distance.

profile bins that are used for fitting. This procedure would allow to fit the halo at smaller radii, while also preserving the excellent handle on the outer reaches afforded by the KiDS and CFHT-INT deep photometry. Of course, this approach comes at the cost of increasing the complexity by forcing to consider both the halo and the thick disk. This has been done by Robin et al. (2014), who used their SDSS plus 2MASS data to explore the thick disk and the halo mostly out to $R_{GC} < 30$ kpc. Their fits favour a break distance located at $R_{break} > 30$ kpc, but it would seem plausible that their lack of data at larger distances prevents them from detecting a closer break distance, just like our lack of data at short distances prevents us from constraining it.

3.4.3 Comparison to previous studies

We compare our results on the structural parameters of the stellar halo to several previous results in the literature, namely: Jurić et al. (2008), Sesar et al. (2011),

Deason et al. (2011), Robin et al. (2014), de Jong et al. (2010), Chen et al. (2001), Bell et al. (2008), Faccioli et al. (2014), Sesar et al. (2010a), Watkins et al. (2009) and Pila-Díez et al. (2015). The results, stellar tracers and distance ranges of these works have been summarized in Table 3.5. A detailed description of their geometry and sky coverage can be found in Pila-Díez et al. (2015).

Although RRLyrae stars have been used as stellar halo tracers out to 110kpc, our data allows us to construct stellar density profiles further out (up to 60 kpc) than any previous analysis. This provides us with an unprecedented constraining power for the outer stellar halo, only comparable to the results presented in Pila-Díez et al. (2015).

In our previous work we already noted that all surveys that reach beyond $R_{GC} = 30$ kpc seem to agree on the need for a break in the power law index. The difference between n, n_{in} and n_{out} for the different surveys is probably not only an effect of the different geometries of the surveys but also a reflection of their different distance ranges and of the sharp or progressive steepening of the halo. The fact that the different works fail to find a consensual break distance or consensual power index values, together with the degeneracy that we detect between n_{in} and R_{break}, are in support of this interpretation.

Nonetheless and independently of the exact interpretation, these works find the break distance to be located between 20 and 34 kpc. The best fit values for R_{break} for the CFHT-INT and the KiDS individual data sets (19.0 ± 0.5 and 30.5 ± 0.5, respectively) lie near the opposite extremes of this distance range, but, as discussed in section 3.4.2, the degeneracy between n_{in} and R_{break} suggests more reliable values in the $[22, 30)$ kpc range.

Several of the other studies that are limited to Galactocentric distances smaller than 30 kpc and only fit a single power law index to the halo, provide indices in the $[-3.3, -2.5]$ range. The n_{in} values of the studies that do detect a break in the power law are roughly consistent with this range, with the most significant discrepancy coming from our KiDS-only result and our KiDS plus CFHT-INT result in case of a large value for R_{break}. For the outer halo, power law indices are generally found to be in the $[-3.5, -5.8]$ range, although the majority of studies seems to cluster around -4.0. Again, the values for n_{out} that we find for our data sets are on the steeper side of the distribution (between -4.6 and -5.0). The recovered steepness of the power law might be related to the inclusion or removal of large, known substructures in the fitted data, as also noted by Robin et al. (2014). In Pila-Díez et al. (2015) we showed that in the case of our CFHT-INT data set the inclusion of the Sagittarius stream leads to a power-law index that is 0.2 dex smaller for the axisymmetric and triaxial halo models. Keeping in mind this effect, together with the fact that our data probes the underlying stellar density distribution of the outer halo further out than other data sets, we conclude that the smooth outer halo follows a power law with index close to -4.6.

The oblateness values of several previous works seem to agree in $0.55 \leq q \leq 0.70$, with the only clear exception of de Jong et al. (2010) ($q = 0.88 \pm 0.03$) and the wider Bell et al. (2008) ($q \in [0.5, 0.8]$). Our results, both for the KiDS-only,

for the CFHT-INT-only and for the combined triaxial and broken fits, all fall in the higher-end of this range, with values within 0.74 ± 0.05 and 0.81 ± 0.05. Therefore it seems safe to conclude that the stellar halo is moderately oblate, and is best represented by a steepening of the density profile at distances larger than 25 kpc.

We also find that a very mild triaxiality ($w = 0.94 \pm 0.05$) is a good representation of the stellar halo, although we do not test this hypothesis in combination with the broken power law model for the sake of simplicity and proper parametrization. The only other works that reported specific values on the triaxiality are Bell et al. (2008) and our previous study with CFHT-INT-only data. Both found that $w \geq 0.8$.

3.4.4 Detection of overdensities and identification

Finally, we look for overdensities in the data-to-model residuals (Figure 3.6) of the KiDS lines of sight, since the CFHT-INT lines of sight were already discussed in Pila-Díez et al. (2015).

We find that the density profiles for regions KiDS-North135W, KiDS-North135E, KiDS-South45W and KiDS-South45E follow the models quite well, with a brief maximum deviation of a factor of 2 for KiDS-North135W.

We also find a very clear overdensity matching the expected distances for the Sagittarius (Sgr) stream in the KiDS-North220E line of sight. We note that this overdensity already starts to smoothly build up as early as $R_{GC} = 20$ kpc, and reaches its maximum (a factor of ~ 10) at around 40 kpc. KiDS-North220W, on the contrary, displays a very mild and constant overdensity of only a factor of 2^{+2}_{-1}. This could indicate that the KiDS-North220W is only partially probing the Sgr stream, that it is probing a less dense region of the stream or that there is no contribution from a stream but simply a departure of the smooth halo component from the theoretical model.

The lines of sight corresponding to the KiDS-North180W and KiDS-North180E regions depart from the models at all probed distances. In the $R_{GC} \in [10, 27]$ kpc range, we were expecting an overdensity caused by the Virgo overdensity. However, the residuals barely decrease beyond this distance range (from an overdensity of a factor of 4 ± 1 to factors of 3 ± 1 and 2 ± 1). This suggests that the Virgo Overdensity extends farther out than previously known or, at least, that its stellar counts fade less sharply than in the case of colder streams. However, to what level the departure from the models at larger distances is due to remnants or influence of this substructure or due to the intrinsic structure of the smooth halo, can not be derived from the density profiles.

The two overdensities showing up in KiDS-South-15E and KiDS-South-15W are identified as the Sagittarius stream, based on the distances and locations recovered by 2MASS and the extrapolation from the SDSS-DR8 footprint. The overdensity in KiDS-South-15E starts to build up at $R_{GC} \approx 15$ kpc and peaks at $R_{GC} \approx 25$ kpc (with a factor of 2^{+3}_{-2}), decreasing slowly past the predicted distance of ~ 35 kpc and persisting at least out to 50 kpc (with a factor of 4 ± 2).

Table 3.5: Comparison between the best fit structural parameters found in this work for the combined KiDS + CFHT-INT data, the CFHT-INT data in Pila-Díez et al. (2015) and those reported by other groups in previous works. The different works have been labelled as follows: PD15 (Pila-Díez et al. 2015), J08 (Jurić et al. 2008), S11 (Sesar et al. 2011), D11 (Deason et al. 2011), R14 (Robin et al. 2014), dJ10 (de Jong et al. 2010), Ch01 (Chen et al. 2001), B08 (Bell et al. 2008), F14 (Faccioli et al. 2014), and S10 (Sesar et al. 2010a) and W09 (Watkins et al. 2009) as reanalysed in F14. The fitted models in F14, S10 and W09 have fixed oblateness and test two different values motivated by the previous findings in S11 and D11. This work, PD15, J08 and S11 use nearMSTO stars as a stellar tracer; D11 use A-BHB and A-BS stars; R14 and dJ10 use multiple stellar tracers; Ch01 and B08 use MSTO stars; and F14, S10 and W09 use RRLyrae stars as a tracer.

Work	dist. range (kpc)	χ^2_{red}	R_{br} (kpc)	n	n_{in}	n_{out}	q	w
CFHT-INT-broken	$[10, 60]$	1.5	19.5 ± 0.4	–	-2.50 ± 0.04	-4.85 ± 0.04	0.79 ± 0.02	–
KiDS-broken	$[10, 60]$	2.1	30.5 ± 0.5	–	-3.70 ± 0.05	-5.00 ± 0.05	0.81 ± 0.05	–
KiDS-CFHT-INT-triax.	$[10, 60]$	2.5	–	-4.26 ± 0.07	–	–	0.74 ± 0.04	0.94 ± 0.05
KiDS-CFHT-INT-broken	$[10, 60]$	2.4	$[22, 30)$	–	$[-3.30, -3.90)$	-4.6 ± 0.1	0.77 ± 0.05	–
J08	$[5, 15]$	$[2, 3]$	–	–	-2.8 ± 0.3	–	0.65 ± 0.15	–
S11	$[5, 35]$	3.9	27.8 ± 0.8	–	-2.62 ± 0.04	-3.8 ± 0.1	0.70 ± 0.02	excluded
D11	$[-, 40]$	–	27.1 ± 1	–	-2.3 ± 0.1	$-4.6^{+0.2}_{-0.1}$	$0.59^{+0.02}_{-0.03}$	–
R14	$[0, 30]$	–	–	-3.3 ± 0.1	–	–	0.70 ± 0.05	–
dJ10	$[7, 30]$	$[3.9, 4.2]$	–	-2.75 ± 0.07	–	–	0.88 ± 0.03	–
Ch01	$[-, 30]$	–	–	-2.5 ± 0.3	–	–	0.55 ± 0.06	–
B08	$[5, 40]$	2.2	~ 20	-3 ± 1	–	–	$[0.5, 0.8]$	≥ 0.8
F14	$[9, 49]$	0.8	28.5 ± 5.6	–	-2.8 ± 0.4	-4.4 ± 0.7	$q_{fix} = 0.70 \pm 0.01$	–
"	$[9, 49]$	1.04	26.5 ± 8.9	–	-2.7 ± 0.6	-3.6 ± 0.4	$q_{fix} = 0.59^{+0.02}_{-0.03}$	–
S10	$[9, 49]$	1.1	34.6 ± 2.8	–	-2.8 ± 0.2	-5.8 ± 0.9	$q_{fix} = 0.70 \pm 0.01$	–
"	$[9, 49]$	1.52	26.2 ± 7.4	–	-3.0 ± 0.3	-3.8 ± 0.3	$q_{fix} = 0.59^{+0.02}_{-0.03}$	–
W09	$[9, 49]$	1.1	27.6 ± 3.3	–	-2.5 ± 0.3	-4.3 ± 0.4	$q_{fix} = 0.70 \pm 0.01$	–
"	$[9, 49]$	0.69	26.9 ± 3.1	–	-2.1 ± 0.3	-4.0 ± 0.3	$q_{fix} = 0.59^{+0.02}_{-0.03}$	–

The overdensity(s) in KiDS-South-15E similarly extend from $R_{GC} \approx 15$ kpc out to 55 kpc, but displays a less strongly peaked distribution and, potentially, two possible crests. These residuals are less significant than those in KiDS-South-15E, with the highest overdensity level reaching a factor of 4^{+3}_{-2}.

A more extensive investigation of all overdensities (expected and unexpected), using additional tools other than stellar density profiles, is planned for a future publication.

3.5 Conclusions

In this work we have used deep wide-field images from the Kilo Degree Survey (KiDS) at VST to explore the stellar density profile of the halo. We have homogenized the PSF of our images in order to obtain more accurate fixed-aperture photometry and enhance the star- galaxy separation. The stellar completeness limit of our catalogues reaches $mag_r = 23.2$ mag. From these catalogues we have selected the near main sequence turnoff point stars (nearMSTO stars) as our stellar tracer for the shape of the halo using colour cuts in $g-r$ and $g-i$, magnitude cuts for faint stars in g, r, i and metallicity and absolute magnitude cuts on the $[Fe/H]$ and M_r estimators. This yields a subset of mainly halo F stars, significantly decontaminated from white-dwarf/M-dwarf pairs and quasars.

We have calculated the galactocentric distances of the nearMSTO stars through the photometric parallax method and used them to build density profiles along ten different lines of sights. We supplement these KiDS lines of sight with eight CFHT-INT lines of sight from our earlier study (Pila-Díez et al. 2015). We have fitted four galactic halo models to these data in order to derive insight on the stellar structure of the halo. For every fit we have masked out the profile sections where we anticipated stellar overdensities of accreted origin, in order to avoid biases on the structural parameters. Our best fits favour slightly a power law distribution with a break in the power law index ($\chi^2_{red} = 2.4$), closely followed by a single power law distribution with a mild triaxiality ($\chi^2_{red} = 2.5$).

Our best fit values for the break distance seem to be biased by the distribution of the data, favouring a value close to the transition between masked out and fitted data in the case of KiDS-only fits ($R_{break} = 30.5 \pm 0.5$ kpc), and favouring a value close to the start of our density profiles in the case of CFHT-INT-only fits and KiDS plus CFHT-INT fits ($R_{break} = 19.5 \pm 0.5$ kpc). This, in combination with a clear degeneracy of the inner power law index for the smaller break distance values and a disappearance of the degeneracy beyond 22 kpc, suggests that the real break distance is located somewhere $R_{break} \in [22, 30)$ kpc, in agreement with previous findings by other works.

We have found that the best fit value for the inner power law index strongly correlates with the break distance. Our data favour values for the inner and the outer indices on the steeper end of previous findings: $n_{in} = [-3.30, -3.90) \pm 0.05$ and $n_{out} = -4.6 \pm 0.1$, where previously most of the works suggested $n_{in} \in [-2.1, -3.3]$ and $n_{out} \in [-3.6, -5.8]$. As demonstrated in Pila-Díez et al. (2015),

the inclusion of large substructures such as the Sagittarius stream in halo fits can significantly influence the recovered parameters. Based on the exclusion of known substructure, together with the constraining power of our data at large distances, we conclude that the smooth outer stellar halo has a power law index close to -4.6.

We have found a disk axis ratio of $w = 0.94 \pm 0.05$, suggesting a very mild triaxiality. We do not test triaxiality in combination with the broken power law to avoid overparametrization problems. Few other works have reported on the triaxiality of the halo, and those who did agreed on $w > 0.8$. We have also found a polar axis ratio of $q = 0.77 \pm 0.05$, where most of the previous works found $0.55 \leq q \leq 0.70$ and some $q \leq 0.8$. Overall there seems to be a significant consensus on the stellar halo being moderately to quite oblate.

We have been able to recover a number of known stellar overdensities in our data-to-model residuals. Particularly, we clearly recover a strong signal matching the Sagittarius stream in the KiDS-North220E and KiDS-South-15E regions, a more moderate signal in KiDS-South-15W and a possible match (yet weak overdensity) in KiDS-North220W. Similarly, we recover overdensities matching the location and extent of the Virgo Overdensity in the KiDS-North180W and KiDS-North180E regions; in these two regions the overdensities seem to fade slowly, indicating either that the feature extends further out than previously thought or that it slowly blends with a smooth halo that does not exactly follow the models at these locations. Finally, we also seem to find overdensities in the already mentioned regions of KiDS-South-15E and KiDS-South-15W at further distances than those expected for the Sagittarius stream; this is suggestive of a previously unknown structure or a departure of the Sagittarius stream from the models. These overdensities will be further explored in future work, with tools more powerful than density profiles for characterizing substructure –such as Colour Magnitude Diagrams or matched filters–.

Chapter 4

Finding halo streams with a pencil-beam survey – new wraps in the Sagittarius stream

Authors

B. Pila-Díez, K. Kuijken, J.T.A. de Jong, H. Hoekstra and R.F.J. van der Burg

Abstract

We use data from two CFHT-MegaCam photometric pencil-beam surveys in the g' and the r' bands to measure distances to the Sagittarius, the Palomar 5 and the Orphan stream. We show that, using a cross-correlation algorithm to detect the turnoff point of the main sequence, it is possible to overcome the main limitation of a two-bands pencil-beam survey, namely the lack of adjacent control-fields that can be used to subtract the foreground and background stars to enhance the signal on the colour-magnitude diagrams (CMDs). We describe the cross-correlation algorithm and its implementation. We combine the resulting main sequence turnoff points with theoretical isochrones to derive accurate photometric distances to the streams. Our results confirm the findings by previous studies, expand the distance trend for the Sagittarius faint southern branch and trace the Sagittarius faint branch of the northern-leading arm out to 56 kpc. In addition, they show evidence for nearby substructures. We argue that these detections trace the continuation of the Sagittarius northern-leading arm into the southern hemisphere, and the northern wrap of the Sagittarius trailing arm.

Published in Astronomy & Astrophysics Volume 564, A18 (2014)

Preprint in arXiv:1311.7580 [astro-ph.GA]

4.1 Introduction

In the past decade our picture of the Milky Way's stellar halo has dramatically changed thanks to the advent of several observational surveys, which have shown the richness and complexity of the substructure in the Galactic halo (Ibata et al. 2001b; Newberg et al. 2002; Majewski et al. 2003; Yanny et al. 2003; Martin et al. 2004; Grillmair & Dionatos 2006b; Belokurov et al. 2006b, 2007b,c). Our Galaxy is still undergoing an assembling process, where part of the infalling material has already been accreted and become dynamically relaxed (Helmi et al. 1999; Sheffield et al. 2012), part of it is still dynamically cold (Bell et al. 2008; Jurić et al. 2008) and another part is in the process of being dynamically stripped or even approaching its first dynamical encounter with our Galaxy (Kallivayalil et al. 2006b,a; Piatek et al. 2008; Besla et al. 2010; Rocha et al. 2012).

The most prominent example of a currently ongoing disruption is that of the Sagittarius stream (Sgr stream). Since its discovery in 1996 (Mateo et al. 1996), the stream has been mapped over roughly 2π radians on the sky, first through 2MASS (Majewski et al. 2003) and later through SDSS (Belokurov et al. 2006b; Koposov et al. 2012). There is general agreement that it is the stellar debris of a disrupting satellite galaxy, the Sagittarius dwarf galaxy (Ibata et al. 1994), which is currently being accreted by the Milky Way (Velazquez & White 1995; Ibata et al. 1997; Niederste-Ostholt et al. 2010). The stream is composed of the leading and the trailing tails of this disruption event (Mateo et al. 1996; Ibata et al. 2001b; Dohm-Palmer et al. 2001; Martínez-Delgado et al. 2001, 2004b; Majewski et al. 2003; Belokurov et al. 2006b, 2014), which wrap at least once around the Galaxy but have been predicted to wrap more than once (Peñarrubia et al. 2010; Law & Majewski 2010b). In addition, a bifurcation and what resembles an extra branch parallel to the main component of the Sgr stream have been discovered both in the northern hemisphere (Belokurov et al. 2006b) and in the southern hemisphere (Koposov et al. 2012). The origin of this bifurcation and the meaning of the two branches are still debated: they could represent wraps of different age (Fellhauer et al. 2006), they could have arisen due to the internal dynamics of the progenitor (Peñarrubia et al. 2010, 2011) or they could indeed be due to different progenitors and a multiple accretion event (Koposov et al. 2012).

On the other hand, one of the simplest and neatest examples of a disrupting satellite is that of the Palomar 5 globular cluster (Sandage & Hartwick 1977; Odenkirchen et al. 2002; Dehnen et al. 2004) and its stream (Odenkirchen et al. 2001, 2003). This stream extends over 20° along its narrow leading and trailing tails. It displays an inhomogeneous stellar density in what resembles gaps or underdensities (Grillmair & Dionatos 2006a); the origin of this stellar distribution has been attributed both to interactions with dark satellites (Carlberg 2012) and to epicyclic motions of stars along the tails (Mastrobuono-Battisti et al. 2012).

Finally, there are also cases of streams with unknown progenitors, such as the so-called Orphan stream (Grillmair 2006a; Belokurov et al. 2006b, 2007b; Newberg et al. 2010). This stream extends for 50° in the North galactic cap,

and the chemical signatures from recent spectroscopic observations associate its progenitor with a dwarf galaxy (Casey et al. 2013b,a). A number of plausible progenitors have been suggested (Zucker et al. 2006; Fellhauer et al. 2007b; Jin & Lynden-Bell 2007; Sales et al. 2008), but it is still possible that the true progenitor remains undiscovered in the southern hemisphere (Casey et al. 2013b).

In general, the discovery of most of the substructures in the halo of the Milky Way has been possible thanks to photometric multi-colour wide area surveys. Such surveys pose several advantages for this kind of search. First, their multiple-band photometry allows for stellar population selections (halo or thick disk; red clump, main sequence turnoff point, etc.) based on colour-colour stellar loci. These selection criteria can be used to make stellar density maps that track the streams all through the survey's coverage area (Majewski et al. 2003; Belokurov et al. 2006b). Second, their continuous coverage of a large area allow the fields adjacent to the substructure to act as control fields. In this way, the colour-magnitude diagrams (CMDs) of the control fields can be used to statistically subtract the foreground and the background stars from the fields probing the substructure. This enhances the signature of the stellar population belonging to the stream or satellite (by removing the noise), and makes it possible to identify age and distance indicators such as the red clump or the main sequence turnoff point (Belokurov et al. 2006b; Koposov et al. 2012; Slater et al. 2013).

In this paper we explore the possibilities of using deep two-band pencil-beam surveys instead of the usual wide-area multi-colour surveys in order to detect and characterize stellar streams of the halo and, in particular, we revisit the Sagittarius, the Palomar 5 and the Orphan streams. We derive photometric distances using purely the main sequence turnoff point and –unlike other works– regardless of the giant branch and its red clump.

4.2 Observations and data processing

4.2.1 Description of data set

We use deep photometric imaging from the MENeaCS and the CCCP surveys (Sand et al. 2012; Hoekstra et al. 2012; Bildfell et al. 2012) as well as several additional archival cluster fields, observed with the CFHT-MegaCam instrument. These surveys targeted pre-selected samples of galaxy clusters; therefore the surveys geometry takes the form of a beam-like survey where the pointings are distributed without prior knowledge of the halo substructure (blind survey).

Our pointings are one square degree wide and spread over the sky visible to CFHT. Each consists of several exposures through the g' and r' filters with image quality of of sub-arcsecond seeing. After stacking the individual exposures, the limiting magnitudes reach ~ 25.0 at the 5.0σ level. Out of the 97 fields, at least 25 fall on the structure of the Sagittarius (Sgr) stream and show distinct signatures in their CMDs, one on the Orphan stream, one on the Palomar 5 stream and three to seven on the Virgo Overdensity and the Virgo Stellar Stream (Duffau et al. 2006; Jurić et al. 2008; Casetti-Dinescu et al. 2009; Prior et al. 2009;

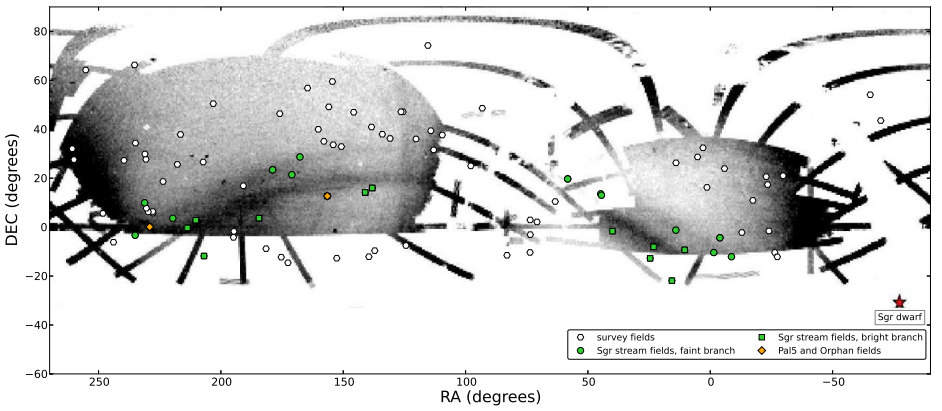


Figure 4.1: Equatorial map showing the position of all the fields from our survey (white hexagons) and highlighting the ones that lay on the Sagittarius stream (green circles for the faint branch and green squares for the bright branch), on the Palomar 5 stream and on the Orphan stream (orange diamonds). The background image is the SDSS-DR8 map of the Sgr stream from Koposov et al. (2012), where the location of the Sagittarius dwarf galaxy has been marked (red star).

Bonaca et al. 2012b) (see Figure 4.1). Further away from the plane of the Sgr stream, we also find three fields to be coincident with the Triangulum-Andromeda structure (Rocha-Pinto et al. 2004; Bonaca et al. 2012a), two to three with the Pisces Overdensity (Watkins et al. 2009; Sesar et al. 2010b; Sharma et al. 2010), one transitional between the Triangulum-Andromeda and the Pisces Overdensity, four with the Anticenter Structure (Grillmair 2006b) and two to three with the NGC5466 stream (Grillmair & Johnson 2006; Fellhauer et al. 2007a). We also find two fields on the Lethe stream (Grillmair 2009), four on the Styx stream (Grillmair 2009), one on a region apparently common to the Styx and Cocytos streams (Grillmair 2009) and two on the Canis Major overdensity (Martin et al. 2004).

In this paper we concentrate on the clearest structures (those where the contrast-to-noise in the CMD is higher) in order to test the capabilities of our method. In particular, we address the Sagittarius stream, the Palomar5 stream and the Orphan stream.

4.2.2 Correction of the PSF distortion and implications for the star/galaxy separation

Before building catalogues and in order to perform an accurate star/galaxy separation, it is necessary to rectify the varying PSF across the fields of the CFHT images.

In order to correct for this effect, we make use of a 'PSF-homogenizing' code

(K. Kuijken et al., in prep.). The code uses the shapes of bright objects unambiguously classified as stars to map the PSF across the image, and then convolves it with an appropriate spatially variable kernel designed to render the PSF gaussian everywhere. With a view to obtaining a PSF as homogeneous as possible, we treat the data as follows (van der Burg et al. 2013): i) we implement an accurate selection of sufficiently bright stars based on an initial catalogue, ii) we run the code on the individual exposures for each field, and iii) we reject bad exposures based on a seeing criterion [1] before stacking them into one final image, on which we perform the final source extraction and photometry.

The advantages of this procedure are twofold. First, because the resulting PSF for each exposure is gaussian, all the stars become round. Second, because the PSF anisotropy is removed from all exposures before stacking, the dispersion in size for the point-source objects becomes smaller, even if the average value increases after stacking the individual exposures (see Figure 4.2). These two improvements significantly reduce the galaxy contamination when performing the star selection (illustrated in Figure 4.3). Additionally, homogenizing the PSF also allows to measure colours in fixed apertures.

From the final images, we extract the sources and produce photometric catalogues using SExtractor (Bertin & Arnouts 1996). To derive the stellar catalogues, we use a code that filters the source catalogues as follows: i) finds the saturated stars and removes them from the stellar catalogue; ii) evaluates the distribution of bright sources ($r' = [18.0, 20.0]$ mag) in the brightness-size parameter space, assumes a gaussian distribution in the size and in the ellipticity parameters (e_1, e_2)[2] of stars, and uses this information to define the boundaries of the stellar locus along the bright range; iii) evaluates the dependence of the width of the stellar locus on brightness and extrapolates the relation to fainter magnitudes; iv) applies the extended stellar locus and an ellipticity criterion to drop galaxies from the stellar catalogue.

For the stars resulting from this selection (Figure 4.3), we correct their photometry from galactic reddening by using the extinction maps from Schlegel et al. (1998). The final stellar catalogues are used to build the CMDs employed for our analysis. The PSF-corrected catalogues yield much cleaner CMDs than the catalogues with similar star/galaxy separation but no PSF-correction (Figure 4.4).

[1] The rejection of exposures derives from trying to optimize the image quality while achieving the desired photometric depth. Thus our seeing criterion is a variable number dependent on the field itself, the seeing distribution for individual exposures and the individual plus total exposure time. In general it takes values $<\approx 0.9\ ''$.

[2]
$$e_1 = \frac{1-q^2}{1+q^2}\cos 2\theta\,, \quad e_2 = \frac{1-q^2}{1+q^2}\sin 2\theta\,,$$

where q =axis ratio, θ =position angle of the major axis.

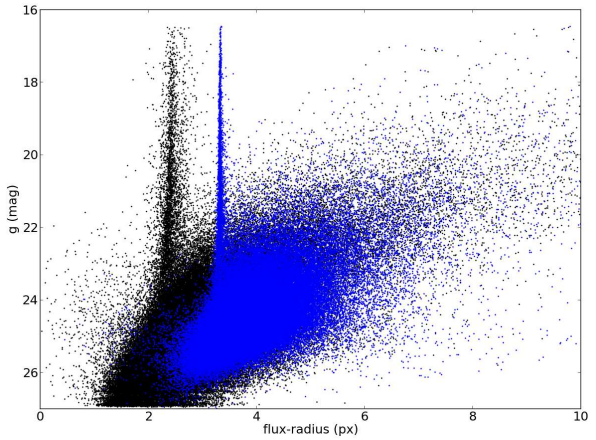


Figure 4.2: Brightness versus size diagram of all the sources in one of our pointings. The stellar locus prior to the PSF-homogenization (black) is wider and therefore subject to greater galaxy contamination at the faint end than the stellar locus posterior to the correction (blue) because the PSF initially varies across the field. The sources more compact than the stellar locus are artefacts from the source extraction; they hold no relevance for our analysis since they do not pass the star selection (see Figure 4.3).

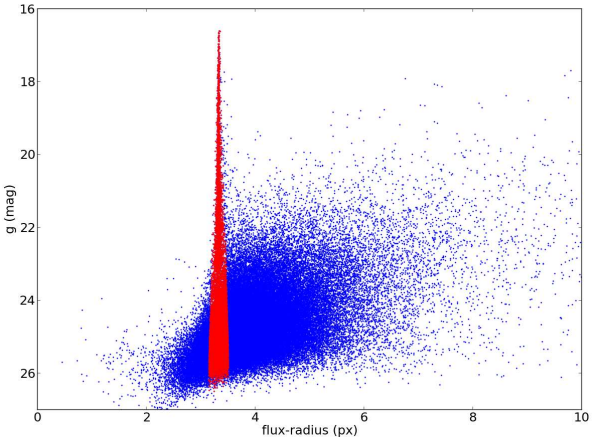


Figure 4.3: Brightness versus size diagram showing all the PSF-corrected sources (blue) and the subset of sources selected as stars through our star/galaxy separation algorithm (red) for one of our pointings. Although the star selection may not be complete at the faint end due to increasing scatter, our algorithm minimizes the galaxy contamination, which otherwise would be the main obstacle for detecting faint structures in the CMD.

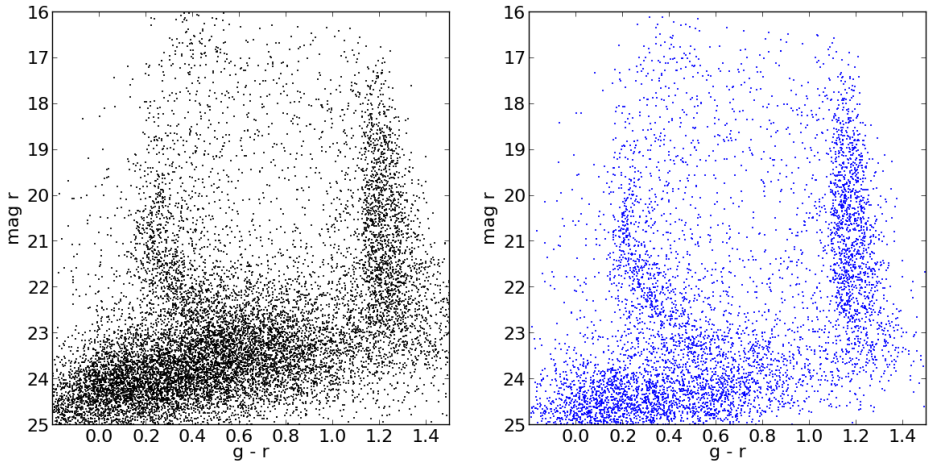


Figure 4.4: Colour-Magnitude Diagram (CMD) displaying the selection of sources considered stars (selected as explained in section 2.2). The plume on the red side ($g - r \approx 1.2$) is composed of the nearby M-dwarfs, whereas the main sequence on the bluer side ($0.18 < g - r < 0.6$) corresponds to a halo overdensity located at a particular well-defined distance. The cloud of sources at faint magnitudes are faint galaxies that enter the star selection. *Left:* CMD derived from an image that has not been PSF-corrected. *Right:* CMD derived from a PSF-corrected image. After homogenizing the PSF, the galaxy contamination decreases markedly below $r \approx 22$.

4.2.3 Identification of the main sequence turnoff point

The photometric depth of our data allows us to detect a number of halo substructures several magnitudes below their main sequence turn-off point. However, because our survey is a pencil-beam survey lacking control fields adjacent to our target fields, we have no reference-CMDs representing a clean foreground plus a smooth halo, and thus a simple foreground subtraction is not possible. Instead the halo substructures in our survey can only be detected in those fields where the contrast in density between the main sequence stream stars and the foreground and background stars is significant in the CMD.

Thus, in order to search for main sequences in the CMDs, we build a cross-correlation algorithm that runs across a region of the CMD (the 'search region'), focused on the colour range associated with the halo turnoff stars ($0.18 \leq g-r \leq 0.30$). Within the boundaries of this search region, we slide a template main sequence-shaped 2D function that operates over the number of stars and, for each step, yields an integral representing the weighted density of stars in such a main sequence-shaped area. When the template main sequence function coincides with a similarly shaped overdensity in the CMD), the value of the cross-correlation (the weighted density) is maximized, and a value for the turnoff point is assigned. This process is illustrated in Figure 4.5.

In some cases a CMD presents more than one main sequence signature with sufficient contrast to noise. When this happens we use the detection of the primary main sequence (the position of its turnoff point and its characteristic width-function) to randomly subtract a percentage of the stars associated with it (lowering its density to the foreground level) and detect the next prominent main sequence feature. We name these main sequence detections as primary, secondary, etc., ranked by their signal to noise. We require the signal to noise to be $> 3.5\sigma$ for primary MSs and $> 4\sigma$ for the secondary or tertiary MSs after partially removing the primary one.

Shape of the template main sequence function

When constructing the template main sequence-shaped 2D function (from now on, 'template-MS'), we use two ingredients. The first one is a theoretical isochrone[3] of age $t = 10$Gyr and metallicity $[Fe/H] = -1.58$, which is used to define the central spine of the template-MS. The position of this central spine is later shifted in magnitude and colour steps during the cross-correlation. Since we are only interested in the shape of this isochrone (its absolute values are irrelevant because it will be shifted) and since we are searching for halo substructures, we choose the above age and metallicity values because they yield an isochrone shape representative of old metal-poor stellar populations. The second ingredient is a magnitude-dependent colour-width, which is used to broaden the isochrone template as illustrated in the left panel of fig. 4.5).

[3]Through all this work we use a subset of theoretical isochrones from http://stev.oapd.inaf.it/cmd. The theoretical isochrones (Marigo et al. (2008), with the

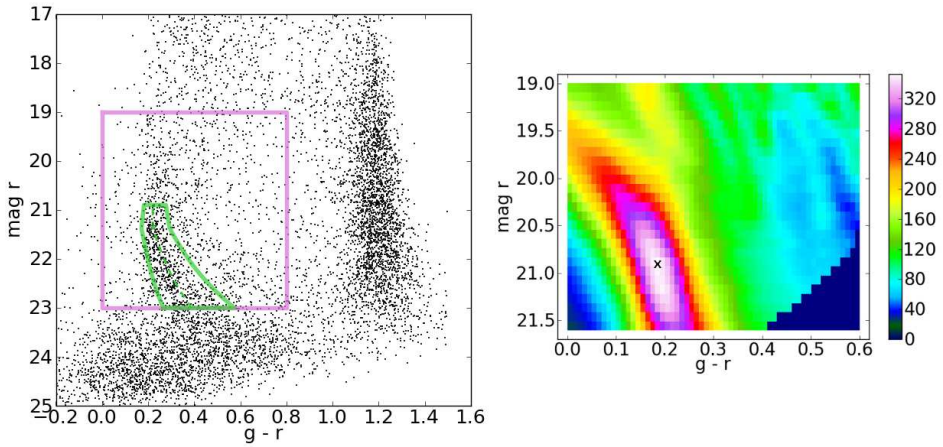


Figure 4.5: *Left*: Dereddened CMD (black dots) with the search region (pink solid-line rectangle) for the cross-correlation and the template main sequence-shaped function (green solid line) at the position of maximum density (peak of the cross-correlation). *Right*: Binned diagram representing the weighted density of stars resulting from the cross-correlation process. The density in each bin corresponds to the integral of the template main sequence-shaped function with top left corner in the position of the bin.

The width is in general directly derived from the width of the locus of nearby M-dwarfs ($1.0 < g - r < 1.4$). The width of this feature is calculated for a number of magnitude bins as three times the standard deviation in colour for each bin. Then a functional form dependent on magnitude is obtained through polynomial fitting. In a few cases, minor tweaking is needed to compensate for extremely large widths (colour shifts become insensitive to any substructure) or for extremely small widths (density values become meaningless due to the built-in weight [see below]). This way of defining the width of the template-MS accounts for the observational broadening of intrinsically well defined stellar loci due to increasing photometric uncertainties at faint magnitudes.

Weights within the template MS-function

In addition to a theoretically and observationally motivated shape for the template-MS, we also give a different weight to each region of the template. This means that, for each step of the cross-correlation, the stars contained within will contribute differently to the enclosed stellar density depending on how far they are from the spine of the template-MS.

corrections from Case A in Girardi et al. (2010) and the bolometric corrections for Carbon stars from Loidl et al. (2001)) are provided as observable quantities transformed into the CFHT photometric system.

The weight in colour (stars near the spine of the template-MS are more likely to belong to the main sequence than stars close to the boundaries) is assigned through the exponential term in a gaussian weight function. We match the standard deviation of the gaussian weight to the standard deviation of the template-MS width ($3\sigma = \omega_{MS}$) so that all the stars contained within the template-MS are assigned a weight. To guarantee that the weight does not favour bright features, we choose the amplitude of the gaussian function to be such that the integral of the weight function between the edges of the template-MS function is the same for all magnitudes.

The resulting weight function for a given star in the template-MS at a particular step of the cross-correlation then follows:

$$W_*(mag, colour) = \frac{A}{\sqrt{2\pi}\sigma(mag)} \cdot exp\left\{-\frac{[colour - \eta_{CC}(mag)]^2}{2[\sigma(mag)]^2}\right\} \quad (4.1)$$

where *mag* and *colour* are the magnitude and colour of the weighted star, $\eta_{CC}(mag)$ represents the theoretical isochrone at that particular step of the cross-correlation, and $\sigma(mag) = \frac{1}{3}\omega_{MS}(mag)$ is proportional to the width of the template-MS function for that particular CMD.

4.2.4 Uncertainties in the turnoff point

The colour and magnitude values for the turnoff point of a given main sequence, (c_{TO}, mag_{TO}), are derived from the position of the template at which the cross-correlation peaks. Therefore the uncertainties for these turnoff point values derive from the contribution of individual stars to the position and shape of the main sequence (the uncertainty from the CMD itself). To evaluate this uncertainty, we carry out a bootstrapping process. In this process first we generate re-sampled stellar catalogues by randomly withdrawing stars from one of our true catalogues. Second we run the cross-correlation and obtain the turnoff points for each of these re-samples. Third we consider the offsets between these turnoff points and the original turnoff point and derive the standard deviation of the distribution. The contribution of any CMD to the uncertainty of its turnoff point can then be calculated as a function of a reference (bootstrapped) standard deviation, s:

$$E_{\rm mag,CMD} = f_{\rm mag,BS} \cdot \frac{(s_{\rm mag,BS})}{\left.\frac{\partial^2\rho_{\rm CC}}{\partial^2 mag}\right|_{\rm TO}}, \quad E_{\rm c,CMD} = f_{\rm c,BS} \cdot \frac{(s_{\rm c,BS})}{\left.\frac{\partial^2\rho_{\rm CC}}{\partial^2 c}\right|_{\rm TO}},$$

where, in practice, $s_{\rm mag,BS}$ and $s_{\rm c,BS}$ are the standard deviations calculated for a number of representative fields, $f_{\rm mag,BS}$ and $f_{\rm c,BS}$ are scale factors that allow to obtain the uncertainty for any field from the standard deviation of the bootstrapped fields, and $\frac{\partial^2\rho_{\rm CC}}{\partial^2 mag}$ and $\frac{\partial^2\rho_{\rm CC}}{\partial^2 c}$ evaluate the prominence of the particular overdensity as a function of magnitude or as a function of colour. In practice, $E_{\rm mag,CMD} = s_{\rm mag,BS}$ and $E_{\rm c,CMD} = s_{\rm c,BS}$ for the bootstrapped fields used as a reference.

The photometric turnoff point distances are derived from the distance modulus. Therefore the uncertainties in the distances can be calculated as a combination of two sources of error: the uncertainty derived from the observed brightness of the turnoff point ($E_{\mathrm{mag,CMD}}$, discussed above) and the uncertainty derived from the absolute brightness of the turnoff point, which depends on the choice of isochrone (and thus on the uncertainty in the age or in the metallicity).

$$E_{\mu,\mathrm{TO}} = \sqrt{E^2_{\mathrm{mag,CMD}} + E^2_{\mathrm{mag,isoch}}}; \tag{4.2}$$

4.3 The Sagittarius stream

4.3.1 Turnoff point distances to the Sgr stream

The Sagittarius stream is clearly probed by at least 25 of our 97 fields (see the green and the orange markers in Figure 4.1). They probe both the faint and the bright branches of the stream (the faint branch lying to the North of the bright one) and also two transitional areas, indicating that the transversal drop in stellar counts between both branches is not dramatic. Some of these fields present more than one main sequence in their CMDs; for those fields the secondary turnoff points are calculated by subtracting the primary MS and re-running the cross-correlation (as explained in section 4.2.3).

Based on the turnoff point values obtained from the cross-correlation, we calculate the distances to the Sagittarius stream in these 25 fields for 31 detections. For this calculation, we assume a single stellar population represented by a theoretical isochrone with age $t_{age} = 10.2$ Gyr and metallicity $[Fe/H] = -1.0$ dex (for a detailed description on the set of isochrones see footnote 2 in section 4.2.3). We choose these age and metallicity values because they match the age-metallicity relation for the Sgr dwarf galaxy (Layden & Sarajedini 2000) –which is also expected to hold for its debris– and are consistent with the range that characterizes old metal-poor populations.

To account for the potential influence on our distance measurements of a possible metallicity gradient along the different Sgr arms (Chou et al. 2007; Shi et al. 2012; Vivas et al. 2005; Carlin et al. 2012), we analyse the dependency of the isochrones turnoff point absolute brightness (M_{TO}) with metallicity throughout the Sgr metal-poor range (see Figure 4.6). We find that for -1.53 dex $< [Fe/H] < -0.8$ dex the absolute brightness remains nearly constant in the r band, with a maximum variation of $\Delta M = \pm 0.1$ mag. We conclude that if we take this variation in absolute brightness as the isochrone uncertainty in the distance modulus ($E_{\mathrm{mag,isoch}} = \Delta M$), we can use the $t_{age} = 10.2$ Gyr and $[Fe/H] = -1.0$ dex isochrone to calculate distances to any region of the Sgr stream.

The resulting distances and distance uncertainties for these fields can be found in Table 4.1, together with the central position of each field (in equatorial coordinates), a 'faint/bright branch' tag (derived from Figure 4.1), a tentative classification as leading or trailing arm where posible (see below), a 'primary/secondary

Table 4.1: Position and distances to the Sgr stream, together with a tag for faint or bright branch membership, a tentative classification as leading or trailing arm and a number specifying the hierarchy of the detection in the CMD (primary, secondary,etc.). The distances are indicated both as distance modulus and as heliocentric distance, with the distance uncertainty ($E_{\rm d}$) in kpc.

Field	arm	detection	RA (deg)	DEC (deg)	$\mu(mag)$	d (kpc)	$E_{\rm d}$ (kpc)
A2104[f]	lead	1	235.040644	-3.33158	18.8	56.6	3.1
RXJ1524[f]	trail	1	231.170583	9.93498	16.2	17.1	2.0
A2050[f]	lead	1	229.080749	0.08773	18.7	54.1	8.7
A1942[f]	lead	1	219.654126	3.63573	18.7	54.1	3.7
A1882[b]	lead	1	213.667817	-0.30598	18.5	49.3	5.7
A1835[b]	lead	1	210.259355	2.83093	18.4	47.1	4.2
RXJ1347[b]	?	1	206.889060	-11.80299	15.5	12.4	7.3
ZwCl1215[b]	?	1	184.433196	3.67469	16.7	21.5	2.9
ZwCl1215[b]	?	3	184.433196	3.67469	15.0	9.8	2.6
A1413[f]	lead	1	178.842420	23.42207	17.5	31.1	2.7
A1413[f]	trail	2	178.842420	23.42207	16.2	17.1	1.9
A1246[f]	lead	1	170.987824	21.40913	17.6	32.6	9.2
A1185[f]	?	1	167.694750	28.68127	16.3	18.7	12
ZwCl1023[b]	?	1	156.489424	12.69030	17.4	29.7	11
A795[b]	lead	1	141.030063	14.18190	16.0	14.2	2.8
A795[b]	?	2	141.030063	14.18190	15.6	14.2	2.8
A763[b]	?	1	138.150298	15.99992	16.7	21.5	2.6
A763[b]	lead	2	138.150298	15.99992	15.8	14.2	1.0
RXJ0352[f]	lead	1	58.263173	19.70387	15.7	13.6	0.7
RXJ0352[f]	trail	2	58.263173	19.70387	17.7	34.1	4.3
A401[f]	trail	1	44.759558	13.58975	17.4	29.7	3.4
A399[f]	trail	1	44.478652	13.05185	17.6	32.6	11
A370[b]	trail	1	39.963713	-1.65806	17.6	32.6	4.8
A223[b]	trail	1	24.557005	-12.77010	17.0	24.7	1.7
RXJ0132[f]	trail	1	23.169048	-8.04556	17.1	25.9	2.3
A133[b]	trail	1	15.673483	-21.88113	16.6	20.6	2.4
A119[f]	trail	1	14.074919	-1.23337	16.9	23.6	2.9
A85[b]	trail	1	10.469662	-9.28824	16.9	23.6	1.6
A2670[f]	trail	1	358.564313	-10.40142	16.6	20.6	1.1
RXJ2344[f]	trail	1	356.059633	-4.36345	16.7	21.5	5.6
RXJ2344[f]	lead	2	356.059633	-4.36345	15.6	13.0	1.2
A2597[f]	trail	1	351.336736	-12.11193	16.9	23.6	1.4

[b] Bright branch

[f] Faint branch

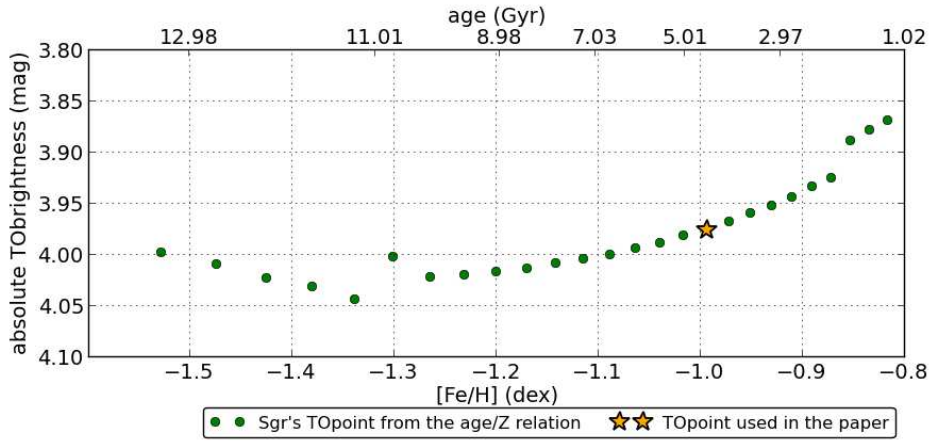


Figure 4.6: Absolute brightness of the turnoff point in the r band as a function of metalllicity and age for metal poor populations (green circles). The values in this diagram meet the age/metallicity relation for the Sgr dwarf galaxy from Layden & Sarajedini (2000). The isochrone used in this paper to derive distances to the Sgr stream is represented with a yellow star, and its maximum difference to the other brightness values in this range is $\Delta M = \pm 0.1$mag.

detection' tag and the distance modulus (μ). In Figure 4.7 we compare our results to values from the literature[4], split in two diagrams (top panel for the faint branches and bottom panel for the bright branches in both hemispheres).

Remarkably our turnoff point distances are not only in agreement with previous distance measurements to known wraps, but also compatible with the distance predictions for nearby wraps by the models of Peñarrubia et al. (2010) and Law & Majewski (2010b). In the following section we discuss in detail these findings.

4.3.2 Comparison with models of the Sgr stream

Using the model predictions shown in figures 4.8 and 4.9, we classify each field as belonging to the leading or trailing arm, by matching the distance and the sky position. It is worth noting, however, that the distance for a given particle in the models is sensitive not only to the right ascension but also to the declination of the particle. While we take into account both coordinates when classifying a detection as faint or bright branch, we do not specifically acount for the declination when comparing the distances of the modelled streams and the distances of our

[4]The SDSS-DR8 measurements shown in this paper for the southern bright arm have been corrected for the difference in the calibration of the red clump absolute magnitude, as pointed out in Slater et al. (2013) and corrected in Koposov et al. (2013)). And the SDSS-DR5 measurements have been decreased by 0.15 mag to match the BHB signal from SDSS, as prescribed in Belokurov et al. (2014).

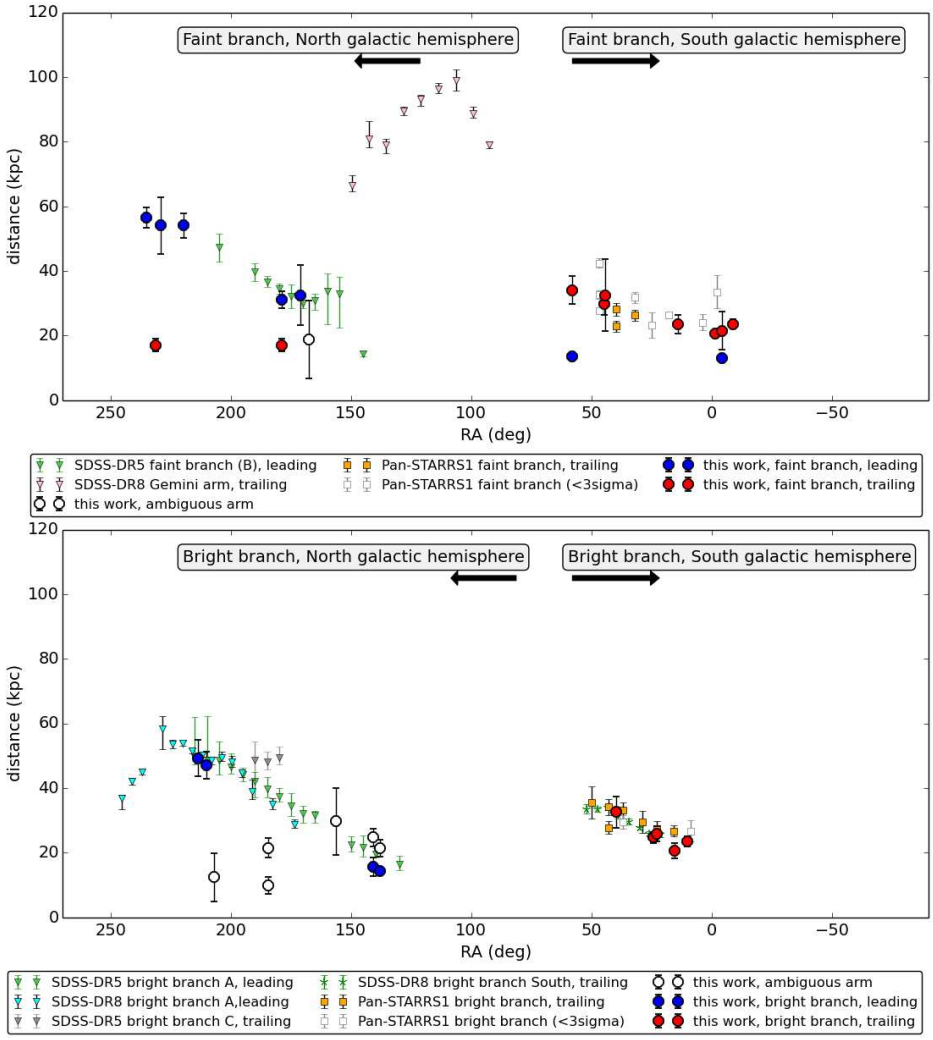


Figure 4.7: Photometric main sequence turnoff point distances for the Sagittarius stream along right ascension (northern-leading tail and southern- trailing tail). The top panel shows results for the faint branch, whereas the bottom panel corresponds to the bright arm. Our data (blue circles for leading tails and red circles for trailing tails) are based on the theoretical isochrones by Marigo et al. (2008) and the corrections by Girardi et al. (2010), for a 10.2 Gyr old stellar population with $[Fe/H] = -1.0$. Other distance values correspond to Belokurov et al. (2006b) (green and grey triangles), Koposov et al. (2012, 2013) (green asterisks), Belokurov et al. (2014) (pink triangles) and Slater et al. (2013) (yellow squares for $> 3\sigma$ detections and white squares for $< 3\sigma$). White circles denote detections that can not be unambiguously tagged as leading or trailing.

detections in figures 4.8 and 4.9. This may have some influence in the significance of the offsets between our distance measurement and the mean distance of the N-body particles for a given RA.

Of these two models, the model by Peñarrubia et al. (2010) was designed to illustrate the effect of internal satellite rotation on the orbit of the Sgr debris, and it seems to recover better the separation in stellar density distribution that gives rise to the northern bifurcation into faint and bright branches (Figure 4.8, upper panel). On the other hand, the model by Law & Majewski (2010b) was designed to reproduce the known observational properties of the stream (angular positions, distances, radial velocities), and it seems to reproduce better the projected 2MASS stellar density distribution (Figure 4.9, upper panel). In relation to the southern region of the stream, although neither of the two models predicted the bifurcation in it, they succeed in reproducing the general distribution of the debris.

Northern leading arm

From our eighteen measurements on the bright and the faint branches of the northern-leading arm (branches A and B, in the terminology of Belokurov et al. (2006b)), nine (blue circles in Figure 4.7) clearly reproduce the distance trends of Belokurov et al. (2006b) and Belokurov et al. (2014) (green+grey and cyan triangles in Figure 4.7, respectively) based on red giant and blue horizontal branch stars. For the faint branch, we extend westwards the distance measurements beyond those of SDSS, and we provide its most distant detections so far –out to 56kpc at RA $\sim 235^{o}$. Comparing these most distant detections to the distance trend of the models and to the bright branch at a similar right ascension, one can argue that these detections likely lie close to the apocenter of the faint branch (or represent the apocenter themselves), and therefore they are probably a good estimation for its distance.

For the other nine detections, we find that the derived distances are either in mild disagreement with the trends of the leading arm (four cases, white circles in Figure 4.7) or incompatible with the leading arm (five cases, red and white circles in Figure 4.7). In the single case of mild disagreement for the faint branch (A1185, RA $\sim 168^{o}$) the distance is well below the trends of both this and previous work (offset ≈ 10 kpc); however its large uncertainty prevents us from ruling out that it belongs to the faint branch. We will discuss an alternative membership in subsection 4.3.2. The three cases of mild disagreement for the bright branch (ZwCl1023, A795-2 and A763-1, RA $\sim 150^{o}$) are slightly above the distance trend of this branch. Particularly, fields A795 and A763 also display two additional detections (primary and secondary, respectively) slightly under the expected distance trend. Fields A795 and A763 lie close in the sky (less than 4° apart) and both yield primary and secondary distance measurements very consistent with each other and with this dichotomy. We interpret this as possibly indicating a region of the sky where the bright branch runs broader in distance.

Out of the five detections incompatible with the distance trends of the leading arm, we will discuss three (RXJ1524,A1413-2 and ZwCl1215-1) in subsec-

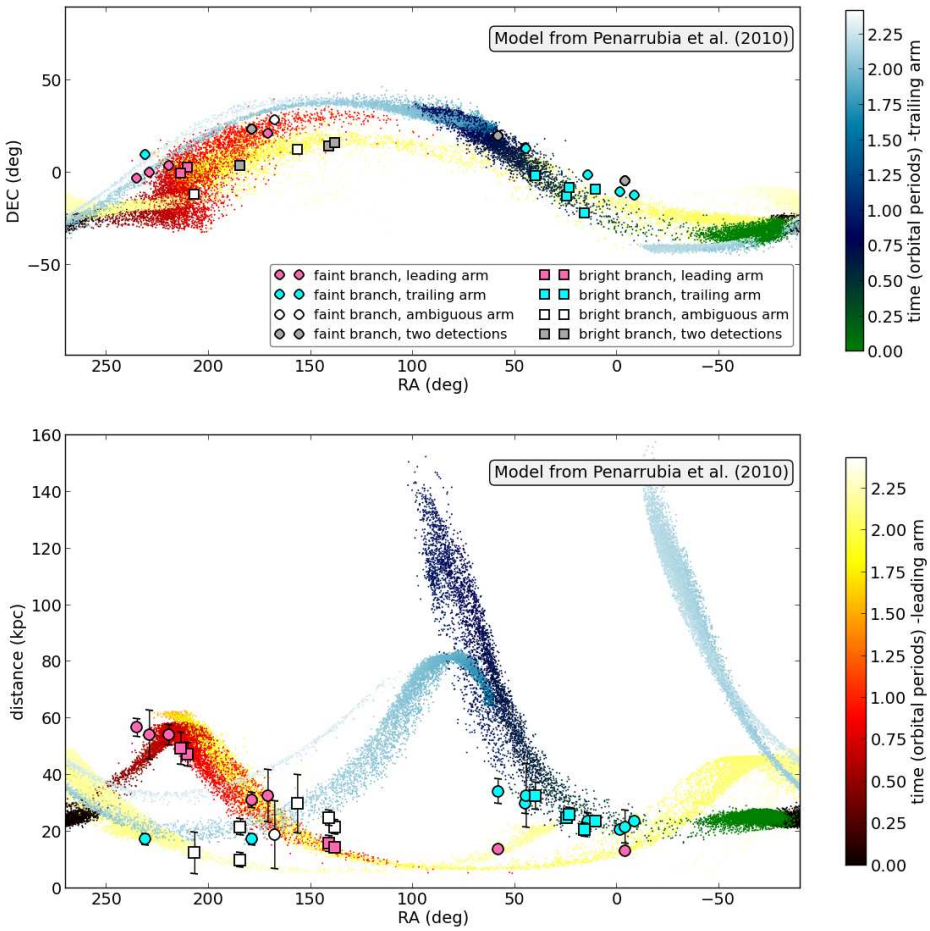


Figure 4.8: Our data compared to the predictions by the model from Peñarrubia et al. (2010). *Top panel*: Equatorial map with the position of our fields plotted over the simulation. *Bottom panel*: Distance vs RA diagram with our results compared to the model predictions. Fields on the faint branch are denoted with circles, and fields on the bright branch are denoted with squares. Measurements matching the leading arm are denoted in pink, whereas those matching the trailing arm are denoted in light blue. White markers represent detections that can not be unambiguously tagged as leading or trailing; grey markers in the upper panel correspond to fields with more than one MS detection (they unfold in the bottom panel). The colour scales represent the time since the particles from the simulations became unbound.

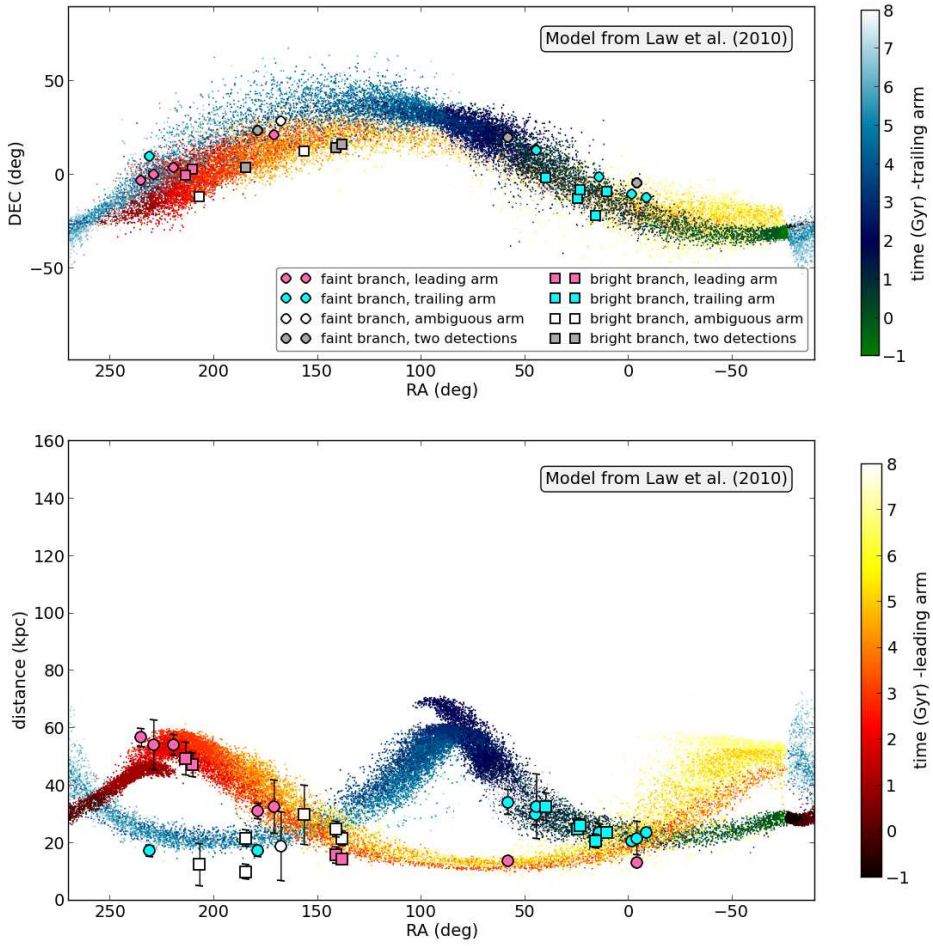


Figure 4.9: Same as in Figure 4.8 but for the model from Law & Majewski (2010b).

tion 4.3.2, together with the above mentioned A1185. Regarding the other two (RXJ1347 and ZwCl1215-3, RA $\sim 205^{o}$ and RA $\sim 185^{o}$ respectively), we have studied them individually and found the following. On the one hand, ZwCl1215-3 matches the distance to the Virgo Overdensity (Bonaca et al. 2012b) when using the appropriate age and metallicity values for the theoretical isochrone, so it is likely a detection of this cloud. On the other hand, RXJ1347 matches the distance and position predicted by the model from Peñarrubia et al. (2010) for an older northern-wrap of the leading arm, but also the distances predicted by the two models for the northern-trailing wrap. However we can not draw conclusions regarding membership for an isolated detection and we lack kinematic data, so at the moment we can not discriminate between both options (or even a third one).

Northern trailing arm

In this subsection we revisit four detections in the galactic northern hemisphere which yield distances incompatible with (or off) the leading arm. These detections are RXJ1524, A1413-2 (red circles in Figure 4.7), A1185 (compatible with the faint leading branch thanks to its large error bars, but severely offset from the distance trend) and ZwCl1215-1 (white marker at RA $\sim 185^{o}$ on the bright branch). The three detections in the faint branch (RXJ1524, A1413-2 and A1185) show distances strongly consistent with each other (~ 17 kpc). And the three of them are the fields most apart from the Sgr orbital plane in our northern sample, spreading 60° along the orbit.

Remarkably both their distances and their positions in the sky are in extremely good agreement with the predictions from the above mentioned models for the Sgr debris in the northern-trailing arm, and they are roughly comparable to the results in Correnti et al. (2010). However they are at odds with the claim in Belokurov et al. (2014) that branch C (at lower declinations and more distant; see grey triangles in Fig. 4.7) is indeed a part of the northern-trailing arm and the continuation of the Gemini stream/arm (Newberg et al. (2003), Drake et al. (2013); see pink triangles from Belokurov et al. (2014) in Fig. 4.7)).

Given the consistency of our distance measurements with each other and with the simulations, and given the distribution of the fields along the faint branch of the stream, we believe these detections are part of the Sgr stream, most likely a wrap of the northern trailing arm. However kinematic data or a spatially broader photometric coverage are needed to confirm this.

Additionally, ZwCl1215-1, which lies on the bright branch, yields a distance measurement compatible with the trend predicted for the northern-trailing arm. But its position on the sky (on the bright branch) can not be reconciled with the current models for the trailing tail, neither with the age, metallicity and distance values for the Virgo Overdensity. Thus, its membership and meaning in the puzzle of the halo remain an open question.

Southern trailing arm

Our measurements on the bright and the faint branches of the southern-trailing arm reproduce the distance trends of Koposov et al. (2012, 2013) and Slater et al. (2013) based on red clump and turnoff point stars. For the faint branch, we confirm the trend set by the $< 3\sigma$ detections in Slater et al. (2013), and we briefly extend westwards and eastwards the distance measurements. Contrary to Slater et al. (2013), we find no evidence for a difference in distance between the faint and the bright branches of the southern-trailing tail. However it is possible that such difference remains hidden in our distance uncertainties.

When comparing to the above mentioned models, we find that the measures are in general agreement with the predictions for both the faint and the bright branches. However the distance gradient in the faint branch seems to be less steep in the data than in the models, and the branch seems to be thinner in distance than predicted for any value of the probed RA range. In this sense it is worth noting that, in contrast to what happens to many of our northern hemisphere fields, only two of the CMDs in the southern galactic hemisphere show secondary MS detections (RXJ0352 and RXJ2344, at RA $\sim 58^{o}$ and RA $\sim 356^{o}$, respectively). And the difference between the turnoff point brightness of these double detections does not favour a thick branch, but rather the detection of a previously unknown nearby wrap (see subsection 4.3.2).

Southern leading arm

In this subsection we revisit the double detections of 4.3.2, namely RXJ0352-1 and RXJ2344-2, (RA $\sim 58^{o}$ and RA $\sim 356^{o}$, primary and secondary detections, respectively). We show their CMDs and their cross-correlation density diagrams in figures 4.10 and 4.11. We find that, using the same isochrone we have used to derive distances to all the Sgr fields, both yield a distance of ~ 13 kpc. These distances are in excellent agreement with the predictions from the two simulations for the leading arm in the South and also with the trend set by the leading-northern data. We thus claim that these two detections are part of the continuation of the northern-leading arm into the southern hemisphere (Chou et al. 2007). The positions of these fields, however, suggest that the leading arm dives into the southern hemisphere at higher declinations than predicted, overlapping in projection with the faint branch of the trailing arm.

If the detection of the southern-leading arm or the northern-trailing arm proposed in this paper are confirmed in future works (with kinematic measurements for membership or photometric follow-up for spatial coverage), our measurements will be the closest and the oldest debris of the Sgr stream detected to date. If so, this would mean that our method has succeeded in detecting nearby substructure in regions of the sky that had already been explored. The explanation to such a performance would lie on the fact that we use a sample of stars (a large part of the main sequence) to identify the overdensities in the CMD larger than the sample of the usual halo tracers (red clump, red giants or blue horizontal branch),

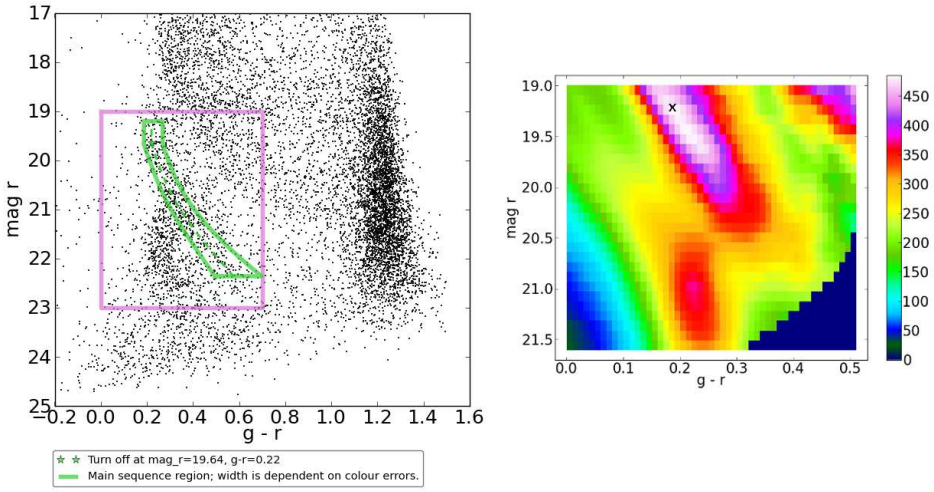


Figure 4.10: *Left*: Dereddened CMD for the westernmost pointing probing the leading arm in the southern hemisphere; the template main sequence function and the turnoff point (green) are plotted for the maximum of the primary cross-correlation. *Right*: Weighted-density diagram resulting from the primary cross-correlation. The maximum (white bin, black cross) marks the top left corner of the template-MS at the position of the southern-leading arm main sequence, whereas the red overdensity at fainter magnitudes corresponds to the southern-trailing arm.

and this could increase the contrast in regions of low concentration and thick disk contamination.

Presence of sparse nearby streams in SDSS

In the much shallower SDSS data the detected MS features are significantly smeared out by photometric uncertainties and poorer star/galaxy separation (see CMD comparison in fig. 4.12). As a consequence, meager main sequences would be more difficult to indentify in SDSS (and meager BHB or RC counterparts would be impossible to identify). This leads us to think that the ability to detect sparse stellar populations like the ones in sections 4.3.2 and 4.3.2 is strongly dependent on the initial image quality and the star selection process.

The strength of SDSS lies in the large area it covers, which might allow the detection of a nearby, dynamically old stream in some statistical way. However this pursuit is beyond the scope of this paper.

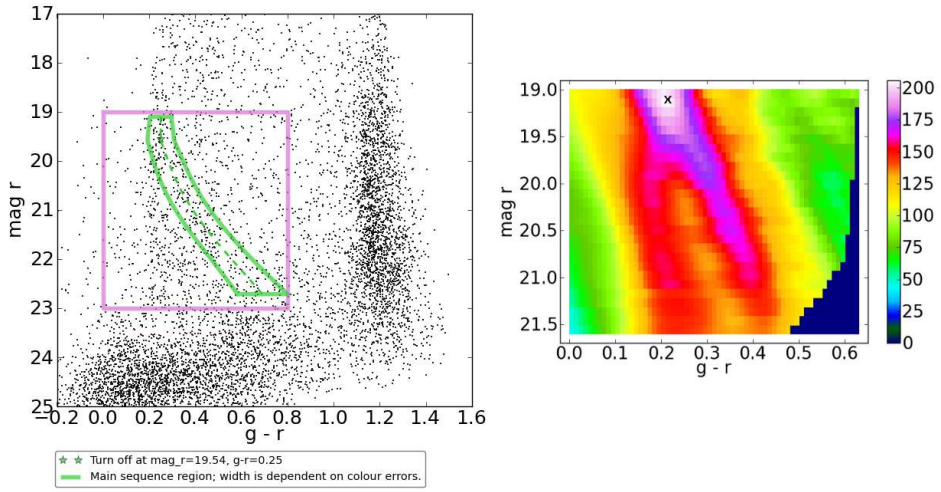


Figure 4.11: *Left*: Dereddened CMD for the easternmost pointing probing the leading arm in the southern hemisphere; the template main sequence function and the turnoff point (green) are plotted for the maximum of the secondary cross-correlation. We have randomly removed 50% of the stars contributing to the primary detection, which corresponds to the southern-trailing arm of the Sgr stream. *Right*: Weighted-density diagram resulting from the secondary cross-correlation. The maximum (white bin, black cross) marks the top left corner of the template-MS function at the position of the Orphan stream's main sequence. The primary detection has been partially removed, and the remainings can be seen as a weak tail at fainter magnitudes and slightly bluer colour.

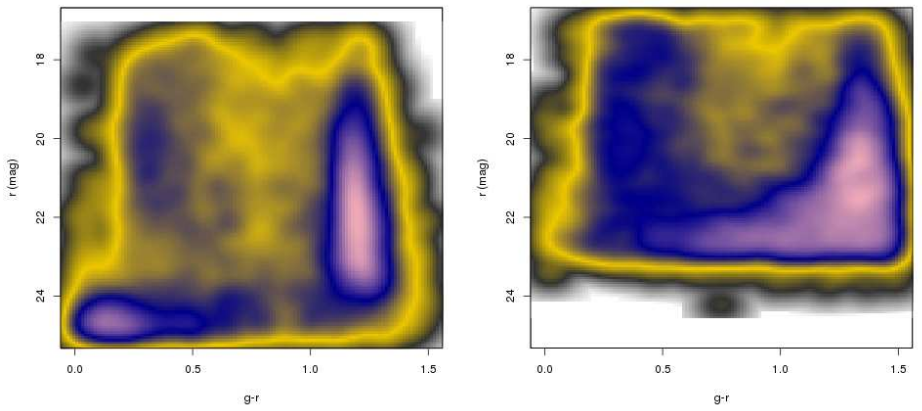


Figure 4.12: *Left*: Smoothed CMD for field RXJ1524 containing the CFHT sources classified as stars by us. *Right*: Same as the diagram in the right for the SDSS sources classified as stars in the database. The weaker features in the left figure are not detectable in the right figure due to photometric uncertainties and the different star/galaxy separations.

4.4 The Palomar 5 stream and the Orphan stream

4.4.1 Turnoff point distances to the Pal5 stream and the Orphan stream

The Palomar5 stream and the Orphan stream are also probed by two of our fields (see orange diamonds in Figure 4.1). Their CMDs and their corresponding turnoff points are shown in figures 4.13 and 4.14, together with their cross-correlation maps.

We use these turnoff point values to calculate photometric distances to each of the streams. Once again we assume single stellar populations characterized by theoretical isochrones but now with $t_{age} = 11.5$ Gyr (Martell et al. 2002) and metallicity $[Fe/H] = -1.43$ (Harris 1996) in the case of the Pal5 stream, and $t_{age} = 10.0$ Gyr and metallicity $[Fe/H] = -1.63$ in the case of the Orphan stream (Casey et al. 2013a). These values correspond to measurements for these particular streams, which are more metal-poor than the Sgr stream for similar ages. Since the absolute brightness of the turnoff point for a given stellar population depends on its age and metallicity, it is important to select representative values in order to derive the right photometric distances.

The resulting distances are collected in Table 4.2 and displayed in figures 4.15 and 4.16, respectively, where they are compared to previous findings by other groups. Both results show good agreement for the adopted age and metallicity

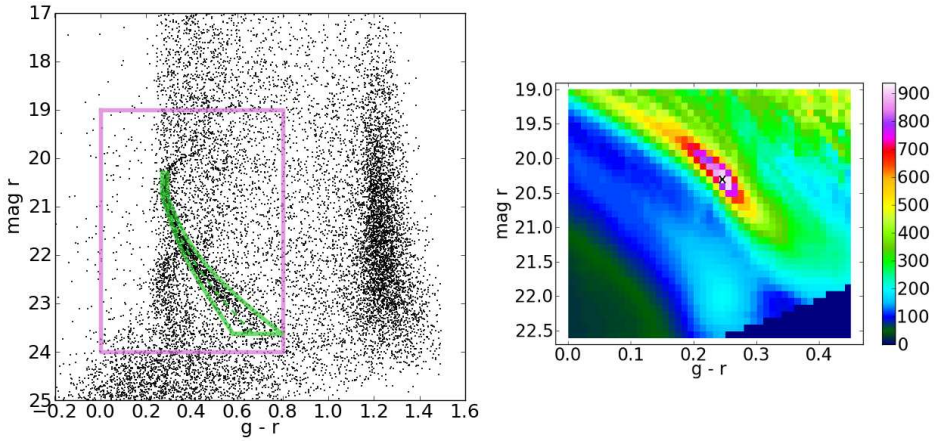


Figure 4.13: *Left*: Dereddened CMD for the pointing containing the Palomar 5 stream as its primary feature; the template main sequence function and the turnoff point (green) are plotted for the maximum of the cross-correlation. The secondary main sequence at fainter magnitudes corresponds to the faint arm of the Sgr stream. *Right*: Weighted-density diagram resulting from the cross-correlation. The maximum (white bin, black cross) marks the top left corner of the template-MS function at the position of the Palomar 5 stream's main sequence, whereas the cyan overdensity at fainter magnitudes corresponds to the Sgr stream.

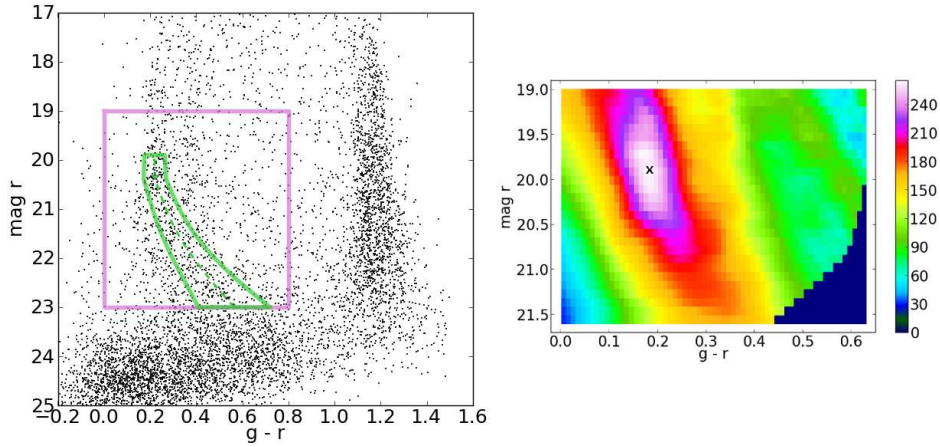


Figure 4.14: *Left*: Dereddened CMD for the pointing containing the Orphan stream as its secondary feature; the template main sequence function and the turnoff point (green) are plotted for the maximum of the secondary cross-correlation. We have randomly removed 60% of the stars contributing to the primary detection, which corresponds to the bright arm of the Sgr stream. *Right*: Weighted-density diagram resulting from the secondary cross- correlation. The maximum (white bin, black cross) marks the top left corner of the template-MS function at the position of the Orphan stream's main sequence. The primary detection has been removed, and thus it does not show in the density diagram.

Table 4.2: Position and distances to the Palomar5 and Orphan streams:

Field	stream	RA (deg)	DEC (deg)	$\mu(mag)$	d (kpc)	Δd (kpc)
A2050	Pal5	229.080749	0.08773	17.0	23.1	1.1
ZwCl1023	Orphan	235.040644	-3.33158	16.6	23.8	2.2

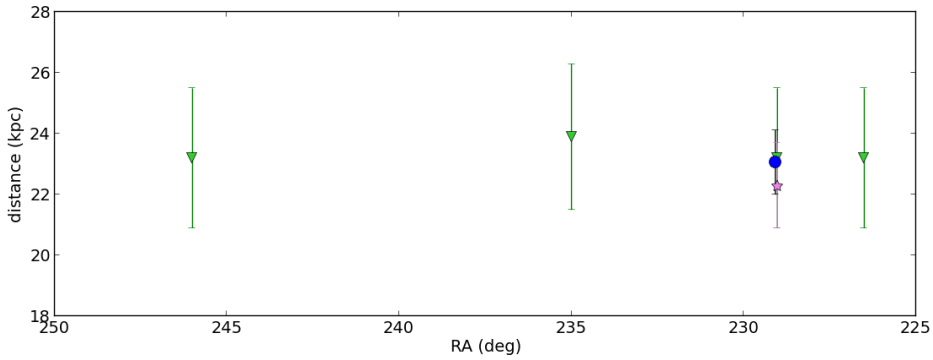


Figure 4.15: Photometric main sequence turnoff point distances along right ascension for the Palomar5 stream. Our data point (blue circle) is based on a single stellar population of age 11.5 Gyr and metallicity $[Fe/H] = -1.43$. The other values correspond to Grillmair & Dionatos (2006a) (green triangles) and Vivas & Zinn (2006) (pink star).

values.

4.4.2 Influence of the age/Z isochrone values on the distances

For the Palomar 5 stream and the Orphan stream, our pencil-beam survey returns only one detection each. We compare their derived distance measurements (Table 4.2) to previous work (figures 4.15 and 4.16, respectively) and find that our measurements are consistent and well within the values to be expected from interpolations. We interpret this as an independent validation of the stellar population parameters for these streams in the literature: 11.5 Gyr and $[Fe/H] = -1.43$dex for the Pal5 stream (Martell et al. 2002; Harris 1996), and 10.0 Gyr and $[Fe/H] = -1.63$dex for the Orphan stream (Casey et al. 2013a). Variations in the absolute magnitude for the turnoff point of the theoretical isochrone assigned to a given stellar population (characterized by a given age and metallicity) propagate into the distance modulus, thus yielding variations in the distance. For the Pal5 stream, our distance measurement can tolerate a relative variation of $\Delta d_{rel} \approx \pm 0.15$ and still be in agreement with the previous distance measurements; this variation threshold translates into an absolute magnitude variation threshold of $\Delta M \approx \pm 0.35$. We find that variations in $\Delta t = ^{+1.7}_{-3.2}$

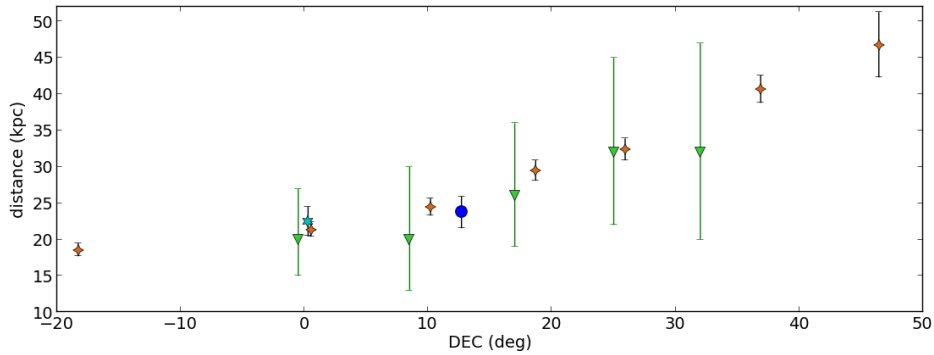


Figure 4.16: Photometric main sequence turnoff point distances along declination for the Orphan stream. Our data point (blue circle) is based on the theoretical isochrone for a 10.0 Gyr old stellar population with $[Fe/H] = -1.63$. The other values correspond to Belokurov et al. (2007b) (green triangles), Newberg et al. (2010) (orange diamonds) and Casey et al. (2013a) (cyan star).

Gyr (limited by the formation time of the first stars) or in $\Delta[Fe/H] = ^{+0.72}_{-0.82}$ dex (limited by the minimum metallicity available in the set of theoretical isochrones) for the age and metallicity of the employed theoretical isochrones meet this tolerance criterion. For the Orphan stream, our distance measurement can tolerate a relative variation of $\Delta d_{rel} = ^{+0.24}_{-0.05}$, which translates into $\Delta M = ^{+0.60}_{-0.11}$. Variations in $\Delta t = ^{+3.2}_{-1.3}$ Gyr or in $\Delta[Fe/H] = ^{+0.83}_{-0.49}$ dex (same limitations as above) for the age and metallicity of the theoretical isochrones respect this requirement.

4.5 Conclusions

In this work we have used data from two deep cluster surveys, which provide randomly scattered photometric pencil-beams in g' and r', and a field of view of 1deg^2 per pointing. We have used this data to characterize previously known substructure in the stellar halo of the Milky Way. We analysed these data using two novel ingredients: a PSF-homogenization for the images and a cross-correlation algorithm for the colour-magnitude diagram (CMD). The PSF-homogenization algorithm corrects the inhomogeneous distortion of the sources across an image caused by the telescope's optics. In this way, it recovers the true shapes and size distribution of the sources, improving the performance of any star/galaxy separation procedure, specially at the faint end. The cross-correlation algorithm explores the CMD of each field searching for an overdensity with the shape of a stellar main sequence, and returns the (colour,magnitude) coordinates of the corresponding turnoff point, from which distances can be derived. Through this method, we have shown that it is possible to exploit a two-filter pencil-beam survey to perform such a study of streams or satellites, provided that the contrast-to-noise ratio of the substructure's main sequence is moderately significant. In

this way our method bypasses the need for nearby control-fields that can be used to subtract a reference foreground from the target CMDs.

Using a set of theoretical isochrones (Marigo et al. 2008; Girardi et al. 2010), we have calculated the distances to different regions of the Sagittarius stream (faint and bright branches in both the northern and southern arms) and obtained results in good agreement with previous work (Belokurov et al. 2006b; Koposov et al. 2012, 2013; Slater et al. 2013) (see Figure 4.7).

We detect what seems to be the continuation of the northern-leading arm into the Southern hemisphere; we find that its distances are in excellent agreement with the predictions by the models in Peñarrubia et al. (2010) and Law & Majewski (2010b), while the trajectory seems to be located at higher declinations. We also find evidence for a nearby branch of the northern-trailing arm at RA $> 160^{o}$. Both the distances and the footprint on the sky are in good agreement with the predictions from the models, and are comparable to work by Correnti et al. (2010). It is also compatible with being the continuation of Gemini arm (claimed as part of a northern-trailing wrap in Belokurov et al. (2014)) if it turns or broadens to higher latitudes as it evolves westwards, but it does not follow the same distance trend as branch C (Belokurov et al. 2006b). The final interpretation of these different overdensities in the context of the Sgr stream will require kinematic data and a photometric connection between the known and the temptatively associated regions.

We have also used age and metallicity measurements from previous work (Martell et al. 2002; Harris 1996; Casey et al. 2013a), to calculate distances to the Pal5 stream and the Orphan stream. These distances are in good agreement with the results in the literature (Grillmair & Dionatos 2006a; Vivas & Zinn 2006; Belokurov et al. 2007b; Newberg et al. 2010; Casey et al. 2013a), attesting –together with the results from the Sgr stream for previously known regions of the stream– the robustness and accuracy of the cross-correlation.

The methods presented in this paper open the possibility of using deeper existing pencil-beam surveys (maybe originally aimed for extragalactic studies) to measure accurate distances (or ages or metallicities, provided that two of the three parameters are known) to streams, globular clusters or dwarf galaxies. The existence of these pencil-beam surveys or the reduced requirements of prospective ones, allow for more complete maps of the Galactic halo substructure at reduced observational costs.

Chapter 5

A search for stellar tidal debris of defunct dwarf galaxies around globular clusters in the inner Galactic halo

Authors

Julio A. Carballo-Bello, Antonio Sollima, David Martínez-Delgado, Berenice Pila-Díez, Ryan Leaman, Jürgen Fliri, Ricardo R. Muñoz, Jesús M. Corral-Santana

Abstract

In the hierarchical formation scenario in which the outer halo of the Milky Way is the result of the continuous accretion of low-mass galaxies, a fraction of the Galactic globular cluster system might have originated in and been accreted with already extinct dwarf galaxies. In this context, we expect that the remnants of these progenitor galaxies might be still populating the surroundings of those accreted globulars. In this work, we present wide-field photometry of a sample of 23 globular clusters in the Galactocentric distance range $10 \leq R_{\rm G} \leq 40\,$kpc, which we use to search for remnants of their hypothetical progenitor systems. Our deep photometry reveals the presence of underlying stellar populations along the line-of-sight of about half of the globulars included in our sample. Among the detections lying in the footprint of the Sagittarius tidal stream, which we identify via the comparison with its orbit derived from numerical simulations, only Whiting 1 and NGC 7492 seem to be inmersed in that remnant at a compatible heliocentric distance. We also confirm the existence of a subjacent Main-Sequence feature in the surroundings of NGC 1851. A tentative detection of the vast Hercules-Aquila cloud is unveiled in the background of NGC 7006.

Published in MNRAS Volume 445, 2971 (2014)

Preprint in arXiv:1409.7390 [astro-ph.GA]

5.1 Introduction

The formation of the outer regions of disc galaxies in the context of the currently most accepted cosmological model, namely Lambda Cold Dark Matter (ΛCDM, Peebles 1974), took place via the hierarchical accretion of minor stellar systems, similar to the nowadays Galactic satellite dwarf galaxies (Font et al. 2011b). Numerical simulations based on this model and focused in our Galaxy (Bullock & Johnston 2005; Cooper et al. 2010; Font et al. 2011a; Gómez et al. 2013) predict that the Galactic halo might be populated by stellar remnants, vestiges of these accretion events. An important observational effort has been made to validate this theoretical work by detecting stellar tidal streams in the halo of the Milky Way.

The first satellite dwarf galaxy discovered that is currently in the process of being accreted is the Sagittarius dwarf spheroidal (Sgr dSph; e.g. Ibata et al. 1994; Bonifacio et al. 2004; Bellazzini et al. 2006b; Siegel et al. 2007) which is following an almost polar orbit around the Galaxy. The destruction of this minor system has generated the largest and most complex halo substructure observed so far (Majewski et al. 2003; Martínez-Delgado et al. 2004a; Belokurov et al. 2006b; Koposov et al. 2012), which has allowed for an investigation of the mass distribution - potential - of the Milky Way by reconstructing its orbit from diverse spectroscopic and photometric datasets (e.g. Law & Majewski 2010b; Peñarrubia et al. 2010). However, there are still significant aspects of this substructure pending for a satisfactory explanation, like the existence of a bifurcation into two parallel streams on its northern section (Fellhauer et al. 2006; Peñarrubia et al. 2011) .

Far from being the only detected tidal debris, wide-sky surveys as the Sloan Digital Sky Survey and the Two Micron All Sky Survey (SDSS and 2MASS respectively; York et al. 2000; Skrutskie et al. 2006), have revealed the existence of substructures such as the Monoceros ring (Newberg et al. 2002; Yanny et al. 2003; Rocha-Pinto et al. 2003; Conn et al. 2005, 2007; Jurić et al. 2008; Sollima et al. 2011), diverse streams such as the Orphan (Grillmair 2006a; Belokurov et al. 2007b; Sales et al. 2008; Newberg et al. 2010), Aquarius (Williams et al. 2011), Cetus (Newberg et al. 2009) and Virgo (Duffau et al. 2006), and the over-densities of Hercules-Aquila (Belokurov et al. 2007a; Simion et al. 2014) and Virgo (Jurić et al. 2008; Martínez-Delgado et al. 2007; Bonaca et al. 2012b) as the best-studied examples. In addition, minor mergers and faint substructures have been observed in spiral galaxies in the Local Universe (e.g. Ibata et al. 2001a, 2007; Martínez-Delgado et al. 2008; McConnachie et al. 2009; Martínez-Delgado et al. 2010b), showing that our Galaxy is not unusual in this respect.

The globular cluster (GC) population of a given galaxy contains valuable information about the formation process of its host galaxy. Evidence for separate populations of GCs in the Milky Way and other galaxies have been steadily accu-

mulating, and it is interpreted as evidence that supports the hierarchical galaxy formation scenario (Zinn 1993; Leaman et al. 2013; Tonini 2013). In their seminal paper Searle & Zinn (1978) showed that while GCs in the inner Galactic halo (at distances < 8 kpc) show a clear radial abundance gradient, GCs in the outer halo do not follow this trend. In terms of the relation between the horizontal branch (HB) type and metallicity found for GCs (and assuming the age as the *second parameter*), Zinn (1993) classified globulars into *old* halo and *young* halo clusters, where the latter would correspond to the accreted fraction of Galactic GCs. Simulations suggest that whereas the outer halo clusters ($R_{\rm G} \geq 15$ kpc) were probably formed in small fragments subsequently accreted by the Galaxy (with the most massive GCs such as Omega Centauri and M 54 as the possible remnant cores of the disrupted progenitor; van den Bergh & Mackey 2004), an inner component of the Milky Way halo (and possibly a fraction of the halo GCs) may have formed *in situ* (e.g. Zolotov et al. 2009). A recent analysis of the relative ages for 55 clusters calculated from the turn-off magnitude (Marín-Franch et al. 2009; VandenBerg et al. 2013) showed that the GCs age-metallicity relation is bifucarted into two distinct groups. Interestingly, these studies find that most of the outer halo GCs belong to the branch characterized by the steeper age-metallicity relation although GCs belonging to both branches cover comparable age ranges.

Among the Milky Way satellites, Fornax and the core of the Sgr dSph host a population of 5 and 4 (at least) GCs respectively (Ibata et al. 1997; Strader et al. 2003), suggesting that accreted low-mass systems might have contributed with their own globulars to the Galactic GC system. The fraction of accreted Galactic clusters estimated by Forbes & Bridges (2010) represents 1/4 of the entire Galactic GC system, when considering parameters such as age-metallicity relations, retrograde orbits and HB morphologies. A higher fraction of $\sim 50\%$ of accreted GCs was estimated by Leaman et al. (2013), which is also consistent with the estimated fraction of accreted halo stars for the Galaxy (Zolotov et al. 2009; Cooper et al. 2013). In this context, we expect part of the Milky Way GC population to be associated with some of the tidal streams that populate the outer halo, similar to what has been observed in M 31, where the location of the outer GC system coincides with the streams observed around that galaxy (Mackey et al. 2010, 2013). If these GCs were formed in subsequently accreted stellar systems, they might be still surrounded by the tidal streams generated by the disruption of their progenitor satellites.

The possible association of Galactic GCs with the stellar tidal stream of Sgr has been extensively considered in the literature using different methods and datasets (e.g. Dinescu et al. 2000; Bellazzini et al. 2002; Martínez-Delgado et al. 2002; Palma et al. 2002a; Forbes et al. 2004; Martínez-Delgado et al. 2004a; Carraro 2009; Forbes & Bridges 2010). Bellazzini et al. (2003) found that, among the Galactic globulars in the distance range $10 \leq R_{\rm G} \leq 40$ kpc, there are at least 18 GCs compatible both in position and kinematics with the orbit proposed for that dSph galaxy by Ibata et al. (1997). More recently, (Law & Majewski 2010a,

hereafter L10) also investigated the association of 64 Galactic GCs with the Sgr stream as predicted by Law & Majewski (2010b). In that case, 9 GCs were suggested as systems formed in the interior of the Sgr dSph, latter accreted by the Milky Way.

The search for Galactic GCs associated with the other possible major accretion event, the Monoceros ring, has been complicated by the uncertainty about the origin and dynamical history of that stellar structure and the unknown location of its tentative progenitor galaxy. Different formation scenarios have been proposed for the stellar ring, from the accretion by the Milky Way of a dwarf companion system (Helmi et al. 2003; Martin et al. 2004; Martínez-Delgado et al. 2005; Peñarrubia et al. 2005; Sollima et al. 2011) to the distortion or detection of more distant Galactic components (Momany et al. 2004; López-Corredoira 2006; Momany et al. 2006; Hammersley & López-Corredoira 2011). Regarding the hypothetical progenitor accreted dwarf galaxy, the controversial Canis Major stellar over-density in the direction $(\ell, b) = (240°, -8°)$ at ~ 7 kpc from the Sun has been proposed as its remnant nucleus (Martin et al. 2004; Dinescu et al. 2005; Martínez-Delgado et al. 2005; Bellazzini et al. 2006b) but its origin has also been the subject of debate during the last years (Momany et al. 2004; Moitinho et al. 2006; Mateu et al. 2009). Nonetheless, several low-latitude GCs have been proposed as members of the Monoceros progenitor galaxy GC system including NGC 1851, NGC 1904, NGC 4590 and Rup 106 (Martin et al. 2004; Forbes & Bridges 2010), NGC 2298 (Crane et al. 2003; Frinchaboy et al. 2004; Martin et al. 2004; Forbes & Bridges 2010) and NGC 7078 (Martin et al. 2004).

In this work, we explore the possibility of the presence of stellar remnants of accreted dwarf galaxies around a sample of GCs in the inner Galactic halo, which have been extensively considered as tracers of the hierarchical formation of the Milky Way halo. With that purpose, we present wide-field deep photometry of a statistically significant sample of clusters and of the area surrounding them.

5.2 Observations and data reduction

5.2.1 Sample selection and observations

The results presented here are part of a systematic survey of stellar tidal debris around GCs of the Galactic halo, based on photometric observations of these systems with wide-field cameras at different intermediate-size telescopes during the last 10 years. Preliminary results of this survey were presented in Martínez-Delgado et al. (2002), Martínez-Delgado et al. (2004a) and Carballo-Bello et al. (2012). In this work, we have focused on clusters lying in the distance range $10 \leq R_{\rm G} \leq 40$ kpc (only 9 Galactic GCs are found beyond that distance), which might include the suggested transition region between accreted and *in-situ* formed Galactic stellar halo ($R_{\rm G} \sim$ 15–20 kpc Carollo et al. 2007). To minimize the presence of disc stars which could severely affect our photometry, we excluded from the initial sample all those clusters at low Galactic latitude ($|b| \leq 20°$) with the exception of NGC 2298 and Rup 106, globulars whose properties suggest an

Table 5.1: Sample of Galactic GCs: positional data, tidal radii and metallicities (Harris 2010; Carballo-Bello et al. 2012).

Cluster	$\ell(^\circ)$	$b(^\circ)$	$d_\odot$(kpc)	R_G(kpc)	r_t (arcmin)	[Fe/H]
Whiting 1	161.2	-60.7	30.1	34.5	3.2	-0.70
NGC 1261	270.5	-52.1	16.3	18.1	10.9	-1.27
NGC 1851	244.5	-35.0	12.1	16.6	11.6	-1.18
NGC 1904	227.2	-29.3	12.9	18.8	11.3	-1.60
NGC 2298	245.6	-16.0	10.8	15.8	10.1	-1.92
NGC 4147	252.8	77.2	19.3	21.4	6.6	-1.80
Rup 106	300.8	11.6	21.2	18.5	9.0	-1.68
NGC 4590	299.6	36.0	10.3	10.2	21.4	-2.23
NGC 5024	332.9	79.7	17.9	18.4	18.0	-2.10
NGC 5053	335.7	78.9	17.4	17.8	13.1	-2.27
NGC 5272	42.2	78.7	10.2	12.0	25.4	-1.50
AM 4	320.3	33.5	32.2	27.8	3.3	-1.30
NGC 5466	42.2	73.6	16.0	16.3	23.4	-1.98
NGC 5634	342.2	49.3	25.2	21.2	9.6	-1.88
NGC 5694	331.1	30.4	35.0	29.4	4.7	-1.98
NGC 5824	332.6	22.1	32.1	25.9	5.7	-1.91
Pal 5	0.8	45.9	23.2	18.6	21.1	-1.41
NGC 6229	73.6	40.3	30.5	29.8	3.8	-1.47
Pal 15	18.8	24.3	45.1	38.4	5.6	-2.07
NGC 6864	20.3	-25.7	20.9	14.7	6.8	-1.29
NGC 7006	63.8	-19.4	41.2	38.5	5.7	-1.52
NGC 7078	65.0	-27.3	10.4	10.4	17.5	-2.37
NGC 7492	53.4	-63.5	26.3	25.3	9.2	-1.78

external origin (Crane et al. 2003; Forbes & Bridges 2010; Dotter et al. 2011). We have also excluded NGC 6715, Terzan 7, Arp 2 and Terzan 8 because their location has already been established within the main body of the Sgr dSph (Bellazzini et al. 2003, 2008) and Pal 12, which has previously been associated to its stream (Dinescu et al. 2000; Martínez-Delgado et al. 2002). Following these criteria, our final sample is composed of 23 of these systems. It represents a half of the GCs in the considered Galactocentric distance range and the 3/4 of the clusters that match our latitude criteria.

Table 5.1 includes the position, distance and other relevant information of our GC sample. The positions and [Fe/H] estimates are taken from the Harris (2010) catalogue. Tidal radii are taken from Carballo-Bello et al. (2012), where structural parameters for these globulars were derived using the same photometric database presented in this paper, with the exception of the clusters Whiting 1, AM 4, Pal 15 and NGC 7006 not included in that work and for which they have been estimated using a similar procedure as the described in Carballo-Bello et al. (2012). The radial density profiles for these 4 GCs have been obtained including information for the inner region of the clusters from the literature (Harris 1991; Trager et al. 1995; Carraro et al. 2007; Carraro 2009).

Our survey strategy was based on obtaining deep photometric observations in a wide field of view (FOV) around the clusters, which allows us to explore for the first time their external regions, poorly represented in shallower photometric data. In this case, the main tracers of the tidal debris of these possible progenitor systems are main-sequence (MS) stars 2–3 magnitudes fainter than the MS turn-off (TO) of the old stellar population. Given the low levels of surface-brightness for known tidal streams ($\mu_V > 30\,\mathrm{mag\,arcsec^{-2}}$, Martínez-Delgado et al. 2001; Majewski et al. 2003), very deep colour-magnitude diagrams (CMDs) are needed to get enough statistic of MS-TO stars in the explored area. In addition, good seeing conditions are essential to undertake a reliable decontamination of background galaxies in the CMD, which would otherwise affect the detection of a MS feature associated to an underlying stellar population in the blue region of the diagram at fainter magnitudes (e.g. see Figures 5.2 and 5.7).

Observations have been performed using the Wide Field Camera (WFC) mounted at the Isaac Newton telescope (INT), established at El Roque de los Muchachos Observatory on the island of La Palma (Canary Islands) and the Wide Field Imager (WFI) at the MPG/ESO2.2 m telescope, at the La Silla Observatory (Chile). The WFC provides, with 4 CCDs with a pixel size of $0.333\,\mathrm{arcsec\,pixel^{-1}}$, a total FOV of 34 arcmin × 34 arcmin. The WFI provides a similar FOV of 34 arcmin × 33 arcmin covered by 8 identical CCDs. A summary of the observations is shown in Table 5.2, including the coordinates of each of the pointings. The typical exposure times were 4×900 s in the B band and 6×600 s in R. The typical seeing was $FWHM < 1''$. Daily sky-flats and bias were obtained and used for bias and flat-field correction by means of reduction routines based on IRAF standard tasks. A set of Landolt (1992) standard stars were observed during the runs, at different airmass ranges to allow a precise calibration of the final photometric catalogs.

Table 5.2: Coordinates, exposure times, mean seeing and dates of the observational campaigns in which the GCs were observed. Service mode observations are denoted by (*s*).

Cluster	RA(2000)	DEC(2000)	t_{exp} B(s)	t_{exp} R/r(s)	seeing(")	Instrument	Obs. run date
Whiting	02:02:56	-03:15:10	4×900	6×600	1.2	WFC	2010/08/17-19
NGC 1261	03:13:41	-55:25:28	4×900	4×600	0.8	WFI	2009/11/08-12
NGC 1851	05:13:04	-39:49:58	3×900	6×600	0.6	WFI	2005/07 (*s*)
	05:15:02	-40:11:57	4×900	6×600	0.8	WFI	2010/02/14-19
NGC 1904	05:23:29	-24:19:21	3×900	5×600	0.5	WFI	2005/07 (*s*)
	05:25:29	-24:19:19	3×900	5×600	0.5	WFI	2005/07 (*s*)
NGC 2298	06:50:05	-35:50:47	4×900	4×600	0.9	WFI	2009/02/19-22
NGC 4147	12:09:40	+18:20:03	4×600	4×600	0.8	WFC	2002/05/15-17
Rup 106	12:38:48	-51:12:36	4×900	6×600	0.9	WFI	2009/02/19-22
NGC 4590	12:38:36	-26:31:45	4×900	6×600	0.8	WFI	2010/02/14-19
NGC 5024	13:12:30	+17:49:59	3×900	3×600	0.7	WFC	2002/05/15-17
NGC 5053	13:16:01	+17:21:51	4×900	6×600	0.6	WFC	2010/06/11-13
NGC 5272	13:41:20	+28:45:32	2×900	3×600	1.1	WFC	2010/05/18 (*s*)
	13:42:11	+28:57:32	3×900	6×600	0.7	WFC	2010/06/11-13
AM 4	13:56:06	-27:19:18	6×900	6×600	0.9	WFI	2009/02/19-22
NGC 5466	14:03:51	+28:16:58	4×900	4×600	0.9	WFC	2008/05/11-12
NGC 5634	14:28:45	-05:45:21	4×900	6×600	0.9	WFI	2010/02/14-19
NGC 5694	14:38:40	-26:21:25	4×900	5×600	0.8	WFI	2010/02/14-19
NGC 5824	15:04:14	-32:53:15	4×900	6×600	1.0	WFI	2010/05/15-19
Pal 5	15:15:41	-00:06:48	2×1000	3×900	0.9	WFC	2001/06/20-27
NGC 6229	16:46:25	+47:20:06	3×900	5×600	1.2	WFC	2010/08/17-19
Pal 15	16:59:36	-00:24:45	4×900	6×600	0.9	WFI	2010/05/15-19
NGC 6864	20:05:46	-21:41:30	3×900	6×600	0.5	WFI	2010/05/15-19
NGC 7006	21:01:29	+16:11:15	4×900	4×600	1.0	WFC	2001/06/22-28
	21:08:48	+18:24:51	3×900	4×600	0.9	WFC	2001/06/22-28
NGC 7078	21:29:36	+12:09:00	3×900	6×600	1.0	WFC	2010/06/11-13
	21:29:58	+12:40:00	4×900	6×600	0.8	WFC	2010/06/11-13
NGC 7492	23:09:16	-15:49:14	4×900	5×600	0.9	WFI	2009/11/08-12

5.2.2 Photometry and completeness test

PSF photometry was obtained using DAOPHOT II/ALLSTAR (Stetson 1987) Our final catalogs only contains objects with |SHARP| ≤ 0.4, reducing the pollution in the CMDs by background galaxies and allowing us to detect the MS of the tentative underlying streams in the region of the diagram dominated by these non-stellar objects. The aperture correction of our magnitudes were performed using bright stellar-shaped objects in the outer regions of the field, far from the GC, with $\sigma < 0.1$. With these criteria, we had a good sample of bright stars to compare the PSF fitting from ALLSTAR with the aperture photometry obtained with DAOPHOT II/PHOT. The typical corrections are below 0.2 mag. To estimate the magnitude of our stars outside the atmosphere, we used the extinction coefficients computed for each observatory: $A_{\rm B} = 0.22$ and $A_{\rm r} = 0.07$ magnitudes per airmass unit for the Roque de los Muchachos Observatory and $A_{\rm B} = 0.19$ and $A_{\rm R} = 0.06$ at La Silla Observatory.

For the calibration of the WFC photometry, we have searched for stars present both in our data and in SDSS. Due to the differences between the filters used by this survey and those used in our project, we transformed the SDSS magnitudes (*ugriz*) to the Johnson-Cousins system (*BR*) using Chonis & Gaskell (2008) equations (for stars in the color range $0.08 < r - i < 0.5$ and $0.2 < g - r < 1.4$). The brightest subsample of common stars (20–30 stars per chip) was used to obtain a correction factor to apply to our objects and that also accounts for the differences between the photometric systems. No significant color trends have been noticed in the comparison between B and R magnitudes in the WFC and Johnson-Cousin photometric system. For this reason we applied only a systematic shift. Mean values for these corrections are found to be $C_{\rm B} = 25.10 \pm 0.08$ and $C_{\rm R} = 25.72 \pm 0.09$. For the WFI data, we derived transformations from the comparison of the instrumental results for the Landolt (1992) standard stars observed and their calibrated magnitudes. The mean values for the transformation coefficients are:

$$B_{Lan} - B_{inst} = 25.09\,(\pm 0.09\,) + 0.19\,(\pm 0.23\,)\,(B-R)_{inst} \tag{5.1}$$

$$R_{Lan} - R_{inst} = 24.57\,(\pm 0.07\,) - 0.02\,(\pm 0.02\,)\,(B-R)_{inst} \tag{5.2}$$

In order to estimate the completeness of our photometric catalogs in the surrounding area of the clusters, we have considered separately the furthest chip with respect to the cluster centre. We have included in the images synthetic stars with magnitudes in the range $17 \leq B, R \leq 26$ and color $0.5 < B - R < 1.5$, randomly distributed throughout the chip. The total number of synthetic stars added in each of the frames was designed not to exceed 15% of the number of originally

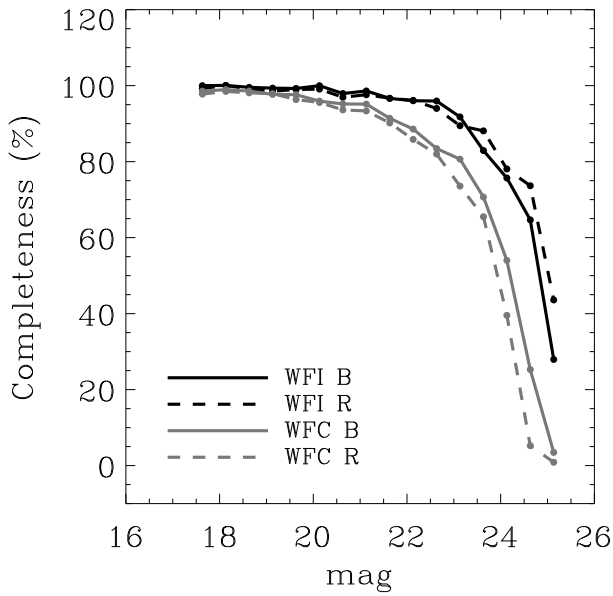


Figure 5.1: Examples of the photometric completeness obtained in this work for the B (solid line) and R (dashed line) bands as a function of the magnitude for WFC (grey) and WFI (black), for the clusters NGC 6229 and NGC 5634 respectively. Synthetic stars with magnitudes below 22 in the WFI are completely recovered, while that percentage drops below 80% at $B, R \sim 24$. As for the WFC photometry, a completeness of 80% is derived up to magnitudes $B, R \sim 23.5$, while it drops to the 60% at $B, R \sim 24$. All the magnitudes are in the Johnson-Cousins system.

observed sources and have been placed in separated cells to avoid self-crowding. For each of the globulars, we obtained 50 of these altered images and they were processed with DAOPHOT II using the same PSF model derived for the observed stars.

We estimated the fraction of synthetic stars recovered by ALLSTAR for all the images and derived a mean variation of that fraction as a function of the magnitude. In Figure 5.1 it is shown the percentage of recovered stars for the B and R bands, corresponding to one of the outer chips in the mosaics obtained for two clusters with typical exposure times and seeing (see Table 5.2), but observed with different instruments. Our results show a similar behaviour for both bands but with small differences between the instruments. On the one hand, our WFI photometry recovers around the 100% of the synthetic stars up to magnitudes $B, R \sim 22$ and in that case the completeness drops marginally below 80% at $B, R \sim 24$. For the WFC, considering the same magnitudes ranges defined above,

we obtained a 90 and 60% of completeness for $B, R \sim 22$ and 24 respectively. Despite these differences regarding the number of recovered sources in both instruments, we conclude that, given the depth of our data, our photometry should be able to detect the presence of subjacent tidal streams if they are present in the surroundings of these GCs. Hereafter we define $< V >= (B + R)/2$.

5.3 Methodology

There are several scenarios where one might expect to observe apparent tidal debris around Galactic halo GCs: *i)* the GC could itself be in the process of tidal disruption due to the tidal field of the Milky Way (e.g. Pal 5; Odenkirchen et al. 2001, 2003), *ii)* the tidal debris could originate from the disruption of the relic of the galaxy that originally hosted the cluster (as is the case with the Sgr dwarf GCs and almost certainly those seen apparently embedded in tidal substructures in and around M 31 (Mackey et al. 2013) and *iii)* the GC could by chance be superimposed in projection against other large-scale halo substructure.

Here, we focus on the detection of debris from a subjacent galaxy remnant. A complete confirmation of such association between GCs and tidal stream would require follow-up spectroscopy (e.g. velocities, chemical tagging) for the members of these tidal debris. With photometry only it is not possible to differentiate between these scenarios, so our results are a first step to identify those Galactic GCs possibly accreted.

5.3.1 Selection of the extra-tidal field of the cluster

An important issue in this work is to estimate the tidal edge of the cluster and separate the possible stellar remnants from the GC stellar content. Tidal radii, commonly denoted by $r_{\rm t}$, are key structural parameters in King models (King 1966) and indicate the distance at which the radial density profile reaches the theoretical zero level. It has been classically used as the physical edge of a GC and all those stars lying beyond this distance have been typically classified as *extra-tidal* content. Carballo-Bello et al. (2012) found that when MS stars are included to derive a more complete radial density profile, the derived $r_{\rm t}$ are a 40% bigger on average than those derived from shallower photometry. Moreover, in many cases the overall shape of the density profile is not well reproduced by King models, especially in the outer parts of the cluster. This indicates that $r_{\rm t}$ is only a rough estimate of the edge of a cluster (see also McLaughlin & van der Marel 2005) and by assuming it as the separation between cluster and fore/background stellar populations, the CMD corresponding to the latter might be still populated by cluster members.

Figure 5.2 illustrates the importance of using that selection criteria in the obtention of the CMDs for the fore/background stellar populations. We have generated both the diagrams corresponding to the stars beyond the tidal radius of NGC 5694 set at $r_{\rm t} = 4.7$ arcmin and $1.5\,r_{\rm t}$, using in this case the value derived from the profiles obtained in Carballo-Bello et al. (2012). It is apparent

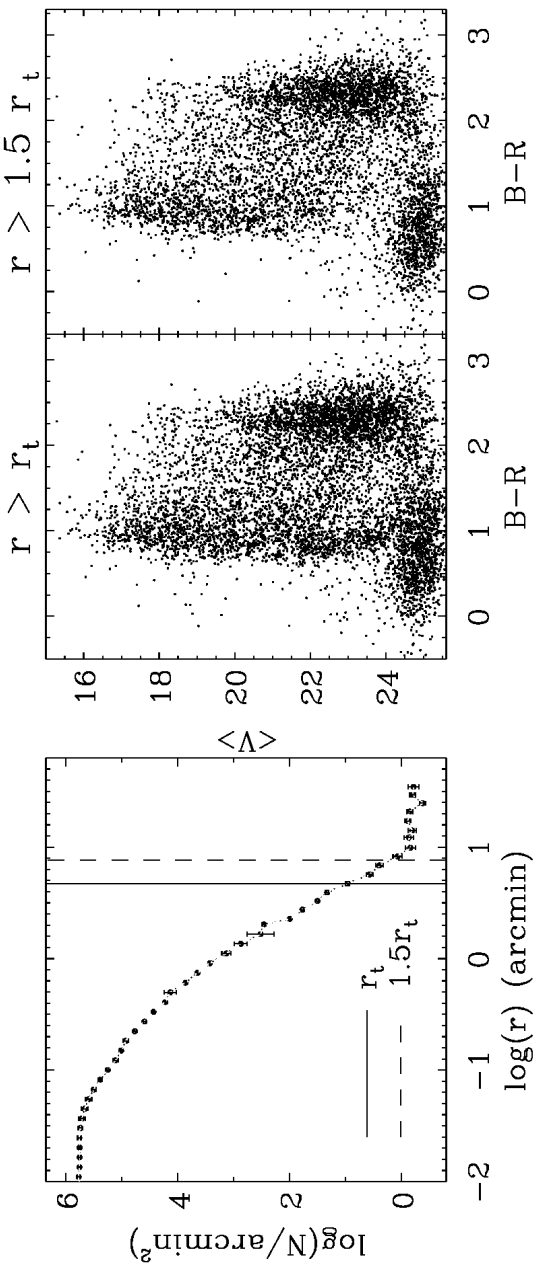


Figure 5.2: Left: radial density profile derived by Carballo-Bello et al. (2012) for NGC 5694, where the vertical lines indicate the position of the King tidal radius (r_t) derived on that work and 1.5 times that distance from the cluster centre. The middle and right panels correspond to the CMDs generated with the stars beyond those distances from the cluster centre. When stars beyond the tidal radius are considered, the CMD shows an over-density associated with the presence of NGC 5694 stars as expected from the position of r_t in relation to the derived radial profile.

that the King tidal radius lies within the outer part of the GC profile, so the contribution of NGC 5694 stars becomes important even outside this distance. On the contrary, when the distance at which the radial density remains nearly constant is considered, the over-density associated to the GC content is not present in the diagram. Trying to avoid as much as possible the contamination by GC stars, our criterion for this separation was set on 1.5 times the formal King tidal radius $r_{\rm t}$, in most cases this coincides with the distance at which the radial density reaches the background level. We adopted the tidal radii determined in Carballo-Bello et al. (2012) using the present photometric dataset (listed in Table 5.1). For the clusters Whiting 1, AM 4, Pal 15 and NGC 7006, not included in the above work, we determined tidal radii using the same procedure described in Carballo-Bello et al. (2012). Hereafter, we define $r_{bg} = 1.5\,r_{\rm t}$. Figures 5.3 to 5.6 show the radial density profiles of our target clusters where the adopted value of r_{bg} is indicated.

Unfortunately, because of the relatively small extra-area and limited angular coverage of our data we are not able to detect any large-scale gradient and/or asymmetry in the distribution of extra-tidal area.

5.3.2 Identification of tidal debris in wide-field photometry with Milky Way synthetic colour-magnitude diagrams

Galactic tidal streams are highly dispersed resulting in a low surface-brightness structure that generates a modest representation of more evolved stars in the CMDs. Thus, we expect that the only feature that may indicate the presence of a stream around a GC is the presence of a MS that might be coincident with that of the GC if they lie at the same distance. However, the same feature could be present if the cluster has developed tidal tails because of its interaction with the Milky Way. In the majority of the cases, the MS stars from the subjacent tidal remnant are hidden in the CMD due to the combination of the contributions of a minor fraction of cluster members, fore/background stellar populations from the different Milky Way components (mainly the disc and halo) and background galaxies.

The best method to correct from these contribution is to obtain observations of adjacent control fields with similar Galactic latitude but several degrees away from the GCs, with similar FOV and exposure time than the target fields. However, we could not obtain these kind of observations during the observing time granted for this project. For this reason, to disentangle the Milky Way stellar halo contribution and to identify any subjacent population, we compared the observed diagrams with synthetic CMDs for the same line-of-sight of each cluster and for a similar solid angle computed assuming a Milky Way model. In this work, we have considered the TRILEGAL (Girardi et al. 2005; Vanhollebeke et al. 2009) and Besançon (Robin et al. 2003) Milky Way models, that provides public available webpage scripts to compute simulated CMDs in selected Galactic fields.

Figure 5.7 shows a CMD observed for one of the GCs in our sample (NGC 2298), together with the diagrams obtained with the two models, for the same direction

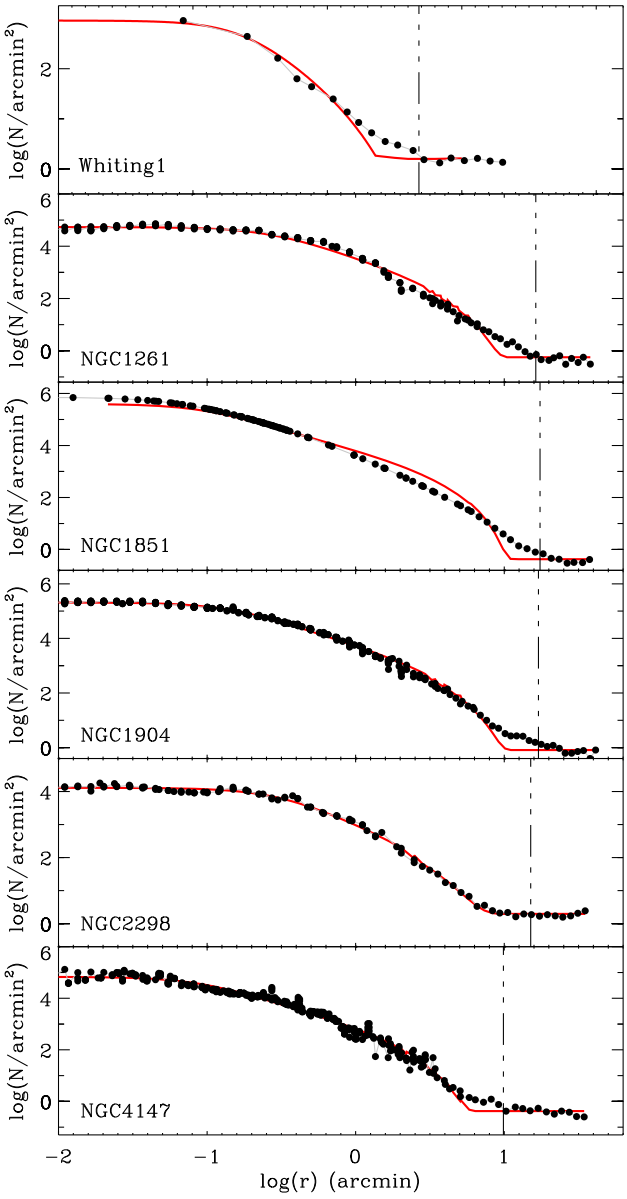


Figure 5.3: Radial density profiles as derived by for Whit 1, NGC 1261, NGC 1851, NGC 1904, NGC 2298 and NGC 4147. The vertical line indicate the distances from the cluster centre where the cluster content has been separated from the rest of objects in the photometric catalogues. The red line corresponds with the best King model fitting (Carballo-Bello et al. 2012).

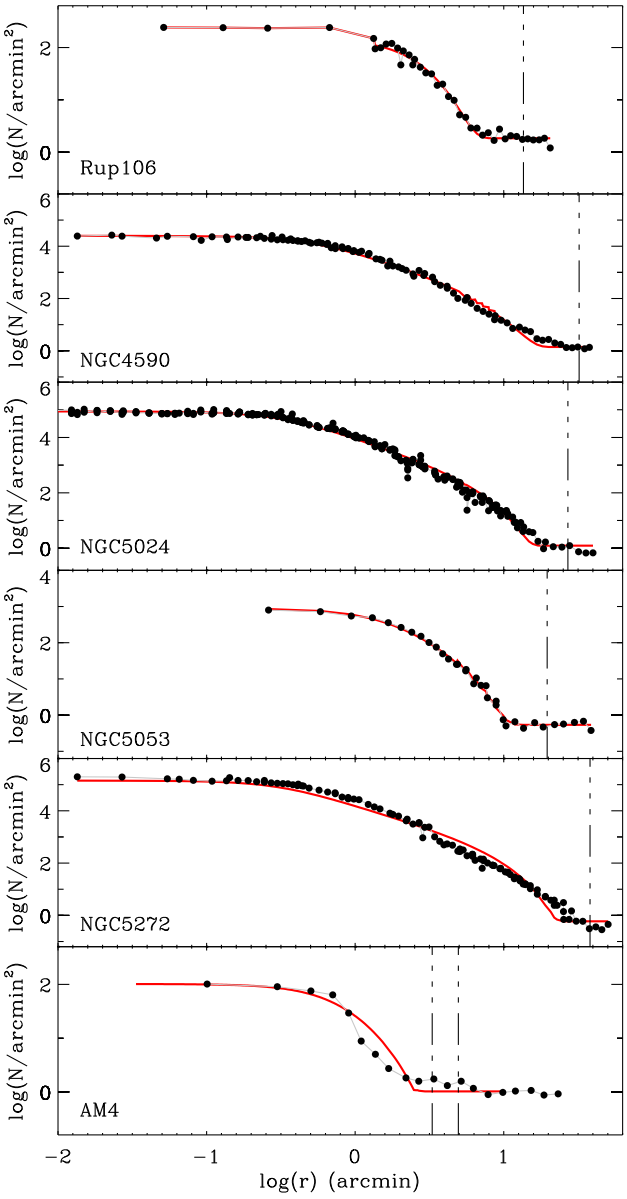


Figure 5.4: Radial density profiles as derived by for Rup 106, NGC 4590, NGC 5024, NGC 5053 and AM 4. The vertical line indicate the distances from the cluster centre where the cluster content has been separated from the rest of objects in the photometric catalogues. The red line corresponds with the best King model fitting (Carballo-Bello et al. 2012).

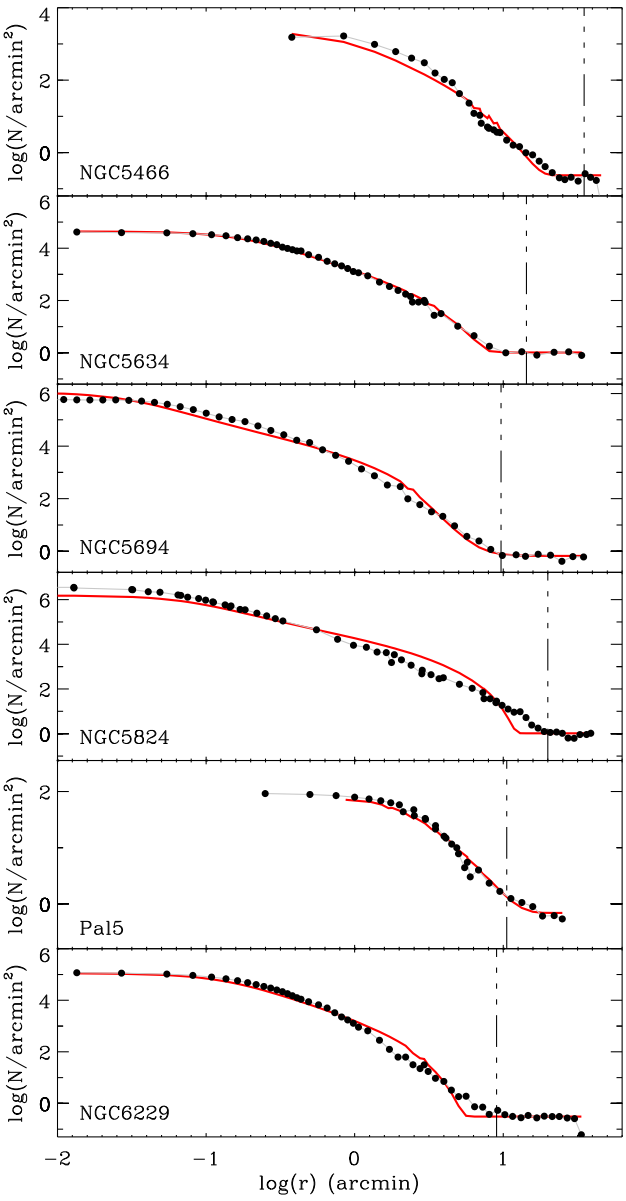


Figure 5.5: Radial density profiles as derived by for NGC 5466, NGC 5634, NGC 5694, NGC 5824, Pal 5 and NGC 6229. The vertical line indicate the distances from the cluster centre where the cluster content has been separated from the rest of objects in the photometric catalogues. The red line corresponds with the best King model fitting (Carballo-Bello et al. 2012).

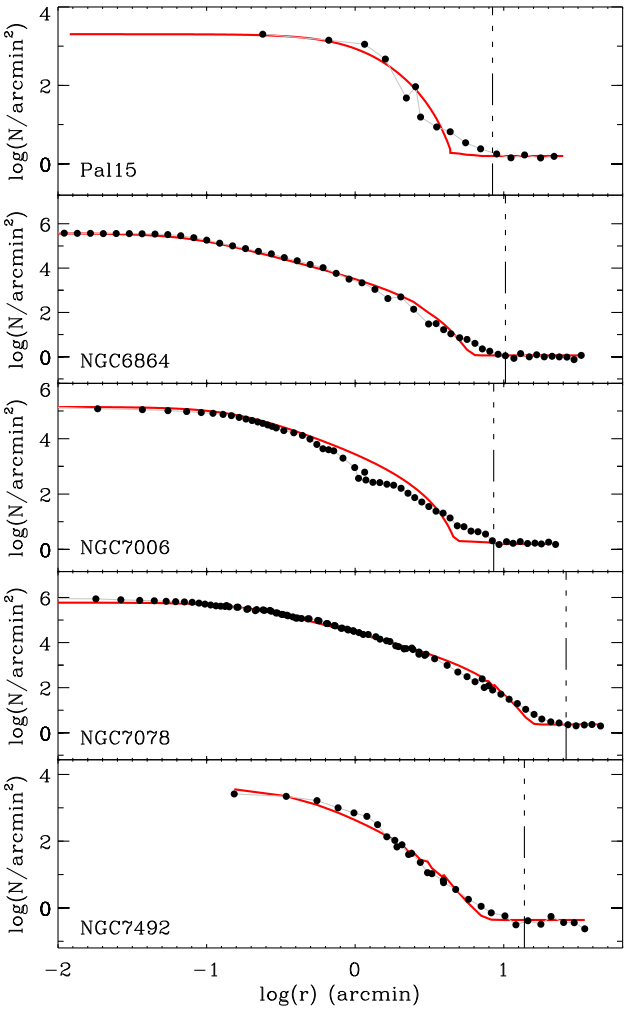


Figure 5.6: Radial density profiles as derived by for Pal 15, NGC 6864, NGC 7006, NGC 7078 and NGC 7492. The vertical line indicate the distances from the cluster centre where the cluster content has been separated from the rest of objects in the photometric catalogues. The red line corresponds with the best King model fitting (Carballo-Bello et al. 2012).

in the sky. This comparison allows us to identify the over-density of objects in the bluer region of the diagram, around $V \sim 24$, as background galaxies, a characteristic feature in wide-field photometry. The differences observed between the synthetic CMDs clearly indicate that the choice of the Milky Way model for comparison would play a relevant role in the detection of Galactic substructures. In that figure, we have delimited a region in the CMD that encompasses the component associated with the Galactic halo, in which this study is focused, defined by $0.6 < B - R < 1.5$ and $21 < V < 23.5$. This clearly shows that the Besançon model predicts a larger number of stellar halo stars than TRILEGAL, affecting the significance of any eventual tidal debris

We have compared the stellar content of TRILEGAL/Besançon in that box of the CMDs for different sections of the Galactic halo. We have obtained 12 synthetic CMDs using both models with an area $\Omega = 0.25\,\mathrm{deg}^2$ for the Galactic longitudes $\ell = 0$, 90 and 180° and latitudes $b = 25$, 40, 60 and 90°. The number of predicted halo stars in that box, for all the directions in the sky considered, is larger for the Besançon results. For $\ell = 180°$ and $\ell = 90°$ we find a similar behaviour, showing that the contribution of halo stars in the TRILEGAL model with respect to Besançon is considerably lower with $\mathrm{N_T/N_B} \sim 0.3-0.4$, where $\mathrm{N_T}$ and $\mathrm{N_B}$ represent the star counts in that box for TRILEGAL and Besançon, respectively. These differences might arise from the different structural parameters assumed by these models to describe the Galactic stellar halo. On the one hand, the TRILEGAL model allows the user to select between a $r^{1/4}$ and an oblate $r^{1/4}$ stellar halo distribution, where in the latter case the oblateness parameter q_h remains as free parameter. Instead, in the Besançon model, the spheroid component is described by a power-law with slope $\alpha = -2.44$ with a fixed value for the oblateness set at $q_\mathrm{h} = 0.76$.

Gao et al. (2013) has recently studied the ability of these models to reproduce Hess diagrams generated from SDSS data in a specific area of the sky. Although in their results both models show problems to reproduce the observations, the section of the CMD dominated by halo stars - area of interest for this work - was more adequately represented by the synthetic diagrams generated by TRILEGAL. Given these significant differences in the contribution of halo stars, we will continue using as reference both the CMDs generated with TRILEGAL and Besançon, although new incoming versions of these models, fitting the parameters to wide-sky surveys (e.g. Robin et al. in preparation), will have to be taken into account in future searches for halo substructures.

To estimate the significance of the detections in our photometry, we have compared the observed stellar counts with those computed from the synthetic CMDs generated with TRILEGAL for the same line-of-sight and solid angle. The input parameters for that model are taken from the optimization obtained by Gao et al. (2013) (see Table 3 on that paper). For the Besançon model, we have used the default parameters. The observed stars considered to derive the significance of a subjacent population are those contained between the V-level of the TO and the level where the CMD is dominated by background galaxies, with a difference

in colour $0.1 < \delta(B-R) < 0.2$ with respect to the corresponding isochrone (see Section 5.3.4). Assuming the uncertainty in the number counts as $\sigma_{\rm N} = \sqrt{N}$, the significance is given by

$$S = \frac{(\mathrm{N_{CMD}} - \mathrm{N_{model}})}{\sqrt{\mathrm{N_{CMD}} + \mathrm{N_{model}}}} \tag{5.3}$$

where $N_{\rm CMD}$ is the number of observed stars following the criteria described above and $N_{\rm model}$ the TRILEGAL/Besançon counts in the same area of the synthetic CMD after correcting for completness. In this work, S will indicate the significance of the detections with respect to the synthetic model. Given the uncertainties linked to the performances of the Galactic models in reproducing the real Galactic field population we defined a conservative treshold for a positive detection of an underlying stellar population when $S > 5$.

Our ability to detect the presence of stellar substructures with surface-brightness comparable to those of Galactic tidal streams is also affected by the position of the fields. It is possible to estimate the surface-brightness detection limit of our method to detect a Sgr-like stellar population that stands out with $S = 5$ above the Galactic stellar populations and as a function of the direction in the sky. We have used the distance-dependent expression proposed by Bellazzini et al. (2006a):

$$\mu_V = -2.5\log(n) + 2.5\log(\Omega) + (m-M)_0 + K \tag{5.4}$$

where n is the number of MS stars, Ω the solid angle observed, $(m-M)_0$ the distance modulus to the stellar population and K includes theoretical elements (see the complete formula in Bellazzini's paper). We have calibrated the latter term applying this expression to the subjacent Sgr population unveiled around Whiting 1, and using a surface-brightness for that portion of the stream of $\mu_{\rm V} = 30.6\,\mathrm{mag\,arcsec^{-2}}$, measured by (Koposov et al. 2012). We define a box in the CMD including all the stars in the subjacent MS to determine K - assuming the same heliocentric distance that of Whiting 1 - and used that box in the synthetic CMDs used in Section 5.3.2 to count the number of stars predicted by TRILEGAL (after correcting for incompletness). After that, we estimated the necessary number of stars in that box to obtain a $S = 5$ detection above the fore/background population using Equation 5.3 and translate those counts into surface-brightness by applying Equation 5.4, assuming the same distance modulus of Whiting 1.

Figure 5.8 shows the limiting surface-brightness (5σ detection) as a function of b and for the ℓ values considered above. As expected, we will be able to detect the presence of fainter halo substructures at higher Galactic latitudes, where the halo component becomes less important in the obtained CMDs. A tidal stream as the one found around Whiting 1 would be detected in the area $b > 80^\circ$ for all ℓ, when the surface-brightness of that structure is as faint as $31.5 < \mu_{\rm V} < 32\,\mathrm{mag\,arcsec^{-2}}$. The surface-brightness required for a tidal stream to

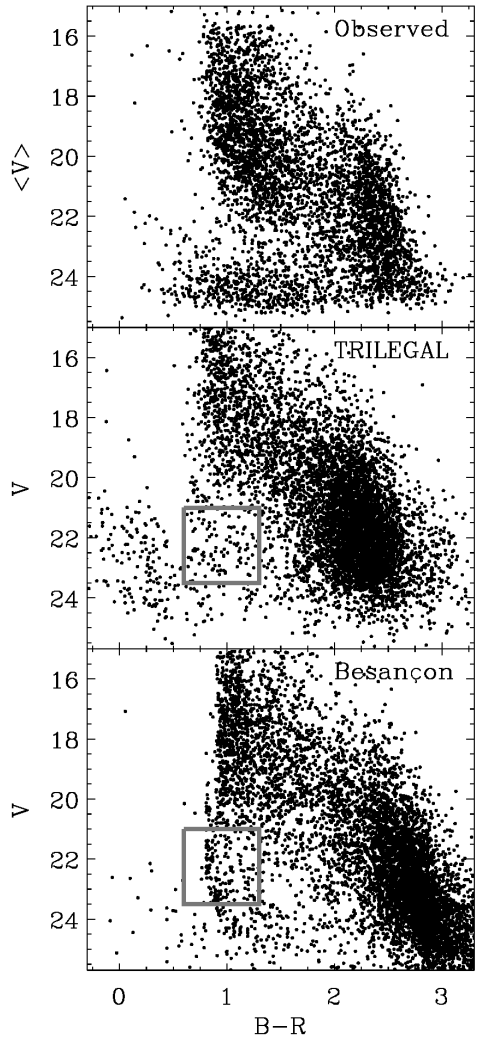


Figure 5.7: Top: example of CMD obtained for the surroundings of NGC 2298 for stars beyond $r_{\rm bg}$ from the cluster centre. Middle and bottom panels: CMDs obtained with TRILEGAL and Besançon models respectively for a field in the direction of NGC 2298, with a similar solid angle to that of the observed area around the cluster. The remarkable over-density observed in the bluer region of the observed CMD with $V > 24$ is generated by the presence of background galaxies in the wide-field photometry. In order to compare both synthetic models, we have selected the area in the CMD defined by $0.6 < B - R < 1.5$ and $21 < V < 23.5$ (over-plotted grey rectangle).

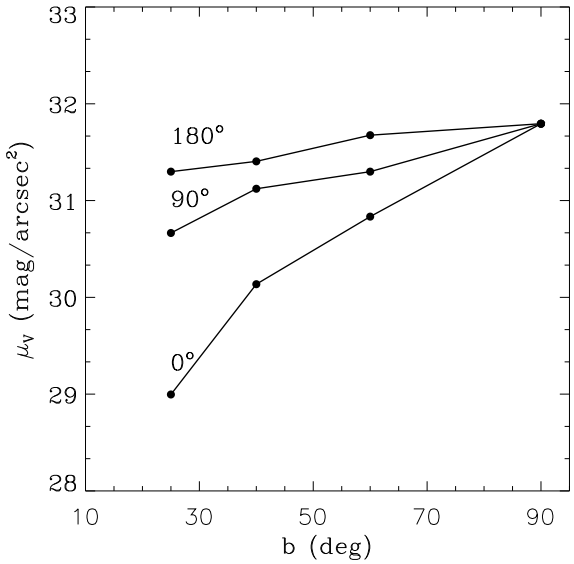


Figure 5.8: Limiting surface-brightness for three directions in the sky (ℓ = 0, 90 and 180°), defined by the star counts required to obtain a 5σ signal above TRILEGAL. As expected, faint substructures as tidal streams will be more easily detectable at higher values of b, far from the Galactic stellar components (disc, bulge).

be differentiated from the fore/background populations in the area around the Galactic centre ($\ell = 0°$, $b < 40°$) is brighter compared to the values obtained for the same stream in the Anticentre direction. These results indicate the areas where faint stellar substructures as the known tidal streams will be more easily detectable.

5.3.3 Finding stellar debris with a cross-correlation algorithm

Given that the detections (and their significances) derived from the synthetic CMDs might depend on the selection of the Milky Way model and the input parameters, we have also used an alternative approach to look for MS features of stellar streams based on the cross-correlation method described in Pila-Díez et al. (2014). This algorithm has been succesfully proven in the case of a photometric pencil-beam survey of the Sgr tidal stream using CFHT MegaCam deep data but lacking control fields adjacent to the target fields, which is the same situation of our GC survey. This method is based on an algorithm that takes a CMD as an input and looks across it for the over-density that best matches a template MS population. The template MS is built from the shape of an old, metal-

poor theoretical isochrone[1](Marigo et al. 2008; Girardi et al. 2010) matching the specific photometric system of the CMD. The width of this template MS is tailored to the photometric quality of the CMD by accounting for the increase in colour error with magnitude of a well defined stellar locus (particularly, the nearby M-dwarf stars at $2 < B - R < 3$). To each region of the MS template a weight based on the distance to the central region of the template is given so that - for each step of the cross-correlation - stars placed in the inner part of the template have a larger weight than stars at the edges of the template. This accounts for possible outliers and statistical contamination.

The algorithm returns two products: the first one is a binned density diagram in the colour-magnitude space recording the stellar density contained within the template MS for each iteration of the cross-correlation. The second one is the MS TO point coordinates (in the colour-magnitude space) for the best match (peak of the cross-correlation). We used these binned density diagrams to evaluate the quality of the detection by estimating the signal-to-noise of the cross-correlation procedure and used this last parameter to determine whether the best match actually represents a real halo feature. We define a positive detection when the S/N is larger than 5. In all cases with S/N>3, we can use the MS TO point magnitude to calculate the distance modulus and the heliocentric distance to the substructure (see below). For the templates in this work we have used two types of theoretical isochrones: one corresponding to the age and metallicity of each GC, which we use on both the corresponding GC and on the extratidal field at $r > r_{\rm bg}$ CMDs, and another one corresponding to possible subjacent streams, which we only use for the outer-region CMDs.

5.3.4 Distances to the underlying populations with isochrone fitting

Distances to the hypothetical tidal debris are fundamental to conclude if they are associated to the GCs or a background, unassociated tidal stream or Galactic substructure. Heliocentric distances were derived from the position of the MS-feature of the tidal debris in the CMD by fitting a reddening-corrected theoretical isochrone. First, the selected isochrone is shifted by varying the distance modulus in the range $12 < (m - M)_{\rm V} < 19$ with a step of $\delta(m - M)_{\rm V} = 0.2$. The χ^2 for each position was computed taking into account all the stars located in the MS feature (mainly populated by the possible stream stars and Galactic halo stellar component). The distance modulus value corresponding to the minimum χ^2 is then selected as initial input for an iterative procedure to obtain a more accurate estimate of the position of the isochrone. In this case, we analyzed the distance modulus range within a 10% above and below that value with a smaller step $\delta(\mathrm{m - M})_{\rm V} = 0.01$ ($\sim$150 pc). This fitting method has been tested using the CMD corresponding to the inner regions of the GCs, for which we used

[1]This isochrone and all the ones associated to the cross-correlation have been retrieved from the Padova Stellar Evolution database, available at http://stev.oapd.inaf.it/cmd.

the isochrones assuming previous estimates for their age t and [Fe/H] (Forbes & Bridges 2010; Harris 2010). Figure 5.9 shows the comparison between the $(m - M)_{\rm V}$ obtained for the 23 globulars and those listed in the Harris catalog. There is no evidence of systematic deviation from the 1:1 line, this is also confirmed by the obtained correlation coefficient ($r = 0.97$). This test confirms that it is possible to obtain the heliocentric distances for stellar remnants using our method and, more importantly, there are not systematic effects in our photometry, even though is based in observing campaigns from two different telescopes spread over ten years.

Because of the lack of a red-giant branch (RGB) feature associated to the detected tidal debris, it is not possible to obtain insights on their metallicity from our CMDs. This also prevents us from selecting the most suitable isochrone for each case. For this reason, we use only two different cases for our derivation of these distances: in the case of the remnants possibly associated to the Sgr stream (see Section 5.5.1), we used an isochrone based on Siegel et al. (2007) results, with an intermediate age of $t = 6\,$Gyr with [Fe/H] = -0.6. For the over-densities found around other clusters, we assume that they are dominated by an old stellar population similar to those of the typical Milky Way dSph galaxies (i.e. Ursa Minor or Draco). In these cases, an isochrone with $t = 12\,$Gyr and [Fe/H] = -1.5 is used for the fitting method described above. We have used the theoretical isochrones generated by Dotter et al. (2008b) in combination with the Galactic extinction maps from Schlegel et al. (1998) and the extinction coefficients from Schlafly & Finkbeiner (2011). Possible effects of spatial variations on the extinction over the FOV are expected to be smalle ($\Delta E(B-V) < 0.02$) even in the clusters at the lowest latitude included in our sample, and have been neglected. The resulting heliocentric distance for the possible tidal remnants detected in this study are given in Table 5.3.

In addition to these distance estimates, the MS TO point coordinates for the best match (i.e. peak of the cross-correlation) obtained from the algorithm described in Section 5.3.3 were used to calculate the distance modulus and the heliocentric distance to the substructures. The potential age and metallicity gradients of the subjacent streams and their effect on the distance calculation have been included in the uncertainties as discussed in Pila-Díez et al. (2014). The results of this method are given in Table 5.4.

5.4 Results

Figures from 5.10 to 5.15 show the calibrated CMDs for the GGs in our sample. For each cluster, we show the CMD for its central region (middle panel) and for those stars situated at a distance beyond $r_{\rm bg}$ from the cluster centre (right panel; with the exception of Pal 5, see below). In order to avoid crowding problems, we have included only a fraction of the central regions of the cluster confined between an arbitrary distance from the centre and the half-mass radius ($r_{\rm h}$), which generates the differences in limiting magnitude between the diagrams in some of the clusters (e.g. NGC 6229 and NGC 4590). The left panels display the

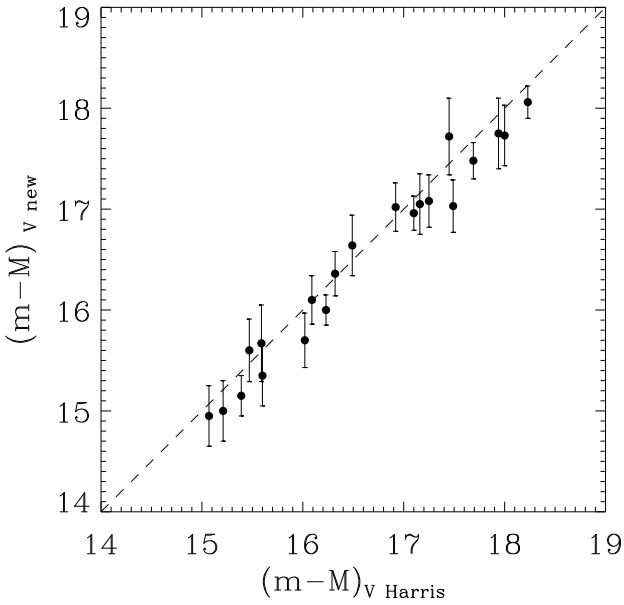


Figure 5.9: Comparison between the Harris (2010) distance modulii and the values derived using the isochrone fitting method described in Section 5.3.4. $(m-M)_{\rm V}$ and $(m-M)_{\rm VHarris}$ represent the distance modulus obtained for the GCs included in our sample and the one taken from the Harris catalog respectively. The dashed line indicates the 1:1 relation.

Table 5.3: Results from the isochrone fitting method described in Section 5.3.4. Areas observed, distances derived for the GCs and for the subjacent populations are given in the columns labeled with A_{bg}, d_{GC} and d_{bg} respectively. Significance of the detections S_T and S_B, with respect to TRILEGAL and Besançon respectively, are computed using the number of star counts in the observed CMD (N_{CMD}) and the counts for the same area of the diagrams obtained with the model considered here (N_T or N_B). The identity of the subjacent population is suggested in function of the projected position of the sample and the considered model. Clusters ordered by S_T.

Cluster	A_{bg} (deg^2)	d_{GC} (kpc)	d_{bg} (kpc)	N_{CMD}	N_T	N_B	S_T	S_B	Note
NGC 5634	0.21	25.7± 3.8	47.9 ± 4.7	190	36.2	50.1	10.2 ± 0.8	9.0 ± 0.9	Sgr
Whiting 1	0.31	25.4± 3.2	26.3 ± 3.3	181	35.2	20.3	10.0 ± 0.8	11.3 ± 0.7	Sgr
NGC 4147	0.23	21.6± 2.3	29.3 ± 4.9	254	95.7	88.2	8.5 ± 0.9	9.0 ± 0.9	Sgr
NGC 5053	0.17	13.2± 3.7	32.8 ± 5.3	86	10.0	29.4	7.8 ± 0.7	5.2 ± 0.9	Sgr
Pal 5	0.18	25.4± 2.9	52.8 ± 5.6	244	106.7	58.5	7.3 ± 0.9	10.7 ± 0.8	Sgr
			27.6 ± 3.8	108	24.6	34.2	7.2 ± 0.8	6.2 ± 0.9	Tail
NGC 7006	0.52	40.9± 2.1	22.3 ± 2.5	705	455.4	410.2	7.3 ± 1.0	8.8 ± 1.0	Her–Aq/?
NGC 7492	0.22	26.3± 2.1	22.0 ± 3.8	136	46.3	85.2	6.6 ± 0.9	3.4 ± 1.0	Sgr
NGC 1851	0.36	24.7± 2.0	11.9 ± 2.0	227	125.2	90.2	5.4 ± 1.0	7.7 ± 0.9	Mon?/GC Halo
NGC 1261	0.21	16.6± 2.0	14.9 ± 2.6	151	71.4	71.8	5.3 ± 1.0	5.3 ± 1.0	Tail?
NGC 5024	0.13	18.7± 2.0	37.7 ± 5.7	48	15.7	26.0	4.1 ± 0.9	2.6 ± 1.0	Sgr
NGC 7078	0.20	10.0± 1.7	14.4 ± 3.7	218	160.2	168.3	3.0 ± 1.0	2.5 ± 1.0	Her–Aq/?
NGC 1904	0.32	13.6± 2.1	15.4 ± 2.4	132	98.4	94.2	2.2 ± 1.0	2.5 ± 1.0	?/GC Halo
NGC 6229	0.24	35.0± 3.1	17.7 ± 3.2	98	71.9	82.2	2.0 ± 0.9	1.2 ± 0.9	Her–Aq/?

position of the stellar sources considered in our final photometric catalogs with respect to the position of the cluster centre. This provides a good reference for the sky area (in degrees; see Table 5.3) covered around each target in this work. The total area observed around each cluster was estimated taking into account the gaps between the chips at both instruments and the position of the cluster centre in the field.

The significance of the underlying populations by means of the comparison with a synthetic CMD from the TRILEGAL and Besançon Galactic models is shown in Table 5.3. The number of observed stars ($N_{\rm CMD}$) and the TRILEGAL and Besançon counts ($N_{\rm T}$ and $N_{\rm B}$ respectively) are used to calculate $S_{\rm T}$ and $S_{\rm B}$ using Equation 5.3. In Table 5.3 we show the derived heliocentric distances for their $r > r_{\rm bg}$ populations. Given that the S values depend clearly on the synthetic Milky Way model and the input parameters used (Table 5.3), our positive detections are compared with the results obtained from the application of the cross-correlation method to the region defined by $0.0 < B - R < 1.6$ and $18.0 < V < 24.0$ in the $r > r_{\rm bg}$ CMDs. According to these results, we group the clusters in the following categories:

- Group A: Clusters for which neither the comparison with Galactic models nor the cross-correlations return significant detections ($S < 5$; $S/N < 5$). These CMDs correspond to the clusters AM4, NGC1904, NGC 2298, NGC4590, NGC5024, NGC5272, NGC5466, NGC 5694, NGC 5824, NGC6229, NGC 6864, NGC 7078, Pal 15 and Rup 106. We refer to this group as "no detections".

- Group B: Clusters for which an overdensity with $S > 5$ is detected with respect one of the adopted reference Galactic field models and the CMD cross-correlation provides a good match with $S/N > 5$. The only cluster in this group is NGC7492. We refer to this group as "uncertain" detections.

- Group C: Clusters for which an overdensity with $S > 5$ using both reference Galactic field models is detected but the CMD cross-correlation provides an inconclusive result. The CMDs in this group correspond to NGC5053 and NGC7006. We refer to this group as "possible" detections.

- Group D: Clusters for which an overdensity with $S > 5$ using both reference Galactic field models is detected and the CMD cross-correlation identifies a distinct MS with $S/N > 5$ and pins its TO point. The CMDs in this group correspond to NGC 1261, NGC 1851, NGC 4147, NGC 5634, Pal 5 (twice) and Whithing 1. We refer to this group as "probable" detections. Their density diagrams are shown in Figure 5.16.

The distance moduli and heliocentric distances to the structures belonging to group D are calculated using the cross-correlation algorithm and the two possible isochrones mentioned above (either the one from the nearby GC or the one from

Table 5.4: Cross-correlation results for every field (both inner and outer). For every field we indicate whether there is a detection (D) or not (B), or if the field presents any problem for the method (A and C). For all the inner cases and the outer D cases, we include the cross-correlation MS TO point in the V band. For these fields we also provide the distance modulus and heliocentric distance (in kpc) as derived from two different theoretical isochrones: one representing the stellar population of the nearby GC ($d_{\mathrm{GC-iso}}$) and the other one representing that one of the Sgr stream ($d_{\mathrm{Sgr-iso}}$).

Cluster	Field	Group	S/N	$\mathrm{TO_V}$	$(m-M)_{\mathrm{V\ GC-iso}}$	$d_{\mathrm{GC-iso}}$	$(m-M)_{\mathrm{V\ Sgr-iso}}$	$d_{\mathrm{Sgr-iso}}$
am4	in		5.4	21.0	17.2	28 ± 2	17.2	28 ± 2
am4	out	A						
ngc1261	in		4.4	19.8	15.9	15 ± 1	16.0	16 ± 1
ngc1261	out	D	6.9	20.0	16.1	16 ± 2	16.2	18 ± 2
ngc1851	in		3.9	19.4	15.5	13 ± 1	15.6	13 ± 1
ngc1851	out	D	7.3	19.0	15.1	11 ± 1	15.2	11 ± 1
ngc1904	in		4.0	19.8	15.9	15 ± 1	16.0	16 ± 1
ngc1904	out	A	4.4	20.2	16.3	18 ± 2	16.4	19 ± 2
ngc2298	in		6.4	19.5	15.5	13 ± 1	15.7	14 ± 1
ngc2298	out	A						
ngc4147	in		6.7	20.5	16.6	21 ± 1	16.7	22 ± 1
ngc4147	out	D	5.0	21.9	18.0	41 ± 6	18.1	42 ± 6
ngc4590	in		4.5	19.1	15.4	12 ± 1	15.3	12 ± 1
ngc4590	out	A						
ngc5024	in		5.4	20.4	16.5	20 ± 1	16.6	21 ± 1
ngc5024	out	A						
ngc5053	in		4.9	19.9	16.1	17 ± 1	16.1	17 ± 1
ngc5053	out	C						
ngc5272	in		6.0	18.1	14.2	6.8 ± 0.3	14.3	7.3 ± 0.3
ngc5272	out	A						
ngc5466	in		5.9	19.9	15.9	15 ± 1	16.1	17 ± 1
ngc5466	out	A						
ngc5634	in		4.3	21.1	17.2	28 ± 1	17.3	29 ± 1
ngc5634	out	D	6.5	22.4	18.5	51 ± 9	18.6	53 ± 10
ngc5694	in		5.0	22.1	18.1	42 ± 2	18.3	46 ± 2
ngc5694	out	A						
ngc5824	in		4.9	22.1	18.1	42 ± 2	18.3	46 ± 2
ngc5824	out	A						
ngc6229	in		5.3	21.5	17.5	32 ± 2	17.7	35 ± 2
ngc6229	out	A						
ngc6864	in		4.7	20.9	17.0	26 ± 1	17.1	27 ± 1
ngc6864	out	A						
ngc7006	in		4.8	22.2	18.3	45 ± 2	18.4	48 ± 2
ngc7006	out	C						
ngc7078	in		4.1	19.8	15.9	16 ± 1	16.0	16 ± 1
ngc7078	out	A						
ngc7492	in		4.7	20.5	16.6	21 ± 1	16.7	22 ± 1
ngc7492	out	B	5.4	20.2	16.3	18 ± 2	16.4	19 ± 2
pal15	in							
pal15	out	A						
pal5	in		6.4	20.8	17.0	25 ± 1	17.0	25 ± 1
pal5	out	D	5.0	22.6	18.8	58 ± 6	18.8	58 ± 6
pal5	out	D	6.1	20.8	17.0	25 ± 2	17.0	25 ± 2
rup106	in		4.7	21.0	17.2	27 ± 1	17.2	28 ± 1
rup106	out	A						
whit1	in		5.4	20.8	17.3	29 ± 3	17.0	25 ± 2
whit1	out	D	5.2	20.5	17.0	26 ± 2	16.7	22 ± 1

the Sgr stream). The derived distances (Table 5.4) are consistent with those obtained using the isochrone fitting method given in Sec. 3.4, without any evidence of systematic offset or trend. We thus conclude that the cross-correlation method independently confirms (within the uncertainties) the distance measurements for the GCs classified as group D.

5.5 Discussion

5.5.1 Overdensities associated with the Sagittarius tidal stream

The stellar debris around clusters possibly associated with the Sgr tidal stream are, in general, the easiest cases to identify since the position and distance along the stream is well known from wide-sky surveys (Majewski et al. 2003; Belokurov et al. 2006b; Koposov et al. 2012) or numerous N-body simulations (Law & Majewski 2010b; Peñarrubia et al. 2010, hereafter P10). To check the possible presence of Sgr tidal debris in our sample, we overplot the position and distances of our sample to the Sgr tidal stream model presented by P10 in the (RA, Dec) and $(\ell, d_{\odot})$ planes (Figure 5.17). We find that 13 GCs of our sample lie within the projected position of the stream: Whiting 1, NGC 4147, NGC 4590, NGC 5024, NGC 5053, NGC 5272, AM 4, NGC 5466, NGC 5634, NGC 5694, Pal 5, NGC 6864 and NGC 7492. In addition to this comparison with theoretical models, we compare the projected position of these clusters with the MS star density map of this structure from the SDSS by Koposov et al. (2012). This shows that NGC 5466 and NGC 5272 are out of the projected path of the stream, which is consistent with our negative detections of tidal debris around these clusters. This could be also the case for NGC 6864, NGC 5694, NGC 4590 and AM 4 (see below).

Our survey around these Sgr stream GC candidates reveals the clear presence of "probable" tidal debris from this stream around four of these clusters (Whiting 1, NGC 4147, NGC 5634 and Pal 5; see CMDs in Figure 5.18) plus a "possible" debris around NGC 5053 and an "uncertain" debris around NGC 7492.

One of the most significant ($S_T, S_B > 10$) detections is unveiled in the area observed around the low-mass cluster Whiting 1, which was also suggested as member of the Sgr GC system by Carraro et al. (2007). The break in the radial stellar distribution found at ~ 6 arcmin (Carraro et al. 2007) suggests that this low-density cluster is currently going through a disruption process due to the forces exerted by the Milky Way. However, it seems unlikely that the highly contrasted MS discovered in the area close to the cluster ($B - R \sim 1$, $20.5 < V < 23$) shown in Figure 5.10, lacking of any collimated spatial distribution, was generated by stars that have (or are close to) left Whiting 1. We identify the subjacent system as the trailing arm of the Sgr tidal strem and the position of the cluster relative to the stellar over-densities associated with that halo substructure supports that scenario (Koposov et al. 2012).

The isochrone fitting shows that Sgr and Whiting 1 are spatially coincident, as also suggested by the cross-correlation results in Table 5.4. The confirmation of the association of such a young GC (6.5 Gyr; Carraro et al. 2007) will help to study

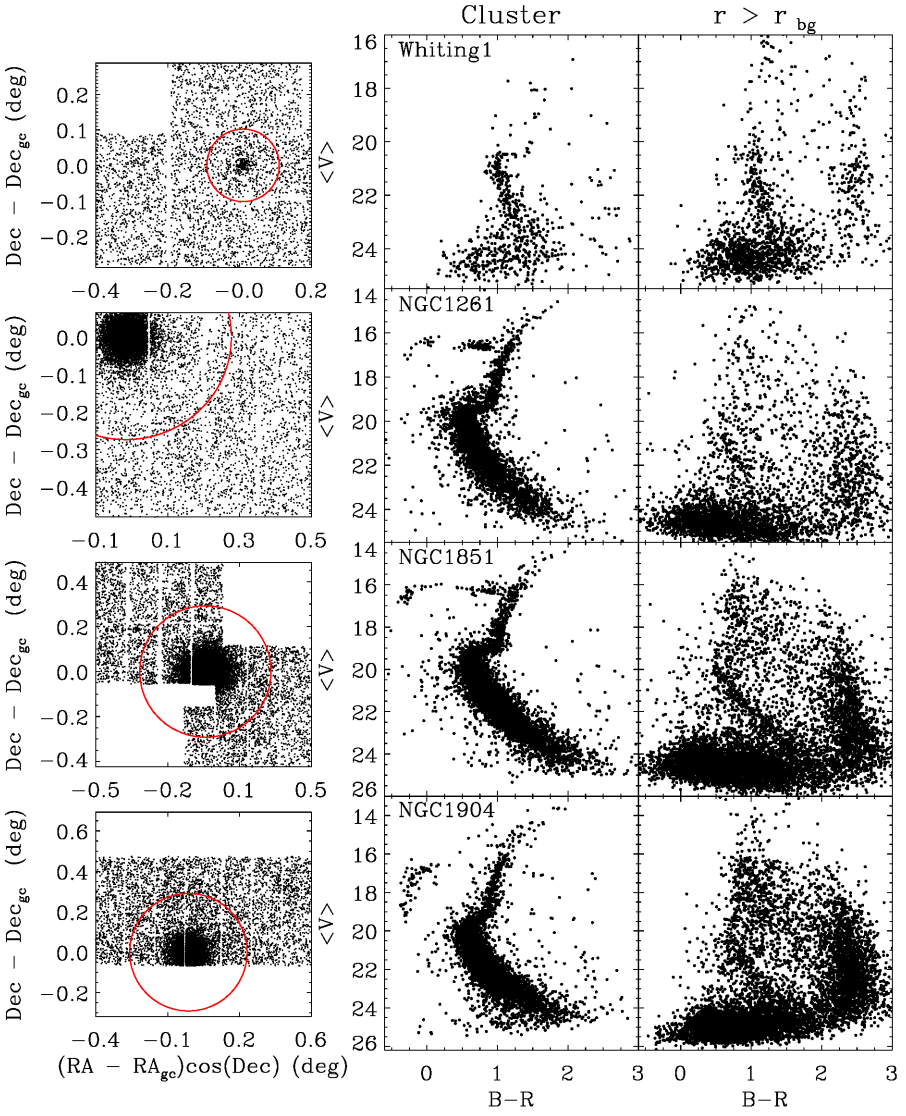


Figure 5.10: CMDs corresponding to the clusters Whiting 1, NGC 1261, NGC 1851 and NGC 1904 (middle column) and to those objects beyond $r_{\rm bg}$ from the cluster centre (right column). A map showing the distribution of the stars in the catalog with respect to the cluster centre is also included (left), where $r_{\rm bg}$ is indicated by a red line.

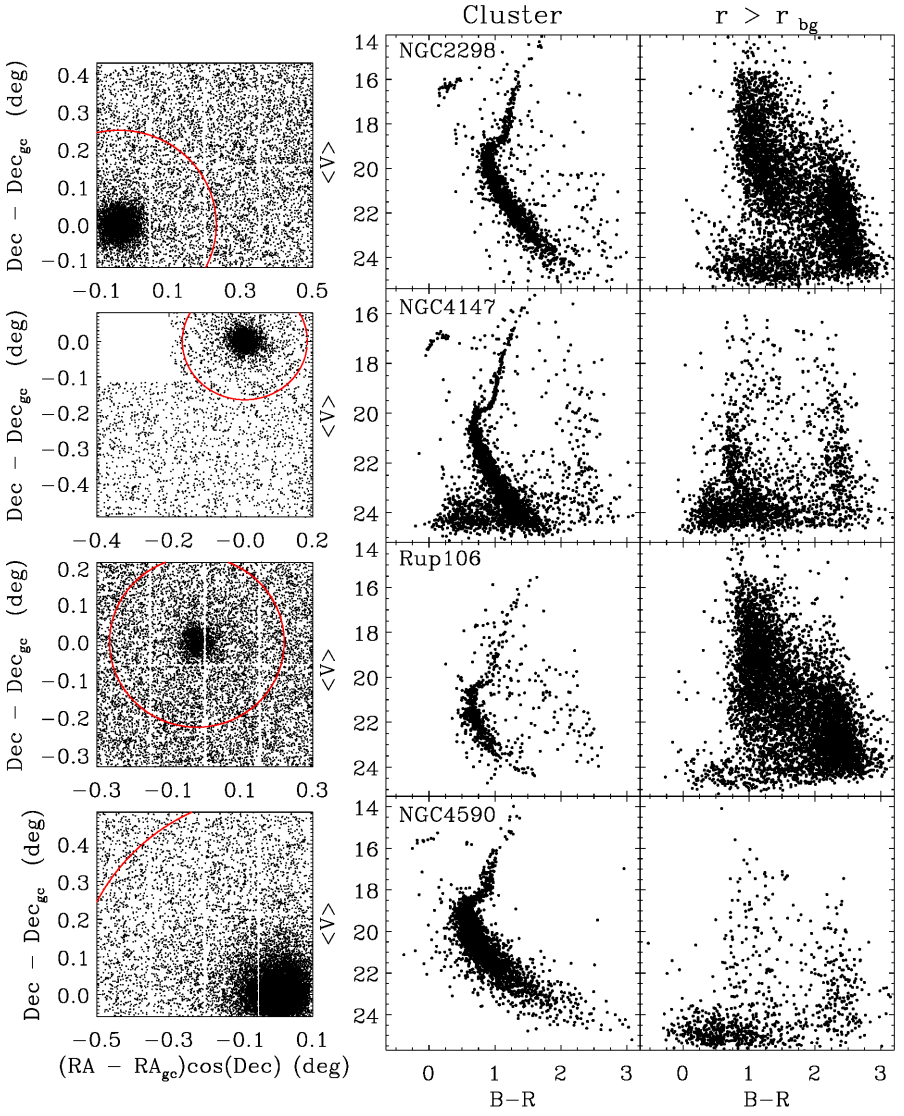


Figure 5.11: CMDs corresponding to the clusters NGC 2998, NGC 4147, Rup 106 and NGC 4590 (middle column) and to those objects beyond $r_{\rm bg}$ from the cluster centre (right column). A map showing the distribution of the stars in the catalog with respect to the cluster centre is also included (left), where $r_{\rm bg}$ is indicated by a red line.

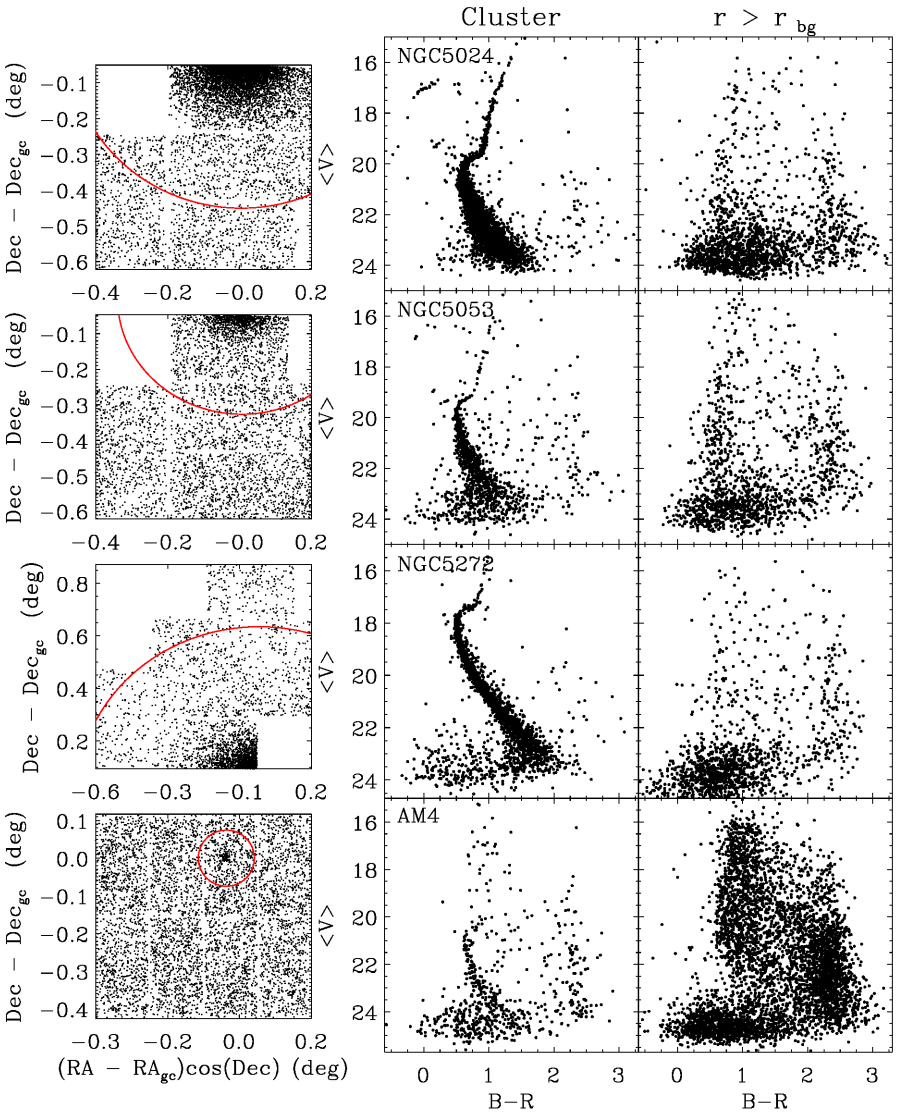


Figure 5.12: CMDs corresponding to the clusters NGC 5024, NGC 5053, NGC 5272 and AM 4 (middle column) and to those objects beyond $r_{\rm bg}$ from the cluster centre (right column). A map showing the distribution of the stars in the catalog with respect to the cluster centre is also included (left), where $r_{\rm bg}$ is indicated by a red line.

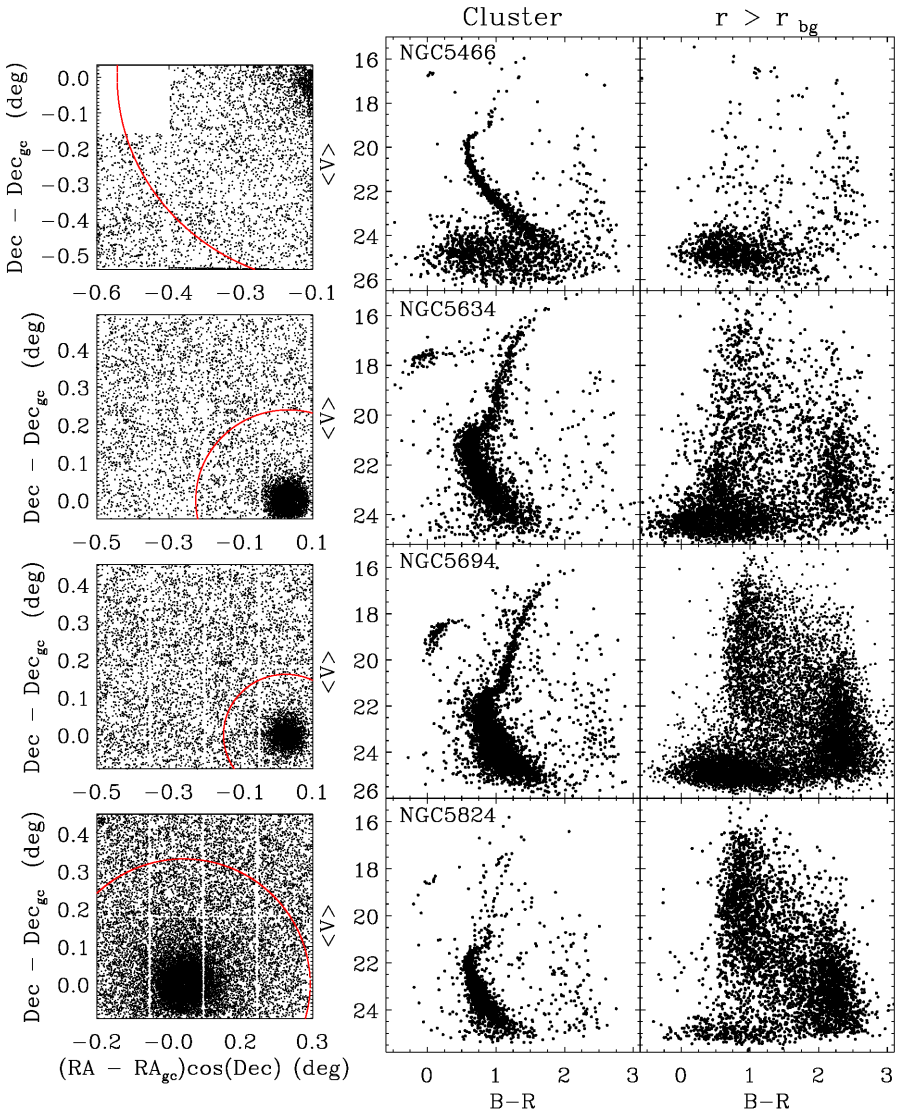


Figure 5.13: CMDs corresponding to the clusters NGC 5466, NGC 5634, NGC 5694 and NGC 5824 (middle column) and to those objects beyond $r_{\rm bg}$ from the cluster centre (right column). A map showing the distribution of the stars in the catalog with respect to the cluster centre is also included (left), where $r_{\rm bg}$ is indicated by a red line.

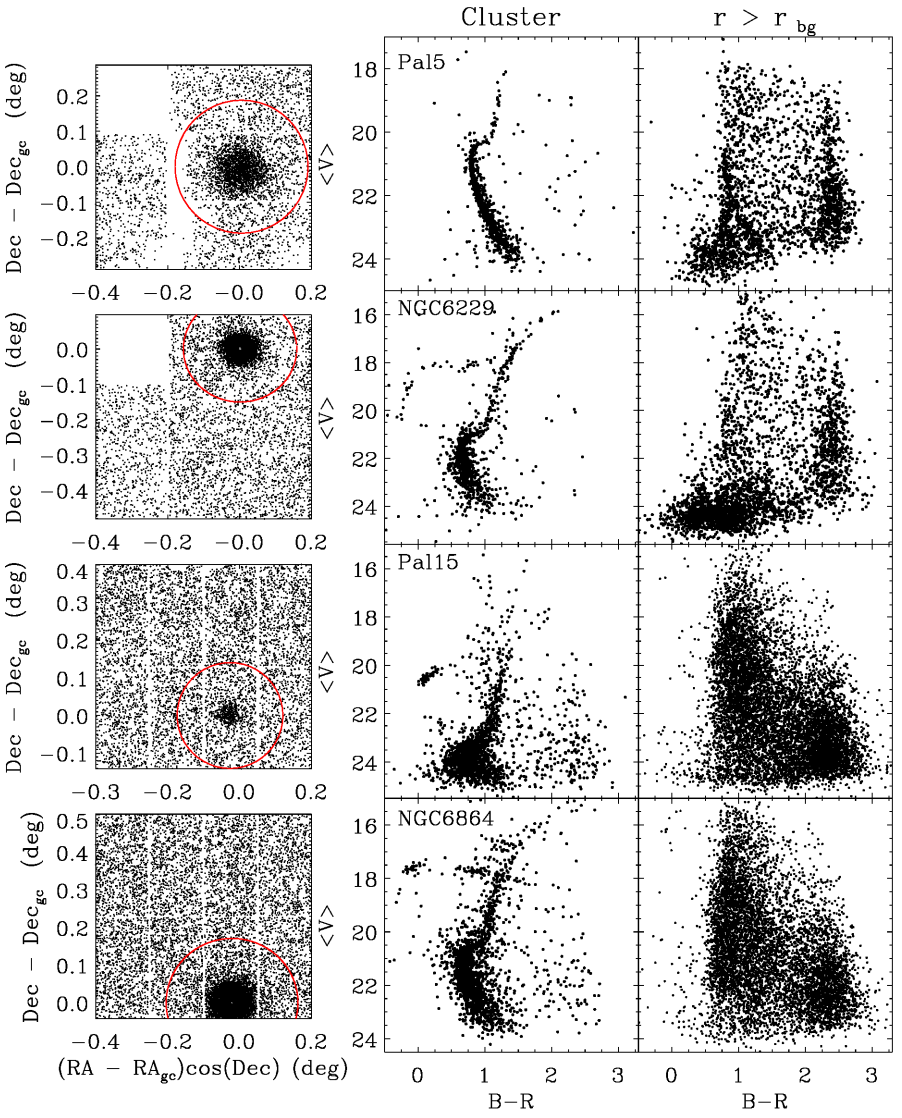


Figure 5.14: CMDs corresponding to the clusters Pal 5, NGC 6229, Pal 15 and NGC 6864 (middle column) and to those objects beyond $r_{\rm bg}$ from the cluster centre (right column). A map showing the distribution of the stars in the catalog with respect to the cluster centre is also included (left), where $r_{\rm bg}$ is indicated by a red line.

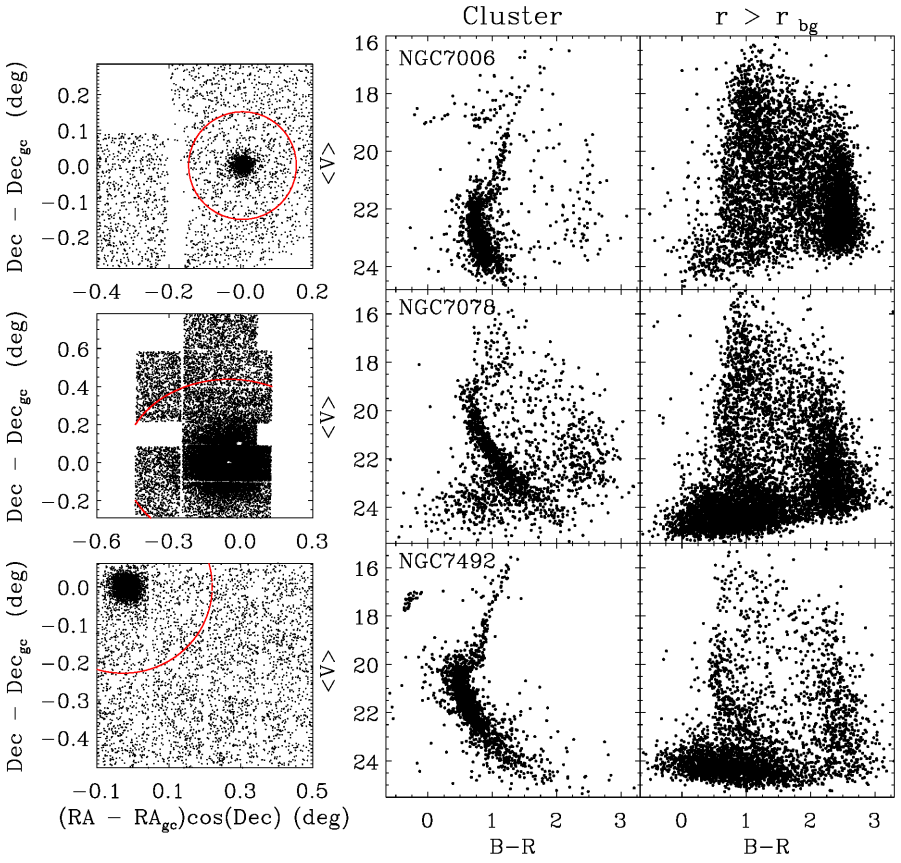


Figure 5.15: CMDs corresponding to the clusters NGC 7006, NGC 7078 and NGC 7492 (middle column) and to those objects beyond $r_{\rm bg}$ from the cluster centre (right column). A map showing the distribution of the stars in the catalog with respect to the cluster centre is also included (left). Note that in the case of NGC 7006, only one of the pointings has been included in that map, where $r_{\rm bg}$ is indicated by a red line.

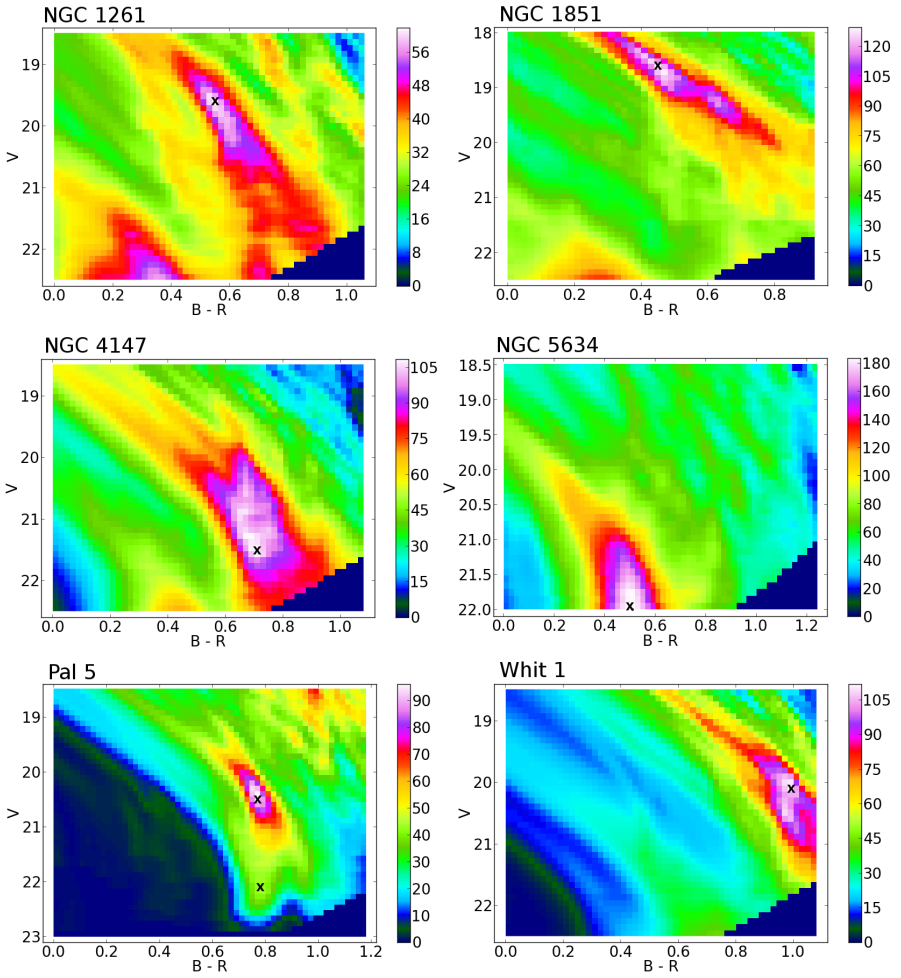


Figure 5.16: Density diagrams resulting from cross-correlating the CMDs of the outer regions with the MS template. From left to right and top to bottom: NGC1261, NGC1851, NGC4147, NGC5634, Pal 5 (twice) and Whiting 1.

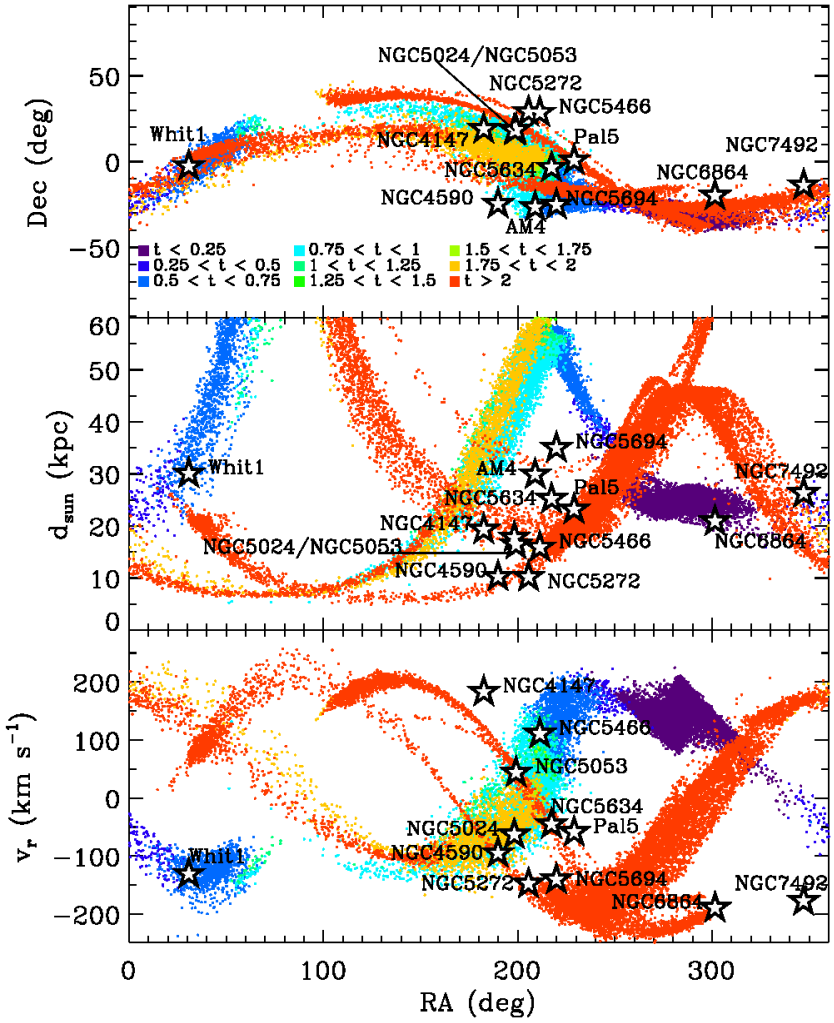


Figure 5.17: The Sgr tidal stream as presented in the model by P10. The upper panel shows the predicted orbit of the stream in the sky where the colour indicate different accretion times for the particles in ranges of 0.25 Gyr long. The middle and bottom panels show the heliocentric distance and radial velocity distribution of the stream, using the same colour scheme. The position and radial velocity of the globulars in our sample are over-plotted as stars. Only the fraction of the substructure with $d_{\odot} < 60$ kpc has been considered.

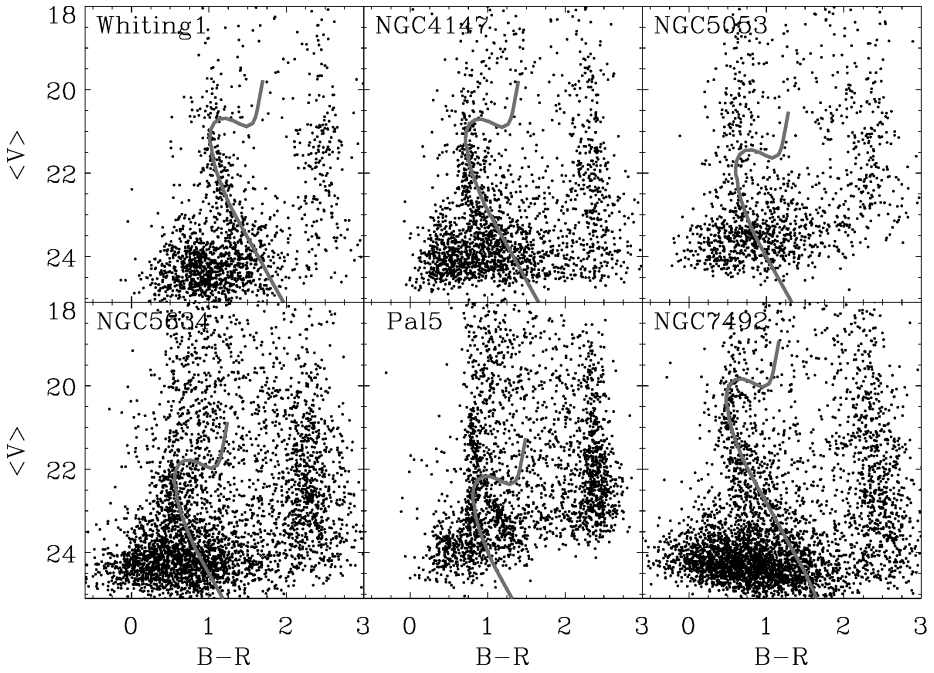


Figure 5.18: CMDs for the surrounding area of the GCs possibly associated with the Sgr tidal stream, with stellar over-densities that stand out in the comparison with the synthetic diagrams. The Sgr isochrone corresponding to the radial distance derived is over-plotted.

the GC formation process in Sgr, given that Whiting 1 might be the youngest GC among the clusters already associated with that dSph (~ 1 Gyr younger than the intermediate–age GCs Arp 2, Ter 7 and Pal 12, already associated to Sgr). This would indicate that Sgr was able to form GCs during a period of 6 Gyr as pointed by Carraro et al. (2007).

NGC 5634 is one of the closest clusters to the plane that contains the orbit of the Sgr dSph (L10) and stream stars were identified by Majewski et al. (2003) in that line-of-sight. Our photometry shows for the first time a CMD morphology compatible with that of the Sgr stream in the surroundings of this cluster. It however does not reveal any underlying population at a similar distance of this cluster. A more important contribution in the background is detected, at a distance nearly twice the distance to NGC 5634, as confirmed by both distance determination methods. On the basis of the P10 model, we identify that system in the background as a distant section of the leading arm of the Sgr tidal stream.

The CMD of Pal 5 presents the most complex morphology in our survey, displaying two MS-like features at different distances as shown in Figure 5.18. The first lies is a high significance stellar population in the background of Pal 5 at a similar distance of the cluster. These stars are likely cluster members populating the well-studied massive tidal tails emerging from this cluster (Odenkirchen et al. 2001; Rockosi et al. 2002; Grillmair & Dionatos 2006a). A second and significant ($S \sim 8$) MS is detected below the feature associated to the tidal tails (see Fig. 12 in Pila-Díez et al. 2014) at a radial distance compatible with that of the Sgr tidal stream according to P10. Interestingly, Sbordone et al. (2005) derived α-element abundances for Pal 5, resembling those obtained for M 54 and Ter 7, members of the Sgr GC system.

Bellazzini et al. (2003) argued for the association of NGC 4147 with the Sgr stream from its radial velocity and the detection of M giant Sgr stars around this cluster. The detection of a MS feature from the Sgr stream stellar population around NGC 4147 in our pencil-beam survey was already reported in Martínez-Delgado et al. (2004a), before the mapping of this structure with large-scale surveys (e.g. Majewski et al. 2003; Belokurov et al. 2006b; Koposov et al. 2012). We detect an underlying stellar population likely associated to that halo substructure at $d_{\odot} \sim 35$ kpc, separated from the GC along our line-of-sight by ~ 15 kpc, in agreement with the position of the leading arm predicted by P10. Our results indicate that this cluster is not immersed in the Sgr tidal stream, as also pointed out in Martínez-Delgado et al. (2004a), where the integrals of motions of both systems were analyzed. SDSS mapping has also showed that the path of the stream crosses the surroundings of NGC 5024 and NGC 5053, which are in the vicinity of NGC 4147 in projected position (see Koposov et al. 2012).

Around NGC 5053 (classified in the group C) we have found an over-density in its background CMD suggesting a subjacent population at ~ 40 kpc, compatible with the radial distances predicted by P10 for the Sgr leading arms on that direction of the sky. The significance for the over-density in NGC 5024 is $S < 5$. However, the cross-correlation method returns unconclusive or ambiguous detec-

tions in the case of both globulars, likely produced by the presence of blended populations in the diagrams, with a second MS possibly corresponding to a more distant wrap of Sgr with a low S/N. From these globulars, only NGC 5053 is presented by L10 as a genuine candidate to belong to the Sgr GC system.

NGC 7492 is the only cluster of our sample for which an "uncertain" detection of an underlying debris (group B) has been found, and it is one of the globulars with low probability of belonging to the Sgr GC system according to L10. We identified a subjacent MS feature at a distance compatible with that of the cluster, which is not predicted in the synthetic TRILEGAL CMDs, while the significance of such a feature drops below the adopted treshold when the Besançon model is adopted. With our photometry only, it is not possible to address the question of whether this detection is real or associated to tidal tails originating from the cluster. However, in the radial profile obtained for this cluster (see Carballo-Bello et al. 2012), the stellar density beyond $r_{\rm bg}$ (~ 14 arcmin) suggests the presence of a homogeneously distributed population. This suggests that the eventual underlying population is associated to a different system in the background of NGC 7492. Figure 5.17 shows that the projected position and distance of the most recent accreted fraction of the Sgr stream trailing arm ($t_{\rm accr} < 0.25$ Gyr) is compatible with the position of this globular. Interestingly, the region around this cluster falls in a sky area without SDSS data (see Figure 5.19), but with evidence of Sgr stars in its vicinity, which strenghtens the hypothesis that this GC is embedded in the Sgr stream.

The negative detections in the surroundings of the other candidates prevent us from obtaining a final conclusion about the possible association of those clusters with the Sgr tidal stream, within our surface-brightness detection limits. Among them, only AM 4 has been suggested as member of the Sgr GC system by Carraro (2009) but, according to the background CMD obtained, there is no evidence of a subjacent stellar population associated to that stream. These negative detections, even in cases where the projected positions are favouring the detection of Sgr stream stars spatially coincident with the globulars (e.g. NGC 5053 or NGC 5634), might be used to establish the limitations of our photometric survey. Indeed, the absence of tidal remnants might be related to the evolution of the Sgr dSph and its interaction with the Milky Way. According to the model of P10, while Whiting 1 and NGC 7492 are spatially coincident with the Sgr stars accreted in the last 0.75 Gyr, NGC 5053, NGC 5634 and Pal 5 are surrounded by the material accreted from the satellite > 2 Gyr ago. This is a consequence of the fact that sections of the stream generated a long time ago are more dispersed, with a lower surface-brightness, and only the most recent arms of the Sgr tidal stream could be detected by our survey . This scenario is also valid for Pal 12, a cluster previously associated to Sgr by Martínez-Delgado et al. (2002), which in the context of the P10 model seems to be associated with the section of the stream accreted in the last 0.75 Gyr.

In the bottom panel of Figure 5.17 we compare the predicted radial velocity of the stream with those values measured for the clusters in our sample (Harris

2010). The globulars that are kinematically compatible and coincident with the position of the P10 tidal stream are Whiting 1, NGC 5053, NGC 5634 and Pal 5 (suggested as members of the Sgr GC system by L10). On the other hand, there is a difference of $\Delta v_{\rm r} \sim 100\,{\rm km\,s^{-1}}$ in the case of NGC 7492. So, for this stellar system, cluster and stream seem to be independent systems, although the orbit and structure of the Sgr stream in the southern sky are not well constrained because of the lack of a deep full-sky photometric database as the one available in the northern hemisphere (see discussion in L10, P10). Further follow-up spectroscopy is required to investigate the nature of the stellar population discovered around NGC 7492.

5.5.2 Other over-densities

The analysis of the CMDs corresponding to the GCs not associated with Sgr suggests the presence of MS features likely associated with subjacent stellar populations in three of them: NGC1261, NGC1851 and NGC7006. In this section, we discuss the possible origin of these tentative remnants and their possible association with other known over-densities or stellar streams already reported in the Milky Way.

An extended stellar over-density around NGC 1851?

One of the most conspicuous over-density of our survey, not associated with the Sgr stream, was detected around NGC 1851, first discovered by Olszewski et al. (2009), who interpreted this featuare as an *extended halo* surrounding this cluster up to distances of 75 arcmin ($\sim 6.5 r_{\rm t}$) from the cluster centre, and independently reported by (Carballo-Bello & Martínez-Delgado 2010).

NGC 1851 is one of the most interesting candidates in our sample because of its multiple stellar populations (Milone et al. 2008; Han et al. 2009) and the well-studied star-to-star abundance variations (e.g. Milone et al. 2009; Zoccali et al. 2009; Carretta et al. 2010, 2011; Campbell et al. 2012; Carretta et al. 2012), which suggest a scenario in which this cluster is the result of the merging of two previous GCs, formed in the nucleus of an accreted dwarf galaxy (Carretta et al. 2010; Bekki & Yong 2012). This cluster is member of a group of GCs formed by NGC 1851, NGC 1904, NGC 2298 and NGC 2808, which seems to be confined in a *sphere* with a radius of 6 kpc. That spatial distribution resembles that of M 54, Terzan 7, Terzan 8 and Arp2, globulars found in the main body of the Sgr dSph (Bellazzini et al. 2004; Martin et al. 2004). In addition, all 4 clusters show extended HB morphologies in their CMDs, feature that has been suggested as an indicator of an extra-Galactic origin in GCs (Lee et al. 2007).

Figure 5.10 shows the presence of the prominent MS population in the surroundings of this cluster, which is the same reported by Olszewski et al. (2009). This feature is not predicted by the TRILEGAL or Besançon models and it is also detected when the cross-correlation method is used (Table 5.4) at a similar heliocentric distance than the cluster. Using low resolution spectra for a sample of 107 stars selected from the same photometry presented in this work, Sollima

et al. (2012) detected a unexpected distinct stellar component with a radial velocity distribution that cannot be associated neither with the Galactic velocity field nor NGC 1851 outliers, with a mean difference with respect to those components of $\Delta v_{\rm r} \sim 150$ km s^{-1} and $\Delta v_{\rm r} \sim 200$ km s^{-1}, respectively. These authors discuss the possible association of this feature with the Monoceros ring, showing that the observed velocity distribution and the prediction made by the P05 model for that ring-like structure are slightly different, although not completely inconsistent given the uncertainties in the adopted Galactic potential. However, a recent spectroscopic analysis by Marino et al. (2014) analysed a set of medium-resolution spectra for a sample of stars in the outer halo of NGC 1851 reporting the lack of any significant over-density of stars at the velocity of such supposed stream. Summarizing, with the present dataset it is not clear if the detected over-density is linked to the precence of an extended halo of cluster member stars (as suggested by Olszewski et al. 2009) or to a subjacent stream (possibly the Monoceros ring). Deep data extending over a wider FOV are needed to distinguish between these two hypotheses.

NGC 7006

NGC 7006 is a cluster slightly younger than other similar clusters in the inner Galaxy (Dotter et al. 2011). In addition, this GC is one of the most energetic clusters in the Milky Way with a very eccentric orbit (Dinescu et al. 2001), suggesting and extra-Galactic origin for that system. Figure 5.15 show the presence of a significant MS feature in the outer region of NGC 7006 (first reported in Martínez-Delgado et al. 2004a). Since our cross-correlation method fails to detect these features due to the crowding of the fields (this cluster is classified in the group C), our distance estimates are only based on isochrone fitting (Table 5.3). Our results show that the hypothetic subjacent stellar population is at different distance from the cluster. In particular, we derived a difference in distance of $\sim$ 8 kpc for this possible tidal debris from the main body of NGC 7006. However, an inspection of the CMD of this cluster (Figure 5.15) shows that the MS TO of this feature is severely affected by the presence of bright Milky Way disc stars at $V \sim$ 20–21, making the estimate of its position very uncertain. Therefore, we believe that this population lies at a distance $d_{\odot} = 15 - 20$ kpc.

Figure 5.19 shows a stellar density map of MS-stars in a region of the sky from the SDSS photometric database, which includes both NGC7006 and NGC7078 (marked as open circles). These globulars seem to be inmersed in a region of high density of halo stars, that extends up to Galactic latitudes $b \sim -40°$ (see also Deason et al. 2014) and that might be the best explanation for the presence of this feature in the CMD of NGC7006. However, an accurate model for the shape of the stellar halo is needed to confirm this possibility.

An alternative scenario might be the presence of the southern component of the Hercules–Aquila over-density in the positions of this cluster. Recent results by Simion et al. (2014) supports the presence of a prominent over-density of RR Lyrae stars associated to this vast over-density in this region of the sky, with a distance

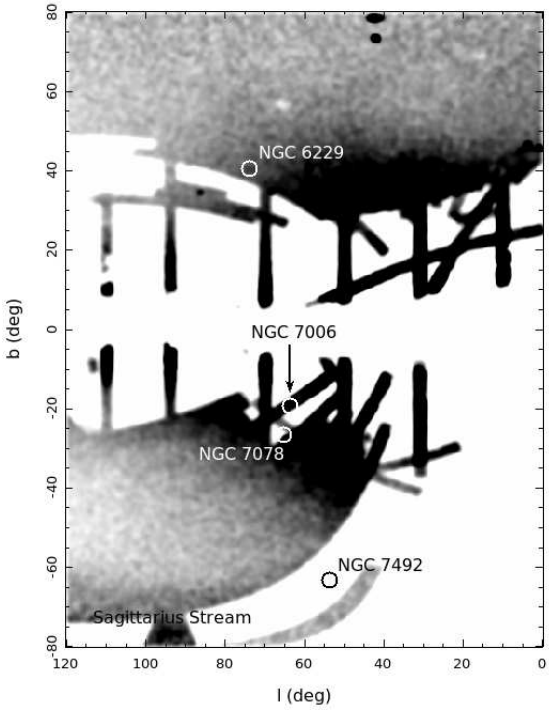


Figure 5.19: Density maps generated from SDSS data of the sky area where the GCs NGC 6229, NGC 7006, NGC 7078 and NGC 7492 are located. The huge stellar overdensity observed might be associated whether with the Hercules-Aquila cloud (Belokurov et al. 2007a; Simion et al. 2014) or with the region of higher density of halo stars reported by Deason et al. (2014). Note the presence of the Sgr stream in the bottom left corner of the map.

range of $10 < d_{\odot} < 25$ kpc (see their Fig. 9), strengthing the hypothesis of its origin from the tidal disruption of an ancient dwarf galaxy. That distance range is compatible with the one derived from our CMDs and suggests that NGC 7006 might be well embedded in (and possibly associated to) this giant cloud of debris. Interestingly, Simion et al. (2014) also found that the Hercules–Aquila cloud is barely visible as a RR Lyrae over-density in the northern hemisphere, suggesting that this cloud is possibly not symmetric with respect to the Galactic plane. This is consistent with the low significance overdensity ($S < 2.5$) of this component in the surroundings of NGC 6229 (see Figure 5.14).

NGC 1261

NGC 1261, lies in a projected position aligned with two other massive GCs showing an extended-HB morphology in their CMDs, NGC 1851 and NGC 1904. Around this cluster we have unveiled a stellar population (see Figure 5.10) that stands out significantly when the background diagram is compared with the ones generated with the considered Galactic models and it is also apparent in the results obtained through the cross-correlation method (see Table 5.4). The radial distance to the underlying component is similar to that of the cluster, suggesting that either it is composed of cluster members or of an unknown stellar population. The possible relation with the group of clusters described in Section 5.5.2 encourages to explore the area between NGC 1261 and those GCs.

5.5.3 Negative detections

There are no signatures of the presence of significant subjacent populations around the remaining candidates (AM4, NGC1904, NGC 2298, NGC4590, NGC5024, NGC5272, NGC5466, NGC 5694, NGC 5824, NGC6229, NGC 6864, NGC 7078, Pal 15 and Rup 106) as we find no evidence of distinct stellar population concentrated at a specific distance within the probed colour-magnitude range using both the cross-correlation and the isochrone fitting methods. The photometric non-detection of tidal debris around the halo GCs in this study is an important result to consider in the context of hierarchical stellar halo assembly theories. Whether or not such non-detections can rule out an accretion origin for these GCs (and a portion of the Milky Way stellar halo) depends on two main factors: 1) how massive were the progenitor dwarf galaxies these GCs were accreted with, and 2) when were these dwarf galaxies and their GCs accreted into the Milky Way? Indeed, GCs hosted in low luminosity dwarfs which were accreted early, may show minimal associated stellar debris when observed at present.

5.6 Conclusions

We have presented the wide-field photometry of 23 Galactic GCs in the Galactocentric distance range $10 \leq R_{\rm G} \leq 40$ kpc, searching in their surroundings for the stellar remnants of their accreted dwarf galaxy progenitors. We have detected a subjacent stellar populations beyond 1.5 times the $r_{\rm t}$ from the centre of 6 out the 23 GCs in our sample, and for three other clusters we found hints of possible

debris. These populations are in some cases consistent with known streams in the same line-of-sight of the GCs, while in other cases these over-densities might be associated with extended halos or tidal tails. Unfortunately our data do not cover a region wide enough to detect the full extension of the observed overdensities and their symmetry with respect to the cluster centre.

We identify the Sgr tidal stream in the direction of 6 GCs in our sample (4 "probable", 1 "possible" and 1 "uncertain" detection) and at distances compatible with the P10 orbital model. However, the heliocentric distances to the subjacent populations are consistent with those of the related GCs only for 2 of them (Whiting 1 and NGC 7492). Around NGC4147, NGC 5634 and Pal 5 (and with a smaller level of significance NGC 5053), previously suggested as members of the Sgr GC system, there are no significant detections corresponding to the same cluster distance, although the signature of the Sgr MS is visible as a background feature. These negative detections might be related with our ability of unveiling faint subjacent tidal streams (at $\mu_V > 32\,\mathrm{mag\,sec^{-2}}$). It is possible that these globulars were accreted from the Sgr dSph a long time ago and the surface-brightness of the tidal remnants lies beyond our detection threshold above the fore/background populations. On the contrary, Whiting 1 and NGC 7492 seem to be immersed in the most recently accreted fraction of the stream ($< 0.75\,\mathrm{Gyr}$). Follow-up spectroscopy is needed to confirm the nature of the stellar population revealed by our photometry, more importantly in the latter case, where the detection is more uncertain and there exists a significant deviation between the radial velocities of the cluster and the prediction of the model by P10.

A subjacent stellar population has been also unveiled in the surroundings of NGC 1851, NGC1261 and (possibly) NGC7006. These clusters lie far from the Sgr predicted orbit and could be therefore related to other streams like the Monoceros ring (NGC1851) the Hercules-Aquila cloud (NGC7006) or other unknown debris.

Acknowledgements

Based on observations made with the Isaac Newton Telescope operated on the island of La Palma by the Isaac Newton Group in the Spanish Observatorio del Roque de los Muchachos of the Instituto de Astrofísica de Canarias and with 2.2 m ESO telescope at the La Silla Observatory under programme IDs 072.A-9002(A), 082.B-0386, 084.B-0666 and 085.B-0765. JC-B received partial support from Centre of Excellence in Astrophysics and Associated Technologies (PFB 06). AS acknowledges the PRIN MIUR 2010-2011 "The Chemical and Dynamical Evolution of the Milky Way and Local Group Galaxies" (PI. Matteucci). RL acknowledges financial support to the DAGAL network from the People Programme (Marie Curie Actions) of the European Unions Seventh Framework Programme FP7/2007- 2013/ under REA grant agreement number PITN-GA-2011-289313. R. R. M. acknowledges partial support from CONICYT Anillo project ACT-1122 and project BASAL PFB-06 as well as FONDECYT project N°1120013. JMC-S acknowledges financial support to CONICYT through the FONDECYT Postdoc-

toral Fellowship N°3140310. We warmly thank the anonymous referee for his/her helpful comments and suggestions. We thank J. Peñarrubia for allowing us to use the model of the Sagittarius tidal stream for this work. Thanks to A. Robin for her useful comments about the Besançon model. Thanks to A. Aparicio, S. Hidalgo, R. Carrera and D. C. Bardalez-Gagliuffi for their participation in the observing runs.

Chapter 6

Search for halo substructure in KiDS

Authors

B. Pila-Díez, J.T.A. de Jong, K. Kuijken and the KiDS consortium

Abstract

We use data from the data release 1 and data release 2 from the Kilo Degree Survey, a public survey at the ESO VLT Survey Telescope, to map the halo using near main sequence stars and red clump stars. We search for stellar overdensities at different distance or magnitude ranges, aiming to detect new satellites or tidal debris. We recover broad structures like the Sagittarius stream (both in the northern and in the southern hemisphere), the Eastern Band Structure, the Virgo Overdensity and part of the Galactic disk, and we also identify a piece of the Palomar 5 tails. Using Colour Magnitude Diagrams and derived stellar density maps, we test several candidate narrow overdensities for both colour-magnitude and spatial coherence, but conclude that none of the candidates is a real satellite or a piece of cold accreted substructure.

6.1 Introduction

The search for satellites and for tidal remnants is one of the main goals of Galactic halo studies, since they provide a look both into the current accretion history of the Galaxy and into the star formation history of the satellite or the progenitor. They can also provide constraints on the mass and shape of the dark matter halo. Additionally they help set constraints on the Λ-Cold Dark Matter cosmological model and serve as a test bench for its predictions.

In the last decade, many satellite galaxies have been discovered, and the first cold stellar streams in the halo of the Galaxy have been revealed. This has been possible thanks to the advent of deep multi-colour large area surveys such as 2MASS, SDSS, Pan-STARRS, DES and others. 2MASS was particularly successful in tracing with red giant stars the two tails of the Sagittarius stellar stream wrapping at least 180 deg each around the galaxy (Majewski et al. 2003). SDSS has uncovered a wealth of new satellite galaxies (Belokurov et al. 2007c; Zucker et al. 2006) and a myriad of streams, associated both to dwarf galaxies (Belokurov et al. 2006b; Grillmair 2006a; Newberg et al. 2010) and to globular clusters (Odenkirchen et al. 2001; Grillmair & Dionatos 2006a; Grillmair & Johnson 2006). Pan-STARRS, on the other hand, has discovered one thin cold stream (Bernard et al. 2014). And the PAndAS survey —which targeted M31's halo— has probed at least five stellar structures in the Milky Way's halo along the line of sight to the Andromeda galaxy: the Monoceros ring, the Pisces/Triangulum globular cluster stream and three structures possibly associated to the Triangulum/Andromeda overdensity (Martin et al. 2014). Most recently, DES has reported the discovery of 9 new satellites in the Southern sky (The DES Collaboration et al. 2015; Koposov et al. 2015), and last year ATLAS also unveiled a new stream in the Southern sky (Koposov et al. 2014).

The Kilo Degree Survey (KiDS), is one of three public surveys currently underway on the ESO VLT Survey Telescope (VST). It is designed to map the large scale dark matter distribution through weak gravitational lensing, and is currently scanning the sky to cover 1500 $\deg^2$ to a depth approximately 2 magnitudes fainter than SDSS. Most of the planned footprint of KiDS targets the Southern hemisphere of the sky which, for logistic reasons, has not been as extensively surveyed as the Northern hemisphere thus far. Ongoing surveys in the South—such as KiDS itself but also ATLAS and DES—are now reporting first results. With the first data releases, KiDS DR-1 and DR-2, now available, it is time to start testing the data set and explore the halo for signs of substructure.

In this chapter we briefly review the observations, survey strategy and data processing of KiDS (section 6.2), describe the techniques we have used to search for new substructure (section 6.3.1), present recovered substructures and candidate overdensities (section 6.3.2) and discuss our results as well as the future prospects (section 6.4). Finally we summarize the main ideas of the work in section 6.5.

6.2 Observations and data processing

The Kilo Degree Survey (de Jong et al. 2013, KiDS) is an optical broad-band multi-filter survey (u, g, r, and i) with the VST, imaging 1500 deg^2 over a northern and a southern field. The field of view of its individual pointings is $1 \times 1\,\mathrm{deg}^2$ with an image quality between $0.7''$ for the r band and $1.1''$ for the u band (PSF FWHM). It reaches limiting magnitudes of 24.3 in u, 25.1 in g, 24.9 in r and 23.7 in i, making it 1.5 to 2.0 magnitudes deeper than SDSS or ATLAS.

In this work we use the images from the first and second public data releases (DR), a total of 148 square degrees. The sky footprint for these DR-1 and DR-2 images is shown in Fig.6.1.

The PSF is homogenized across each image in order to be able to obtain accurate shapes, PSF-corrected matched-aperture photometry, improved colours and a refined star-galaxy separation. We produce photometric catalogues using the "Gaussian Aperture and PSF" (GAaP) code described in section 2.1 of chapter 3, and use the flux ratio between two apertures in the r band ($0.5''$ and $0.7''$) to separate (Gaussian) stars from (more extended) galaxies. We correct for interstellar extinction using the Schlegel et al. (1998) dust maps and we cut the source catalogues at a magnitude limit of $r < 23.2$ mag to avoid small, round, faint galaxies. Finally, we correct the photometry for a seeing-dependency and transform the KiDS magnitudes to the SDSS system.

Finally, from these catalogues we select near main sequence turnoff point (nearMSTO) stars, red clump (RC) stars and blue horizontal branch (BHB) stars following the prescriptions in Pila-Díez et al. (2015) (chapter 2), Correnti et al. (2010) and Belokurov et al. (2014) (after Yanny et al. (2000) and Deason et al. (2011)), respectively. We note that the RC sample may suffer contamination from K0-K2 main sequence field stars, and may be locally enhanced if a main sequence overdensity is present. This precludes us from directly inferring distances for the RC sample but, nonetheless, it does not prevent us from using the sample in search for spatially localized overdensities in the apparent magnitude space.

More details on the survey, on the data processing, on the production of the stellar catalogues and on the photometric transformations described above can be found in chapter 3.

6.3 Search for overdensities

6.3.1 Methodology

We use the nearMSTO, the RC and the BHB stars catalogues to build stellar maps and stellar density maps for different distance or magnitude ranges. The BHB maps result in very few counts with no clear overdensities, so we do not use them further. On the other hand, the nearMSTO and the RC maps return sufficiently populated maps to be used in the search for spatial enhancements. The distance-sliced stellar and stellar density maps for the nearMSTO stars in the different KiDS fields are shown in figures 6.6 to 6.9. We present the star density in eight

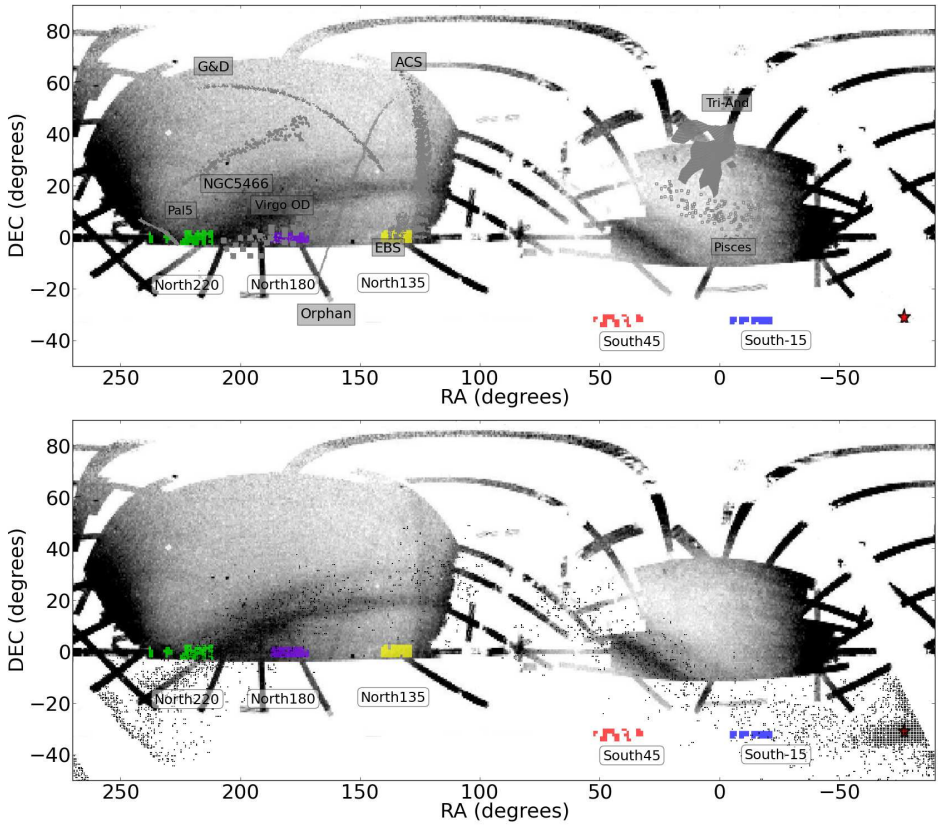


Figure 6.1: Top panel: equatorial map showing the KiDS DR-1 and DR-2 footprint (in colour) and several of the halo stellar streams (grey scale). Bottom panel: equatorial map showing the KiDS DR-1 and DR-2 footprint (in colour) together with the Sagittarius stream as seen by SDSS (background image) and by 2MASS (scattered black dots). The SDSS density map is from Koposov et al. (2012) while the 2MASS data are from Majewski et al. (2003). The red star indicates the position of the stream's progenitor, the Sagittarius dwarf galaxy.

Table 6.1: KiDS fields of view as shown in Figure 6.1. The table indicates the total area probed by KiDS DR-1 and DR-2 for each field and the a factor used to calcualte the kernel's bandwidth for the stellar density maps. Parameter a is a magic number chosen to optimize the granularity of the density maps.

Group	a	*Area* (deg^2)
KiDS-North220	4.8	29
KiDS-North180	6.6	37
KiDS-North135	5.4	37
KiDS-South45	3.6	14
KiDS-South-15	14.1	16

distance slices (from $[10, 15]$ kpc to $[40, 55]$ kpc) in two forms: i) scatterplots showing individual stars, and ii) density maps built with a k-Nearest Neighbours algorithm that uses a gaussian kernel with spatially variable bandwidth. The bandwidth is tailored to each KiDS field, and is calculated as $a/std(map)$, where a is a constant (see table 6.1) and $std(map)$ is the standard deviation of the stellar counts in that field at the specific distance range of each map. The density for each map is normalized over the mean density for that particular field and distance range, resulting in a pixel by pixel signal-to-background function.

On these maps we look for two things: first, we look for broad density gradients across the maps, as a sign of large substructures spanning several degrees in width and length. Second, we look for specific small overdensities spanning only a few degrees in width (if they are elongated) or in diameter (if they are rounded). We request these features to have high signal-to-background values and to fade out into more than one distance slice.

For the large gradients and structures, we look for a spatial overlap with known overdensities given that most of our continuous coverage is in the North fields (where SDSS has already probed the halo). This helps us identify the overdensities. We also produce magnitude (distance) vs RA maps for the North and the South fields as a way to recover again these features and trace their evolution along RA (Figures 6.12 to 6.15).

For the candidate small overdensities, we plot the individual CMD of the tile where each one is located and look for distinct main sequences or red clumps. A plot of the positions of just these stars in an equatorial map of the tile can then be used to assess whether this is a distinct object or a chance enhancement. Results of our analysis of the most promising overdensities are presented in Table 6.2).

6.3.2 Results

We identify large structures in all the KiDS fields except in KiDS-South45. In particular, Figure 6.12 and 6.13 show the Eastern Band Structure (Li et al. 2012, EBS) in KiDS-North135, the Virgo Overdensity (Bonaca et al. 2012b) in KiDS-North180 and both the Galactic disk and the Sagittarius stream in KiDS-

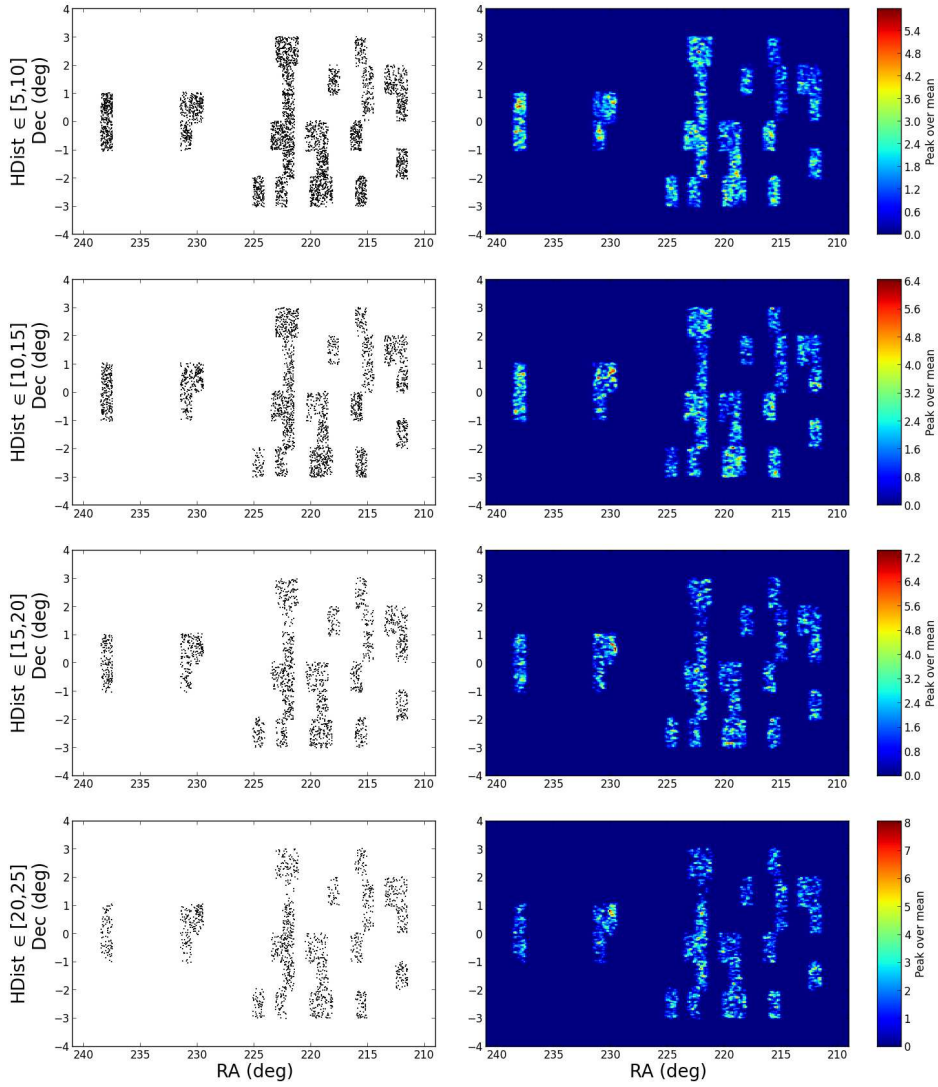


Figure 6.2: Stellar scatter maps and stellar density maps for the closest distance slices in field KiDS-North220.

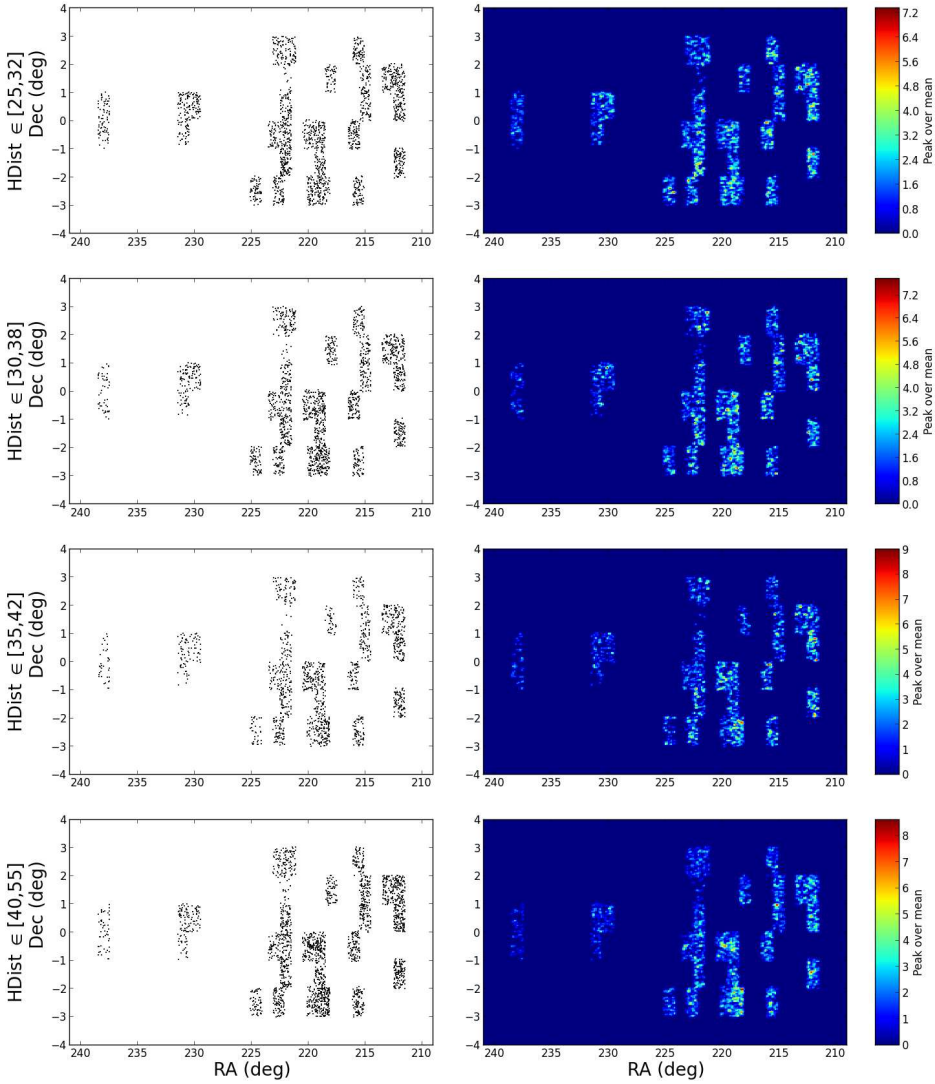


Figure 6.3: Stellar scatter maps and stellar density maps for the furthest distance slices in field KiDS-North220(continuation of Figure 6.2).

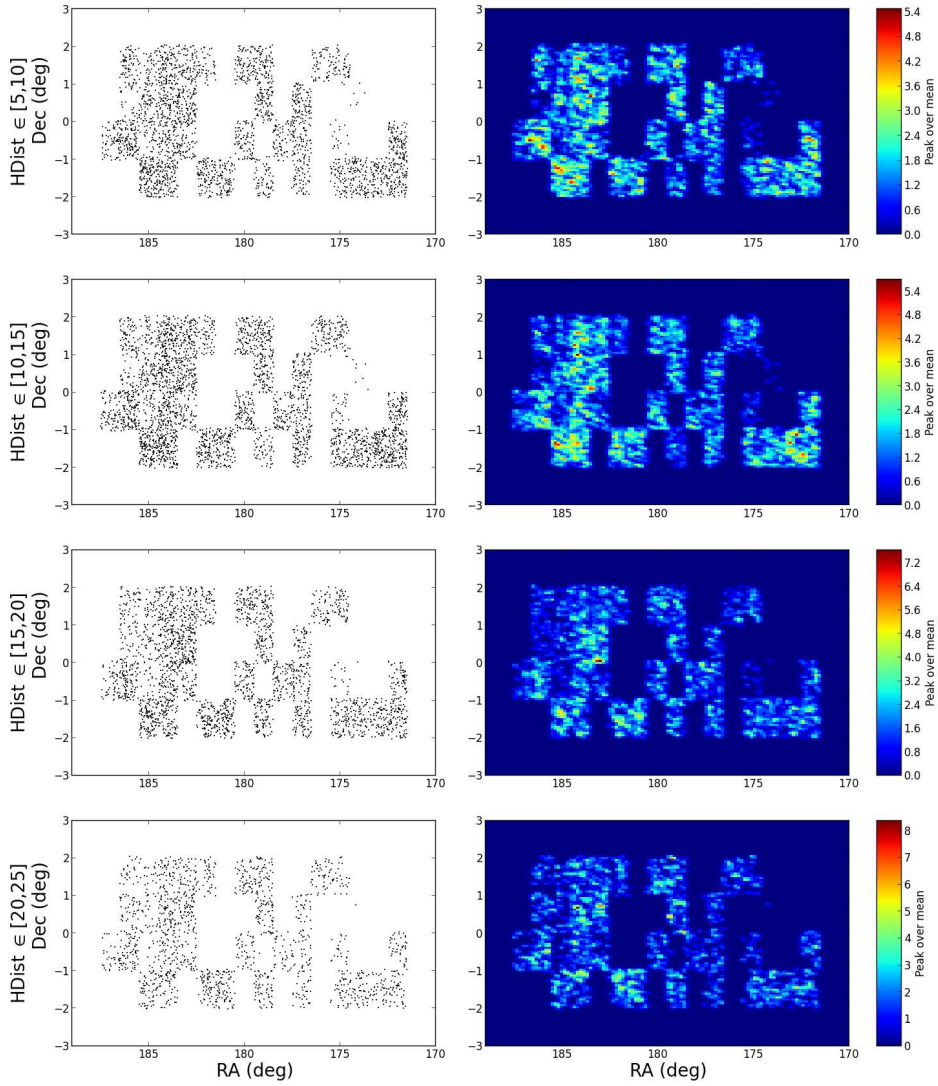


Figure 6.4: Stellar scatter maps and stellar density maps for the closest distance slices in field KiDS-North180.

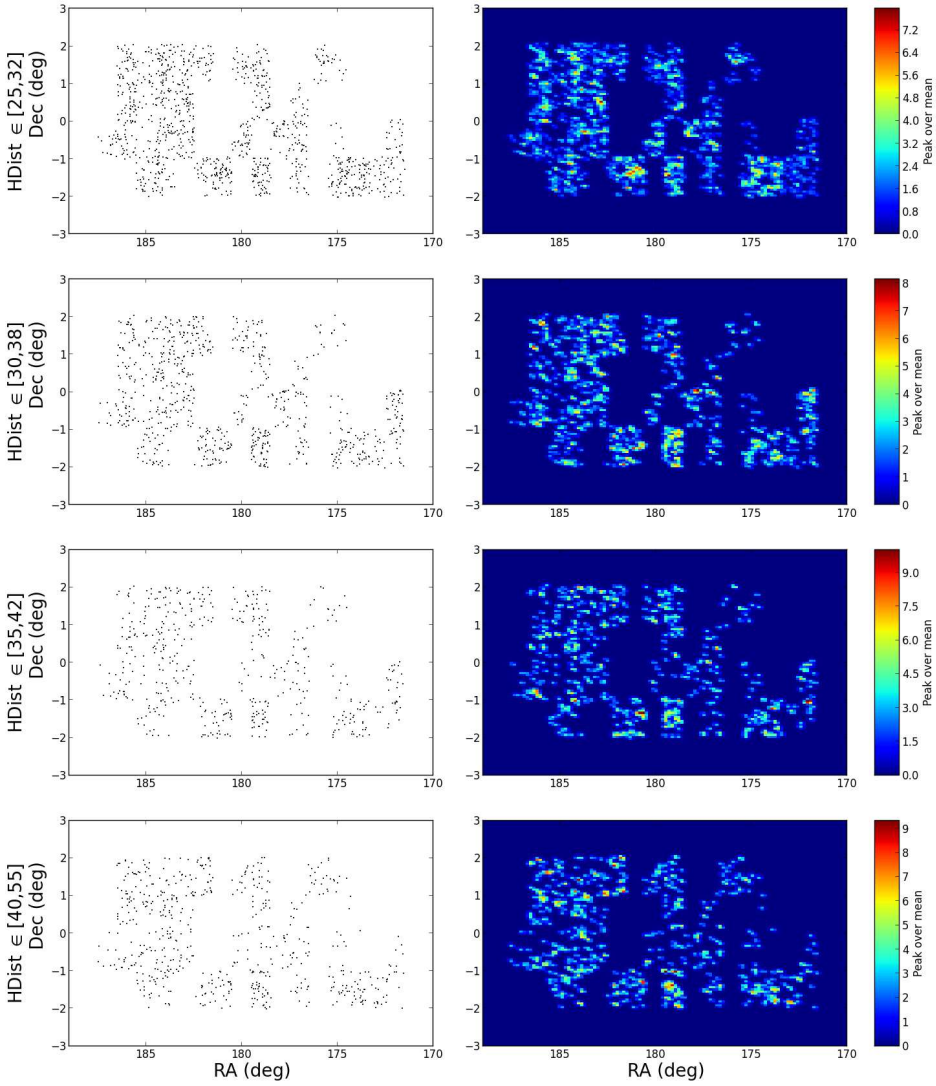


Figure 6.5: Stellar scatter maps and stellar density maps for the furthest distance slices in field KiDS-North180(continuation of Figure 6.4).

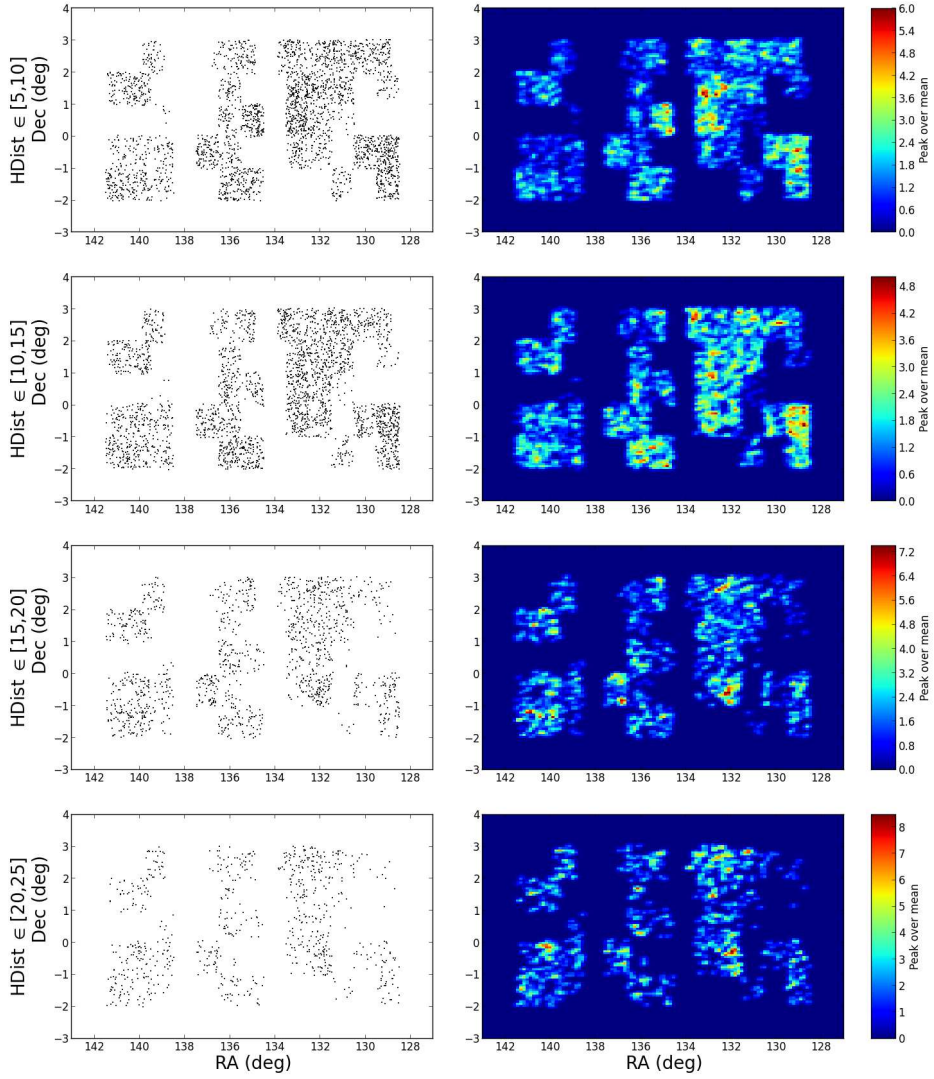


Figure 6.6: Stellar scatter maps and stellar density maps for the closest distance slices in field KiDS-North135.

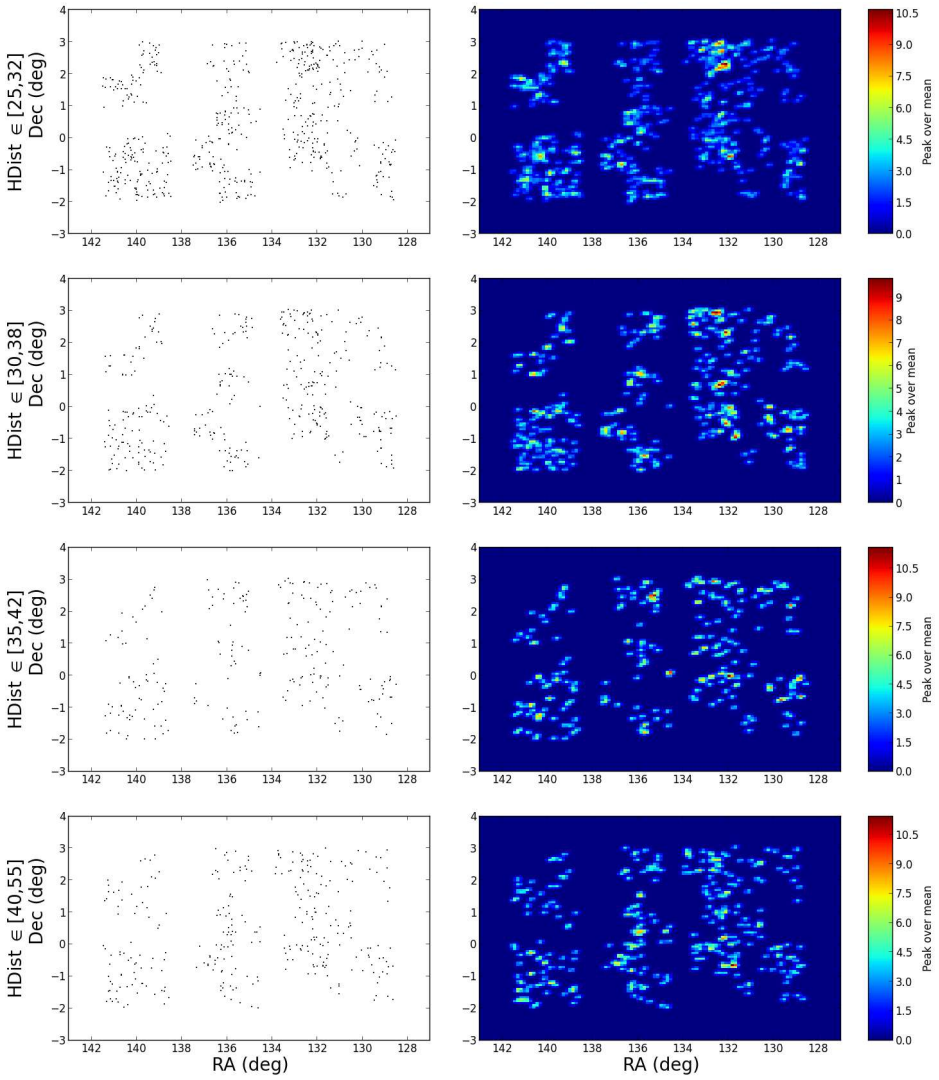


Figure 6.7: Stellar scatter maps and stellar density maps for the furthest distance slices in field KiDS-North135 (continuation of Figure 6.6).

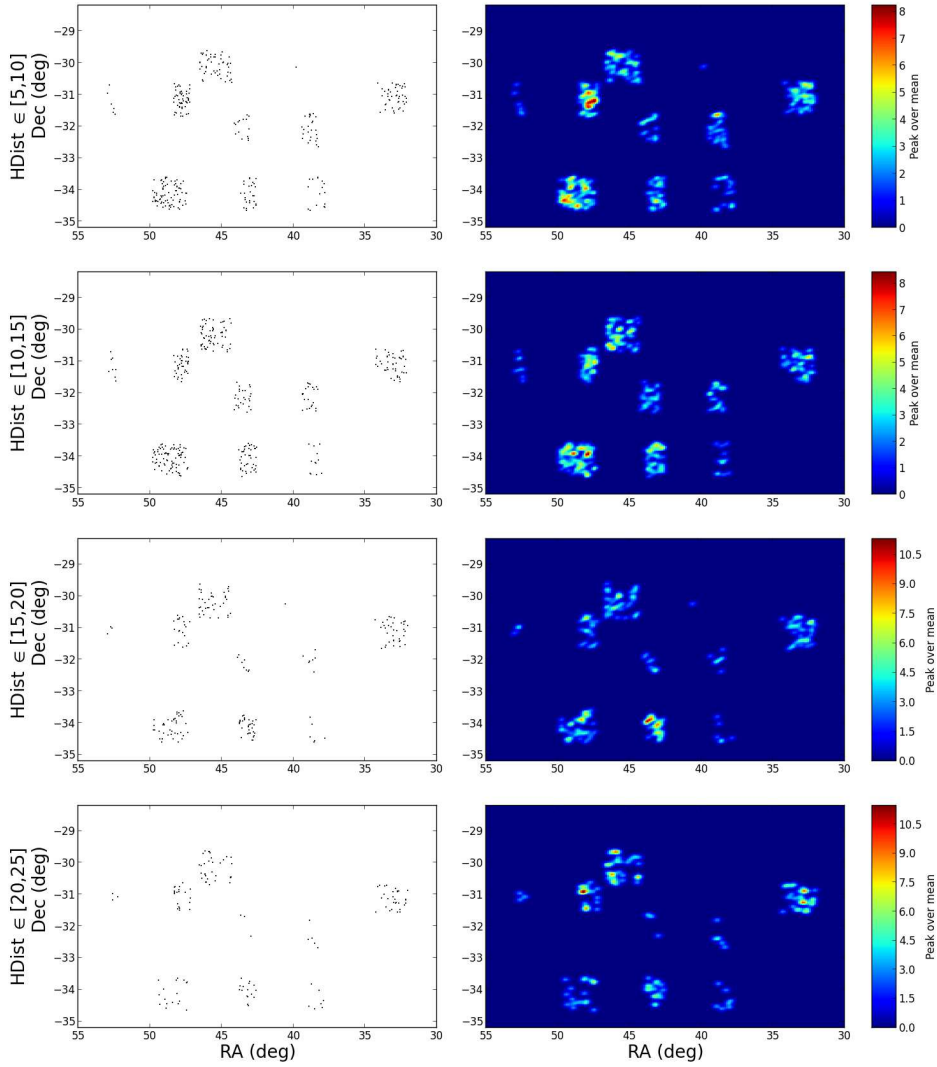


Figure 6.8: Stellar scatter maps and stellar density maps for the closest distance slices in field KiDS-South45.

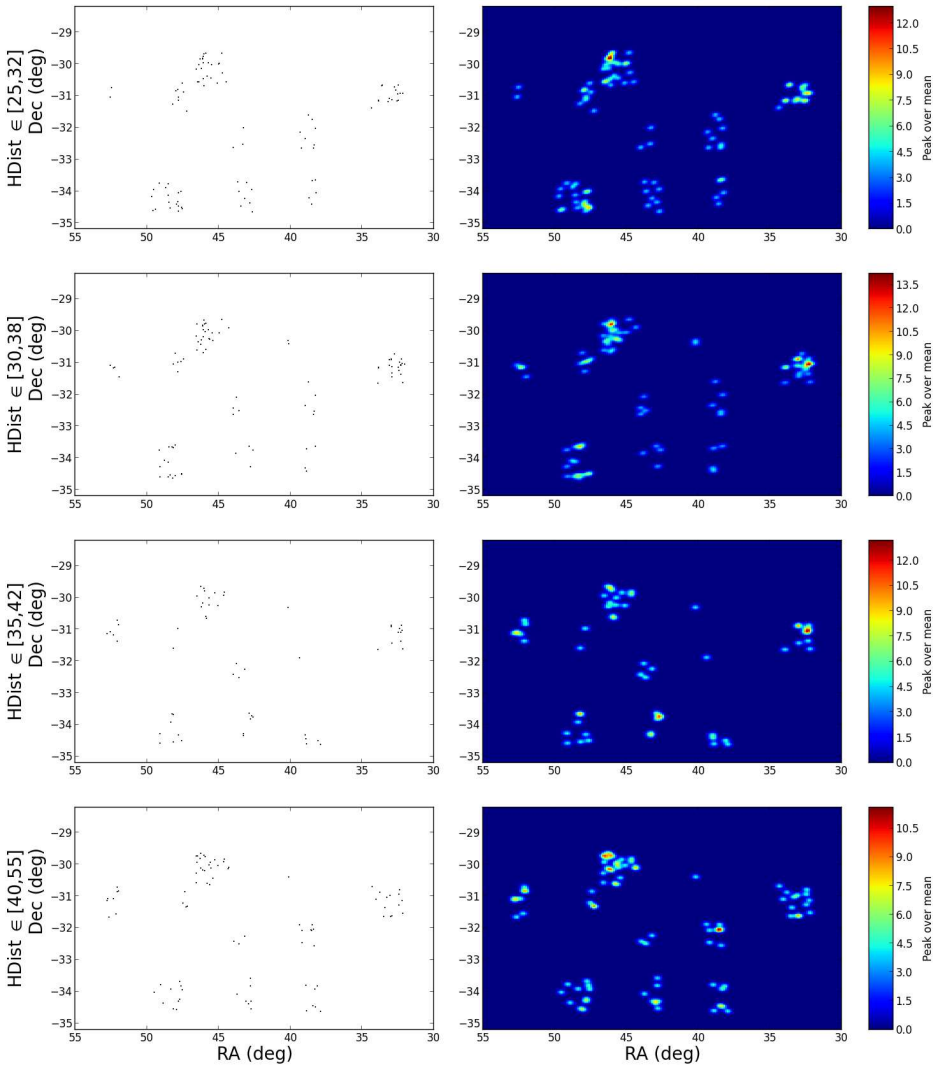


Figure 6.9: Stellar scatter maps and stellar density maps for the furthest distance slices in field KiDS-South45(continuation of Figure 6.8).

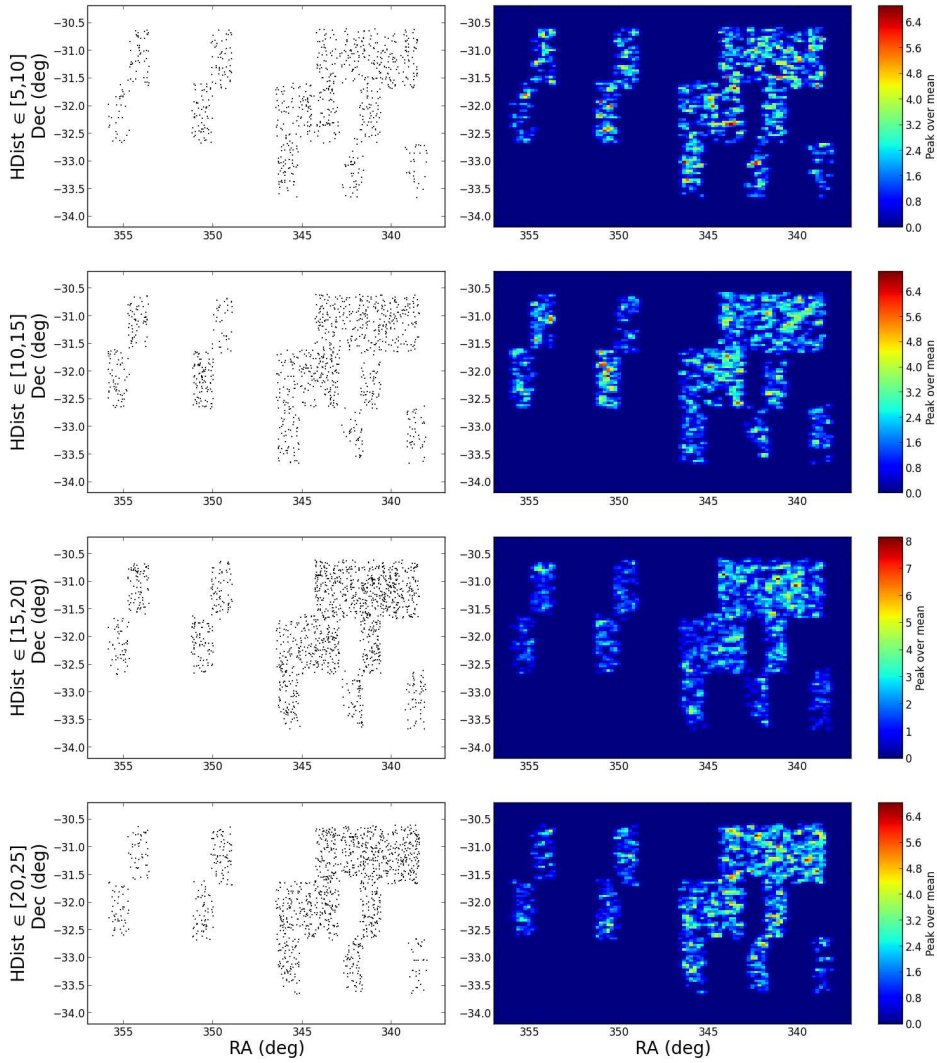


Figure 6.10: Stellar scatter maps and stellar density maps for the closest distance slices in field KiDS-South-15.

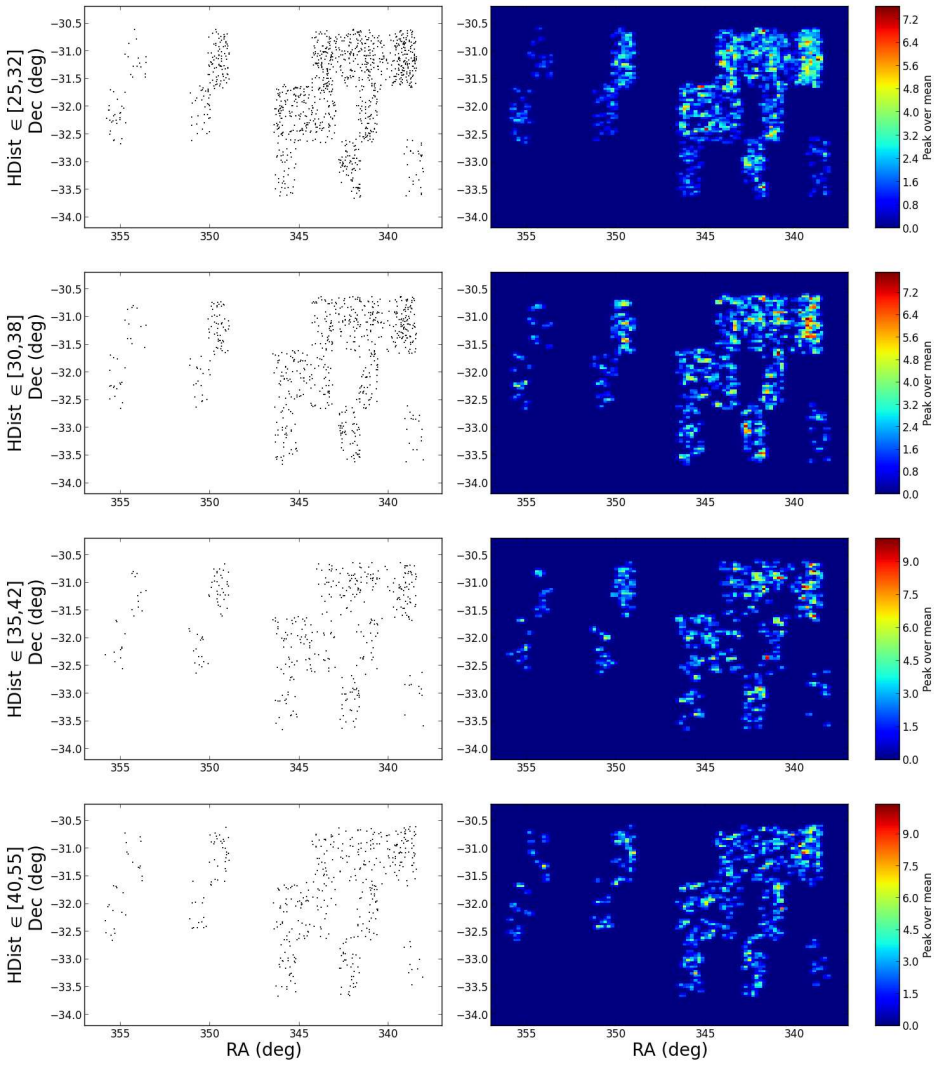


Figure 6.11: Stellar scatter maps and stellar density maps for the furthest distance slices in field KiDS-South-15(continuation of Figure 6.10).

North220. It is worth noting that the inner-halo or disk structures are more easily recognizable in the distance-RA maps than in the mag-RA maps, whereas the outer halo structures show the opposite effect. The reason for this is the logarithmic concentrating power of magnitudes in relation to distances as distances increase, which becomes very relevant when large volumes are probed and the average stellar densities decrease. Conversely, the same effect washes out short scale overdensities when these ones are located nearby.

In the KiDS-North220 field, the presence of disk stars is detected at least out to $12-15$ kpc. The Virgo Overdensity stretches out to 20 kpc in heliocentric distances and, in its western-most regions, possibly out to $25-30$ kpc. The EBS is mostly concentrated at under 15 kpc, with some potential debris extending further out to 20 kpc. The Sagittarius stream's nearMSTO stars overdensity in KiDS-North220 clearly peaks at $22.0-22.2$ mag in r but extends from ~ 21.6 to ~ 22.9, indicating a broad branch and possibly a dependence of distance with declination. Assuming an average absolute magnitude of $M_{r,TO} = 4.00$ for the MSTO of the Sagittarius stream (Pila-Díez et al. 2014), these magnitudes translate into a peak distance of 40 kpc and $[33, 60]$ kpc (soft) boundaries.

Figure 6.14 and 6.15 show the Sagittarius stream in KiDS-South-15, in agreement with its location on the 2MASS maps. At these latitudes, the stream sits at a distance between ~ 15 kpc and ~ 30 kpc, in agreement with the predictions of Law & Majewski (2010b) and Peñarrubia et al. (2010). Such a wide range of distances suggests the possible presence of two wraps (the leading and the trailing) or a quite thick branch in this region of the sky.

Among the small candidate overdensities, we identify one as a fragment of the Palomar 5 (Pal5) globular cluster tidal tails (Grillmair & Dionatos 2006a). The still patchy coverage of KiDS in the $RA > 225\,\mathrm{deg}$ range unfortunately prevents us from fully tracing the stream. Nonetheless, we follow the procedure described above to analyse the CMD of this overdensity and demarcate the excess of stars within the tiles area. A clear main sequence and main sequence turnoff point are visible in the CMD corresponding to the tile centred at $(RA, Dec) = (230.0, 0.5)\,\mathrm{deg}$ (left panel on Figure 6.16), and even a secondary main sequence turnoff point is located at fainter magnitudes. As discussed in Pila-Díez et al. (2014), these originate in the Pal5 tail and the underlying Sagittarius stream, respectively. We isolate the stars in the Pal5 tail's main sequence, and build a stellar density map of the tile specific to this substructure (right panel on Figure 6.16). This map nicely shows the Pal5 tail crossing the tile through its North-East quadrant.

For the rest of the small overdensities (Table 6.2) we follow the same procedure. From their CMD and stamp maps we find that these are either i) spurious enhancements in the distance/magnitude-sliced maps (this is, RC/nearMSTO-colour overdensities in the CMD without the companion RGB/main sequence overdensity), or ii) apparent main sequences in the CMD but without a coherent spatial feature in the stamp map (meaning that, when plotting different colour-magnitude sections of the apparent main sequence on the stamp map, they popu-

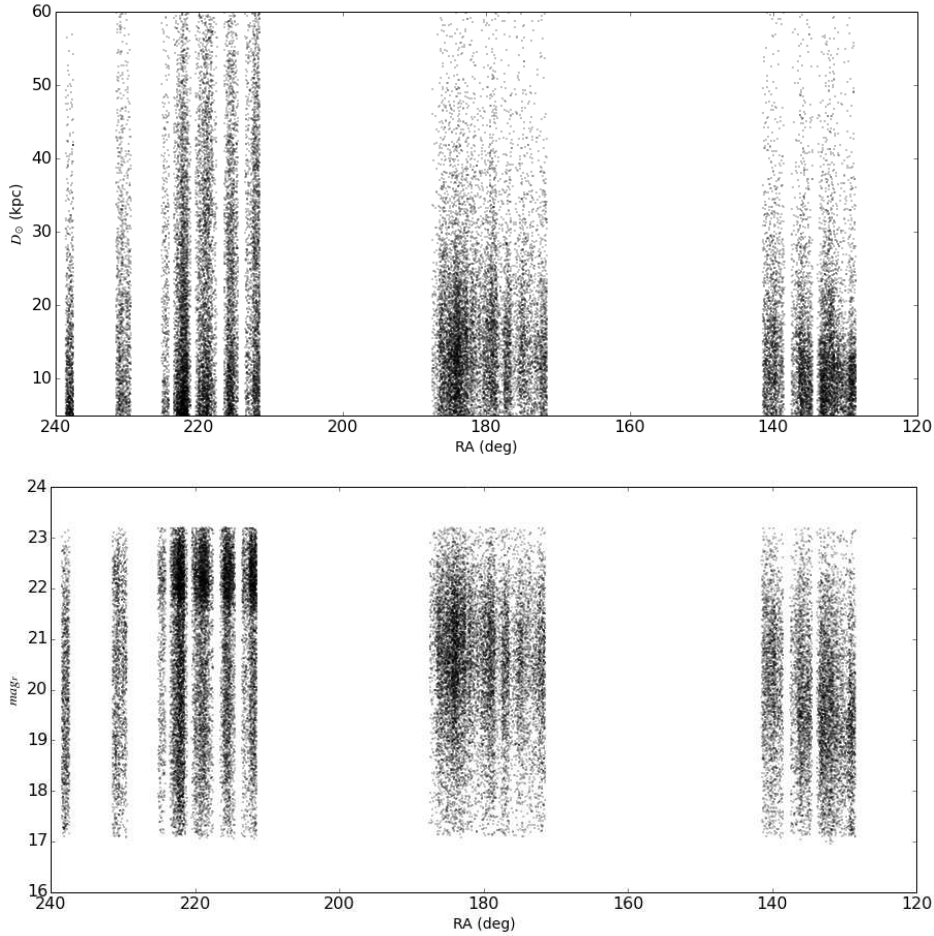


Figure 6.12: Distance vs RA (top) and magnitude vs RA (bottom) scatter maps for the nearMSTO stars in the KiDS Northern fields. Both the disk and large halo structures like the Sagittarius stream, the Virgo Overdensity and the EBS are visible. This figure illustrates that the nearby structures are more easily recognizable in the distance space than the far structures, whereas the far structures are more easily recognizable in the magnitude space. This is due to the logarithmic concentrating power of magnitudes in relation to distances.

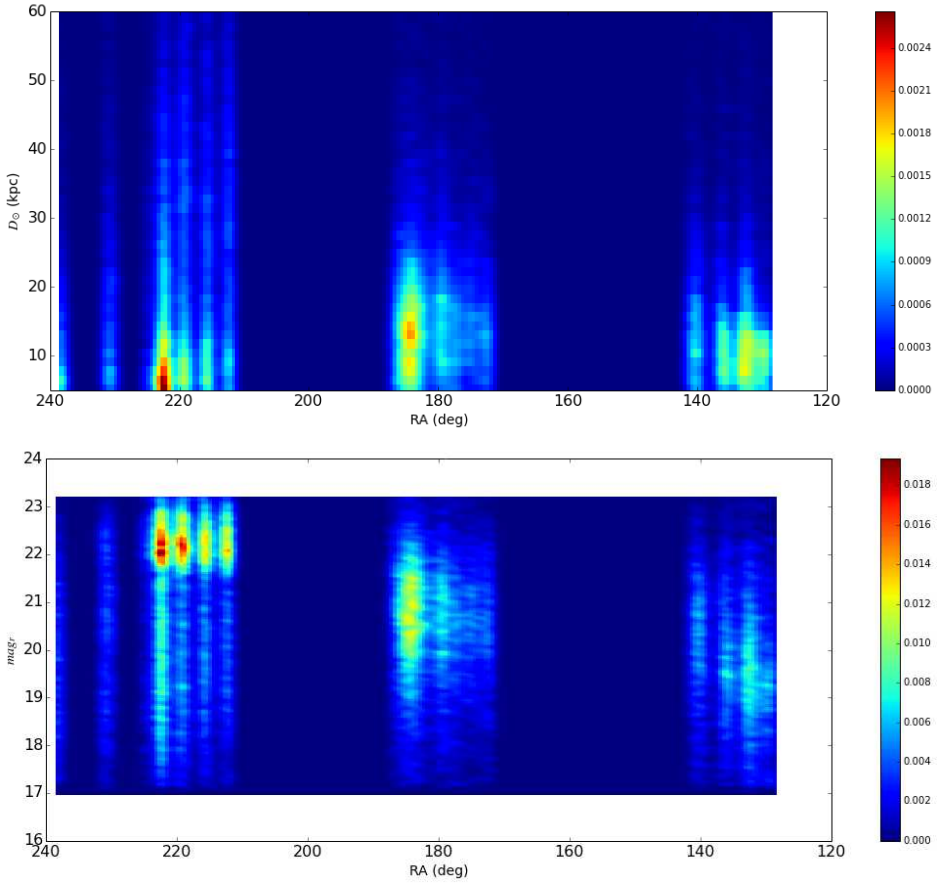


Figure 6.13: Same as in Figure 6.12 but showing the stellar density map instead of the stellar counts map. The density has been calculated with a gaussian kernel of variable bandwidth.

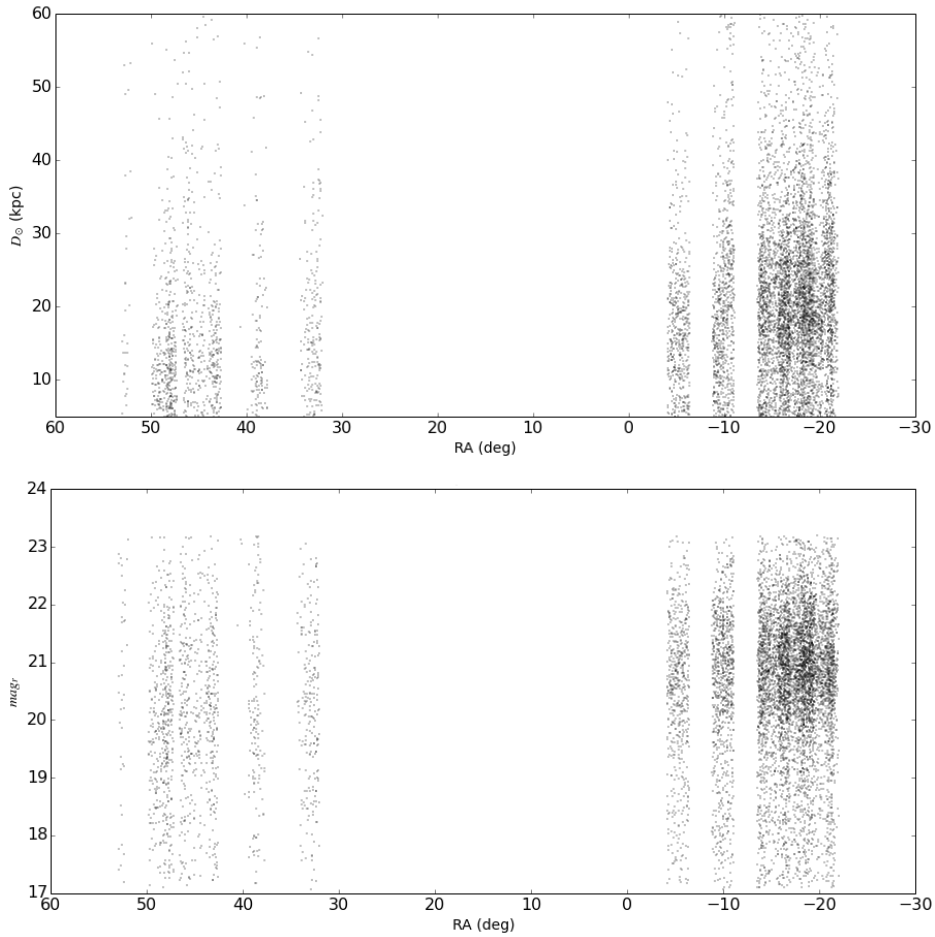


Figure 6.14: Distance vs RA (top) and magnitude vs RA (bottom) scatter maps for the nearMSTO stars in the KiDS Southern fields. The Sagittarius stream is visible in the eastern part of the field.

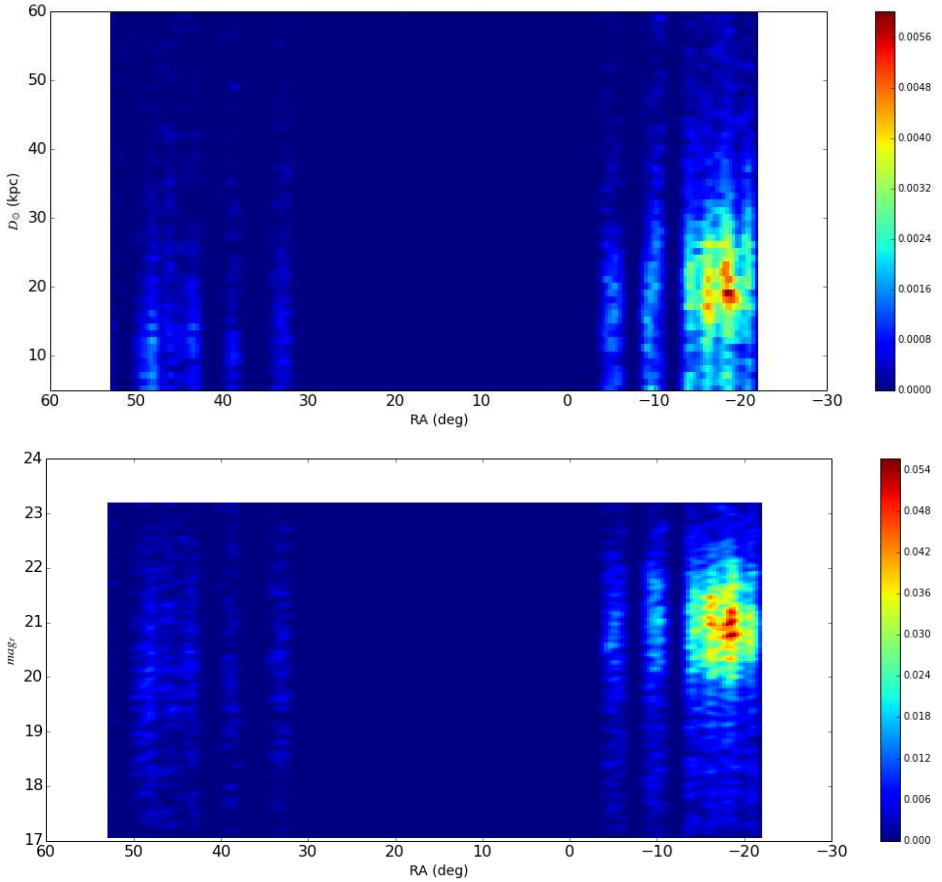


Figure 6.15: Same as in Figure 6.14 but showing the stellar density map instead of the stellar counts map.The density has been calculated with a gaussian kernel of variable bandwidth.

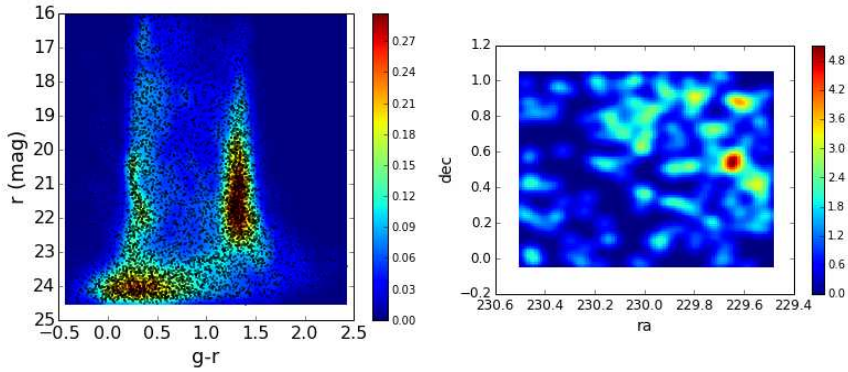


Figure 6.16: CMD (left) and stellar density map (right) for the stars in the main sequence of the CMD (right), pointing centered at $(RA, Dec) = (230.0, 0.5)$ deg. The main sequence at $20.0 < r < 22.0$ represents the Palomar 5 stream. The secondary main sequence visible at $r \approx 23$ is the Sagittarius stream.

Table 6.2: Potential small overdensities identified in the distance-sliced/magnitude-sliced nearMSTO or RC density maps. The table indicates the central coordinates of the tile where each was identified, tags them and provides a diagonisis (true or false positive).

Overdensity	Field	RA_{tile} (deg)	Dec_{tile} (deg)	positive
Pal5	KiDS-North220	230.0	0.5	true
A	KiDS-North180	179.0	-0.5	false
B	KiDS-North135	135.0	0.5	false
C	KiDS-North135	132.0	-0.5	false
D	KiDS-South45	47.8	-31.2	false
E	KiDS-South-15	350.6	-32.1	false

late different regions of the tile). Examples for the two types of cases are provided in Figures 6.17 and 6.18, respectively, corresponding to overdensities A and E. We conclude that all A to E overdensities are false positive halo substructures.

6.4 Discussion

The methods used in this work are technically robust (k-Nearest Neighbours, CMDs, distance or magnitude slicing, colour-colour star selection) and their effectivity for the halo has been amply tested in the literature. Indeed we are able to recover large known halo structures and also a fragment of the Palomar 5 tidal tails.

Therefore we associate the lack of a new discovery in the KiDS DR1/2 data to the small sky coverage that KiDS has so far achieved in areas of the sky not

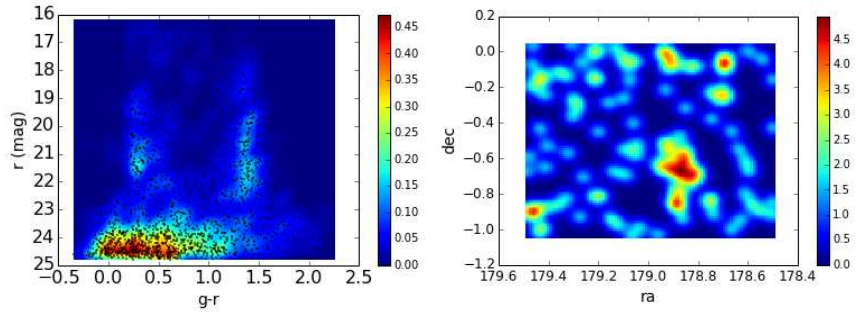


Figure 6.17: CMD (left) and stellar density map (right) corresponding to the pointing centered at $(RA, Dec) = (179.0, -0.5)$ deg (labelled as A in Table 6.2). The stellar density map contains the stars in the apparent main sequence of the whole pointing (not shown), and the CMD is built of the stars located in the vicinity of the overdensity at $(RA, Dec) \approx (178.9, -0.7)$ deg. The lack of a main sequence and an RGB on this CMD indicates that this overdensity in nearMSTO stars is a spurious enhancement and, therefore, is a false positive. Similar analysis on weaker spatial overdensities in this pointing lead to conclude that there is no localized main sequence in this pointing.

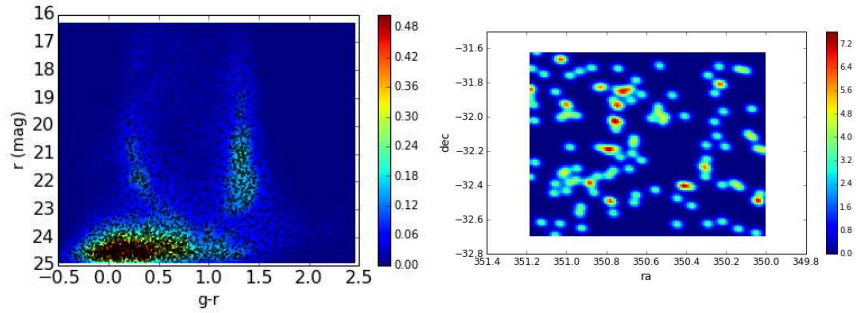


Figure 6.18: CMD (left) and stellar density map for the stars in the main sequence of the CMD (right). They correspond to the pointing centered at $(RA, Dec) = (350.6, -32.1)$ deg and to the overdensity labelled as E in Table 6.2. The lack of a coherent spatial feature indicates this is a false polsitive.

probed yet by other surveys. In particular, in the KiDS' northern fields there is a total overlap with the footprint of the latest SDSS data releases, and there was originally a $\sim 80\%$ overlap planned. Of the current $133\,\mathrm{deg}^2$ scanned by KiDS DR-1 and DR-2 in the four bands, only 23% belongs to the southern hemisphere. This limits KiDS current chances of detecting new globular clusters or satellite galaxies, and limits its ability to detect and trace weak streams.

Based both on the claims of a fundamental plane of satellite galaxies (Palma et al. (2002b), Zentner et al. (2005), Pawlowski et al. (2012)) and on the possibility of such a fundamental plane being probed wrong, but based mainly on the satellite population in the northern sky, the number of satellite galaxies expected to inhabit the southern sky is high. Furthermore the recent results by DES and ATLAS show good prospects, and do not suggest a fundamental asymmetry in the density of satellites between the northern and southern Galactic hemispheres. Given the current estimates for the Galactic satellite luminosity function (Koposov et al. 2008) and KiDS unprecedented power to probe faint objects, the prospects for KiDS are particularly good at the faint end. Therefore there is no reason for discouragement and future data releases of KiDS should uncover new satellites and stellar debris.

6.5 Conclusions

The Kilo Degree Survey is currently mapping $1500\,\mathrm{deg}^2$ of the sky at an unprecedented depth among large area surveys. Its good image quality, seeing constraints and multi-colour photometry make it particularly suited to explore the Galactic halo in depth. It targets both the North and the South Galactic hemispheres, overlapping with SDSS and ATLAS in each region respectively, but probing an average of two magnitudes deeper than any of the two surveys in any of the four photometric filters. The PSF-homogenization that we carry out allows us to accurately separate stars from galaxies, reaching a stellar magnitude limit of $mag_r = 23.1$ without significant galaxy contamination. This allows us to properly exploit main sequence turnoff point stars out to large heliocentric distances (~ 60 kpc).

In this work we present magnitude-sliced or distance-sliced maps for photometrically selected red clump stars and near main sequence turnoff point stars. We identify broad halo structures such as the Sagittarius stream, the Virgo Overdensity and the Eastern Band Structure in the northern hemisphere, and the Sagittarius stream in the southern hemisphere. In the northern hemisphere we also identify the disk stars at longitudes and latitudes neighbouring the Galactic centre. We trace these features in distance space and magnitude space and report heliocentric distances compatible with previous works.

We also identify in these distance/magnitude-sliced maps a number of small overdensities potentially representative of halo substructure. Of the seven identifications, we recognize one as a piece of the Palomar 5 tidal tails. The rest are classified as false positives after close inspection of their CMDs and the spatial

distribution of any CMD overdensities.

The Kilo Degree Survey is promising in the search for small, sparse and faint substructure, given both its technical capabilities and the fact that it is probing uncharted halo territory in the Southern hemisphere. The current methodology presented in this chapter, together with state-of-the-art matched-filter algorithms, should suffice to identify new substructure in the halo once the spatial coverage of KiDS reaches a more mature stage and allows for more lines of sight (to detect new overdensities) and their spatial continuous follow-up.

BIBLIOGRAPHY

Ahn, C. P., Alexandroff, R., Allende Prieto, C., et al. 2014, ApJS, 211, 17

Battaglia, G., Helmi, A., Morrison, H., et al. 2006, MNRAS, 370, 1055

Bekki, K. & Yong, D. 2012, MNRAS, 419, 2063

Bell, E. F., Zucker, D. B., Belokurov, V., et al. 2008, ApJ, 680, 295

Bellazzini, M., Correnti, M., Ferraro, F. R., Monaco, L., & Montegriffo, P. 2006a, A&A, 446, L1

Bellazzini, M., Ferraro, F. R., & Ibata, R. 2002, AJ, 124, 915

Bellazzini, M., Ferraro, F. R., & Ibata, R. 2003, AJ, 125, 188

Bellazzini, M., Ibata, R., & Ferraro, F. R. 2004, in Astronomical Society of the Pacific Conference Series, Vol. 327, Satellites and Tidal Streams, ed. F. Prada, D. Martinez Delgado, & T. J. Mahoney, 220–+

Bellazzini, M., Ibata, R., Martin, N., et al. 2006b, MNRAS, 366, 865

Bellazzini, M., Ibata, R. A., Chapman, S. C., et al. 2008, AJ, 136, 1147

Bellazzini, M., Newberg, H. J., Correnti, M., Ferraro, F. R., & Monaco, L. 2006c, A&A, 457, L21

Belokurov, V., Evans, N. W., Bell, E. F., et al. 2007a, ApJ, 657, L89

Belokurov, V., Evans, N. W., Irwin, M. J., Hewett, P. C., & Wilkinson, M. I. 2006a, ApJ, 637, L29

Belokurov, V., Evans, N. W., Irwin, M. J., et al. 2007b, ApJ, 658, 337

Belokurov, V., Koposov, S. E., Evans, N. W., et al. 2014, MNRAS, 437, 116

Belokurov, V., Zucker, D. B., Evans, N. W., et al. 2006b, ApJ, 642, L137

Belokurov, V., Zucker, D. B., Evans, N. W., et al. 2007c, ApJ, 654, 897

Bernard, E. J., Ferguson, A. M. N., Schlafly, E. F., et al. 2014, MNRAS, 443, L84

Bertin, E. & Arnouts, S. 1996, A&AS, 117, 393

Besla, G., Kallivayalil, N., Hernquist, L., et al. 2010, ApJ, 721, L97

Bildfell, C., Hoekstra, H., Babul, A., et al. 2012, MNRAS, 425, 204

Bonaca, A., Geha, M., & Kallivayalil, N. 2012a, ApJ, 760, L6

Bonaca, A., Jurić, M., Ivezić, Ž., et al. 2012b, AJ, 143, 105

Bond, N. A., Ivezić, Ž., Sesar, B., et al. 2010, ApJ, 716, 1

Bonifacio, P., Sbordone, L., Marconi, G., Pasquini, L., & Hill, V. 2004, A&A, 414, 503

Bullock, J. S. & Johnston, K. V. 2005, ApJ, 635, 931

Campbell, S. W., Yong, D., Wylie-de Boer, E. C., et al. 2012, ApJ, 761, L2

Carballo-Bello, J. A., Gieles, M., Sollima, A., et al. 2012, MNRAS, 419, 14

Carballo-Bello, J. A. & Martínez-Delgado, D. 2010, in Highlights of Spanish Astrophysics V, ed. J. M. Diego, L. J. Goicoechea, J. I. González-Serrano, & J. Gorgas, 383
Carlberg, R. G. 2012, ApJ, 748, 20
Carlin, J. L., Majewski, S. R., Casetti-Dinescu, D. I., et al. 2012, ApJ, 744, 25
Carollo, D., Beers, T. C., Lee, Y. S., et al. 2007, Nature, 450, 1020
Carraro, G. 2009, AJ, 137, 3809
Carraro, G., Zinn, R., & Moni Bidin, C. 2007, A&A, 466, 181
Carretta, E., D'Orazi, V., Gratton, R. G., & Lucatello, S. 2012, A&A, 543, A117
Carretta, E., Gratton, R. G., Lucatello, S., et al. 2010, ApJ, 722, L1
Carretta, E., Lucatello, S., Gratton, R. G., Bragaglia, A., & D'Orazi, V. 2011, A&A, 533, A69
Casetti-Dinescu, D. I., Girard, T. M., Majewski, S. R., et al. 2009, ApJ, 701, L29
Casey, A., Keller, S., Da Costa, G., Frebel, A., & Maunder, E. 2013a, ArXiv e-prints
Casey, A. R., Da Costa, G., Keller, S. C., & Maunder, E. 2013b, ApJ, 764, 39
Chen, B., Stoughton, C., Smith, J. A., et al. 2001, ApJ, 553, 184
Chonis, T. S. & Gaskell, C. M. 2008, AJ, 135, 264
Chou, M.-Y., Majewski, S. R., Cunha, K., et al. 2007, ApJ, 670, 346
Cole, S., Aragon-Salamanca, A., Frenk, C. S., Navarro, J. F., & Zepf, S. E. 1994, MNRAS, 271, 781
Conn, B. C., Lane, R. R., Lewis, G. F., et al. 2007, MNRAS, 376, 939
Conn, B. C., Lewis, G. F., Irwin, M. J., et al. 2005, MNRAS, 362, 475
Cooper, A. P., Cole, S., Frenk, C. S., et al. 2010, MNRAS, 406, 744
Cooper, A. P., D'Souza, R., Kauffmann, G., et al. 2013, MNRAS, 434, 3348
Correnti, M., Bellazzini, M., Ibata, R. A., Ferraro, F. R., & Varghese, A. 2010, ApJ, 721, 329
Covey, K. R., Ivezić, Ž., Schlegel, D., et al. 2007, AJ, 134, 2398
Crane, J. D., Majewski, S. R., Rocha-Pinto, H. J., et al. 2003, ApJ, 594, L119
de Jong, J. T. A., Verdoes Kleijn, G. A., Kuijken, K. H., & Valentijn, E. A. 2013, Experimental Astronomy, 35, 25
de Jong, J. T. A., Yanny, B., Rix, H.-W., et al. 2010, ApJ, 714, 663
Deason, A. J., Belokurov, V., & Evans, N. W. 2011, MNRAS, 416, 2903
Deason, A. J., Belokurov, V., Koposov, S. E., & Rockosi, C. M. 2014, ApJ, 787, 30
Dehnen, W., Odenkirchen, M., Grebel, E. K., & Rix, H.-W. 2004, AJ, 127, 2753
Dinescu, D. I., Majewski, S. R., Girard, T. M., & Cudworth, K. M. 2000, AJ, 120, 1892
Dinescu, D. I., Majewski, S. R., Girard, T. M., & Cudworth, K. M. 2001, AJ, 122, 1916
Dinescu, D. I., Martínez-Delgado, D., Girard, T. M., et al. 2005, ApJ, 631, L49
Dohm-Palmer, R. C., Helmi, A., Morrison, H., et al. 2001, ApJ, 555, L37
Dotter, A., Chaboyer, B., Jevremović, D., et al. 2008a, ApJS, 178, 89
Dotter, A., Chaboyer, B., Jevremović, D., et al. 2008b, ApJS, 178, 89
Dotter, A., Sarajedini, A., & Anderson, J. 2011, ApJ, 738, 74
Drake, A. J., Catelan, M., Djorgovski, S. G., et al. 2013, ApJ, 765, 154
Driver, S. P., Hill, D. T., Kelvin, L. S., et al. 2011, MNRAS, 413, 971
Duffau, S., Zinn, R., Vivas, A. K., et al. 2006, ApJ, 636, L97
Erben, T., Hildebrandt, H., Lerchster, M., et al. 2009, A&A, 493, 1197

Faccioli, L., Smith, M. C., Yuan, H.-B., et al. 2014, ApJ, 788, 105
Fellhauer, M., Belokurov, V., Evans, N. W., et al. 2006, ApJ, 651, 167
Fellhauer, M., Evans, N. W., Belokurov, V., Wilkinson, M. I., & Gilmore, G. 2007a, MNRAS, 380, 749
Fellhauer, M., Evans, N. W., Belokurov, V., et al. 2007b, MNRAS, 375, 1171
Font, A. S., Benson, A. J., Bower, R. G., et al. 2011a, MNRAS, 417, 1260
Font, A. S., McCarthy, I. G., Crain, R. A., et al. 2011b, MNRAS, 416, 2802
Forbes, D. A. & Bridges, T. 2010, MNRAS, 404, 1203
Forbes, D. A., Strader, J., & Brodie, J. P. 2004, AJ, 127, 3394
Frayn, C. M. & Gilmore, G. F. 2003, MNRAS, 339, 887
Frinchaboy, P. M., Majewski, S. R., Crane, J. D., et al. 2004, ApJ, 602, L21
Gao, S., Just, A., & Grebel, E. K. 2013, A&A, 549, A20
Girardi, L., Groenewegen, M. A. T., Hatziminaoglou, E., & da Costa, L. 2005, A&A, 436, 895
Girardi, L., Williams, B. F., Gilbert, K. M., et al. 2010, ApJ, 724, 1030
Gómez, F. A., Helmi, A., Cooper, A. P., et al. 2013, MNRAS, 436, 3602
Grillmair, C. J. 2006a, ApJ, 645, L37
Grillmair, C. J. 2006b, ApJ, 651, L29
Grillmair, C. J. 2009, ApJ, 693, 1118
Grillmair, C. J. & Dionatos, O. 2006a, ApJ, 641, L37
Grillmair, C. J. & Dionatos, O. 2006b, ApJ, 643, L17
Grillmair, C. J. & Johnson, R. 2006, ApJ, 639, L17
Hammersley, P. L. & López-Corredoira, M. 2011, A&A, 527, A6+
Han, S.-I., Lee, Y.-W., Joo, S.-J., et al. 2009, ApJ, 707, L190
Hansen, B. M., Richer, H. B., Anderson, J., et al. 2013, in American Astronomical Society Meeting Abstracts, Vol. 221, American Astronomical Society Meeting Abstracts 221, 213.02
Hansen, B. M. S., Brewer, J., Fahlman, G. G., et al. 2002, ApJ, 574, L155
Harris, W. E. 1991, AJ, 102, 1348
Harris, W. E. 1996, in Astronomical Society of the Pacific Conference Series, Vol. 92, Formation of the Galactic Halo...Inside and Out, ed. H. L. Morrison & A. Sarajedini, 231
Harris, W. E. 2010, preprint (arXiv:1012.3224)
Helmi, A., Navarro, J. F., Meza, A., Steinmetz, M., & Eke, V. R. 2003, ApJ, 592, L25
Helmi, A., White, S. D. M., de Zeeuw, P. T., & Zhao, H. 1999, Nature, 402, 53
Hildebrandt, H., Pielorz, J., Erben, T., et al. 2009, A&A, 498, 725
Hoekstra, H., Mahdavi, A., Babul, A., & Bildfell, C. 2012, MNRAS, 427, 1298
Ibata, R., Irwin, M., Lewis, G., Ferguson, A. M. N., & Tanvir, N. 2001a, Nature, 412, 49
Ibata, R., Irwin, M., Lewis, G. F., & Stolte, A. 2001b, ApJ, 547, L133
Ibata, R., Lewis, G. F., Irwin, M., Totten, E., & Quinn, T. 2001c, ApJ, 551, 294
Ibata, R., Martin, N. F., Irwin, M., et al. 2007, ApJ, 671, 1591
Ibata, R. A., Gilmore, G., & Irwin, M. J. 1994, Nature, 370, 194
Ibata, R. A., Wyse, R. F. G., Gilmore, G., Irwin, M. J., & Suntzeff, N. B. 1997, AJ,

113, 634
Ivezić, Ž., Sesar, B., Jurić, M., et al. 2008, ApJ, 684, 287
Jin, S. & Lynden-Bell, D. 2007, MNRAS, 378, L64
Jurić, M., Ivezić, Ž., Brooks, A., et al. 2008, ApJ, 673, 864
Kallivayalil, N., van der Marel, R. P., & Alcock, C. 2006a, ApJ, 652, 1213
Kallivayalil, N., van der Marel, R. P., Alcock, C., et al. 2006b, ApJ, 638, 772
King, I. R. 1966, AJ, 71, 64
Koposov, S., Belokurov, V., Evans, N. W., et al. 2008, ApJ, 686, 279
Koposov, S. E., Belokurov, V., Evans, N. W., et al. 2012, ApJ, 750, 80
Koposov, S. E., Belokurov, V., Torrealba, G., & Wyn Evans, N. 2015, ArXiv e-prints
Koposov, S. E., Belokurov, V., & Wyn Evans, N. 2013, ApJ, 765, 162
Koposov, S. E., Irwin, M., Belokurov, V., et al. 2014, MNRAS, 442, L85
Landolt, A. U. 1992, AJ, 104, 340
Law, D. R. & Majewski, S. R. 2010a, ApJ, 718, 1128
Law, D. R. & Majewski, S. R. 2010b, ApJ, 714, 229
Layden, A. C. & Sarajedini, A. 2000, AJ, 119, 1760
Leaman, R., VandenBerg, D. A., & Mendel, J. T. 2013, MNRAS, 436, 122
Lee, Y.-W., Gim, H. B., & Casetti-Dinescu, D. I. 2007, ApJ, 661, L49
Li, J., Newberg, H. J., Carlin, J. L., et al. 2012, ApJ, 757, 151
Loidl, R., Lançon, A., & Jørgensen, U. G. 2001, A&A, 371, 1065
López-Corredoira, M. 2006, MNRAS, 369, 1911
Mackey, A. D., Huxor, A. P., Ferguson, A. M. N., et al. 2010, ApJ, 717, L11
Mackey, A. D., Huxor, A. P., Ferguson, A. M. N., et al. 2013, MNRAS, 429, 281
Madore, B. F. & Freedman, W. L. 1993, in Bulletin of the American Astronomical Society, Vol. 25, American Astronomical Society Meeting Abstracts, 1395
Majewski, S. R., Skrutskie, M. F., Weinberg, M. D., & Ostheimer, J. C. 2003, ApJ, 599, 1082
Malkin, Z. 2012, ArXiv e-prints
Marigo, P., Girardi, L., Bressan, A., et al. 2008, A&A, 482, 883
Marín-Franch, A., Aparicio, A., Piotto, G., et al. 2009, ApJ, 694, 1498
Marino, A. F., Milone, A. P., Yong, D., et al. 2014, MNRAS, 442, 3044
Martell, S. L., Smith, G. H., & Grillmair, C. J. 2002, in Bulletin of the American Astronomical Society, Vol. 201, American Astronomical Society Meeting Abstracts, 711
Martin, N. F., Ibata, R. A., Bellazzini, M., et al. 2004, MNRAS, 348, 12
Martin, N. F., Ibata, R. A., & Irwin, M. 2007, ApJ, 668, L123
Martin, N. F., Ibata, R. A., Rich, R. M., et al. 2014, ApJ, 787, 19
Martínez-Delgado, D., Aparicio, A., Gómez-Flechoso, M. Á., & Carrera, R. 2001, ApJ, 549, L199
Martínez-Delgado, D., Butler, D. J., Rix, H.-W., et al. 2005, ApJ, 633, 205
Martínez-Delgado, D., Dinescu, D. I., Zinn, R., et al. 2004a, in Astronomical Society of the Pacific Conference Series, Vol. 327, Satellites and Tidal Streams, ed. F. Prada, D. Martinez Delgado, & T. J. Mahoney, 255–+
Martínez-Delgado, D., Gabany, R. J., Crawford, K., et al. 2010a, AJ, 140, 962

Martínez-Delgado, D., Gabany, R. J., Crawford, K., et al. 2010b, AJ, 140, 962
Martínez-Delgado, D., Gómez-Flechoso, M. Á., Aparicio, A., & Carrera, R. 2004b, ApJ, 601, 242
Martínez-Delgado, D., Peñarrubia, J., Gabany, R. J., et al. 2008, ApJ, 689, 184
Martínez-Delgado, D., Peñarrubia, J., Jurić, M., Alfaro, E. J., & Ivezić, Z. 2007, ApJ, 660, 1264
Martínez-Delgado, D., Zinn, R., Carrera, R., & Gallart, C. 2002, ApJ, 573, L19
Mastrobuono-Battisti, A., Di Matteo, P., Montuori, M., & Haywood, M. 2012, A&A, 546, L7
Mateo, M., Mirabal, N., Udalski, A., et al. 1996, ApJ, 458, L13
Mateu, C., Vivas, A. K., Zinn, R., Miller, L. R., & Abad, C. 2009, AJ, 137, 4412
McConnachie, A. W., Irwin, M. J., Ibata, R. A., et al. 2009, Nature, 461, 66
McLaughlin, D. E. & van der Marel, R. P. 2005, ApJS, 161, 304
Milone, A. P., Bedin, L. R., Piotto, G., et al. 2008, ApJ, 673, 241
Milone, A. P., Stetson, P. B., Piotto, G., et al. 2009, A&A, 503, 755
Mo, H., van den Bosch, F. C., & White, S. 2010, Galaxy Formation and Evolution
Moitinho, A., Vázquez, R. A., Carraro, G., et al. 2006, MNRAS, 368, L77
Momany, Y., Zaggia, S., Gilmore, G., et al. 2006, A&A, 451, 515
Momany, Y., Zaggia, S. R., Bonifacio, P., et al. 2004, A&A, 421, L29
Muzzin, A., Marchesini, D., Stefanon, M., et al. 2013, ApJ, 777, 18
Newberg, H. J., Willett, B. A., Yanny, B., & Xu, Y. 2010, ApJ, 711, 32
Newberg, H. J., Yanny, B., Grebel, E. K., et al. 2003, ApJ, 596, L191
Newberg, H. J., Yanny, B., Rockosi, C., et al. 2002, ApJ, 569, 245
Newberg, H. J., Yanny, B., & Willett, B. A. 2009, ApJ, 700, L61
Niederste-Ostholt, M., Belokurov, V., Evans, N. W., & Peñarrubia, J. 2010, ApJ, 712, 516
Odenkirchen, M., Grebel, E. K., Dehnen, W., Rix, H.-W., & Cudworth, K. M. 2002, AJ, 124, 1497
Odenkirchen, M., Grebel, E. K., Dehnen, W., et al. 2003, AJ, 126, 2385
Odenkirchen, M., Grebel, E. K., Rockosi, C. M., et al. 2001, ApJ, 548, L165
Olszewski, E. W., Saha, A., Knezek, P., et al. 2009, AJ, 138, 1570
Palma, C., Majewski, S. R., & Johnston, K. V. 2002a, ApJ, 564, 736
Palma, C., Majewski, S. R., & Johnston, K. V. 2002b, ApJ, 564, 736
Pawlowski, M. S., Pflamm-Altenburg, J., & Kroupa, P. 2012, MNRAS, 423, 1109
Peñarrubia, J., Belokurov, V., Evans, N. W., et al. 2010, MNRAS, 408, L26
Peñarrubia, J., Martínez-Delgado, D., Rix, H. W., et al. 2005, ApJ, 626, 128
Peñarrubia, J., Zucker, D. B., Irwin, M. J., et al. 2011, ApJ, 727, L2
Peebles, P. J. E. 1974, ApJ, 189, L51+
Piatek, S., Pryor, C., & Olszewski, E. W. 2008, AJ, 135, 1024
Pila-Díez, B., de Jong, J. T. A., Kuijken, K., van der Burg, R. F. J., & Hoekstra, H. 2015, ArXiv e-prints
Pila-Díez, B., Kuijken, K., de Jong, J. T. A., Hoekstra, H., & van der Burg, R. F. J. 2014, A&A, 564, A18
Prior, S. L., Da Costa, G. S., Keller, S. C., & Murphy, S. J. 2009, ApJ, 691, 306

Robin, A. C., Reylé, C., Derrière, S., & Picaud, S. 2003, A&A, 409, 523
Robin, A. C., Reylé, C., Fliri, J., et al. 2014, A&A, 569, A13
Rocha, M., Peter, A. H. G., & Bullock, J. 2012, MNRAS, 425, 231
Rocha-Pinto, H. J., Majewski, S. R., Skrutskie, M. F., & Crane, J. D. 2003, ApJ, 594, L115
Rocha-Pinto, H. J., Majewski, S. R., Skrutskie, M. F., Crane, J. D., & Patterson, R. J. 2004, ApJ, 615, 732
Rockosi, C. M., Odenkirchen, M., Grebel, E. K., et al. 2002, AJ, 124, 349
Sakamoto, T., Chiba, M., & Beers, T. C. 2003, A&A, 397, 899
Sales, L. V., Helmi, A., Starkenburg, E., et al. 2008, MNRAS, 389, 1391
Sand, D. J., Graham, M. L., Bildfell, C., et al. 2012, ApJ, 746, 163
Sandage, A. & Hartwick, F. D. A. 1977, AJ, 82, 459
Sbordone, L., Bonifacio, P., Marconi, G., Buonanno, R., & Zaggia, S. 2005, A&A, 437, 905
Schlafly, E. F. & Finkbeiner, D. P. 2011, ApJ, 737, 103
Schlegel, D. J., Finkbeiner, D. P., & Davis, M. 1998, ApJ, 500, 525
Searle, L. & Zinn, R. 1978, ApJ, 225, 357
Sesar, B., Ivezić, Ž., Grammer, S. H., et al. 2010a, ApJ, 708, 717
Sesar, B., Jurić, M., & Ivezić, Ž. 2011, ApJ, 731, 4
Sesar, B., Vivas, A. K., Duffau, S., & Ivezić, Ž. 2010b, ApJ, 717, 133
Sharma, S., Johnston, K. V., Majewski, S. R., et al. 2010, ApJ, 722, 750
Sheffield, A. A., Majewski, S. R., Johnston, K. V., et al. 2012, ApJ, 761, 161
Shi, W. B., Chen, Y. Q., Carrell, K., & Zhao, G. 2012, ApJ, 751, 130
Siegel, M. H., Dotter, A., Majewski, S. R., et al. 2007, ApJ, 667, L57
Simion, I. T., Belokurov, V., Irwin, M., & Koposov, S. E. 2014, MNRAS, 440, 161
Skrutskie, M. F., Cutri, R. M., Stiening, R., et al. 2006, AJ, 131, 1163
Slater, C. T., Bell, E. F., Schlafly, E. F., et al. 2013, ApJ, 762, 6
Sollima, A., Gratton, R. G., Carballo-Bello, J. A., et al. 2012, MNRAS, 426, 1137
Sollima, A., Valls-Gabaud, D., Martinez-Delgado, D., et al. 2011, ApJ, 730, L6+
Stetson, P. B. 1987, PASP, 99, 191
Strader, J., Brodie, J. P., Forbes, D. A., Beasley, M. A., & Huchra, J. P. 2003, AJ, 125, 1291
The DES Collaboration, Bechtol, K., Drlica-Wagner, A., et al. 2015, ArXiv e-prints
Tonini, C. 2013, ApJ, 762, 39
Toomre, A. & Toomre, J. 1972, ApJ, 178, 623
Totten, E. J. & Irwin, M. J. 1998, MNRAS, 294, 1
Trager, S. C., King, I. R., & Djorgovski, S. 1995, AJ, 109, 218
van den Bergh, S. & Mackey, A. D. 2004, MNRAS, 354, 713
van der Burg, R. F. J., Muzzin, A., Hoekstra, H., et al. 2013, A&A, 557, A15
VandenBerg, D. A., Brogaard, K., Leaman, R., & Casagrande, L. 2013, ApJ, 775, 134
Vanhollebeke, E., Groenewegen, M. A. T., & Girardi, L. 2009, A&A, 498, 95
Velazquez, H. & White, S. D. M. 1995, MNRAS, 275, L23
Vivas, A. K. & Zinn, R. 2006, AJ, 132, 714
Vivas, A. K., Zinn, R., & Gallart, C. 2005, AJ, 129, 189

Watkins, L. L., Evans, N. W., Belokurov, V., et al. 2009, MNRAS, 398, 1757
White, S. D. M. & Rees, M. J. 1978, MNRAS, 183, 341
Williams, M. E. K., Steinmetz, M., Sharma, S., et al. 2011, ApJ, 728, 102
Yanny, B., Newberg, H. J., Grebel, E. K., et al. 2003, ApJ, 588, 824
Yanny, B., Newberg, H. J., Kent, S., et al. 2000, ApJ, 540, 825
York, D. G., Adelman, J., Anderson, Jr., J. E., et al. 2000, AJ, 120, 1579
Zentner, A. R., Kravtsov, A. V., Gnedin, O. Y., & Klypin, A. A. 2005, ApJ, 629, 219
Zinn, R. 1993, in Astronomical Society of the Pacific Conference Series, Vol. 48, The Globular Cluster-Galaxy Connection, ed. G. H. Smith & J. P. Brodie, 38–+
Zoccali, M., Hill, V., Lecureur, A., et al. 2008, A&A, 486, 177
Zoccali, M., Pancino, E., Catelan, M., et al. 2009, ApJ, 697, L22
Zolotov, A., Willman, B., Brooks, A. M., et al. 2009, ApJ, 702, 1058
Zucker, D. B., Belokurov, V., Evans, N. W., et al. 2006, ApJ, 650, L41

Samenvatting

De rol van galactisch kannibalisme in het heelal

Sterrenstelsels zijn systemen die bestaan uit sterren, planeten, stof, gas, ijsmoleculen en donkere materie. Ze worden gekarakteriseerd door de emissie van licht in een groot golflengtebereik waardoor wij de nucleaire (kern-) en chemische reacties kunnen bestuderen die de drijfveer zijn van de verschillende processen. De kernreacties vinden plaats in sterren terwijl de meeste chemische reacties zich afspelen in het zogenaamde interstellaire medium (gas wolken en stofdeeltjes) of in planeten en circumstellaire wolken. Sterrenstelsels worden geregeerd door de wetten van de zwaartekracht die alle elementen bij elkaar houden en de grondslag leggen voor de algehele structuur en evolutie.

De eerste sterrenstelsels zijn ontstaan uit hele kleine kiemen met bijzonder hoge dichtheid die zich bevinden in het hele Universum, als gevolg van de groei van donkere materie, gaswolken, en later de geboorte van sterren onder invloed van de zwaartekracht. Deze regio's met hoge dichtheid waren het resultaat van de kwantum fluctuaties die aanwezig waren na de Big Bang en zijn versterkt tijdens de zogenaamde Inflatie periode. Echter, de grootte van (en het aantal) sterrenstelsel dat vandaag de dag wordt waargenomen kan niet volledig worden uitgelegd door alleen gravitationele groei in acht te nemen gedurende de hele geschiedenis van het Universum. Het kan wel worden verklaard door een proces dat galactisch kannibalisme heet. In dit proces *eet de grotere vissen de kleinere*, wat zoveel inhoudt als dat het grootste (meest massieve) sterrenstelselde de kleinere (minder massieve) sterrenstelsels dichterbij doet komen, doet opsplitsen en het vrijgekomen materiaal in zich opnemen. Het grootste sterrenstelsel oefent in feite de eigen zwaartekracht uit wat leidt tot de vernietiging van het kleinere sterrenstelsel. Wanneer beide sterrenstelsel ongeveer een gelijke massa en grootte hebben noemen we dit proces *grote samensmelting* en als ze verschillende massa's hebben wordt het galactisch kannibalisme of *kleine samensmelting* genomend. Beide processen kunnen niet alleen de grootte en het aantal sterrenstelsels verklaren, maar ook hun geschiedenis en morfologie.

Maar galactisch kannibalisme is niet alleen een theoretisch concept aangezien sterrenstelselsamensmeltingen van verschillende groottes nu zijn waargenomen in een groot aantal sterrenstelsels. De zwaartekracht zorgt ervoor dat, mits er genoeg

tijd is (de leeftijd van het Universum is 13,800 millioen jaar!), veel sterrenstelsels telkens dichtbij genoeg komen om te kunnen samensmelten ondanks de grote afstanden tussen de verschillende stelsels.

In de context van het huidige kosmologische kader – het Λ Koude Donkere Materie model, dat de dynamiek en evolutie van het Universum probeert te verklaren – is galactisch kannibalisme een belangrijke drijfveer in de evolutie van sterrenstelsels en naar deze twee modellen samen wordt vaak verwezen als het Hiërarchische Vormings scenario. Deze theorie is succesvol gebleken in het uitleggen van de evolutie van het Universum zowel op kosmologische als galactische lengte schalen.

Het *levende* en *fossiele* archief van sterrenstelsels

Aangezien het proces van galactisch cannibalisme al sinds het begin van het Heelal gaande is, is het logisch om niet alleen naar huidige voorbeelden te zoeken, maar ook naar sporen van vroegere gebeurtenissen.

Huidige of recente episodes van galactisch kannibalisme kunnen herkend worden aan het sterrenpuin en het overblijfsel van het melkwegstelsel dat uit elkaar gerukt wordt. Omdat het een langzaam process is, kan het satellietsterrenstelsel vaak een aantal keer om het grotere stelsel heen draaien voordat het volledig vernietigd is. Terwijl het satellietstelsel geleidelijk gas en sterren verliest, blijven deze bestanddelen een baan volgen die dicht bij de oorspronkelijke baan ligt maar worden ze uitgespreid zodat ze een stroom of schil vormen, afhankelijk van de ellipticiteit en energie van de baan (zie Figuur 1.2 voor een voorbeeld).

Oude episodes zijn moeilijker te identificeren omdat het sterrenpuin de oorspronkelijke baan niet meer volgt, maar vermengd is met de sterren van het grotere stelsel. Desondanks kan informatie over chemische samenstelling en kinematica gebruikt worden om groepen sterren met een gezamenlijke oorsprong te vinden, mits hun gezamenlijke eigenschappen afwijken van de rest van de populatie.

Bolhopen, kleine ronde groepen sterren die geboren worden uit dezelfde gaswolk in de buitendelen van sterrenstelsels, kunnen ook door getijden uit elkaar getrokken en door hun sterrenstelsel gekannibaliseerd worden.

Ons sterrenstelsel, de Melkweg, is geen uitzondering wat betreft galactisch cannibalisme en hiërarchische groei. Huidig onderzoek suggereert dat de Melkweg de afgelopen 10,000 miljoen jaar geen grote "merger" (een samensmelting tussen twee sterrenstelsels met vergelijkbare massa) heeft ondergaan, maar verschillende kleine samensmeltingen. Bovendien is het op dit moment verschillende satellietstelsels en bolhopen aan het kannibaliseren. Dit maakt de buitendelen van het Melkwegstelsel (het gebied ver van de schijf, de halo) een zeer interessant gebied.

Dit proefschrift

Dit proefschrift gaat over het bestuderen van de buitendelen van de Melkweg, met twee doelen: het bepalen van de onderliggende sterverdeling van de halo, en het identificeren en karakteriseren van nieuwe satellieten en van nieuwe sterstromen

als gevolg van kannibalisatie.

Het eerste doel staat beschreven in hoofdstukken 2 en 3. Dit werk is gebaseerd op waarnemingen gedaan met de Canada-France-Hawaii Telescope (CFHT) in Hawaii, de Isaac Newton Telescope (INT) in de Canarische eilanden en de VLT Survey Telescope (VST) in Chili. De halo van spiraalstelsels is een ijle, ellipsoidale verdeling van sterren die de schijf en centrale bulge omgeeft. Halo sterren zijn zeldzaam en staan ver weg, wat het moeilijk maakt om ze in statistisch interessante aantallen waar te nemen. Daardoor is het niet eenvoudig om de algemene structuur van de halo, zoals de vorm of het verloop van de dichtheid met afstand tot het centrum van de Melkweg, te bepalen. Met gevoelige breedbeeld camera's op de bovengenoemde telescopen (resp. MegaCam, WFC en OmegaCAM) hebben we halo sterren tot op grote afstand kunnen identificeren. Op basis van deze data hebben we kunnen aantonen dat de sterdichtheid afneemt met straal als een gebroken machtswet, en hebben we de vorm van de halo kunnen bepalen. De halo heeft een afgeplatte vorm (zoals een mandarijn of een walnoot, niet zoals een rechtopstaand ei), maar is vanaf de poolas bekeken praktisch rond.

Hoofdstukken 4 tot 6 gaan over het tweede doel. Eén van de belangrijkste uitkomsten van dit proefschrift is een cross-correlatie algoritme waarmee sterconcentraties kunnen worden gezocht in een twee-kleuren kaart bestaande uit vele kleine losse velden. Hiermee kunnen sterstromen, bolhopen of satellietstelseltjes geïdentificeerd worden. Met deze techniek is het mogelijk om twee-kleuren data te gebruiken waar voorheen minstens drie kleuren (fotometrische banden) nodig waren, wat een flinke besparing van waarneemtijd kan opleveren. Ook zijn nabije controle velden niet meer nodig. Het blijft wel zo dat een volledige meerkleuren kaart meer informatie bevat, maar deze techniek maakt het wel mogelijk om diepe archiefdata in te zetten voor dit soort analyse.

Met deze methode hebben we sterconcentraties gevonden die deel uitmaken van drie verschillende sterstromen (de Sagittarius, Orphan en Palomar-5 stromen), en nauwkeurige fotometrische afstanden tot deze sterren bepaald door gebruik te maken van bestaande metingen van de leeftijd en metalliciteit van deze populaties. In het bijzonder hebben we voor enkele delen van de Sagittarius stroom voor het eerst afstanden bepaald, en twee sterconcentraties geïdentificeerd die tentatief overeenkomen met de voorspelde positie van een nabije tweede staart van deze stroom.

We hebben ons algoritme ook gebruikt om dichtheidsconcentraties te zoeken in de buurt van bolhopen in de Melkweg. Als een bolhoop geassocieerd is met een belangrijke sterstroom dan kan dat er op wijzen dat deze sterhoop deel uitmaakte van de satelliet waaruit de stroom is ontstaan. Een kleine extra sterconcentratie nabij een bolhoop suggereert juist dat de bolhoop zelf aan het oplossen is, of wordt uiteengetrokken door de Melkweg. In totaal hebben we 23 bolhopen bestudeerd, en in 8 gevallen duidelijke sterconcentraties gevonden (met mogelijke detecties in nog 5). Aan de hand van schattingen van de aftanden tot die sterren, en enkele kinematische indicatoren, hebben we per geval bekeken of het om een bekende sterstroom ging, of om materiaal dat geassocieerd kon worden met de bolhoop.

In de meeste gevallen was er niet zo'n verband.

Tot slot hebben we de traditionele stertelling techniek toegepast op de eerste grote kaarten van het KiDS project op de VST, om te zoeken naar nieuwe stromen en satellieten. De verwachte structuren (zoals de Sagittarius stroom, de 'Virgo Overdensity' en de 'Eastern Band Structure') hebben we inderdaad teruggevonden, net als de 'dikke schijf' van de Melkweg en het einde van de Palomar-5 stroom. Met de huidige staat van de data hebben we echter geen nieuwe structuren kunnen ontdekken: de 140 vierkante graden KiDS data die we hebben geanalyseerd (10% van wat de uiteindelijke totale kaart moet worden), hoewel dieper dan eerdere data, beslaan slechts ~ 30 vierkante graden die niet eerder in kaart zijn gebracht, en zijn nog gefragmenteerd. Hier zal echter snel verandering in komen: er komen continu meer KiDS data binnen, op gebieden die nog niet eerder zijn waargenomen, wat de kans biedt op nieuwe ontdekkingen in de halo van de Melkweg.

Summary

The role of galactic cannibalism in the Universe

Galaxies are systems composed of stars, planets, dust, gas, ice molecules and dark matter, and they are characterised by the emission of light in a wide range of wavelengths, which allow us to study the nuclear and chemical reactions that power them. The nuclear reactions take place in stars, whereas most the chemical reactions take place in the so called interstellar medium (gas clouds and dust grains) or in planets and circumstellar clouds. Galaxies are governed by gravity, which holds together all their elements and sets the basic constraints for their overall structure and evolution.

The first galaxies formed out of very small overdense seeds spread throughout the Universe, through the gravitational accretion of dark matter and gas clouds and the later birth of stars. These overdensities were the result of quantum fluctuations that followed the Big Bang and were amplified during the Inflation period. However, the size (and number) of galaxies today cannot be fully explained by the simple gravitational accretion of gas over the whole history of the Universe. It is explained, though, by a process called galactic cannibalism. In this process *the big fish eats the smaller fish*, meaning that the largest (most massive) galaxy brings closer, breaks apart and incorporates the material of the smaller (less massive) galaxy. The largest galaxy is basically exerting its gravitational pull on the smaller galaxy in a destructive way. When both galaxies are of similar mass and size, we call this process *major merging*, and when they are of different masses, we call it galactic cannibalism or *minor merging*. Galactic cannibalism and major merging can explain not only the size and number of galaxies observed nowadays, but also their history and morphology.

But galactic cannibalism is not just a theoretical construct, since galaxy mergers of varying magnitudes have now been observed in a large number of galaxies. Despite the large distances between galaxies, provided enough time (the life time of the Universe is 13,800 million years!), gravity ensures that many galaxies will move close enough to each other to merge or to have one of them cannibalise the other, in a recurrent process.

In the context of the current cosmological framework —the Λ Cold Dark Matter model, which attempts to explain the dynamics and evolution of the

Universe—, galactic cannibalism is a major driver for galaxy evolution, and together they are often referred to as the Hierarchical Formation scenario. This theory succeeds in explaining the evolution of the Universe both at cosmological and galactic scales.

The *life record* and the *fossil record* of galaxies

Since the process of galactic cannibalism has been ongoing for most of the Universe's history, it is natural to search not only for current examples of it but also for the traces of previous events.

Ongoing or recent episodes of galactic cannibalism can be recognised by the stellar debris and the dissolving remnant of the galaxy being torn apart. Because galactic cannibalism is a slow process, the satellite galaxy often has time to complete a few orbits around the larger galaxy before being completely destroyed. As the satellite galaxy is progressively stripped off its gas and stars, these constituents keep a path close to the original orbit of the satellite, but spread out forming a stream or a partial shell, depending on the ellipticity and energy of the orbit (see Figure 1.2 for an example).

Old episodes are harder to identify since, by now, their stellar debris have already abandoned the original orbit and have mixed up with the "indigenous" stars. Nonetheless, both chemical tagging and kinematic properties can be used to group stars with a similar origin provided their collective fingerprint is different from that of the local stars.

Globular clusters, which are small spherical associations of stars mostly born from the same parental gas cloud in the outskirts of galaxies, can also be tidally stripped and cannibalised by their host galaxy.

Our host galaxy, the Milky Way, is no exception to the process of galactic cannibalism and hierarchical growth. The current research suggests that it has not undergone any major merger at least in the last $10,000$ million years (a merger between two galaxies of comparable mass), but instead various minor accretion events. In addition, it is currently in the process of cannibalising several satellite galaxies and a few globular clusters. This makes the outskirts of our galaxy (the region away from the galactic disk, known as the halo) a very interesting place.

This thesis

This thesis has focused on expanding our knowledge of the outskirts of our own galaxy, the Milky Way, with two particular aims. The first aim has been to understand the overall underlying distribution of stars in the halo, and the second aim has been to identify and characterise new satellite galaxies and stellar streams resulting from ongoing cannibalisation events.

The first aim is covered in chapters 2 and 3 and makes use of observations carried out with the Canada-France-Hawaii Telescope (CFHT) in Hawaii, the Isaac Newton Telescope (INT) in the Canary Islands and the VLT Survey Telescope (VST) in Chile. The halo of spiral galaxies is an ellipsoidal component that extends beyond the disk and the bulge of the galaxies, thinly populated with stars in

comparison to the other two components. Because of their low numbers and large distances, observing these stars in statistically useful numbers poses technical and instrumental challenges, and makes it difficult to infer general properties of the halo such as its exact shape or the dependence of the stellar number density with the distance from the centre of the Galaxy. Using extremely sensitive cameras in the previously mentioned telescopes (the MegaCam, the WFC and the OmegaCAM, respectively), we have obtained large samples of stars out to remarkable distances. With these data, we have been able to confirm that the density of stars in the halo decreases with distance as broken power law. We have also been able to set strong constraints in the shape of the stellar halo. These constraints indicate that the halo is moderately flattened towards the poles (as a mandarin or a walnut would be, as opposed to an egg standing vertical) but practically circular on its main plane (as seen from above).

The second aim is addressed in chapters 4 to 6. One of the main products of this thesis is a cross-correlation algorithm that allows us to exploit pencil-beam sky imaging surveys with only two colours to identify stellar overdensities in the halo, such as those that may be associated with streams, globular clusters or satellite galaxies. The power of this algorithm is that it yields competitive results where previously three colours (three photometric filters) were needed, reducing the observing time and costs. This algorithm also obviates the need for control or comparison sky fields near the target fields. Of course the traditional spatially-continuous wide-area surveys and the surveys with more than two colours still provide significant advantages, but this algorithm opens the door to using extremely deep, high quality archival data that has never been used before for this type of work.

Through this method, we have identified overdensities associated with three different streams (the Sagittarius stream, the Orphan stream and the Palomar 5 tails) and, in combination with independent measurements of the age and metallicity of the stars in those streams, we have derived accurate distances to them. Notably, we have expanded the catalogue of distance measurements to the Sagittarius stream along its Southern hemisphere tail and along its furthest Northern piece, and we have also identified two overdensities matching a predicted secondary nearby old wrap of this same stream, which needs further confirmation.

We have also used this algorithm in the search for stellar overdensities near globular clusters in the Milky Way. We do these in order to determine whether any of the globular clusters is associated with an underlying stream or overdensity. On the one hand, if a globular cluster was associated with a major stream, it would indicate that the globular cluster was part of the globular cluster system of the disrupted satellite galaxy that originated the stream. On the other hand, if a globular cluster was associated with a minor adjacent overdensity, it would suggest that the globular cluster was either slowly becoming internally unbound or that it was being cannibalised by the host galaxy. We have explored the vicinity of 23 globular clusters and found eight clear overdensities but potentially up to thirteen. Using distance estimations and the position of the overdensities in

the sky (and occasionally kinematic comparisons), we have analysed whether the overdensities could be associated with a known stream or to the adjacent globular cluster. The three situations (no association, association with a major stream and possible association with a new overdensity) appeared in the sample, with a majority of no association cases.

Finally, we have applied the traditional techniques of distance slicing and density mapping to the first wide-area maps from the VST KiDS survey, in order to search for new streams and satellites. In these data products we have successfully recovered the expected major halo structures (such as the Sagittarius stream, the Virgo Overdensity and the Eastern Band Structure) and the Galactic thick disk contribution, as well as the tail of the Palomar 5 stream. No new streams or satellites have been unveiled due to the currently small area of newly sampled sky ($\sim 30\,\mathrm{deg}^2$) and to the still rather patchy state of these newly sampled areas. However, as the KiDS observations keep coming in, more data in new areas of the sky will become available. With currently only 10% of the total survey analysed and most of the data so far targeting previously surveyed areas of the halo, the future KiDS data releases should bring the chance for exciting discoveries in the halo of the Milky Way.

Curriculum Vitae

I was born on May 29th, 1986 in Logroño, La Rioja, in Spain. The first years of my life I grew up in the city of Madrid and the town of Chinchón, until my family finally settled down in Collado Villalba (province of Madrid). I attended most of my elementary school at the Integrated Programme at the Padre Antonio Soler Conservatory, a curriculum combining primary school and the four years elementary grade in music.

Next I attended secondary school at Colegio Santa María –while continuing my formal education in music as an external student for two more years– and Colegio Parque, where I won a national narrative award for the international programme "Europe at School". I completed my last year of high school at Colegio San Agustín (Madrid, 2004), where I graduated with First Class Honours.

Soon thereafter I enrolled in the Complutense University of Madrid (UCM) and its five years degree in Physics. On my first two years (2005 and 2006) I was awarded the Schollar of Excellence grant by the Community of Madrid. During the summer of 2009 I was a fellow for the Canary Astrophysics Institute (IAC) within their Introduction to Research programme. In 2010 I embarked upon a light-pollution research project as a collaboration fellow in the UCM Observatory. Finally, in September 2010 I graduated as a *Licenciada* in Physics with a major in Astrophysics. During my undergraduate years I was an active member of the Amateur Astronomers Association of the UCM (including vicepresident in 2007) and the Group for Planetary Sciences.

In the fall of 2010 I started my PhD research at Leiden Observatory (Leiden Sterrewacht) under the supervision of Prof. dr. Koenraad Kuijken. My thesis research has consisted of the study of the stellar halo of the Milky Way within the context of galaxy formation and galactic cannibalism. In particular, I have focused on paremetrising the general structure of the halo and searching for tidal debris and satellites, using observations from international state-of-the-art telescopes. As an employee for Leiden Observatory, I have been an organizer of the National Astronomical Olympiad of 2012 and I have also been a teaching assistant for the Bachelor Research course (2012, 2013) and supervised two observing projects for the Bachelor Observing course (2014). In spring 2013 I was awarded a prize for Best Teaching Assistant of the Semester.

As of June 2015 I am switching careers and starting a job as a data scientist in London, United Kingdom.

Acknowledgements

What you get by achieving your goals is not as important as what you become by achieving your goals (Henry David Thoreau).

My first and foremost gratitude goes to the people of The Netherlands, for their support of public science and for having funded this PhD. Likewise, I am also grateful to the people who run and make NOVA (the Dutch Research School for Astronomy) possible.

My thesis work would have been quite harder if it was not for the invaluable help of Jelte and the vigilant company of Xander. Jelte, I have learned most of what I know about stellar populations from you, and that has made a great difference. I have also been lucky to count on a few collaborators who were always happy to advise and discuss ideas: Henk Hoekstra, Eline Tolstoy and Jorge Peñarrubia, thank you. In addition I have had the pleasure to collaborate with Julio Carballo-Bello and David Martínez-Delgado. Thank you both for your interest and your share of science, and for the opportunity to get involved in your project. To the factual powers in my research group, I am thankful for the thorough reviews of paper drafts, which always needed minor changes in the referee phase, and for the support towards a career change.

To the members of the 'lensing + other stuff' research group (Edo, Malin, Elisabetta, Stefania, Marijn, Cristóbal, Fabian, Ricardo, Margot, Massimo, Marcello), thank you for creating such an open and inquisitive atmosphere. A special mention goes to Remco, not only for teaching me so much regarding image stacks and Linux shell, but for so many lessons on Dutchness, your good sense of humour, the many talks on ice and fire and my first natural ice skating. It's always a pleasure to share a "bukje" and a good laugh with you. I am also grateful to the people at the "Pan-NL Local Group" research meetings, who regularly shared their enthusiasm, expertise and exciting new results, and provided the most stimulating environment for my thesis. It was a pleasure to work side-by-side with the organisers of the Nederlandse Astronomisch Olympiade 2012: Jens, Nienke, Renske and Irene, you are all great, reliable, enthusiastic hard-workers. Remember you can reach as far as you set your eyes upon, because you have the strength and the will it takes in you.

My time in Leiden and the Sterrewacht would have been quite different without the presence and sometimes guidance of Jeanette, Ernst K., Ernst de M., Rafa,

Sergio, Olmo, Pawel and some special friendships. Renske and Jesse, you have been my reference for everything Dutch, but more than that I appreciate having shared NOVA trips or salsa lessons, tips, goals and frustrations with you. For the 'Italian crew' –Silvia, Nicola, Marco, Alessandra, Fabio, Matteo, Thanja, Irene–, I would need more space than I possibly have to mention all the ways in which you have contributed to this thesis and my well-being. But lets say that learning to survive to the Dutch Winters and the PhD together, and sharing all the good experiences that come with it has been an outstanding experience. My office mates have been a great source of relief and *gezelligheid*: Ben, thanks for your positive mood and your patience towards those two annoying first year PhDs you were 'blessed' with; Silvia, I only wish I had got to know you earlier and better, and anyone moving into the office will be most lucky to have you as an office mate; Mattia, it's been a long and exhausting way, but I am happy I've had you to share so many thoughts, plans, hopes and random facts along the way. Among all the fun, friendly and attentive PhDs, a special thanks goes to Jeroen, Cristóbal, Clément, Vachail, Heather, Wendy, Carmen, David, Carl and Daniel H., for everything we have shared, and a big hug to those among the new batch I've had the chance to meet more: Gabriela, Aayush, Mieke and Eva. To my non-Sterrewacht friends, Fernando, Violeta, Bas and Theo, Alex, Tom and Emilio, you have provided me with many good moments, a fresh perspective and helped me keep the difficulties of a PhD in good perspective. Marion, having our paths come across has been both enriching and light-heartening. You are an outstanding professional and I thank you for having granted me with your unexpected friendship. Rhea, yours is one of those serendipitous friendships for which a blinking of the eyes would have been enough to miss on it, and I really cherish it. Dominique, Lorentz and Jannis, Andrea and Ludo: you've gone beyond the boundaries of friendship and made Leiden my home, and you are now forever the best kind of family, the type one gets to choose.

Of course one does not get on board a thesis without some previous key influential encounters in life. In Madrid, Enrique Maciá, Jaime Zamorano, Jesús Gallego, Francisco Anguita, Gema Piquero and J.P. García Villaluenga, you all provided the most stimulating environment and fed fuel to more than one scientific vocation. A special thank you goes to Marina Ramón-Medrano: without your flexibility and understanding, I would have never started a PhD in Leiden. At the different highschools I have walked, Luis Quirce, Maximino and Medina, Ofelia, Maria Ángeles and Carmela, you all contributed greatly to my interests and skills, and made the most of your disciplines and of me.

I've had the privilege of sharing scientific enthusiasm, intellectual curiosity, many Thursday paellas and a countless number of mind-blowing or hilarious conversations with my colleagues and friends from ASAAF: Zeta, Raúl, Claudia, Elena, Garrido, Cristian, Álvaro, Belén, Marta, Pablo, Irene, Lucía, Guillermo, Judith, Idoia, Íñigo, Jesús R., Mario, Alexandru, Dapid, Rafa Cercedilla... I have also been extremely lucky to have my time in The Netherlands overlap with that of Adrián, and become much closer friends in the meantime. David, Álex, Paco,

Sara and Ángela: the last ten years with you go far beyond ASAAF and extend into the realms of adventures, dreams and challenges. Your friendship is thrilling and energising, honest, deep and grounding. And life needs of Napoleon, a jedi, a reflective lady, an eccentric poet and a rugby fighter to keep its balance.

I have been granted in life with the constant, enriching and unquestionable friendship of a few people: Raquel, Patricia, Lorenzo, Álex and Gonzalo. Sharing life, curiosity, the Sierra and the Laguna with you, growing-up –and eventually old– together and rejoicing in each other's achievements is among the greatest treasures. Alejandro M., you are my oldest and most seasoned friend, and somehow we have managed to get through all the changes of childhood and our teenage years only to grow closer. You have taught me all I know about black and white or night photography, for which I am forever thankful, and sharing a day trip, a conversation or a picture session with you always reminds me of who I am.

The time of my PhD mostly overlaps one in which I have met and got to know a number of people in the beautiful region of Extremadura. To the Galufos I am most thankful for your warm welcome, your friendship and the love you show towards me. You are the most amazing non-blood family I have ever met, and I am honoured to be part of it. To Lupe, Antonio and Rubén, it's always a pleasure to be around such beautiful and high-quality people as you are. To Neli, Encarna, María and Javier, thanks for opening your doors to me with such generosity and warm hearts, and for making me a part of your lives.

To my parents, Derlinda and Augusto, I owe not just what I am, but most of who I am. My achievements are also your achievements. But most importantly, thank you for your guidance, your thoughts, your love of reading, for educating us in freedom, respect and responsibility and, above all, for making us "talked-children". I have been extremely fortunate to enjoy all my grandparents for long, and even have a third grandmother and a close grand-uncle. To all of you, thanks for your infinite love, your priceless example and the values you each impersonate: you are and have been the greatest role-models one could hope for. The full meanings of camaraderie, complicity and mutual understanding would be partially foreign to me if it was not for my brother, Ulises. Growing-up together had its ups and downs, as it has for most of siblings, but has had the reward of becoming who we are together and building the greatest of trusts. You are my brother, my paranymph and my first sword. And I couldn't be more grateful for the meaning of that.

Finally, thanks to my greatest and most unconditional ally, Jesús. You have been my strength in the hard times, a sharp and upright mind with whom to disentangle all of life's late conundrums, and the one encouraging me not to take negatives for granted. Thanks for sharing the best and worst of times with me, for keeping me close, for nurturing my self even when I did not realise what I needed most, and for embarking confidently and enthusiastically on the smallest and greatest journeys with me. My life today and my PhD would have been quite different if it was not for you. New endeavours lie now ahead of us, and I can't wait to face them and keep growing together.